This is to certify that the
dissertation entitled

TRANSPORT PHENOMENA IN HEAVY-ION REACTIONS

presented by

LIJUN SHI

has been accepted towards fulfillment
of the requirements for the

Ph.D. degree in Physics

Pawel Danielewicz
Major Professor's Signature

10/27/03
Date

TRANSPORT PHENOMENA IN HEAVY-ION REACTIONS

By

LIJUN SHI

A DISSERTATION

Submitted to
Michigan State University
in partial fulfillment of the requirements
for the degree of

DOCTOR OF PHILOSOPHY

Physics

2003

ABSTRACT

TRANSPORT PHENOMENA IN HEAVY-ION REACTIONS

By

LIJUN SHI

This thesis is devoted to various aspects of transport in heavy-ion reactions. In the beginning, I give a brief introduction of heavy-ion reactions, transport theory for the reactions and transport simulations. The subsequent discussions are devoted to different issues. First, a phenomenological phase-transition model for nuclear matter is introduced in order to understand the neutron enrichment in the midrapidity source in a heavy-ion reaction. The effect of cluster formation process on the neutron enrichment is discussed by considering droplet formation in the gas phase. The variational nature of the results in the phenomenological model is utilized to understand isospin transport process during a heavy-ion reaction. Moreover, microscopic transport theory, for uses in heavy-ion reaction transport simulations, is introduced relying on Landau theory. As one of the key ingredients of microscopic transport theory, the mean field interaction is introduced into the theory through the energy-density functional. The functional provides the nuclear equation of state (EOS), and both the momentum independent and momentum dependent mean fields are discussed. Given the recent interest in systems with varying isospin content, I also discuss isospin dependence of the EOS within the functional method. The symmetry potential, which measures the difference in optical potentials between the proton and neutron, is parameterized in either momentum independent or momentum dependent form. I also discuss some practical issues for transport simulations, like the initialization of a simulation and the numerical methods for integrating the Boltzmann equations. Besides the mean fields within transport, I discuss the in-medium cross section. Next, the transport coefficients are derived

from a systematic expansion of the Boltzmann equations. The isospin diffusivity, shear viscosity and heat conductivity are calculated using free N-N cross section. Finally, transport theory is used to simulate heavy-ion reactions. Within transport simulations, I discuss the spectator-participant interaction, and the effects of such interaction on the development of elliptic flow, as well as on the dynamics of the spectators. The changes of the spectator properties after a collision are linked to the nuclear equation of state. Spectator acceleration by the reaction is observed in the simulations of a heavy system at low impact parameter. Transport simulations are also employed to understand isospin diffusion process in a heavy-ion reaction. It is found that isospin dependence of the mean field and isospin diffusion process are closely linked. The results from the simulation are compared with that from an experiment, and the experimental results favor an isospin stiff type of nuclear EOS.

For Jin

Acknowledgements

I would like to express my sincere gratitude to my advisor, Prof. Pawel Danielewicz, for his insightful guidance, invaluable encouragement and countless support. I started my Ph.D. pursuit five years ago, with absolutely no experience in theoretical research. It is the enthusiasm he has toward research that attracted me into the field of heavy-ion reactions in the first place. With his strong background in field theory and nuclear reaction theory, and his broad knowledge in many areas of physics, Pawel could often show me the destination at the beginning of my researches. His intuition and persistency are the key reasons I could successfully finish each of the research topics. I also would like to thank him for allowing me to take a formal class in programming, and the experiences and rules learned from the class are invaluable to the computer programs I wrote later on. Pawel also gives me numerous advices on writing papers and dissertation, and the experiences I learned from him is invaluable.

I am much obligated to Prof. Bill Lynch for his encouragement and many advices. Also special thanks to Betty Tsang, for her push on the idea of isospin diffusion. She is an exceptional scientist, with strong intuition and persistence. Her requests and ideas inspired my research on isospin physics.

I am deeply obliged to Prof. C. P. Yuan for his encouragement. His ideas of the simplicity in physics is always an inspiration to me. And he also encouraged me to pursuit a degree in theoretical physics.

I would also like to thank Prof. Scott Pratt, Prof. Mark Dynkman and Prof. Giuseppe Verde for being so kind to be in my Ph.D. guidance committee and for offering many helps during my studies. Scott and Giuseppe carefully read through my thesis, and gave me numerous helps in Grammar. Mark also gave me advises on how to improve the readability of the thesis.

I also would like to express my special thanks to Prof. Vladimir Zelevinsky. I learned a lot from his lectures on many-body theory and from the discussions with

him. No matter how difficult the questions is, he can always explain it in simple ways for the students to understand.

I would like to thank my friends Wanpeng Tan, Tianxiao Liu and Hushan Xu. I learned a lot from them, especially about the ideas and details from the experiment side of nuclear reaction studies.

Also I would like to thank the Brown family and the Simon family for helping me out and giving me a home away from home.

At last but not the least, I would like to thank my parents and my parents in law for their faith in me. My special thanks to my wife Jin, for her endless love. I would not be able to go through all the challenges in the Ph.D. research without their support and understanding.

Table of Contents

List of Tables

List of Figures

LIST OF ABBREVIATIONS

AMD ..... Antisymmetrized Molecular Dynamics

BUU ..... Boltzmann-Uheling-Ulenbeck

EOS ..... equation of state

HG ..... Hadron Gas

HIC ..... Heavy-Ion Collisions

IEOS ..... equation of state based on isospin dependent mean fields

LGP ..... Liquid-Gas Phase

LHC ..... Large Hadron Collider

MD ..... Momentum Dependence

MD EOS ..... equation of state based on momentum dependent mean fields

MD IEOS ..... equation of state based on momentum dependent mean fields sensitive to isospin asymmetry

MF ..... Mean Field

MI ..... Momentum Independence

MI EOS ..... equation of state based on momentum independent mean fields

MI IEOS ..... equation of state based on momentum independent mean fields sensitive to isospin asymmetry

NS ..... Neutron Star

QCD ..... Quantum Chromodynamics

QMD ..... Quantum Molecular Dynamics

QGP ..... Quark-Gluon-Plasma

RHIC ..... Relativistic Heavy-Ion Collider

RIA ..... Rare Isotope Accelerator

SMM ..... Statistical Multifragmentation Model

LIST OF FREQUENTLY USED SYMBOLS

A	Baryon number.
a_s	Coefficient of the gradient term in the energy density in Eq. (3.21).
$\langle A \rangle$	Average mass number for a spectator.
b	Impact parameter in a heavy-ion collision.
B/A	Binding energy per nucleon.
$\mathbf{d}_{12}$	Isospin-asymmetric thermodynamic driving force of Eq. (4.24).
D_δ	Binary diffusion coefficient.
D_I	Isospin diffusion coefficient.
e	Energy per nucleon.
E	Net energy.
$\tilde{e}$	Energy density per unit volume.
$\tilde{e}_0$	Energy density per unit volume of Eq. (3.23), excluding isospin-dependent interaction energy.
$\tilde{e}_I$	Isospin-dependent part of the energy density per unit volume in Eq. (3.23), associated with interactions.
$\tilde{e}_{kin}$	Kinetic energy density per unit volume in Eq. (3.1a).
$\tilde{e}_{int}$	Potential energy density per unit volume in Eq. (3.1a).
$\tilde{e}_{grad}$	Energy density per unit volume from the gradient correction term defined in Eq. (3.21).
$\tilde{e}_{coul}$	Coulomb energy density per unit volume.
$\tilde{e}_{NM}$	Energy density for homogenous nuclear matter in Eq. (3.19).
$\mathcal{E}$	Electric field in Chapter 4.
$\overline{E}$	Lattice energy within the Hamiltonian Method Eq. (3.82).
$\underline{E}$	Average kinetic energy per particle utilized in Chapter 4.

e_{sym}^{kin}	Kinetic contribution to the symmetry energy in Eq. (3.47).
e_{sym}^{int}	Interaction contribution to the symmetry energy in Eq. (3.47).
e_{sym}	Symmetry energy in Eq. (3.47).
$\langle E^*/A \rangle$	Excitation energy per nucleon for the spectator.
f	Free energy per particle.
$\mathbf{F}$	Force.
$\mathcal{F}$	Net free energy of a system.
$f(\mathbf{p}, \mathbf{r}, t)$	Quasiparticle distribution function.
f_y	Isospin-dependent part of the free energy per nucleon in Eq. (2.1).
$\tilde{f}$	Pauli blocking factor $\tilde{f} = 1 - f$.
$f^{(0)}$	Fermi-Dirac distribution in Eq. (4.17).
F_0^a	Spin-antisymmetric Landau coefficient.
F	Sideward-flow parameter.
g	Spin-degeneracy factor.
I_{ij}	Linearized integrals for collisions between particle i and j, defined in Eq. (4.21).
J_i	Collision integral for particle i in Eq. (4.13).
K	Compressibility of nuclear matter at normal density.
k_T	Coefficient ratio in Eq. (4.40).
$\mathcal{K}_X^>$	Loss term due to collisions in the Boltzmann equation (3.14).
$\mathcal{K}_X^<$	Gain term due to collisions in the Boltzmann equation (3.14).
m	Particle mass in vacuum.
$m(\rho_s, \beta)$	Medium-modified Lorentz mass.
m^*	Quasiparticle effective mass at the Fermi momentum.
m_{iso}^*	Effective mass isospin dependence parameter defined in Eq. (3.65).
n	Nucleon density in Chapter 4.
$\mathbf{p}$	Quasiparticle momentum.

$\mathbf{P}$	Net momentum vector.
P	Pressure.
p_f^e	Electron Fermi momentum.
p_F	Fermi momentum.
p^μ	Covariant momentum $p^\mu = (\epsilon, \mathbf{p})$.
p_f^n	Neutron Fermi momentum.
p_f^p	Proton Fermi momentum.
$\langle P^X/A \rangle$	Average in-plane transverse momentum per nucleon for the spectator.
$\Delta\|\langle \mathbf{P}/A \rangle\|$	Change in the average c.m. momentum per nucleon for the spectator.
$\overline{\overline{P}}$	Kinetic pressure tensor.
$\mathbf{Q}$	Heat flux.
R^{nn}	Ratio of the real to imaginary parts of the neutron-neutron scattering amplitude in Eq. (3.59).
R^{pn}	Ratio of the real to imaginary parts of the proton-neutron scattering amplitude in Eq. (3.59).
R^{pp}	Ratio of the real to imaginary parts of the proton-proton scattering amplitude in Eq. (3.59).
S_α	Form factor in the Lattice Hamiltonian Method.
$T_{\rm lab}$	Beam energy.
$T^{\mu\nu}$	Energy-momentum tensor.
t_3	Third component of particle isospin.
t_H	Isospin equilibration time.
u^μ	Covariant velocity $u^\mu = (\gamma, \gamma\mathbf{v})$.
U_{iso}^X	Isospin dependent part of the nucleon optical potential in Eq. (3.31).
U_n	Neutron optical potential.
U_p	Proton optical potential.
U_{grad}	Potential related to the gradient correction in Eq. (3.30).

U_T	Density-dependent factor in the isospin dependent part of the scalar potential.
U_{opt}	Optical potential in Eq. (3.5).
U_{sym}	Symmetry potential in Eq. (3.39).
U_{TC}	Density-dependent factor in the optical-potential term stemming from the self-consistency requirement with regard to isospin dependence in Eq. (3.43).
U^v	Potential resulting from the self-consistency requirement in the case of a density-dependent velocity, given by Eq. (3.35).
v_2	Elliptic-flow parameter.
V_n	Neutron optical potential from the T-matrix approximation.
V_p	Proton optical potential from the T-matrix approximation.
$\mathbf{v}$	Quasiparticle velocity.
y_{cr}	Critical proton fraction in Eq. (3.69).
Z	Charge number.
β	Used to represent isospin asymmetry in Chapter 3.
γ	Lorentz contraction factor $\gamma = 1/\sqrt{1-v^2}$.
$\mathbf{\Gamma}$	Dissipative particle flow.
δ	Isospin asymmetry.
$\Delta\mu$	Chemical potential conjugate to isospin asymmetry in Chapter 2.
ϵ_F	Fermi energy.
$\tilde{\epsilon}_p^F$	Proton Fermi energy.
$\tilde{\epsilon}_n^F$	Neutron Fermi energy.
η	Shear-viscosity.
ϵ	Quasiparticle energy.

κ	Heat conductivity.
μ'_{12}	Isospin asymmetric chemical potential in Sec. (4.3.3).
ξ	Reduced density.
Π^{δ}_{12}	Coefficient multiplying the asymmetry gradient in the isospin asymmetric driving force in Eq. (4.29c).
Π^{P}_{12}	Coefficient multiplying the pressure gradient in the isospin asymmetric driving force in Eq. (4.29a).
Π^{T}_{12}	Coefficient multiplying the temperature gradient in the isospin asymmetric driving force in Eq. (4.29b).
ρ	Used to represent baryon density and, in Chapter 4, the net mass density.
$\rho_{ch}(\mathbf{r})$	Charge density.
ρ_c	Central density for participant matter.
ρ_0	Normal density $\rho_0 = 0.16$ fm^{-3}.
ρ_s	Scalar baryon density.
$\rho_{\rm bnd}$	Bound particle density.
σ_{nn}	Neutron-neutron cross section.
σ_{pn}	Proton-neutron cross section.
σ_{pp}	Proton-proton cross section.
σ_{NN}	Nucleon-nucleon cross section.
$\Phi(\mathbf{r})$	Coulomb potential.
ϕ	Azimuthal angle.
∇	Spatial gradient.
$\overline{\overline{B}}$	Tensor.
$\overset{\circ}{\overline{\overline{B}}}$	Traceless tensor.
$\mathbf{B}$	Vector.
$\{\cdot,\cdot\}$	Brace product.
$[\cdot,\cdot]$	Square-bracket product.

Chapter 1: Introduction

Much research has been recently done on the properties of matter at extremely high density, which is many orders of magnitude higher than the ordinary matter we encounter everyday. The typical baryon density of nuclear matter is of the order of $\rho_0 = 0.16\,\mathrm{fm}^{-3}$, which, when converted into mass density, is about $10^{27}\,\mathrm{g/cm}^3$. For comparison, the density of water is $\rho(\mathrm{water}) = 1\,\mathrm{g/cm}^3$, and even the density of the most dense metal is only $\rho(\mathrm{Os}) = 22.5\,\mathrm{g/cm}^3$.

When the high density is generated in reactions, the temperature of the matter is also often high. The typical temperatures of our interest here are in the range of a few MeV to a few hundred MeV. If we convert the scale of MeV to regular temperature scale, 1 MeV is equivalent to about 10 billion degrees Kelvin. Room temperature is about 300 K and even the surface temperature of the Sun is only 6000 K.

High temperature and density matter, or hot dense matter, has some specific established and/or speculated properties. Fig. 1.1 is a schematic phase diagram of dense matter. The horizontal axis is density in units of normal density, and the vertical axis is temperature. Normal nuclear matter at ($\rho = \rho_0, T \sim 0$) represents the liquid phase. The liquid-gas phase (LGP) transition region at the lower left corner of the figure is characterized by temperatures less than $\sim$ 15 MeV and densities below normal density ($\rho/\rho_0 < 1$). The quark-gluon plasma (QGP) phase is likely characterized by temperatures of more than 170 MeV at low densities, and it might exist at lower temperatures if the densities are high. The hadron gas (HG) phase exists at intermediate temperature and density. The neutron star (NS) density region extends from low densities up to more than 10 times normal nuclear matter density. The typical temperatures are less than 10 MeV for newly born neutron stars and less than 0.001 MeV for cold neutron stars. The line that

separates the QGP phase from the HG phase is the phase coexistence and/or transition region. One of the theories predicts a cross-over phase-transition at lower density, a first order phase transition at higher density and a critical point (the solid square symbol) that separates the two phase transitions, cf. Fig. 1.1. The chemical freeze-out points reached at SPS and RHIC experiments are plotted here as open symbols. The compression reached in heavy-ion collisions (HIC) is indicated by the solid line and the expansion of nuclear matter right after the maximum compression is indicated by the dashed lines.

In the study of the hot dense matter, heavy-ion reactions offer advantages over other methods. Though the dense matter exists in neutron stars, only indirect information may be extracted from the astronomical observations. The Quark-Gluon Plasma phase and dense hadron gas phases, likely existed in the early stage of the Universe (about 15 billion years ago) but are quite inaccessible today. Nuclear structure studies have provided us much information about nuclear matter properties, but only at around normal density and at low temperature. Heavy-ion reactions, during which the matter goes through a compression and an expansion stage, are a true testing ground for the hot dense matter. The maximum compression in a heavy-ion reaction could reach a few times normal nuclear matter density in a head-on collision, and could possibly produce a QGP phase at the highest reaction energies. The expansion of nuclear matter after the compression stage usually leads to a freeze-out for interactions at subnormal densities ($\rho < \rho_0$). The freeze-out temperature and density could be in the phase transition regions (QGP to HG phase transition , or LGP), or in the hadron gas phase.

The specific regions of the phase diagram and the type of the strong-interaction physics that dominates the reactions depends on the incident energy. Thus, the highest energy reaction experiments at relativistic heavy-ion collider (RHIC) and future large hadron collider (LHC) explore the most dense matter, where quarks and

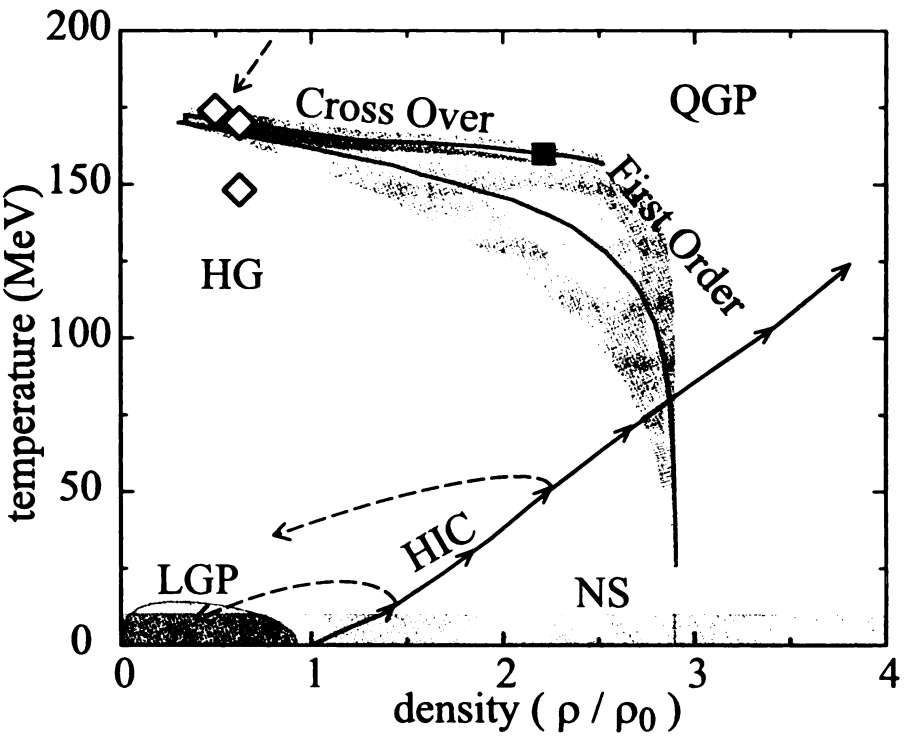

Figure 1.1: Schematic phase diagram for the hot dense matter. The shaded region at the lower left corner is the liquid-gas phase (LGP) transition region for symmetric nuclear matter (adapted from [1]). The shaded region at low temperature but with densities ranging from subnormal density all the way up to several times normal nuclear matter density, refers to matter that occurs in neutron stars(NS). The hadron gas (HG) region lies at intermediate temperature and density region. The very high density and temperature region corresponds to the quark-gluon-plasma phase (QGP). The two lines that separate the hadron gas phase from the quark-gluon-plasma phase represent the phase transition region converted from the two lattice predictions [2] and [3]) with excluded volume corrections from [4]. The solid square is the critical point that separates a cross over phase transition from a first order phase transition [2]. The open symbols represent the chemical freeze-out points from SPS and RHIC experiments [4]. The head-on heavy-ion collision will likely follow the arrows on the solid line, starting at cold normal nuclear matter ($\rho = \rho_0$, $T = 0\,\mathrm{MeV}$) ([5]). The maximum density and temperature achieved are determined by the incident energy. After the compression to maximum density, the reaction system expands and cools as indicated by the dashed lines. Some low energy reaction systems will dive into the liquid-gas phase transition region. The high energy reaction systems could enter a QGP phase.

gluons become the elementary degrees of freedom and quantum chromodynamics (QCD) is the basic theory. There are many interesting issues in the highest energy reactions, including the possible occurrence of the QGP phase, the degree of thermalization, the production of exotic particles and collective flow. Reactions at lower energies, often termed as intermediate energies, are violent enough to excite the system to very high temperature, but not enough to break the internal structure of the hadrons. The description of the interactions with only hadrons and mesons is sufficient for the intermediate reactions. The direct application of QCD theory at the low energies is somewhat difficult due to confinement; instead, effective nuclear interactions are often employed in the theoretical studies. My Ph.D. research has mostly concentrated on the heavy-ion reactions at intermediate energies.

The research at intermediate energies involves many topics of interest, including the nuclear equation of state (EOS), collective flow, the possible liquid-gas phase transition, and recently also isospin physics. The nuclear equation of state describe the energy-density relations in nuclear matter. The flow phenomena are results of the compression of nuclear matter during heavy-ion reactions, and is a primary tool for the studies of EOS. The liquid-gas phase transition has been predicted long ago, but its actual impact on a heavy-ion reaction is still under debate. Isospin physics is relatively new, and is mostly spurred by the development in rare isotope facilities and by the success in the nuclear structure research. Here I will give a brief introduction to these topics at intermediate energies.

Compared to the phase transitions common in everyday life, the liquid-gas phase transition in heavy-ion reactions occur in an environment complicated by small size of the reacting system, the strong nature of the nuclear forces and the nonequilibrium aspects of the reaction. The multifragmentation process in heavy-ion reactions, as a critical phenomena, is often thought to be closely related to the LGP transition. The multifragmentation process refers to the process where

large number of particles were produced in the energetic heavy-ion reactions; and the produced particles include free nucleons, deuterons, tritons, alpha particles, and all the way to very heavy clusters. Studies of multifragmentation processes reveals its universal behavior, and critical exponents are determined from experiment [13, 14, 15]. Some recent work has concentrated on the caloric curve extracted from heavy-ion reactions, even though the use of isotopic temperature is still questioned. One of the experimental caloric curves is shown in Fig. 1.2, and the appearance of a plateau in the isotope temperature as a function of excitation energy is attributed to the latent heat in the phase transition. The liquid-gas phase transition and phase coexistence, if present in heavy-ion reactions, could bring in new phenomena, which are often explored on a phenomenological basic. One example of such exploration for the liquid-gas coexistence region will be shown in Chapter 2.

The research on the nuclear equation of state combines both experimental and theoretical effort. The development of collective flow is closely related to the pressure build-up during the compression stage of reactions, and gives us information about the pressure and particle density relation (that is, the EOS). But such information is hard to extract directly because of the complex evolution of the reaction system. The particles measured in the experiments are produced through out the emitting process from the beginning of compression stage till the end of the expansion stage, and it is difficult to know when the particles are produced. However, microscopic transport theory could simulate the dynamic reaction, reproduce the particle emission process, and link the observed flow to the nuclear EOS. Transport simulation has become an important tool for understanding the dynamics of the heavy-ion reactions.

As an example of the research on nuclear equation of state, Fig. 1.3 shows one of the flow signals F measured in experiments as well as simulation results for the flow signal. The flow F measures the magnitude of the sideward flow, which

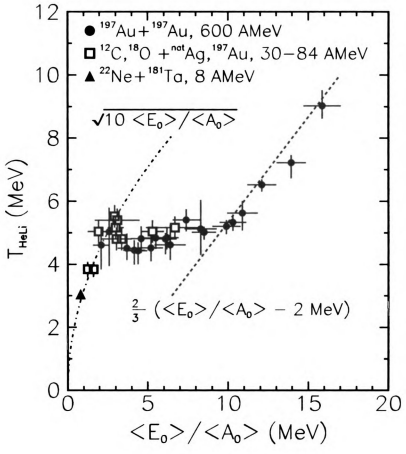

Figure 1.2: Experimental caloric curve of nuclear matter. The symbols represent the isotope temperature T_{HeLi} as a function of the excitation energy per nucleon. The dashed lines for $T = \sqrt{10 < E_0 > / < A_0 >}$ and $T = 2/3(< E_0 > / < A_0 > -2\text{MeV})$ are interpreted as the caloric curve of the liquid and the gas phase respectively, and the plateau region in between the two curves is believed to be related to the liquid-gas phase transition. (from [6]).

represents the collective deflection of particles away from the beam direction in the reaction plane. At different beam energy, the compression and pressure build up in the reaction region will be different, thus causing different deflection of particles. The different lines in the plot represent the simulation results with different EOS

and are labeled by the corresponding compressibility value for that particular EOS. Systematic studies of the sideward flow from experiment and theory were able to greatly constraint the uncertainties of the nuclear equation of state, eliminating some of the very stiff or very soft type of EOS (see [16] for a more comprehensive review on this subject).

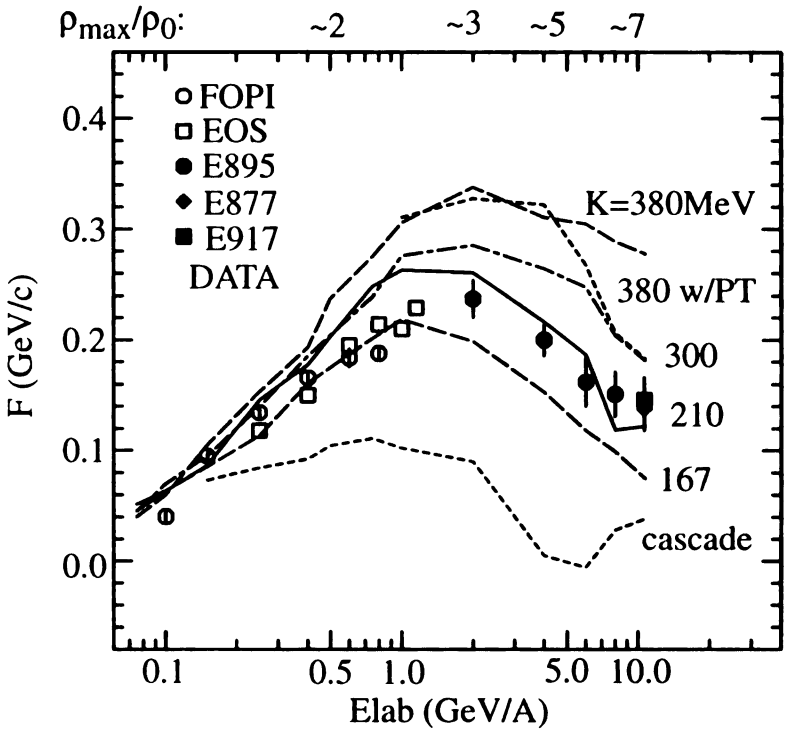

Figure 1.3: The flow parameter F as a function of energy. The symbols represent the experimental result for sideward flow at different energies. The lines are theory prediction for the flow, and different equation of states are labelled by their corresponding compressibility value. (from [7]).

In microscopic transport simulations, the nuclear equation of state often enters through a parameterized form for practical reasons. The nuclear EOS obtained from various microscopic theories are often quite complicated, and the results based on different assumption for the nuclear force often differ considerably. On the other hand, as transport simulations are already quite involved, a simplified form of the EOS can simplify transport simulations. The validity of the adopted EOS form is

checked when comparing results from simulations and experiments. As the guidelines for the parameterization of the EOS, the parameterized form should be simple enough to be easily incorporated into transport simulations and also be versatile enough to accommodate the different features of the microscopic predictions. I will introduce the parameterization method in Chapter 3, and the parameterized mean field will then be used in the simulations in Chapter 5.

In microscopic transport theory, the mean field is often used in either a momentum independent (MI) or a momentum dependent (MD) form. The MI form, with only density dependence, was used to explain the systematics of the sideward flow and was quite successful. But pure density dependence is not enough to explain the more detailed experimental results, especially the momentum dependence of the elliptic flow signals. Elliptic flow is a measure of the squeeze-out of nuclear matter and has been successfully used for determining the momentum dependence of the mean field. The momentum dependence of the mean field can be seen in Fig. 1.4, where the optical potential is plotted as a function of both density ρ and momentum k. The implementation of the momentum dependence is more difficult, and will be also shown in Chapter 3.

The recent progress in rare isotope facilities has also raised interest in the isospin degree of freedom at high densities. The term isospin refers to the pair of similar particles, the proton and the neutron, which are almost identical in nuclear matter when the electric charge difference is ignored. In many transport simulations, the nuclear interaction differences between protons and neutrons are simply ignored, or in other words, these simulations only explore the reactions in the symmetric nuclear matter limit. Such a simplification is used because of the limited beam and target combinations, but needs to be refined in view of the rare isotope beam reactions offered by the future facilities. The isospin dependence of the nuclear equation of state is often expressed in terms of symmetry energy. An

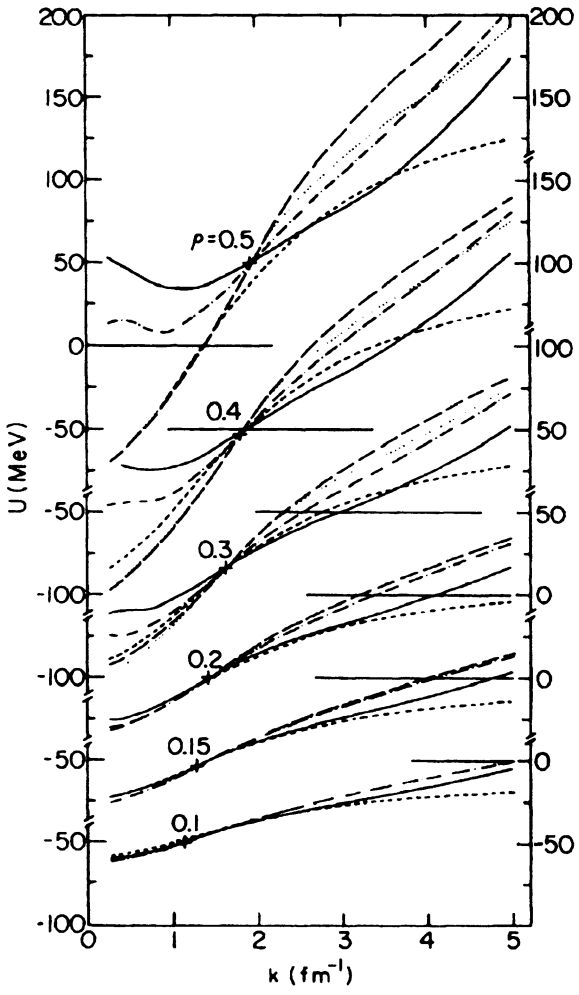

Figure 1.4: An illustration of the momentum dependence of the mean field. The optical potential U is not only a function of density ρ, but also a function of momentum k. The different lines represent different results from different microscopic theories. (from [8]).

elementary illustration of the concept of symmetry energy is shown in Fig. 1.5. Symmetric matter is represented by the lower line, while pure neutron matter is represented by the upper line. The difference between the two lines is the symmetry energy, which expresses the effect of the isospin on nuclear matter energy density.

As with the case of the symmetric matter, the nuclear equation of state based on isospin dependent mean fields (IEOS) could also be put into either a MI form or a MD form. Specific parameterizations of IEOS are shown in Chapter 3.

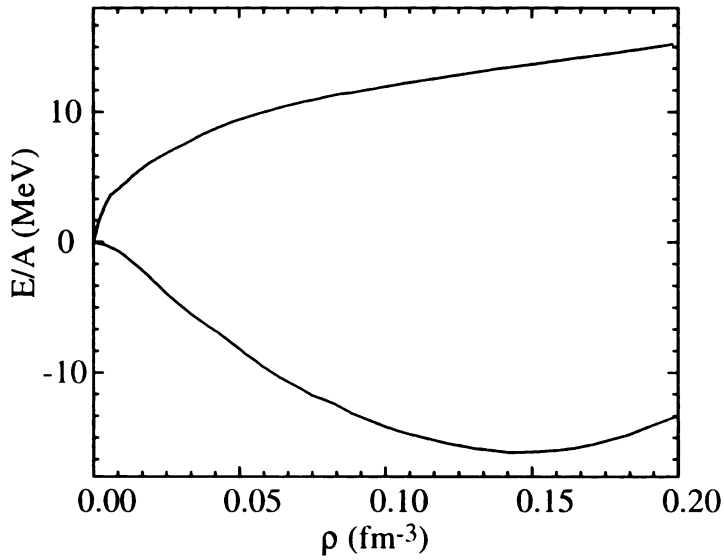

Figure 1.5: The concept of symmetry energy. The top line is the energy density for pure neutron matter and the lower line is that for symmetric nuclear matter. The difference of the two line is the symmetry energy. (from [9]).

In the simulation of heavy-ion reactions, microscopic transport theory has a close relation to the hydrodynamic theory. In fact, microscopic transport theory could reproduce the hydrodynamic equations for high density matter. Such a close relation makes it possible to use certain concepts in both theories. If the hydrodynamic limit is valid for heavy-ion reactions, then the nuclear EOS would exclusively determine the dynamics of the reaction. Microscopic transport theory, which does not make such an approximation, still shows the importance of the nuclear EOS on the evolution of the reaction system. In hydrodynamic theory, the elementary transport properties of matter are often characterized by transport coefficients. Even though a direct application of the transport coefficients is not easy because of the complex nature of the reactions, the transport coefficients still

could be used in the understanding of the basic transport process in the reactions and serve as bridge to the transport process in the infinite nuclear matter limit. The transport coefficients could be calculated analytically from transport theory in the small perturbation limit. As an example, the isospin diffusion coefficient is calculated in Chapter 4. The calculated isospin diffusion coefficient is then used in Chapter 5 to gain an understanding of the isospin transport process in heavy-ion reactions. The analytic solutions, such as that for the transport coefficients, are limited to a few cases where transport equations could be solved exactly. For heavy-ion reactions, the transport equations with complicated initial conditions are difficult to solve, and we often resort to simulations.

Transport simulations not only reproduce the particle emission patterns, but also provide a model space for understanding the dynamics of the reactions. There are many factors that affect the simulation results, and we can vary each individual factor separately in the model to find the most relevant factors. We can find not only what happens after the reaction, but also what happens during the reaction through a simulation. Such information about the intermediate steps gives us additional help in the understanding of the heavy-ion reactions. I will present two examples of transport simulations in Chapter 5.

In the first example of transport simulations, I try to understand the interaction of the spectator with the participant region during a heavy-ion reaction. The concept of the spectator and the participant regions is illustrated in Fig. 1.6. The participant region refers to the strongly interacting hot zone in the middle, where the opposite moving nuclear matter collide with each other; while the spectator regions refer to the forward and backward moving zone that do not directly interact with the opposite moving matter.

The interaction between the participant and the spectators has two important effects. First, the interaction strongly affects the development of collective motion in

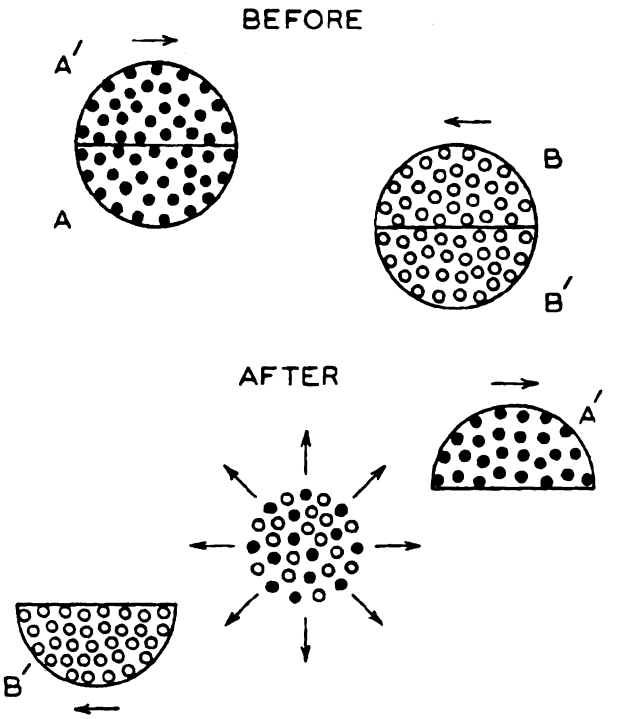

Figure 1.6: The concept of participant and spectators in a heavy-ion reaction. The regions initially labelled A and B collide with each other, go through a violent process and form a single hot emitting source, which is called the participant region. The regions labelled A' and B', on the other hand, are only moderately excited and do not actively participate the reaction. They are called the spectator regions. (from [10]).

the participant region and thus links collective flow to the nuclear EOS. Second, the interaction also affects spectator motion. The link between the participant matter motion and the nuclear EOS has been explored extensively, but less is known about the spectator motion after a heavy-ion reaction. To gain a more complete understanding of the reaction dynamics, I will explain the spectator-participant interaction and the impact on the spectators in Chapter 5.

In the second example of transport simulations, I will try to understand isospin diffusion process during a heavy-ion reaction. The basic idea of isospin diffusion is illustrated in Fig. 1.7. In the initial system, the projectile and the target have

different isospin concentration, and are shown with different colors. During the reaction, the projectile-target could interchange isospin content. After the reaction, the projectile (or the target) picks up or loses isospin. The change of isospin concentration in the projectile (or the target) region could be measured experimentally and thus provides a measure of isospin diffusion process in a heavy-ion reaction. It is interesting to know that isospin diffusion process is governed by a single isospin diffusion coefficient in the quasi equilibrium limit and is thus connected to the isospin diffusion coefficient I calculated in Chapter 4.

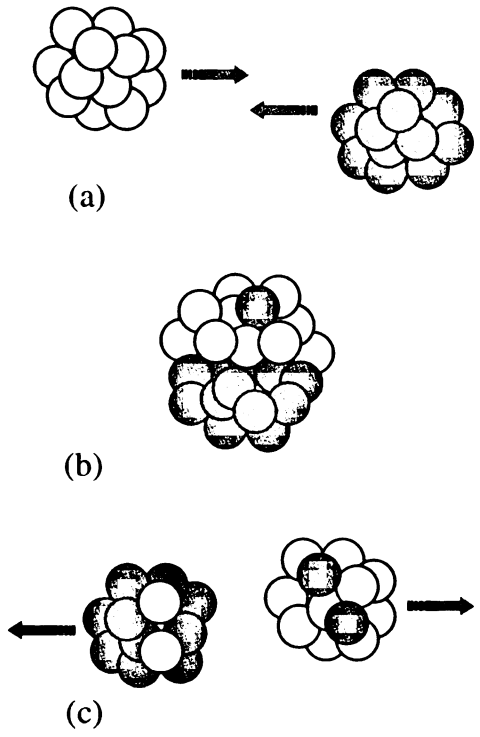

Figure 1.7: The concept of isospin diffusion in a heavy-ion reaction. Initial projectile and target have different isospin concentration, and are shown with different colors in (a). During the reaction, the projectile and target could exchange isospin content, as shown in (b). After the collision, both the projectile and the target isospin concentrations have changed, as shown in (c). The change of isospin concentration in the projectile (or the target) region measures isospin diffusion process in a heavy-ion reaction.

Chapter 2: Isospin Asymmetry and Cluster Formation in the Liquid-Gas Phase Transition Region

As mentioned before, the nuclear Liquid-Gas phase (LGP) transition has attracted much attention in the field of heavy-ion reactions. Here I will introduce a simple model for the LGP transition in isospin asymmetric nuclear matter. This phase transition model is then used to explore phase equilibrium conditions in isospin asymmetric matter and the effect of cluster formation on those conditions. The imbalance of isospin asymmetry in the phase transition region is described in terms of an isospin asymmetry amplification ratio R. The ratio is used to explain the neutron enrichment in the low density source as compared to the high density source in reactions.

A brief introduction of the physical background, and a simple statistical phase space argument for the features of isospin asymmetry in the phase transition region, are given in section 2.1. A formula for the free energy of isospin asymmetric nuclear matter is given in section 2.2. The isospin equilibrium condition in the liquid-gas phase transition region, and the effects of the cluster formation in the gas phase, are discussed in section 2.3. The isospin asymmetry amplification factor R is also defined in section 2.3. Results from the current phenomenological model analysis are compared in section 2.4 to the experimental results from analyzing the midrapidity source. A discussion about the complexity of the isospin flow in realistic heavy-ion reactions is given in section 2.5. The effects of isospin asymmetry and cluster

formation in the LGP transition region in this model are summarized in section 2.6.

2.1 Introduction to the Liquid-Gas Phase Transition

Physical Background

The liquid-gas phase transition in nuclear matter is an analog of that in ordinary matter. Such a phase transition is often explained by the Van der Waals type of interaction between molecules in ordinary matter, like water. The interaction between nucleons exhibit similar characteristics as the Van der Waals force: repulsion at short distance and attraction at long distance. Based on this similarity, the liquid-gas phase for nuclear matter was proposed more than two decades ago (see the review on this subject in [17] and [18]). Many theoretical models were proposed for the LGP transition in nuclear matter [19, 20, 21, 17, 22, 23]. Search for such a phase transition has always been the focus of interest, and some evidence has been proposed for the critical behavior within the phase transition region [13, 24]. Moreover, the recent experimental studies on the caloric curve for nuclear matter [6] have been an indication of a transition and have inspired many related studies [25, 26, 27, 1, 28, 29, 18].

The nuclear liquid-gas phase transition in isospin asymmetric matter is generally different from that in symmetric matter. The theoretical models were often based on symmetric nuclear matter, but experimental studies mostly concerned the asymmetric matter. As pointed by Müller and Serot, the additional isospin degree of freedom relaxes the system and changes the phase transition from first-order to second-order [1]. Additionally, the recent experimental temperature measurements in [6] are intimately related to the isospin asymmetry of the system.

So it is important to learn more about the isospin effects on the nuclear liquid-gas phase transition. Some recent data analysis also tried to explore isospin observables and to relate them to a possible occurrence of the phase transition [30].

One possible occurrence of the liquid-gas phase transition is in the midrapidity region formed in heavy-ion collisions [30, 31, 32]. In simulations of semiperipheral collisions, formation of a low-density neck region between the nuclei is observed that likely contributes to the midrapidity emission [33]. The low-density region in contact with high-density regions (the projectile and target) opens up the possibility for a liquid-gas phase coexistence and phase conversion. In a dynamical simulation with the Boltzmann-Uehling-Uhlenbeck equation, Sobotka *et al.* [33] observed neutron enrichment in the low-density neck region. However, a high n/p ratio (much higher than in the composite system) was found when counting only free nucleons in the neck region, *i.e.* excluding nucleons in clusters. The paper argued that the symmetric clusters (deuterons and alphas) contributed much to the enrichment of neutron in the neck region. Specific results were, however, purely numerical.

In this chapter, I shall discuss the isospin asymmetry in the phase transition region in a heavy-ion collision and the effect of clusters on that asymmetry. I will first follow crude statistical phase space arguments, to gain a general understandings of the physics involved. Thereafter, I will construct a model for the asymmetric nuclear matter, and used the phase equilibrium condition to reach more concrete results illustrating the general ideas.

Qualitative Discussion

In the general discussion, I will consider the isospin effect on the liquid-gas phase transition region without complications from cluster formation in the gas phase. For a given temperature and density, a large isospin asymmetry will increase the total energy, which is unfavorable. The extra energy needed for maintaining the

same asymmetry will be much larger in a dense phase than in a dilute phase. Thus, if a dilute phase is in isospin equilibrium with a dense phase, the asymmetry in the dilute phase will be larger.

This argument, when applied to the heavy-ion reactions, could explain the neutron enrichment in the neck region. The initial nuclei are in the liquid phase, while the low density neck formed during the reaction could be viewed as in gas phase. For the scenario of a neck region (gas phase) neighbored by a dense region (liquid phase), the isospin asymmetry in the liquid phase is close to that of the whole system, while asymmetry in the neck region could be much larger than in the composite system. In a neutron-rich reaction system, as often the case in heavy-ion reactions, the result is neutron enrichment of the neck region.

Next, I will consider letting the clusters be formed in the gas phase. Then the available phase space for liquid does not change while the phase space for the gas phase increases. The added phase space, which corresponds to clusters, has an overall n/p mean value lower than the old phase space for gas. From a statistical equal-partition point of view, partition into the new liquid and gas phase space will make the whole gas phase more symmetric. If the percentage of clusters is small, however, then there is essentially not much change in the phase space distribution, and asymmetry in the gas phase excluding clusters should not change much. This idea also applies to the neck region and points to a reduced neutron enrichment as a result of cluster formation.

2.2 Free-Energy Formula

The free energy for the isospin asymmetric nuclear matter can be expanded in powers of the isospin asymmetry parameter $\delta = (N - Z)/(N + Z)$:

$$f = \mathcal{F}/A = f_0 + f_y = f_0 + C\delta^2 , \tag{2.1}$$

where f_0 and C are functions of both temperature and density. The second term on the r.h.s. of Eq. (2.1) is due to isospin asymmetry and may be called the asymmetric free energy. Since nuclear interaction is symmetric with respect to proton-neutron interchange, the expansion of the free energy contains no odd powers of δ. Only the lowest two terms in the power expansion are retained in Eq. (2.1), and numerical analysis indicates that a quadratic form in δ is adequate up to almost $\delta = 1$ (similar conclusions have been reached in [34, 35]).

Isospin asymmetric nuclear matter can be viewed as a two component interacting Fermi gas of neutrons and protons, and the mean field interaction can be represented by an energy density consistent with the empirical nuclear equation of state (EOS). For simplicity I assume no temperature dependence for the interaction energy, and the Coulomb interaction is not considered here. The total free energy of the system is then a sum of the free energies of two non-interacting Fermi gases and of a density-dependent nuclear potential energy. For a single phase at temperature $T = 0$ and density ρ, the free energy per nucleon may be written out explicitly:

$$\begin{aligned} f = \mathcal{F}/A \;=\; & a_1 (\rho/\rho_0)^{2/3} + a_2 (\rho/\rho_0) + a_3 (\rho/\rho_0)^{\sigma-1} \\ & + \left(a_4 (\rho/\rho_0)^{2/3} + a_5 (\rho/\rho_0) \right) \delta^2 , \end{aligned} \tag{2.2}$$

where $\rho_0 = 0.16\text{fm}^{-3}$ is the normal density. The $(\rho/\rho_0)^{2/3}$ terms come from the non-interacting Fermi gas. The terms $a_2 (\rho/\rho_0) + a_3 (\rho/\rho_0)^{\sigma-1}$ are associated with a simple parameterization of the nuclear EOS [10, 36, 37]. As I am only concerned with the isospin asymmetry in the liquid-gas phase transition, details of the parameterization do not affect the later discussion (though the exact numerical results may change). Given that the interaction generally contributes to the asymmetry energy [38] , I adopt a simple parameterization in Eq. (2.2) for that contribution, of the form $a_5 (\rho/\rho_0) \delta^2$. At $T > 0$, the free energy could not be

written in a simple analytic form, but one can still expand the free energy per nucleon about $\delta = 0$. The forms for f_0 and C will be more complicated at non-zero temperatures and will not be shown here.

In the numerical calculation, I use $\rho_0 = 0.16$ fm^{-3}, $\sigma = 2.1612$, $a_2 = -183.05$ MeV, $a_3 = 144.95$ MeV, $a_5 = 11.72$ MeV, and at $T = 0$, $a_1 = 22.10$ MeV, and $a_4 = 12.28$ MeV The total symmetry energy $a_4 + a_5 \simeq 25$ MeV could be obtained from optical potential analysis [39] or from the mass formula [40]. This value is a little low in view of a more recent analysis of the symmetry energy [41].

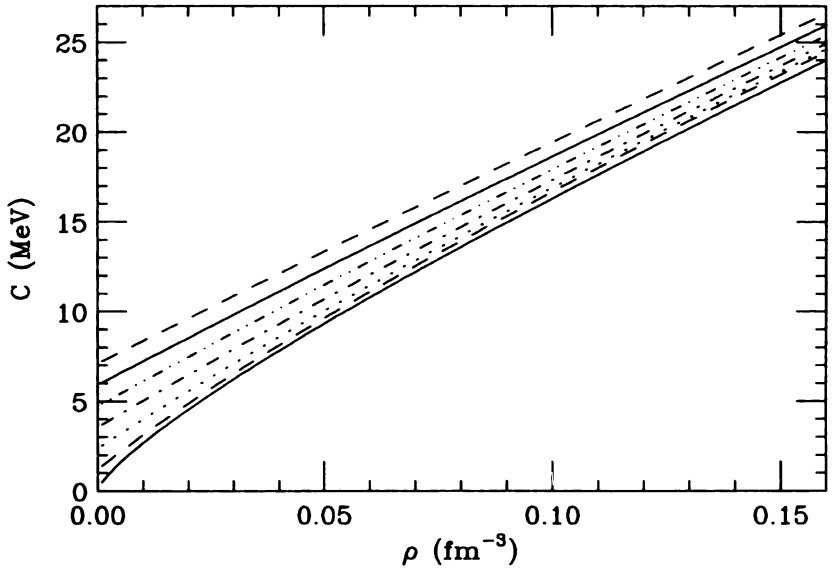

Figure 2.1: The asymmetry coefficient C in the phase transition model as a function of density and temperature. The lines, from bottom to top, correspond to temperatures of 0, 2, 4, 6, 8, 10 and 12 MeV, respectively.

Figure 2.1 shows the calculated the asymmetry coefficient C in the current model as a function of density and temperature in the Fermi gas. The general trend is that C increases with increasing density and temperature. Therefore, at a given temperature, a dense phase will need more extra energy for maintaining a given

asymmetry than a dilute phase.

2.3 Phase Equilibrium and Clusterization in the Gas Phase

Phase Equilibrium Condition

Now I will consider a system that has two phases of liquid and gas, respectively, in contact with each other. The general conditions for phase equilibrium require the pressure, temperature and chemical potentials to be the same in the two phases. If the isospin equilibrium is the only concern, it is more convenient to use the isospin chemical potential defined by $\Delta\mu = \partial f/\partial\delta$, and the equilibrium condition is:

$$\Delta\mu_l = \Delta\mu_g \ . \tag{2.3}$$

Here $\Delta\mu_l$ and $\Delta\mu_g$ denote the isospin chemical potential in the liquid phase and in the gas phase respectively. Specifically for the phase transition model presented in the last section, the isospin chemical potential is just $\Delta\mu = 2C\delta$, and the equilibrium condition is now:

$$C_l\ \delta_l \ = \ C_g\ \delta_g\,, \tag{2.4}$$

At a given temperature, the liquid phase is denser than the gas phase, and the coefficient C is a monotonically increasing function of density, $C_l > C_g$. Thus, the asymmetry in the gas phase δ_g is always larger than that in the liquid phase δ_l. To characterize the relative asymmetry of the two phases, one may define the isospin asymmetry amplification ratio:

$$R \ = \ C_l/C_g \ = \ \delta_g/\delta_l \tag{2.5}$$

Figure 2.2 displays R vs. temperature for the phases in equilibrium. For my

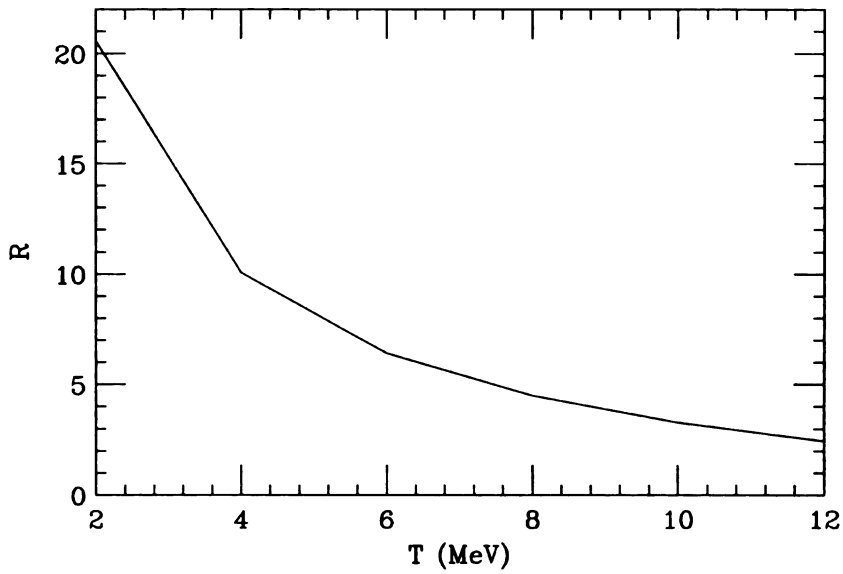

Figure 2.2: The amplification factor R for the liquid-gas phase transition, as a function of temperature.

model calculation, the ratio R stays always larger than 1, which means that the gas phase will always have a higher neutron content than the liquid phase. Notably the amplification ratio is independent of the net isospin asymmetry of the whole system. The ratio R decreases as temperature increases, so that a large overall n/p ratio in the gas phase is more easily reached at low temperature.

In the case of a nonequilibrium process, Eq. (2.3) is still of a use due to a variational origin of the equation. If a local equilibrium assumption is met, *i.e.*, if statistical variables are still valid locally, then Eq. (2.3) tells us the direction of development for the system. The gradient of chemical potential could result in a net flow of isospin asymmetry, which tries to restore the isospin equilibrium condition Eq. (2.3). The flow direction is to the steepest decrease of isospin chemical potential $\Delta\mu$. If there is a gradient of $\Delta\mu$ in a nonequilibrium system, then there could be a flow of isospin asymmetry in the system, with the direction to the lower isospin chemical potential region. Isospin diffusion process will be discussed in some detail

in Chapter 4.

Effect of Cluster Formation in the Gas Phase

One knows that, if the nucleon density is not too low, the mean field description is quite good. But when the density is low, particle-particle correlations become important, and the validity of a mean field description worsens. One way to incorporate particle correlations is to allow for the formation of clusters in the system (as is done in the BUU calculations [42]). Since clusters are in practice only important for the gas phase, I will only allow clusters there and no clusters in the liquid phase at all. To further simplify the discussion, I shall adopt a droplet model for the clusters (as used by Goodman [27] and many others). I will assume that droplets have the same properties as the liquid phase, that is the same density and asymmetric coefficient; for the present discussion I shall ignore the surface energy term. Suppose the average size of droplets is A, and asymmetry in terms of average proton and neutron numbers in droplets is δ_d. The density of nucleons in clusters may be represented as $\rho_d = \alpha\rho$ and of free nucleons as $\rho_f = (1-\alpha)\rho$, where ρ is the density of the gas phase. The asymmetric free energy of the new (free nucleons + droplets) gas phase is:

$$f_y = (1-\alpha)\ C_f\ \delta_f^2 + \alpha\ C_d\ \delta_d^2 . \tag{2.6}$$

Here, the subscripts f and d refer to free nucleons and droplets, respectively. To get the isospin equilibrium condition, I can carry out a similar variation of asymmetry parameters in the liquid, free-nucleon gas, and in droplets, as before, obtaining:

$$\delta_d = \delta_l, \text{ and } \delta_f/\delta_l = C_l/C_f . \tag{2.7}$$

As the density of the gas phase is low, one may use the ideal gas EOS $p = \rho T$ for

clusters in a calculation. And adding clusters will necessarily decrease ρ_f in order to satisfy the mechanical equilibrium condition. However, in Fig. 2.1 one can see that C decreases only slightly as density decreases. To first order, one can take $C_f \simeq C_g$, so that δ_f is nearly the same as the in old gas phase. Overall, the asymmetry of the new gas phase is:

$$\delta \;=\; \alpha\,\delta_d + (1-\alpha)\,\delta_f\,. \tag{2.8}$$

This may be compared to the asymmetry for the old gas phase, $\delta_g \approx \delta_f$, which is much larger than $\delta_d = \delta_l$. It is clear that the more droplets are added to the gas phase, the more it looks like the liquid phase. The amplification ratio now is:

$$R \;=\; \delta/\delta_l \;=\; \alpha + (1-\alpha)\,C_l/C_f \approx \alpha + (1-\alpha)\,R_0\,. \tag{2.9}$$

where $R_0 = C_l/C_g \gg 1$. The case of $\alpha = 0$ corresponds to no cluster formation in the reaction, and the isospin amplification ratio reaches then the maximum R_0. The gas phase acquires then the largest possible net asymmetry at a given temperature. On the other hand, $\alpha = 1.0$ corresponds to the gas phase with only clusters and the same net asymmetry as for the liquid phase.

Figure 2.3 shows the decrease of the amplification factor R as a function of the cluster concentration α. As one adds more clusters, the low-density gas phase will need more energy for the same isospin asymmetry, comparable with that of the liquid phase. As a result, the density and asymmetry in clustered gas will both approach those in the liquid phase.

2.4 Data Analysis

Short of simple tools to estimate typical relative numbers of free neutrons, free protons and clusters in the gas phase in a reaction, one may seek help from

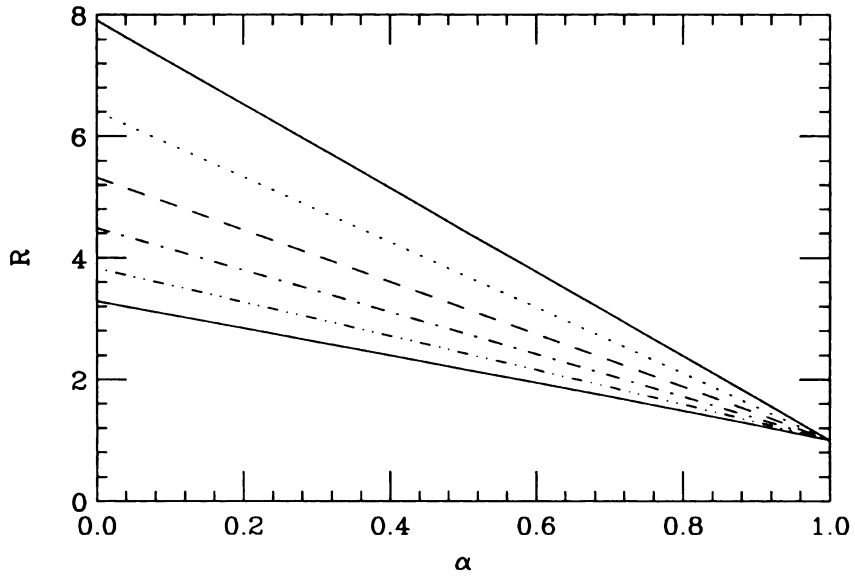

Figure 2.3: The amplification factor R as a function of cluster concentration α. The lines from top to bottom are for temperatures of 5, 6, 7, 8, 9, and 10 MeV, respectively.

experiments. Different regions of velocity space are generally believed to reveal characteristics of different sources, with the midrapidity particle region revealing the low-density neck region. Several intermediate-energy experiments pointed out to a neutron-rich midrapidity source in peripheral heavy-ion collisions [30, 32, 43]. Sobotka *et al.* [44] measured neutron and ^4He emission from a midrapidity source formed in mid-central $^{129}Xe + ^{120}Sn$ collisions at 40 MeV/nucleon. They compared their results with results of the INDRA collaboration for the same system [43, 45] and gave a quantitative description of the midrapidity source. About half of the charged particles from this source are ^4He and only 10% are free protons. Similiar results have been obtained in other papers [32, 43, 45, 30]. The number of neutrons is approximately the same as the number of charged particles, or 10 times the number of protons in this source [44]. If one takes the average cluster size in the midrapidity as about 5 [46], then the percentage of nucleons inside clusters will be $\alpha \sim 80\%$. The N/Z ratio for the midrapidity source is found to be higher than for

the full system [44]. Thus the midrapidity source has $(N/Z)_{mid} \sim 1.65$ or $\delta_{mid} \sim 0.25$ while the system has $(N/Z)_{sys} \sim 1.39$ or $\delta_{sys} \sim 0.16$. The asymmetry amplification ratio is then $R \sim 1.5$. For a mid-rapidity source formed in peripheral heavy-ion collision at similiar energy, a fully consistent comparision of different experiments is not easy. Neverthless, comparison of the peripheral data from [30, 32, 47] also suggests a high cluster concentration and a high n/p ratio for free neutrons and protons.

In the current model calculation, Fig. 2.3 shows that for the cluster concentration α as high as 80%, the asymmetry amplification ratio R will decrease by more than a half when compared with the nonclustered gas phase. This large decrease of R will largely limit the isospin asymmetry in the gas phase when the asymmetry in the liquid phase is fixed. Sobotka *et al.* [44] extracted temperature for the midrapidity source as $6 \sim 7$ MeV. For this temperature and the cluster concentration $\alpha \sim 80\%$, one can read off from Fig. 2.3 the corresponding equilibrium value as $R \sim (1.9 \sim 2.1)$. This value is higher than the extracted $R \sim 1.5$ in the experiment, which means that the system only achieved a partial isospin equilibrium and the asymmetry amplification in the gas phase did not reach its full value.

As another interesting test case, I will consider the isospin equilibrium condition between the free nucleons (as gas phase) and the clusters (as liquid phase) produced in central collisions. The isospin asymmetry of the free nucleon gas could be extracted from the isotope yield ratios, and a value of 0.429 is obtained from a fitting in the $^{112}Sn + ^{112}Sn$ system at beam energy of 50MeV/nucleon [48]. The total liquid phase should have about the same asymmetry as the original system, which is 0.107 for the $^{112}Sn + ^{112}Sn$ system. And thus the amplification ratio is $R = 4.0$. Similar argument for the $^{124}Sn + ^{124}Sn$ system gives $R = 3.6$. Tracing back these values in Fig. 2.2, I find the temperature is in the range of $9 \sim 9.6$ MeV. This temperature is in agreement with the thermal temperature obtained from the

central collisions of similar reaction system at this energy [49].

2.5 Isospin Flow in Heavy-Ion Collisions

While equilibrium consideration provide general indications for the role of asymmetry in liquid-gas phase-transition region, the asymmetry evolves in a reaction in a process that is principally a nonequilibrium one. As such, the asymmetry may deserve more thorough investigations than can be comprised in the simple analysis, possibly requiring simulations. For now, I will only give a general discussion of the possible isospin asymmetry development in the system.

Because of the transient nature of heavy-ion collision, the development of isospin equilibrium depends on two time scales. One time scale is for the separation of the midrapidity source from the remaining sources in the reaction, and the other is for isospin equilibration. At high enough energy, the three sources separate quickly before isospin equilibration could set in between sources. The isospin asymmetry is then determined by the reaction geometry and the isospin content of the target and projectile. Isospin equilibration and cluster formation operate only as post-reorganization processes, changing only isospin asymmetry for free nucleons and clusters within individual sources. The large isospin asymmetry for free nucleons could be the result of clusterization in the low-density phase, with clusters taking over the role of the liquid phase, consistently with the arguments by Sobotka *et al.* [33]. From the previous discussion, the R ratio in Fig. 2.2 sets an upper limit to the asymmetry of free nucleons in the midrapidity source.

On the other hand, if the energy is low enough, partial isospin equilibrium will set in before different sources separate from each other, and the reaction scenario becomes more complex. As the two heavy ions collide against each other, initial compression of the participants produces a dense phase in the center, while the two

spectators remain less dense. As the asymmetry coefficient for the dense phase is larger than for the less dense phase (cf. Fig. 2.1) at the interfaces between the two spectator regions and participant region, there could be a local density gradient from the center out to the two spectators. The isospin asymmetries of the participant and the spectator regions are almost the same in the early stage of reaction because of the short time scale of compression, and gradient of isospin asymmetry could be ignored until later in the expansion stage. From the arguments following Eq. (2.3) and (2.4), the net effect of compression is to produce a gradient of isospin chemical potential. There then could appear an isospin asymmetry flow, and it would be out to the two spectators. As the compression stage ends, the center region begins to expand, and the density drops, the asymmetry coefficient also drops as a result. When the gradient of the asymmetry coefficient changes direction, so does the isospin chemical potential, and so should the flow of isospin asymmetry. Cluster formation in the center region counteracts the decrease of the asymmetry coefficient, and thus delays the change of flow direction. Further development of the system separates the three sources, and net isospin asymmetries for different sources do not change after the separation. But clusterization still plays a role changing the isospin asymmetry of free nucleons within individual sources. Since dynamical simulations suggest a much longer expansion time than the compression time, one could expect that the isospin asymmetry flow to the midrapidity region dominates. This could give rise to an enhanced asymmetry in the midrapidity region. The experiments also suggest a neutron-rich midrapidity source, which is consistent with the present picture.

2.6 Summary

In conclusion, I have investigated the isospin asymmetry in the nuclear liquid-gas phase-transition region. In the framework of the two-component Fermi-gas with a parameterized interaction, under the assumption of isospin equilibrium, I found that a neutron enrichment in the gas phase is due to the density-dependent part of the asymmetry energy. Meeting the isospin equilibrium condition, Eq. (2.3) and (2.4), drives extra neutrons out to the low-density phase. The formation of clusters, which have average asymmetry smaller than the gas phase, will make the gas phase more liquid-like, and counteract neutron enrichment in the gas phase. The ^4He clusters will be the most important due to their predominance in the neck region [32, 30]. Considering the gradient of local isospin chemical potential, the flow of isospin asymmetry was suggested to establish the global isospin-equilibrium requirement. Since the midrapidity undergoes compression and expansion, I also suggested a possible change of the direction of the isospin asymmetry flow during the evolution of the system. The flow of isospin asymmetry will be discussed in some detail in Chapter 4.

Chapter 3: Transport Theory

In this chapter, I will formally introduce microscopic transport theory for heavy-ion reaction simulations. A brief introduction of the physical background for transport theory is given in section 3.1. The Landau-Fermi Liquid theory for nuclear matter, and the concept of quasiparticle excitations for heavy-ion reactions are presented in section 3.2. The Boltzmann equation set for heavy-ion reactions is introduced in section 3.3. The nuclear equation of state is discussed in section 3.4, where both the momentum independent and momentum dependent interactions are considered. The recent advances in rare isotope facilities have stimulated much interest in the nuclear reaction community to investigate isospin effects, and I will introduce the isospin related physics, and especially the isospin dependence of the nuclear equation of state in section 3.5. For transport simulations of reactions, the reaction system needs to be properly initiated. The set of Boltzmann equations needs to be properly integrated. The quasiparticle collision cross sections will determine the pace of the thermalization process and the production of most energetic particles. All these details contribute to the interpretation of the results from the simulations, and will be discussed in section 3.6.

3.1 Introduction

The applicability of the semiclassical transport theory to the heavy-ion collisions generally improves as the bombarding energy increases. Thus, in the ground-state, the characteristic de Broglie wave length is $\lambda = \hbar/p \gtrsim \hbar/p_F \sim 1$ fm. However, at an incident energy of 1 GeV/nucleon, the incident momentum is $p = 1.7$ GeV/c. This yields $\lambda = \hbar/p = 0.12$ fm, which is much smaller than either the characteristic mean-free path $\lambda_{mfp} \simeq 1/(\sigma_{NN}\, n_0) \simeq 2.1$ fm, or the characteristic

size of nuclei: $R \simeq 1.2A^{1/3} \simeq 5.6$ fm for $A = 100$.

Early on in the research of heavy-ion reactions, the cascade model and the classical hydrodynamic model had been used for reaction simulations. The cascade model, which includes collisions between elementary classical particles, is able to explain the inclusive proton energy spectrum in heavy-ion reactions at intermediate and high energies. The classical fluid hydrodynamical model, which includes the mean field interactions, had success in predicting qualitative features of the collective motions for nuclear matter.

Semi-classical transport models, which combine the inter-particle collisions with a semiclassical movement in the mean field, have been quite successful in describing a variety of data. The Boltzmann type of transport models [10], often labelled as BUU (for Boltzmann-Uheling-Ulenbeck), have become an important tool for the studies of heavy-ion reaction dynamics [16, 50, 7]. The Boltzmann equation set is appealing because it naturally reproduces the rare gas dynamics in the low density limit and the hydrodynamic equations in the high density limit. The Boltzmann type transport simulations are able to reproduce the inclusive proton spectrum from inclusive experiments [10] at intermediate to high energies, and they allow the linking of collective flows observed in exclusive experiments to the empirical nuclear equation of state (EOS) [51, 36, 12, 52, 53]. The efforts carried both from the sides of simulations and experiments allowed extraction of the nuclear EOS at densities from normal density up to neutron star densities (see [16] and reference therein). Nuclear stopping power, the development of a shock wave in nuclear collision, the spectator-participant interactions could be explained within the transport models (see [7] for a review of the success of transport models in heavy-ion reactions). Such transport models were also combined with the statistical multifragmentation model (SMM) or coalescence models to calculated the production of heavier fragment produced in reactions.

The Boltzmann equation of utility for nuclear reactions may be derived from the Kadanoff-Baym equation [54] in non-equilibrium field theory by following different approximations, including the weak gradient expansion [55], and/or small scattering amplitude approximation [55, 56, 57]. Numerical solution of the Kadanoff-Baym equation turns out to be very difficult [58], and only limited success has been achieved in extremely simplified situation [59, 60, 61, 62]. While the application of transport equations has been very successful, a number of improvements are continuously being added to the understanding of the basic approach. The Boltzmann equation for quasi-particle interactions was first used by Bertsch *et al.* [10], the inclusion of three particle interaction for cluster formation was introduced by Danielewicz and Bertsch [42] and relativistic covariant transport equations have been introduced by Blattel *et al.* [63, 64]. The relativistic structure for the single particle potential has been introduced by Danielewicz and Pan [51] and Weber *et al.* [65]. Finally, the fully self-consistent energy functional method for the parameterization of the mean field was introduced by Danielewicz [12]. Moreover, momentum dependence of the mean field was investigated [66, 67, 68], and the relation to elliptic flow was established [12, 53]. The effects of off-shell transport [69, 70, 71, 72], and non-local collisions [55] have also been investigated.

Originally, the Boltzmann equation was derived for a classical dilute gas with predominantly binary collisions. Its extension to quantum gas was postulated by Uehling and Uhlenbeck [73, 74]. A systematic expansion of the Boltzmann equation in density gradients give rise to hydrodynamic equations [75]. In the zeroth order, one obtains the Euler equations [75, 76]. In the first order, one finds the equations of dissipative hydrodynamics with coefficients given through the linearized Boltzmann equations [75, 76, 74]. Successive expansion of the Boltzmann equation in density and velocity gradients will give higher order corrections for the hydrodynamical equations [76, 75].

While the semi-classical method for QED plasmas has long been established [77, 78], the most recent progress has been in the development of the semiclassical transport equations for the hot QCD plasmas produced in ultra-relativistic heavy-ion collisions. In the non-equilibrium dense quark matter, the soft quantum fields are well approximated by soft classical field and the weakly coupled hard excitations behave like quasiparticles [79], the transport equations were derived on resuming the hard thermal loops [80, 81, 79, 82, 83]. The resulting non-Abelian transport equations, which contain nonlinear color field coupling, have been used to simulate the production of the Quark-Gluon-Plasmas in ultra-relativistic heavy-ion reactions [84, 85].

Another important type of transport models in the simulations of the relativistic heavy-ion reactions are the Quantum Molecular Dynamics (QMD) [86] and closely related antisymmetrized molecular dynamics (AMD) [87, 88]. Though nominally theoretically less rigorous, the QMD equations are similar to the Boltzmann transport equations. Rather than sampling over the quasiparticle distribution and follow the time evolution of the ensemble, the QMD method follows each initial random condition on an event-by-event basis, and the ensemble average is taken at the end [86, 87, 88]. The QMD approach naturally incorporates particle correlations into dynamical simulations and provides insight into the cluster formation process in an energetic heavy-ion reaction. AMD uses antisymmetrized wave function for the reaction system, and can nicely reproduce the ground state properties of composite particles [87, 88].

3.2 Landau Theory

Standard descriptions of heavy-ion reactions rely on the Wigner distributions for the particles in the reactions. The natural framework for the description of

systems exclusively in terms of Wigner functions is the Landau quasiparticle theory [10]. In this section, I will give a brief introduction to the Landau theory, to the nuclear equation of state within that theory, and the relativistic transformations for quasiparticle motions that are relevant to relativistic reaction simulations.

Energy Density and Quasiparticle Excitation

Quasiparticles in Landau theory are excitations of the strongly interacting system (in this case, nuclear matter), and, for a normal Fermi system, they have a one-to-one correspondence to the particles in the system. In other word, each quasiparticle has the same quantum number as the corresponding particle, including baryon number, charge, spin, isospin and possibly other quantum numbers [89]. The energy ϵ_X and momentum $\mathbf{p}_X$ of the quasiparticle are, however, related differently than for a free particle. The occupation of these quasiparticle states are described by the quasiparticle distribution function $f_X(\mathbf{p}, \mathbf{r}, t)$ [89].

The total energy of the system in the theory is the sum of two terms: the quasiparticle energy from summing over the quasiparicle distribution function and the additional term from quasiparticle interactions; the total momentum of the system is a sum of momenta for the quasiparticles.

$$\begin{aligned} E &= \int d\mathbf{r}\, \tilde{e} = \int d\mathbf{r}\, (\tilde{e}_{kin} + \tilde{e}_{int}) \\ &= \int d\mathbf{r} \int \frac{d\mathbf{p}}{(2\pi)^3}\, \epsilon_X(\mathbf{p}) f_X(\mathbf{p}, \mathbf{r}) + \int d\mathbf{r}\, \tilde{e}_{int}\,, \qquad (3.1a) \\ \mathbf{P} &= \int d\mathbf{r} \int \frac{d\mathbf{p}}{(2\pi)^3}\, \mathbf{p}\, f_X(\mathbf{p}, \mathbf{r})\,. \qquad (3.1b) \end{aligned}$$

In Eq. (3.1a), the energy density $\tilde{e}$ is divided into a kinetic energy density $\tilde{e}_{kin}$ and a potential energy density $\tilde{e}_{int}$ to be further discussed. If the system contains multiple components, then there is an additional summation over all particle species in the above expressions. The degeneracy factor for spin and isospin, which could also be

viewed as a special type of summation over particle species, is also omitted for simplicity.

The particle number, total charge and other additive quantum numbers could be easily obtained following the correspondence between the quasiparticles and the particles:

$$A = \int d\mathbf{r} \int \frac{d\mathbf{p}}{(2\pi)^3} A_X f_X(\mathbf{p}, \mathbf{r}) , \tag{3.2}$$

where A_X is the baryon number (or other quantum numbers) of the quasiparticles, and A is the total baryon number (or total number of other summational quantum number) in the system. The scalar baryon density is defined by:

$$\rho_s = \int \frac{d\mathbf{p}}{(2\pi)^3 \gamma} A_X f_X(\mathbf{p}, \mathbf{r}) , \tag{3.3}$$

where the factor γ is the lorentz contraction factor.

Once the total energy of the interacting system is known, the quasiparticle energy and momentum $(\epsilon_X, \mathbf{p}_X)$ are easily derived:

$$\epsilon_X = \frac{\delta E}{\delta f_X} , \tag{3.4a}$$

$$\mathbf{p}_X = \frac{\delta \mathbf{P}}{\delta f_X} . \tag{3.4b}$$

The relation between the quasiparticle energy and momentum reflects the dynamical behavior of the excitation, and is called the dispersion relation. In free space, the dispersion relation is just $\epsilon_X(\mathbf{p}) = \sqrt{m_X^2 + p^2}$. In the strongly interacting system, the relation generally gets modified due to interaction, and the optical potential U_{opt} is often used to characterize the change:

$$U_{opt} = \epsilon_X(\mathbf{p}) - \epsilon_X^{free}(\mathbf{p}) . \tag{3.5}$$

From the dispersion relation, one can also get the Euler equations for quasiparticle motions under the mean field interactions:

$$\mathbf{v} = \frac{d\mathbf{r}}{dt} = \frac{\partial \epsilon}{\partial \mathbf{p}}, \tag{3.6a}$$

$$\mathbf{F} = \frac{d\mathbf{p}}{dt} = -\frac{\partial \epsilon}{\partial \mathbf{r}}. \tag{3.6b}$$

The dynamics of the quasiparticle motions should also include the collisions between quasiparticles. Collisions are described by Boltzmann equations and are discussed in section 3.3.

Nuclear Equation of State

The energy-density relation for nuclear matter, often simply referred to as the nuclear equation of state (EOS), determines the motion of quasiparticles under the influence of the mean field through quasiparticle energy ϵ in Eq. (3.6). Since quasiparticle energy could be derived from either Eq. (3.4a) or (3.5), so the nuclear EOS could be uniquely specified by providing the form of the energy density $\tilde{e}$, or equivalently in the form of the optical potential U_{opt}. The nuclear EOS is often discussed in terms of energy per particle $e(\rho)$, defined by $e = \tilde{e}/\rho$. The nuclear EOS has been the subject of intense investigation in heavy-ion reactions in the context of transport simulations.

As mentioned in Chapter 1, the nuclear EOS in simulations could be classified into two types, the momentum independent (MI) or momentum dependent (MD) EOS, depending on whether the momentum dependence of the optical potential is ignored or not. Since the quasiparticle energy ϵ in Eq. (3.4a) generally depends on the distribution function, so does the optical potential U_{opt}, and the most simple implementation of this dependence is realized through the density dependence of the optical potential (this is the case of momentum independent EOS). To characterize

the density dependence of the nuclear EOS, the compressibility is often defined:

$$K = 9\frac{\partial P}{\partial \rho}, \tag{3.7}$$

where the pressure P is defined by:

$$P = -\frac{\partial E}{\partial V} = \rho^2 \frac{\partial e}{\partial \rho}, \tag{3.8}$$

The compressibility of nuclear matter at normal density is often used to label different density dependencies of the EOS. In the more general momentum dependent case, the optical potential in Eq. (3.5) is also a function of momentum, $U_{opt} = U_{opt}(\rho, \mathbf{p})$. The effective mass for the quasiparticle is often used to signify the momentum dependence of the nuclear EOS:

$$m^* = \frac{p}{v}, \tag{3.9}$$

where $p = |\mathbf{p}|$, and $v = |\mathbf{v}|$. The velocity vector $\mathbf{v}$ for the quasiparticle is defined as:

$$\mathbf{v} = \frac{\partial \epsilon}{\partial \mathbf{p}}. \tag{3.10}$$

The effective mass at the Fermi surface is often used to label the different MD EOS.

As mentioned in Chapter 1, the nuclear equation of state is also isospin dependent. The isospin dependence is related to the additional summation over particle species in Eq. (3.1) (here, over protons and neutrons respectively). The isospin dependence results in different dispersion relations and different optical potentials for protons and neutrons, and thus different Euler equations for the corresponding quasiparticles in nuclear matter. Isospin dependence has recently raised some interest in nuclear reaction studies, and the relevant physical ideas and

parameterization of the isospin dependence will be discussed in detail in section 3.5.

Relativistic Transformations

As microscopic transport theory will be frequently applied to heavy-ion collisions at relativistic energies, the relativistic covariance transformations of the quasiparticle motions becomes important. The relativistic transformations have been derived by Baym and Chin [90], and I will only list the covariant formula that are relevant to transport theory.

The total energy and momentum of the interacting system forms a relativistic 4-vector $P^\mu = (E, \mathbf{P})$. From Eq. (3.4) and the scalar structure of the distribution function $f_X(\mathbf{p}, \mathbf{r})$, we find that the quasiparticle energy and momentum also form a covariant vector $p^\mu = (\epsilon, \mathbf{p})$. The covariant velocity is $u^\mu = (\gamma, \gamma\mathbf{v})$, where $\gamma = 1/\sqrt{1-v^2}$. In a moving frame, the particle density is multiplied by the boost factor γ for the moving frame, but the scalar density ρ_s remains invariant.

In general, the energy-momentum tensor is:

$$T^{\mu\nu} = \int \frac{d\mathbf{p}}{\gamma} p^\mu u^\nu f(\mathbf{p}, \mathbf{r}) + g^{\mu\nu}\tilde{e}_{int} \,. \tag{3.11}$$

And the the energy-momentum conservation law is just $\partial_\nu T^{\mu\nu} = 0$. The energy density $\tilde{e}$ is a component of the energy-momentum tensor:

$$\tilde{e} = T^{00} = \int d\mathbf{p}\epsilon f(\mathbf{p}, \mathbf{r}) + \tilde{e}_{int} \tag{3.12}$$

In view of Eq. (3.11), one could see that the first term and second term in Eq. (3.12) have different Lorentz structure and transformation laws. The interaction term $\tilde{e}_{int}$ is Lorentz invariant, while the kinetic term will be different in different reference frame.

In terms of the energy-momentum tensor, the total energy and momentum

could be written as:

$$\begin{aligned} E &= \int d\mathbf{r} T^{00}, \\ P_i &= \int d\mathbf{r} T^{0i}. \end{aligned} \tag{3.13}$$

The tensor structure of the energy-momentum tensor in the Eq.(3.11) is important for accessing of the excitations of nuclear matter, and can be used to test energy and momentum conservation in transport simulations.

3.3 Boltzmann Equation Set

As the basic equations in transport theory, the Boltzmann equations describe the quasiparticle motions in the nuclear medium under the influence of mean field interaction and inter-particle collisions. In this section, I will introduce the Boltzmann equation set, and the covariant form of the collision integral.

In the quasiparticle approximation, the state of a system is completely specified when the phase-space distributions $f_X \equiv f_X(\mathbf{p}, \mathbf{r}, t)$ are given for all particle species. The distribution function satisfies the Boltzmann equation:

$$\frac{\partial f_X}{\partial t} + \frac{\partial \epsilon_X}{\partial \mathbf{p}} \frac{\partial f_X}{\partial \mathbf{r}} - \frac{\partial \epsilon_X}{\partial \mathbf{r}} \frac{\partial f_X}{\partial \mathbf{p}} = \mathcal{K}_X^< (1 \mp f_X) - \mathcal{K}_X^> f_X \,. \tag{3.14}$$

The l.h.s. accounts for the motion of particles in the MF, while the r.h.s. accounts for collisions. If the collision terms are ignored, one arrives at the Vlasov equations, that is, the mean field dynamics for the quasiparticles. Factors $\mathcal{K}^<$ and $\mathcal{K}^>$ on the r.h.s. of (3.14) are the feeding and removal rates. The factor $(1 \mp f_X)$ is the reduction or enhancement factor in the Fermi-Dirac or Bose-Einstein system. The degrees of freedom in the Boltzmann equations are usually nucleons, pions, Δ and N^* resonances. While most BUU models do not describe cluster formation, a

description for the production of light ($A \leq 3$) clusters, an option in the current model, was developed by Danielewicz and Bertsch [42].

The combination of relativity and momentum dependence brings in some peculiarities into the collision rates and cross sections, beyond what is encountered in the non-relativistic dynamics. Thus, to be consistent with the Fermi Golden Rule for transition rates and the requirements of covariance, the contribution of binary collisions of particles X to the removal rate in (3.14) is written as:

$$\begin{aligned}
\mathcal{K}_X^>(\mathbf{p}_1) &= \frac{g_X}{\gamma_1}\int\frac{d\mathbf{p}_2}{(2\pi)^3\gamma_2}\int\frac{d\mathbf{p}_1'}{(2\pi)^3\gamma_1'}\int\frac{d\mathbf{p}_2'}{(2\pi)^3\gamma_2'}\frac{1}{2}\overline{|\mathcal{M}_{2X\to 2X'}|^2} \\
&\quad\times(2\pi)^3\delta(\mathbf{p}_1+\mathbf{p}_2-\mathbf{p}_1'-\mathbf{p}_2') \\
&\quad\times 2\pi\,\delta(\epsilon_1+\epsilon_2-\epsilon_1'-\epsilon_2')\,f_2\,(1-f_1')\,(1-f_2') \\
&= \frac{g_X}{\gamma_1}\int\frac{d\mathbf{p}_2}{(2\pi)^3\gamma_2}\frac{1}{2}\int d\Omega^{*\prime}\,\frac{p^{*\prime 2}}{4\pi^2\gamma_1^{*\prime}\gamma_2^{*\prime}v_{12}^{*\prime}}\overline{|\mathcal{M}_{2X\to 2X'}|^2} \\
&\quad\times f_2\,(1-f_1')\,(1-f_2') \\
&= g_X\int\frac{d\mathbf{p}_2}{(2\pi)^3}\frac{1}{2}\int d\Omega^{*\prime}\,v_{12}\,\frac{d\sigma}{d\Omega^{*\prime}}\,f_2\,(1-f_1')\,(1-f_2')\,. \qquad (3.15)
\end{aligned}$$

In the above, $\overline{|\mathcal{M}|^2}$ represents a squared invariant matrix element for the scattering, averaged over initial and summed over final spin directions. The factors γ are associated with the respective velocities and $d\mathbf{p}/\gamma$ is the invariant measure in the momentum space. The starred quantities in Eq. (3.15) refer to the two-particle c.m. quantities defined by the vanishing of the three-momentum in the entrance channel, $\mathbf{P}=0$, where $P^\mu = p_1^\mu + p_2^\mu$ is initial system 4-momentum. The cross section in (3.15) is given by:

$$\frac{d\sigma}{d\Omega^{*\prime}} = \frac{p^{*\prime 2}}{4\pi^2\gamma_1^*\gamma_2^*v_{12}^*\gamma_1^{*\prime}\gamma_2^{*\prime}v_{12}^{*\prime}}\,\overline{|\mathcal{M}_{2X\to 2X'}|^2}\,. \qquad (3.16)$$

The relativistic relative velocity in Eq. (3.15) and (3.16) is defined through the

invariant form:

$$\gamma_1 \gamma_2 v_{12} = \left[-\frac{[(P \cdot u_2)\, u_1 - (P \cdot u_1)\, u_2]^2}{P^2} \right]^{1/2} . \tag{3.17}$$

The above definitions ensure the standard form of the detailed balance relation, i.e.:

$$p^{*2} \frac{d\sigma}{d\Omega^{*\prime}} = p^{*\prime 2} \frac{d\sigma}{d\Omega^*} . \tag{3.18}$$

In the c.m. frame, the relative velocity reduces to the velocity difference. The factor of 1/2 in front of the angular integrations in Eq. (3.15) accounts, in the standard manner, for the double-counting of the final states in scattering for like particles.

3.4 Nuclear Equation of State

As mentioned in Chapter 1, the nuclear equation of state plays an essential role in the dynamics of the heavy-ion reaction, and transport simulations often employ parameterized forms of the EOS. In this section and the next section, I will show the parameterizations for the nuclear EOS. The parameterized EOS will be used in transport simulations, and some examples of the simulations will be given in Chapter 5.

While many of the mean field parameterizations start directly from the optical potential U, I will introduce the energy density functional method. As seen in Section 3.2, the optical potential U completely determines the mean field dynamics for the quasiparticles through the Euler equations(3.6). So it is sufficient to parameterize the optical potential for all transport simulations, the only pitfall is that the formula for the total energy and the excitation energy may become quite complicated. As will be apparent, the energy density functional method is superior: the single particle energies are determined self-consistently through Eq.(3.4), the

total energy and excitation are easily accessible, the relativistic transformations are already derived in Section 3.2. The nuclear equation of state based on momentum-independent mean fields (MI EOS) will be used in exploring the compression effects in nuclear reactions; the nuclear equation of state based on momentum-dependent mean fields (MD EOS) will be used for exploring the additional effects of changed particle velocities. The energy density functional method was first used as the starting point for the parameterization of the EOS in [12].

3.4.1 Energy Density Functional

As already mentioned in section 3.2, the energy density functional in Eq.(3.1) uniquely determines the quasiparticle energy and the optical potential, and thus completely specifies the mean field dynamics. In this section, I will start from a general functional form for the nuclear equation of state, and the next two subsections will be devoted to the details of the momentum independent and the momentum dependent mean field parameterizations.

With finite-range effects in the system energy, the energy density of the reaction system could be written as:

$$\tilde{e} = \tilde{e}_{NM} + \tilde{e}_{grad} + \tilde{e}_{coul} \,. \tag{3.19}$$

The last term in Eq. (3.19) is the Coulomb energy. When beam energy is not so high, the radiation retardation effect can be ignored and the Coulomb interaction is given in a static form:

$$\tilde{e}_{coul} = \frac{1}{2}\rho_{ch}(\mathbf{r})\Phi(\mathbf{r}) \,. \tag{3.20}$$

where $\Phi(\mathbf{r})$ is the Coulomb field produced by all other particles and $\rho_{ch}(\mathbf{r})$ is the charge density at position $\mathbf{r}$.

The second term in Eq. (3.19) involves spatial gradients of the distribution function. It allows us, primarily, to account for the effect of the finite range of nuclear forces, which is similar to the lowest-order quantal effect of the curvature in the wave functions. In a finite nuclear system, the energy density due to density gradient corresponds to the additional energy required to form a surface (other than the change of the volume energy at the surface region).

$$\tilde{\epsilon}_{grad} = -\frac{a_s}{2\rho_0}\rho(\nabla)^2\rho, \tag{3.21}$$

After partial integration, I find that the surface energy is positive definite if a_s is positive.

$$E_{grad} = \int d\mathbf{r}\tilde{\epsilon}_{grad} = \frac{a_s}{2\rho_0}\int d\mathbf{r}\,(\nabla\rho)^2\,, \tag{3.22}$$

This gradient term is important in the Thomas-Fermi (TF) initialization of the nuclei [91, 92] for the reaction simulations. I take the coefficient in (3.21) equal to $a_s = 21.4$ MeV fm^2 for the density dependent MFs. For the momentum-dependent fields, I take a bit lower $a_s = 18.2$ MeV fm^2 from adjustments to ground-state data on nuclear shapes. The initialization of the nuclei for the simulation is described in the subsection 3.6.1.

The energy density for nuclear matter is often written as the sum of the energy density term $\tilde{\epsilon}_0$ with no isospin interaction considered and an additional contribution $\tilde{\epsilon}_I$ when isospin interaction is considered:

$$\tilde{\epsilon}_{NM} = \tilde{\epsilon}_0 + \tilde{\epsilon}_I\,. \tag{3.23}$$

The term $\tilde{\epsilon}_0$ will also contain isospin dependence if the protons and neutrons are treated differently, but is not sufficient to explain fully the total isospin dependence

of the nuclear EOS. The additional isospin dependent part $\tilde{e}_I$, which is usually smaller in magnitude than the term $\tilde{e}_0$, will be discussed in detail in section 3.5.

The isospin independent strong-interaction field is chosen to act only on baryons in the current calculations. Pions, which should also contribute to the mean field interaction, are infrequent in the energy range I am interested in and are ignored in the consideration of mean field, except in the case of isospin dependence, in order to simplify the energy conservation. I should note that, when the vector and scalar type MFs may be momentum dependent with no exclusive dependence on the vector and scalar densities, there is neither a benefit nor a phenomenological basis, in the absence of spin dynamics, for a separate consideration of these fields.

The parameterizations of the nuclear equation of state are constrained by known physical properties of nuclear matter. Nuclear matter saturates at normal density $\rho_0 = 0.16$ fm^{-3} and the binding energy per particle at normal density is about 16 MeV. Also at zero density, the strongly interacting system became a free system and the quasiparticles became free particles. In a mathematical form, I require the EOS to satisfy:

$$\frac{\partial e}{\partial \rho}(\rho = \rho_0) = 0\,, \tag{3.24a}$$

$$e(\rho = \rho_0) = -16 \text{ MeV}\,, \tag{3.24b}$$

$$e(\rho = 0) = 0\,. \tag{3.24c}$$

These constraints are satisfied by many of the EOS used in transport simulations. There are also other constraints for the isospin dependence of the EOS, and these constraints will be discussed in later section.

3.4.2 Momentum Independent Mean Fields

Guided solely by calculational convenience, I choose the fields that could be easily identified as either vector or scalar [52]. Thus, in the case of the mean field with only density dependence in their nonrelativistic reduction, I choose the isospin interaction independent part of the energy density to be of the form [93]:

$$\tilde{e}_0 = \sum_X g_X \int \frac{d\mathbf{p}}{(2\pi)^3} f_X(\mathbf{p}) \sqrt{p^2 + m_X^2(\rho_s)} + \int_0^{\rho_s} d\rho_s' U(\rho_s') - \rho_s U(\rho_s) , \qquad (3.25)$$

where $m_X(\rho_s) = m_X + A_X U(\rho_s)$, A_X is baryon number, and the scalar density is defined by:

$$\rho_s = \sum_X g_X A_X \int \frac{d\mathbf{p}}{(2\pi)^3} \frac{m_X(\rho_s)}{\sqrt{p^2 + m_X^2(\rho_s)}} f_X(\mathbf{p}) . \qquad (3.26)$$

This definition is equivalent to the definition in Eq. (3.3). The variational derivative of the energy in Eq. (3.25) alone gives rise to single-particle energies:

$$\tilde{\epsilon}_X(p, \rho_s) = \frac{\delta \tilde{e}_0}{\delta f_X(p)} = \sqrt{p^2 + m_X^2(\rho_s)} . \qquad (3.27)$$

For the MF interaction, I take the form:

$$U(\xi) = \frac{a\,\xi + b\,\xi^\nu}{1 + (\xi/2.5)^{\nu-1}} , \qquad (3.28)$$

with $\xi = \rho_s/\rho_0$ as the reduced density, and the parameters a, b, and ν adjusted to produce average nuclear ground-state properties. The role of the denominator in Eq. (3.28) is to prevent supraluminous behavior at high densities. The energy functional in Eq. (3.25) does not incorporate the momentum dependence of the scalar mean fields. The resulting equation of state will be referred to as MI EOS, *i.e.*, EOS based on momentum-independent MFs.

To the single-particle energy in Eq.(3.27), I add in the system frame the

Coulomb, gradient, and isospin corrections. The coulomb and gradient term will contribute to the forces but drop out from the collision integrals and velocities.

$$\epsilon_X = \tilde{\epsilon}_X + Z_X \, \Phi + A_X \, U_{grad} + U_{iso}^X \,, \tag{3.29}$$

where Φ is the Coulomb potential,

$$U_{grad} = \delta \tilde{e}_{grad} / \delta f_X = -a_s \, \nabla^2 (\rho / \rho_0) \,, \tag{3.30}$$

is the gradient term, and the isospin dependent potential

$$U_{iso}^X = \delta \tilde{e}_I / \delta f_X \tag{3.31}$$

will be discussed later in section 3.5.

To determine a, b, and ν, I required the energy per nucleon to minimize in nuclear matter at $\rho = \rho_0$ at the value of $B/A = e/\rho - m_N \approx -16.0$ MeV for incompressibility $K = 210$ MeV, and at -17.0 MeV for $K = 380$ MeV. For the higher K, the energy cost for the surface is higher. That leads to difficulties, for the TF theory, in reproducing the average dependence of nuclear binding energy on mass number (especially in the low mass region), which one can partly compensate for with the stronger binding in the infinite-volume limit. A more thorough discussion can be found in [94]; adjustments of a_s in (3.21) cannot be done without worsening the Thomas-Fermi description of measured rms radii. The parameter sets from such adjustments are listed in table (3.1). Generally, reproducing the binding-energy curve helps us to assess the excitation energy of matter formed in low-energy or peripheral reactions.

Table 3.1: Parameters for the momentum independent MFs.

a MeV	b MeV	ν	K MeV	B/A MeV
-187.24	102.62	1.6339	210	-16.0
-121.26	52.10	2.4624	380	-17.0

3.4.3 Momentum Dependent Mean Fields

As mentioned in Chapter 1, the momentum dependence of the nuclear equation of state, which is predicted by microscopic theories, is found to have a strong influence on elliptic flow in heavy-ion reactions. I will next introduce the MD EOS parameterizations for transport theory, and these parameterized forms will be use in transport simulations in Chapter 5.

For the momentum dependent MF, I will parameterize the energy density in the local frame where baryon flux vanishes [52, 93, 95],
$\mathbf{J} = \sum_X g_X A_X \int \frac{d\mathbf{p}}{(2\pi)^3} f_X \mathbf{v}_X = 0$, with

$$\tilde{e}_0 = \sum_X g_X \int \frac{d\mathbf{p}}{(2\pi)^3} f_X(\mathbf{p}) \left(m_X + \int_0^p dp' \, v_X^*(p', \rho) \right) + \int_0^\rho d\rho' \, U(\rho'), \tag{3.32}$$

where U is of the same form as expressed by Eq. (3.28), and $\xi = \rho/\rho_0$. The local particle velocity v_X^* depends on (kinematic) momentum and density through:

$$v_X^*(p, \xi) = p \Big/ \sqrt{p^2 + m_X^2 \Big/ \left[1 + c\left(\frac{m_N}{m_X}\right) \frac{A_X \, \xi}{(1 + \lambda p^2/m_X^2)^2} \right]^2} \, . \tag{3.33}$$

The energy (3.32) alone yields the local single-particle energies

$$\tilde{\epsilon}_X(p, \rho) = m_X + \int_0^p dp' \, v_X^* + A_X \left[U^v(\rho) + U(\rho) \right] , \tag{3.34}$$

where the density dependence of the velocity gives rise to an additional potential of

Table 3.2: Parameter values for the momentum-dependent mean fields. U_{opt}^{∞} is the asymptotic value of the potential at ρ_0 as $p \to \infty$.

a (MeV)	b (MeV)	ν	c	λ	m^*/m	U_{opt}^{∞} (MeV)	K (MeV)	set
185.47	36.291	1.5391	0.83889	1.0890	0.65	55	210	S1
185.56	32.139	1.5706	0.96131	2.1376	0.65	23	210	S2
209.79	69.757	1.4623	0.64570	0.95460	0.70	40	210	S3
214.10	95.004	1.4733	0.37948	0.55394	0.79	25	210	S4
123.62	14.653	2.8906	0.83578	1.0739	0.65	56	380	H1
128.22	22.602	2.5873	0.64570	0.95460	0.70	39	380	H2

the form:

$$U^{r}(\rho) = \sum_{Y} g_Y \int \frac{d\mathbf{p}_1}{(2\pi)^3} f_Y(\mathbf{p}_1) \int_0^{p_1} dp' \frac{\partial v_Y^*}{\partial \rho} . \tag{3.35}$$

In their nonrelativistic reduction, the energies (3.34) are similar to the energies proposed for the nonrelativistic transport by Bertsch, Das Gupta *et al.* [10, 96]. Different sets of parameters for (3.32), which give different values for the group effective mass [97] in normal matter at the Fermi surface ($m^* = p^F/v^F$) and for the incompressibility, are exhibited in Table 3.2. The energy functional in Eq. (3.32) incorporates additional momentum dependence of the mean fields. The resulting equation of state will be referred to as MD EOS, *i.e.*, EOS based on momentum-dependent MFs.

3.5 Isospin Dependence of Nuclear EOS

3.5.1 Introduction to Isospin Physics

The proposed Rare Isotope Accelerator (RIA) and other radioactive beam facilities have made it possible to explore heavy-ion physics along the isospin degree of freedom toward the proton or neutron drip lines. In fact, recent nuclear structure studies on nuclei with large neutron or proton excess have revealed new phenomena

that are characteristically different from that in the stable isotopes. Especially interesting results have been produced by the studies on very neutron rich isotopes, where new shell structures, neutron skins and neutron halos have been found. It is hoped that heavy-ion reactions studies with extremely neutron-rich or proton-rich isotopes could also reveal new features of the reaction dynamics not encountered before.

Signals related to isospin are also important tools for exploring heavy-ion reaction dynamics. Isotope ratios have been used to differentiate equilibrated reaction processes from non-equilibrated processes [98]. Large isospin asymmetric system has been used as a probe for measuring nuclear stopping power [99]. The non-equilibrium features of heavy-ion reactions with respect to isospin have been suggested and used as tools to measure isospin diffusion process during a heavy-ion reaction [100]. It is envisaged that extreme neutron excess could totally change the reaction mechanism or even open possibilities for extrapolating to pure neutron matter at varying densities and temperatures [9, 101]. The prospect of heavy-ion reaction studies on rare isotopes has been reviewed nicely by Li *et al.* [9].

As mentioned in Chapters 1 and 2, the isospin asymmetry of a reaction system impact, in a nontrivial manner, the possible nuclear Liquid-Gas Phase (LGP) transition. The nuclear multifragmentation process, the isotope yield and the isotope temperature, the specific heat also strongly depend on isospin. The multifragmentation process and the related liquid gas phase phase transition have been reviewed by Pochodzalla and Trautmann [102].

The theoretical studies on isospin physics in heavy-ion reactions have been a considerable success, but many issues are still unresolved. The strong isospin dependent nature of the multifragmentation process has been explored intensively, and some qualitative results are quite interesting [103, 104, 29]. However, the dynamics of cluster formation following particle correlation and the statistical phase

space partition are both not well understood. The dynamical evolution of a reaction system is significantly affected by isospin dependence of the nuclear equation of state [9, 103, 101]. The studies on the nuclear equation of state based on isospin dependent mean fields (IEOS) are an important extension of the studies on nuclear EOS with stable isotopes. Not only the density dependence of the symmetry potential is quite uncertain, but also the momentum dependence of the symmetry potential has still to be explored. The nuclear equation of state based on momentum independent mean fields sensitive to isospin asymmetry (MI IEOS) will be used for exploring the effects of the density dependence of the symmetry energy; the nuclear equation of state based on momentum dependent mean fields sensitive to isospin asymmetry (MD IEOS) will be used for exploring the additional effects of velocities changed differently for protons and neutrons. The isotope yields from heavy-ion reactions are also affected by the IEOS. The IEOS studies are important for understanding the explosion mechanism of supernovae as well as for the direct Urca cooling process of neutron stars [105]. I shall come to this last point in section 3.5.4.

In this section, I will introduce a parameterization of the isospin dependence of the nuclear equation of state. The isospin density dependence and momentum dependence are parameterized in section 3.5.2 and 3.5.3. As with other EOS studies, these parameterizations should be used to explore the possible physics in simulations, and the success or failure of these forms will be tested when comparing results from simulations and experiments. Some of these IEOS forms will be used later in the simulations in Chapter 5, and the results for isospin diffusion processes will be compared with the experimental results.

3.5.2 Density Dependence of Symmetry Potential

The isospin dependence of the nuclear EOS stems from the isospin dependence of the nuclear force. Since the isospin asymmetry is often small in heavy-ion

reactions, I can expand the energy density per particle as a power series in isospin asymmetry $\beta = (\rho_n - \rho_p)/\rho$:

$$e(\rho, \beta) = \frac{\tilde{e}}{\rho} = e(\beta = 0) + e^{(2)}\beta^2 + e^{(4)}\beta^4 + \dots . \tag{3.36}$$

Note that, in the discussion of energy density functional for isospin dependent mean fields, I will temporarily use β for isospin asymmetry in stead of the more standard symbol δ, just to distinguish it from the symbol δ for variational derivative.

The odd powers of asymmetry parameter β in the expansion in Eq. (3.36) vanishes because of charge symmetry for the nuclear force. Various microscopic calculations suggest a parabolic approximation for the isospin dependence to be quite good even up to pure neutron matter [106, 35], so that I can safely ignore higher order terms in the expansion in Eq. (3.36). The $e^{(2)}$ term is often called the symmetry energy of nuclear matter and is labelled ϵ_{sym}.

$$\epsilon_{sym} = \frac{1}{2}\frac{\partial^2 e}{\partial \beta^2} . \tag{3.37}$$

When the higher powers of isospin asymmetry β are ignored, I can also write the symmetry energy in the difference form:

$$\epsilon_{sym} = e(\beta = 1) - e(\beta = 0) , \tag{3.38}$$

which is the same as given in Chapter 1.

The isospin dependence of the nuclear EOS inevitably introduces isospin dependence to the quasiparticle energies, and thus gives rise to the different optical potential for the proton and the neutron. To characterize the isospin dependence of

the optical potential, I can define the symmetry potential by:

$$U_{sym} = \frac{1}{2} \left. \frac{\partial (U_n - U_p)}{\partial \beta} \right|_{\beta=0} \simeq \frac{(U_n - U_p)}{2\beta} . \tag{3.39}$$

The last equality is valid because the higher order terms in β in the energy can be ignored.

There is some knowledge on the magnitude of the symmetry energy at normal nuclear matter density. The nuclear mass models that fit many or even most of the known isotope data suggest the symmetry energy for normal nuclear matter is around $27 - 36$ MeV [107], where the large uncertainty of the value reflect the fact that the current nuclear data are mostly limited to nuclei close to the line of stability. Many theoretical calculations give a similiar value for the symmetry energy at normal density. Some of the recent results stem from the phenomenological Skyrme Hartree-Fock calculations [108], Brueckner-Hartree-Fock calculations [109, 35, 110, 111], Dirac-Brueckner-Hartree-Fock calculations [112, 113], variational many-body theory [8], chiral perturbation calculations [114, 115, 116] and relativistic mean field calculations [117, 118, 119].

However, the experimental results give little hint as to the density dependence of the symmetry energy, and different theories give different density dependence. The Skyrme interactions in use yield many different density dependencies for the symmetry energy, ranging from extremely soft to extreme stiffly density dependence [108]. Relativistic mean field interactions tend to produce stiff density dependencies and Brueckner calculation results vary depending on the resummations and theory cut-offs and on the inclusion of the three body-force [110, 113]. More recent relativistic mean field calculation, with either explicit density dependence of coupling constants [120] or with momentum dependence yield less stiff density dependencies [119] as compared to the original nonlinear models.

The isospin studies in nuclear reactions usually parameterize the density dependence of symmetry energy, and compare simulations with data to arrive at the best fit. Nuclear structure studies, including rare isotope experiments and high precision measurements of stable isotopes, will explore the isospin dependence of the nuclear effective interaction below normal density. Nuclear reaction studies will be the key for determination of the high density behavior of the isospin dependent EOS.

Energy Functional

The density dependence of the symmetry energy in the nuclear EOS will be specified in parameterized form. These forms will be used later in transport simulations. The results from these simulations will be compared with the experimental results, allowing to test the assumption on the density dependence of symmetry energy. One such comparison will be given in Chapter 5.

In consistency with the energy density functional used in the MI EOS parameterizations in section 3.4.2, the energy density of isospin asymmetric nuclear matter will be first parameterized as:

$$\begin{aligned}\tilde{e} = & \sum_X g_X \int \frac{d\mathbf{p}}{(2\pi)^3} f_X(\mathbf{p}) \sqrt{p^2 + m_X^2(\rho_s, \beta)} \\ & + \int_0^{\rho_s} d\rho_s' U(\rho_s') - \frac{1}{2} U_T \rho_s \beta^2 - \rho_s U(\rho_s) - \frac{a_s}{2\rho_0} \rho \nabla^2 \rho + \frac{1}{2} \rho_z \Phi \,. \end{aligned} \quad (3.40)$$

The Lorentz mass above depends both on the scalar density and isospin asymmetry, through the scalar optical potentials:

$$m_X(\rho_s, \beta) = m_X + A_X U(\rho_s) + 2 t_{3x} U_T(\rho_s) \beta \,. \quad (3.41)$$

The energy functional in Eq. (3.40) does not incorporate momentum dependence in the isospin part of the scalar potential. The resulting EOS will be referred to as MI

IEOS, *i.e.*, EOS based on momentum-independent MFs with isospin sensitivity.

The single particle energy derived from Eq. (3.40) with inclusion of finite-range and coulmb terms, is then:

$$\epsilon_X(p) = \sqrt{p^2 + m_X^2(\rho_s, \beta)} + \frac{1}{2}U_{TC}\beta^2 + A_X\, U_{grad} + Z_X\Phi. \tag{3.42}$$

The first order term in β enters into the energy through the Lorentz mass $m_X(\rho_s, \beta)$, while the self-consistent isospin dependent MF always introduces additional potential of the order β^2, through:

$$U_{TC} = {\rho_s}^2 \frac{\partial(U_T/\rho_s)}{\partial\rho_s}. \tag{3.43}$$

In principle, there is an additional correction factor for U_{TC} which comes from the derivative of the scalar density with respect to distribution function. The correction term is only on the order of $10^{-3}U_{TC}$ and will be neglected here. Note that the β^2 term in eq. (3.42) is a second-order correction that arises from the self-consistency requirement, and is very small for small asymmetries. The optical potential calculated from Eq. (3.42) is approximately linear in isospin asymmetry:

$$\begin{aligned} U_{opt} &\sim U(\rho_s) + 2t_{3x}U_T(\rho_s)\beta + \frac{1}{2}U_{TC}\beta^2\,, \\ &\sim U(\rho_s) + 2t_{3x}U_T(\rho_s)\beta\,, \end{aligned} \tag{3.44}$$

and so is the difference between the proton and neutron potentials. With this, U_T may be viewed as the symmetry potential defined before, and can be compared to the symmetry potential in [121].

Symmetry Energy

For the isospin density dependent MF parameterization in Eq. (3.40), the symmetry energy is of the form:

$$e_{sym} = \frac{1}{3}\frac{{p_F}^2}{2\epsilon_F} + \left(\frac{4m_X + 3U_T}{4\epsilon_F} - \frac{1}{2}\right)U_T + \frac{9}{4}\frac{m_X^2 U_T^2}{p_F^3}\left[\log\left(\frac{m_X}{\epsilon_F + p_F}\right) + \frac{p_F}{\epsilon_F}\right], \tag{3.45}$$

where p_F is Fermi momentum for the corresponding symmetric nuclear matter at a given density in the local frame, and

$$\epsilon_F = \sqrt{(p_F)^2 + (m_X(\rho_s, \beta = 0))^2}, \tag{3.46}$$

is the Fermi energy. The last term in Eq. (3.45) contributes to less than 5% of the total symmetry energy at normal density, but became significant at higher densities for the iso-stiff type of IEOS. The first term in Eq. (3.45) is associated with the Fermi motion of the quasi-particles, and will be called the kinetic symmetry energy e_{sym}^{kin}. The last two terms in Eq. (3.45), with powers of the symmetry potential U_T, could be called the interaction symmetry energy e_{sym}^{int}.

$$e_{sym} = e_{sym}^{kin} + e_{sym}^{int}. \tag{3.47}$$

At around normal densities in the non-relativistic reduction, if one uses $\epsilon_F \sim m_X \sim m$ and ignore higher powers of the symmetry potential U_T than first order, the symmetry energy in Eq. (3.45) reduces to:

$$e_{sym} \simeq \frac{1}{3}\frac{p_F^2}{2m} + \frac{1}{2}U_T. \tag{3.48}$$

At normal density $\rho_0 = 0.16$ fm^{-3}, I find the kinetic contribution to the symmetry

energy is about 12 MeV for a free Fermi gas. The experimental data on binding energy suggest a net symmetry energy value of $27 - 36$ MeV [107]. Thus, the interaction part of the symmetry energy is about the same magnitude as the kinetic part. The recent analysis of the binding energy of known isotopes, with separate fit parameters for volume and surface asymmetry terms, suggested a value of around $27 - 31$ MeV [41]. Many theoretical models have been tuned to yield the symmetry energy within the range of the previous values of $27 - 36$ MeV.

The Isospin Dependent Potential

The asymmetry part of the symmetry potential U_T is often represented as a simple power of density:

$$U_T(\rho_s) = 2.0\, A_i\, \xi^{\tau}. \tag{3.49}$$

where $\xi = \rho/\rho_0$ is the reduced density, the normalizing constant A_i is the interaction contribution to the symmetry energy at normal density and the exponent τ defines the stiffness of the density dependence. Because the kinetic symmetry energy scales as $\epsilon_F \sim \rho^{2/3}$ in the non-relativistic limit, I will define the iso-stiff type as $\tau > 2/3$ and iso-soft type otherwise. The isospin super stiff (iso-SH) case, $\tau = 2$, gives a very stiff density dependence similar to the dependence in some of the Skyrme-Hartree-Fock models [108] or in the non-linear coupling model in relativistic mean field theory; the isospin normal stiff (iso-NH) case, $\tau = 1$, which has the most naive form for density dependence, corresponds to the linear coupling model in relativistic mean field theory and is close to some of the Skyrme model dependencies. The normal isospin soft (iso-NS) case, $\tau = 1/3$, mimics the results from the Brueckner-Hartree-Fock calculations [35] and the density dependence from the relativistic mean field calculations with density or momentum dependent couplings

Table 3.3: Parameters for the nuclear equation of state based on momentum independent mean fields sensitive to isospin asymmetry (MI IEOS), all MI IEOS have the same symmetry energy at normal density $e_{sym} = 30MeV$.

MI IEOS	A_i MeV	B_i MeV	C_i	τ
iso-SH	19.17			2.0
iso-NH	19.17			1.0
iso-NS	19.17			1/3
iso-SKM	38.34	-15.34	0.2	

[120, 119]. Another type of utilized isospin soft EOS (iso-SKM) is of the form:

$$U_T = 2.0\frac{A_i\xi + B_i\xi^2}{1 + C_i\xi^2}. \tag{3.50}$$

where the constants A_i, B_i are adjusted to reproduce the symmetry energy at normal density, and the C_i term serves to limit the symmetry potential at high densities. This type of symmetry energy density dependence has been suggested by a special type of Skyrme interaction [101], and is similar to the dependence from chiral perturbation theory [114] and from variational many-body theory [8]. The symmetry potential from iso-SKM in [101] will generally fall below zero at high densities if the constant B_i is negative. The negative total symmetry energy would make the energy of pure neutron matter lower than nuclear matter with a finite proton fraction. Thus, for this density dependence, a neutron star would contain no protons at high densities.

The net symmetry energies for different IEOS are plotted as a function of density in Fig. 3.1. The IEOS are named after the behavior of the symmetry energy at densities higher than normal: the IEOS with the most stiff symmetry energy density dependence is the iso-SH, followed by iso-NH, while the iso-NS and iso-SKM are subsequently softer. The features of the symmetry energy are directly related to the features of the optical potential experienced by the particles, as shown in

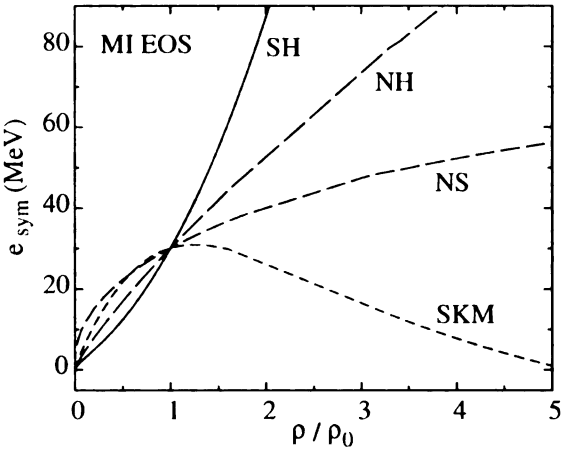

Figure 3.1: Density dependence of the net symmetry energy for four different IEOS: iso-SH, iso-NH, iso-NS, iso-SKM.

Fig. 3.2. Notice the optical potential lines for proton and neutron at $\beta = 0.4$ in Fig. 3.2 are almost equal spaced on the two side of the optical potential at zero asymmetry, this justifies the last approximation in Eq. (3.44).

A Non-Relativistic Reduction

In the past, a non-relativistic form of the isospin interaction was used for simulations. To facilitate comparisons with the past results, I will give here the optical potential formula in the non-relativistic limit.

If the isospin potential or the isospin asymmetry is small, the energy density Eq. (3.40) will reduce to Eq. (3.25) plus an extra isospin dependent energy density given by:

$$\tilde{e}_I = \frac{1}{2} U_T \rho_s \beta^2 . \tag{3.51}$$

The isospin dependent part of the optical potential derived from Eq. (3.51) will be:

$$U_{iso}^X = 2t_{3X} U_T \beta + \frac{1}{2} A_X U_{TC} \beta^2 . \tag{3.52}$$

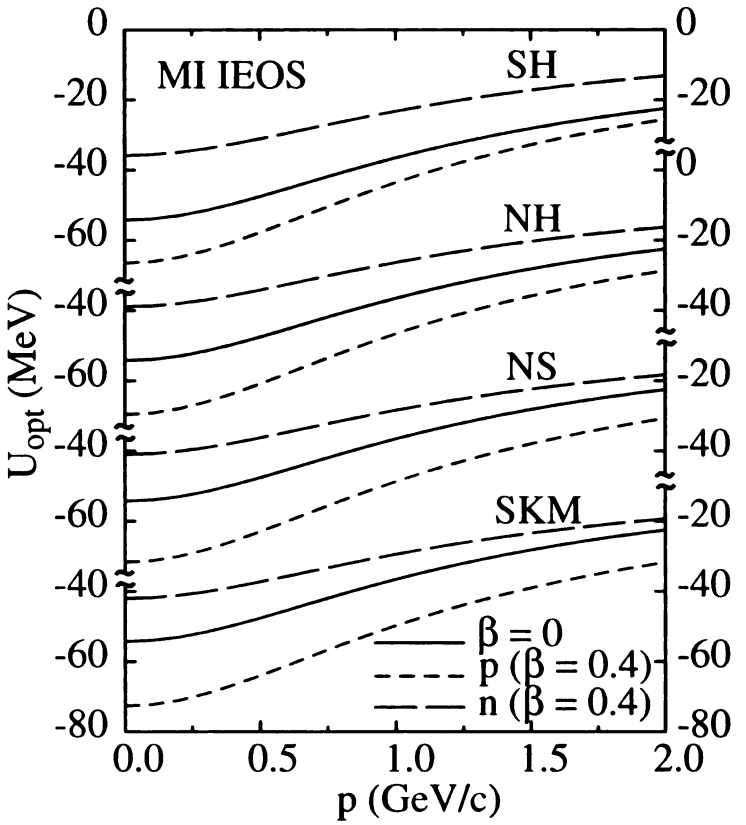

Figure 3.2: Optical potentials for four different IEOS: iso-SH, iso-NH, iso-NS and iso-SKM, at asymmetries $\beta = 0$ and 0.4 for protons and neutrons. At zero asymmetry, the optical potential are the same for protons and neutrons because of assumed exact symmetry between proton and neutron.

The explicit expression for the power-law types in particular, is:

$$U_{iso}^{X} = 4t_{3X}A_i\xi^{\tau}\beta + (\tau - 1)A_i\xi^{\tau}\beta^2 . \tag{3.53}$$

The isospin dependent part of the optical potential for the iso-SKM type is slightly more complicated:

$$U_{iso}^{X} = 4t_{3X}\frac{A_i\xi + B_i\xi^2}{1 + C_i\xi^2}\beta + \frac{B_i - 2A_iC_i\xi - B_iC_i\xi^2}{(1 + C_i\xi^2)^2}\xi^2\beta^2 . \tag{3.54}$$

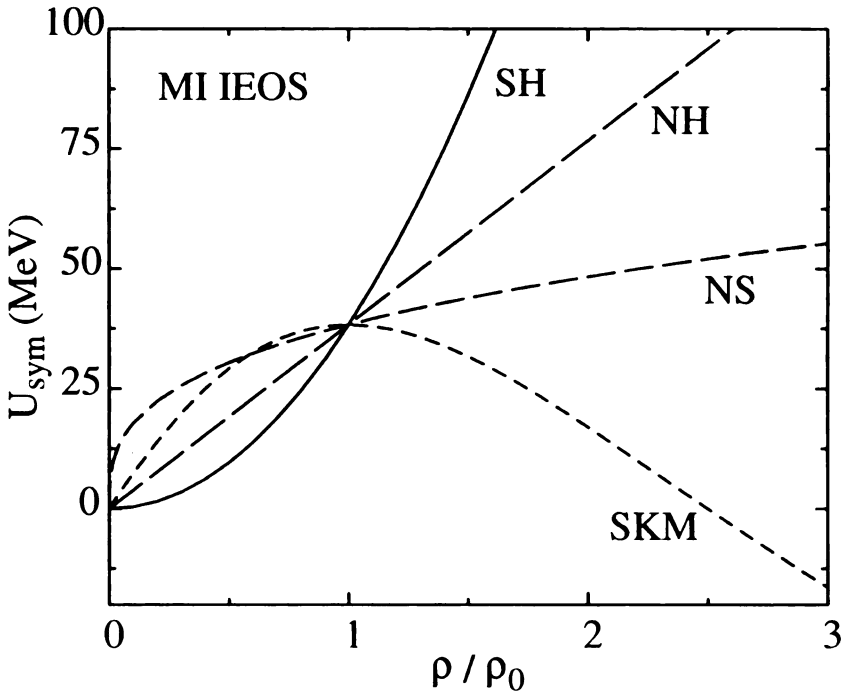

Figure 3.3: Symmetry potentials for particle of zero momentum are plotted as a function of density. The four different isospin dependent nuclear EOS are iso-SH, iso-NH, iso-NS and iso-SKM respectively.

The symmetry potential will then be:

$$U_{sym} = U_T = \begin{cases} A_i \xi^\tau, & \text{for power-law type;} \\ (A_i \xi + B_i \xi^2)/(1 + C_i \xi^2), & \text{for iso-SKM type.} \end{cases} \tag{3.55}$$

The non-relativistic formulation of isospin dependence is generally sufficient at low energies, where the non-relativistic reduction works well. As many of the experiments on isospin related heavy-ion reaction studies have concentrated on the low energy side, the non-relativistic reductions introduced here will be useful due to the simplicity of the formulas.

3.5.3 Momentum Dependence of Symmetry Potential

The symmetry potential, which represents the optical potential difference for protons and neutrons in isospin asymmetric nuclear matter, is not only density dependent, but also momentum dependent. Such momentum dependence for IEOS stems from isospin dependence of the non-local nuclear force as well as from exchange interaction [118]. An analysis of the forward nucleon scattering data by Grein [122] demonstrates a definite isospin momentum dependence of the scattering amplitude that is proportional to the optical potential S in the impulse approximation. Both the Bruecker-Hartree-Fock [123, 35] and the Dirac-Bruecker-Hartree-Fock [113, 124] calculations, which use the G-matrix generated from the various nuclear force, show a strong isospin momentum dependence for the nuclear mean fields. The relativistic mean field theories with explicit derivative coupling [119] or with exchange interaction [118, 117] and the chiral perturbation theory [114] also result in a strong isospin momentum dependence. In this section, I will present a general functional form for the IEOS, which could incorporate the isospin momentum dependence seen in various microscopic theories.

The common features of results from the microscopic calculations suggest the general functional form for the energy density. Given that, under the assumption of charge symmetry, the interaction between p-p and n-n should be the same, the proton and neutron should have the same properties in the symmetric nuclear matter. In neutron rich nuclear matter, the proton and neutron potentials and single particle energies will in general be different and the momentum dependence is seen to be different in the theoretical calculations. For low momentum particles, the n-p interaction is more attractive than the corresponding p-p or n-n interaction, resulting in a more attractive potential and a lower effective mass for the particles at a lower concentration (that is, typically the protons). But at higher momentum,

at around $p \sim 2$ GeV/c, the interactions between nucleons are repulsive and the optical potential becomes just the reverse of that at low momentum. Within a T-matrix analysis for high momentum particle, to be presented, I find that the proton optical potential is more repulsive in neutron rich matter than the neutron potential. The different behavior of the optical potential at high and low momentum suggests a cross-over that should occur at some intermediate momentum for the asymmetric nuclear matter. Such a cross-over is also directly supported by some theoretical results [123, 35, 121].

Optical Potential Within the T-matrix Approximation

As I have mentioned earlier, the optical potential for particles with a high momentum could be obtained from an analysis of the forward elastic scattering data within the T-matrix approximation (also called impulse approximation). In what follows, I will present the T-matrix approximation and employ it to obtain the optical potential for high-momentum particles in asymmetric matter, using nucleon-nucleon scattering data. The resulting high momentum characteristics will be used in the construction of the energy functional form in the present section.

Within the T-matrix approximation, valid for high-momentum particles, the optical potential is related to the real part of the elementary forward scattering amplitude.

$$U_{opt} = \rho T = -\frac{4\pi}{E}\Re(\mathcal{F})\,. \tag{3.56}$$

Here, ρ is the density of the scatterers, T is T-matrix and $\mathcal{F}$ is the scattering amplitude. The forward elastic scattering data have been analyzed by Grein [122]. This analysis, utilizing Coulomb-nuclear interference, produced ratio of the real-to-imaginary forward scattering amplitude $R = \Re(\mathcal{F})/\Im(\mathcal{F})$.

As the imaginary part of the scattering amplitude in the forward direction is

related to the total cross section through the optical theorem,

$$\sigma_{NN} = \frac{4\pi}{p}\Im(\mathcal{F}). \tag{3.57}$$

One can express the optical potential in terms of cross section and the amplitude ratio R:

$$U_{opt} = -\rho\frac{p}{E}R\sigma_{NN}. \tag{3.58}$$

In the two component system, the optical potential for a given particle is the sum of optical potential contributions from each species:

$$\begin{aligned} V_p &= -\frac{p}{E}(\rho_p\,\sigma_{pp}R^{pp} + \rho_n\,\sigma_{pn}R^{pn}), \\ V_n &= -\frac{p}{E}(\rho_p\,\sigma_{pn}R^{pn} + \rho_n\,\sigma_{nn}R^{nn}). \end{aligned} \tag{3.59}$$

For the momenta $p \lesssim 2$ GeV/c, the ratios R are $R^{np} \simeq -0.59$ and $R^{pp} \simeq -0.28$, and the total cross sections are $\sigma_{pn} \simeq \sigma_{pp} \simeq 4$ fm^2. At the normal density of $\rho = 0.16$ fm^{-3} and $\beta = 0.2$, the optical potentials at $p \lesssim 2$ GeV/c, assuming charge symmetry, are $V_p \simeq 43.2$ MeV and $V_n \simeq 37.5$ MeV. This kind of considerations give guidance concerning the behavior of optical potentials at high momentum: the difference $V_p - V_n$ is small and positive and increases only linearly with increasing density. This will help in constructing the energy functional for mean fields with combined momentum and isospin dependencies.

The specific values of the optical potential should not be treated quite literally, because of possible limitations of the impulse approximation and because of uncertainties in measuring proton-neutron interactions. The Dirac phenomenological analysis of the nucleon-nucleus scattering data yield *e.g.* $V_p = 25.8$ MeV for a 2 GeV/c momentum particle ([125] fit 1). Similar values for the optical potential were also obtained in the relativistic mean field model [126]. Both results are not

very far away from the proton optical potentials estimated in this section.

Energy Functional

Extending the development of energy functional for isospin independent but momentum dependent mean field in section 3.4.3, I parameterize the energy density in the local rest frame as:

$$\begin{aligned} \tilde{e} &= \sum_X g_X \int \frac{d\mathbf{p}}{(2\pi)^3} f_X(\mathbf{p}) \left(m_X + \int_0^p dp' \, v_X^*(p', \rho, \beta) \right) \\ &+ \int_0^\rho d\rho' \, U(\rho') + \frac{1}{2} U_T \, \rho \beta^2 - \frac{a_s}{2\rho_0} \rho \nabla^2 \rho + \frac{1}{2} \rho_z \Phi. \end{aligned} \tag{3.60}$$

The essential difference here is the isospin dependence of the single particle velocity:

$$v_X^*(p, \xi, \beta) = p \Bigg/ \sqrt{p^2 + m_X^2 \Bigg/ \left(1 + c \frac{m_N}{m_X} \frac{A_X \, \xi (1.0 - 2 t_{3x} a \beta)}{(1 + \lambda p^2 / m_X^2)^2} \right)^2}. \tag{3.61}$$

where the extra term $(1.0 - 2t_{3x}a\beta)$ is different for protons ($t_{3x} = -1/2$) and neutrons ($t_{3x} = 1/2$), and gives rise to a different momentum dependence for those particles. In the case of zero asymmetry, the dispersion relations are exactly the same for protons and neutrons. The parameter a is within the range $0.0 \leq a \leq 1.0$, and it controls the isospin momentum dependence of the IEOS. Since the velocity is just the slope of the quasiparticle energy as a function of momentum, the larger values of a produce a bigger difference in the slope between protons and neutrons. I will later introduce a model independent parameter that quantifies the sensitivity of momentum dependence of the symmetry potential.

The energy density in Eq. (3.60) gives rise to the single particle energy in the

local rest frame of the form:

$$\begin{aligned}\epsilon_X(p,\rho) &= m_X + \int_0^p dp' v_X^*(p,\xi,\beta) + A_X U(\rho) + U_X^v(\rho) \\ &+ 2t_{3X}U_T\beta + \frac{1}{2}U_{TC}\beta^2 + A_X U_{grad} + Z_X\Phi\,. \end{aligned} \tag{3.62}$$

As compared to Eq. (3.42), the additional isospin dependent potential U_X^v stems from the variation of the density dependent velocity and is given by:

$$U_X^v(\rho) = \sum_Y g_Y \int \frac{d\mathbf{p}}{(2\pi)^3} f_Y(\mathbf{p}) \left(\int_0^p dp' \frac{\partial v_Y^*}{\partial \rho_X} \right) . \tag{3.63}$$

The energy functionals in Eqs. (3.61) and (3.62) incorporate additional momentum dependence in the isospin part of the scalar potential. The resulting EOS will be referred to as MD IEOS, *i.e.*, EOS based on momentum-dependent MFs with isospin sensitivity.

The isospin dependent potential term U_T has the same form as for the momentum-independent mean fields given by Eq. (3.49) and (3.50). Since they are independent of momentum, these potentials do not change the velocity as a function of momentum. Notably, the density dependence of the current IEOS parameterizations is mostly determined by the potential term U_T. The effects of asymmetry on the optical potential at normal density and twice normal density are displayed in Fig. 3.4 and Fig. 3.5. As may be apparent in Fig. 3.4 in asymmetric nuclear matter at normal density, the optical potentials for protons and neutrons cross at some intermediate momentum. As mentioned before, this cross-over is consistent with the T-matrix analysis. The parameterizations generate the expected behavior for the symmetry potential at low and high momenta for three of the IEOS. However, different density dependencies of the isospin dependent optical potential show up clearly at twice normal densities in Fig. 3.5. The symmetry energy in

zero-temperature matter is both impacted by the symmetry potential $U_T(\rho)$ and by the parameter a describing the sensitivity of particle velocities to asymmetry. The symmetry potential as a function of momentum is plotted in Fig. 3.6. The density dependence of the symmetry energy for a few MD IEOS is next plotted in Fig. 3.8. Three of the MD IEOS have identical symmetry potential at normal nuclear matter density, because the three power-law forms for U_T in Eq. 3.49 yield identical values at normal density. The symmetry potential for zero-momentum particles is also plotted as a function of density in Fig. 3.7. The density dependencies of the symmetry potential for both MI IEOS and MD IEOS stem from the potential of $U_T(\rho)$, which is exemplified by the similarities between Fig. 3.3 and Fig. 3.7.

For those parameters that already appeared in the isospin-independent parameterization of velocity in section 3.4.3, I will take the parameters from set $S3$ in Table 3.2, which were tested in the previous BUU simulations [12] and were found to agree well with the data on elliptic flow. The parameters for the MD IEOS are listed in Table 3.4. Because of the sensitivity of momentum dependence to isospin, the parameters A_i and B_i in the potential U_T need to be adjusted so as to produce the symmetry energy of nuclear matter at normal density of around 30 MeV.

For the iso-SKM type of density dependence, the above implementation of the sensitivity to isospin results in some pathological behavior at higher densities. Specifically, as the symmetry potential becomes negative at high densities, the proton optical potential at zero momentum gets higher than the neutron optical potential in neutron rich nuclear matter. If the momentum dependence is still governed by Eq. 3.61, the proton and neutron optical potential difference is going to increase with increasing momentum. Such behavior is not expected at high momentum given the results from the T-matrix approximation and the forward NN scattering data. To allow the optical potential difference between protons and neutrons decrease as momentum increases at high density, I have to allow for a sign

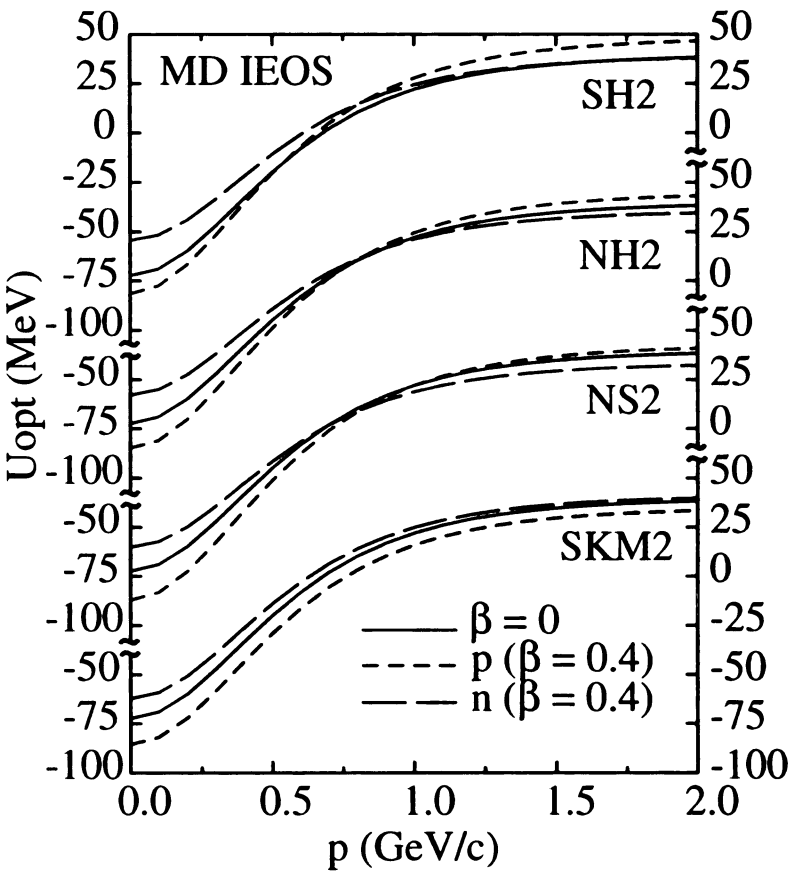

Figure 3.4: Optical potential for protons and neutrons at normal density, for four of the MD IEOS: iso-SH, iso-NH, iso-NS and iso-SKM, in symmetric ($\beta = 0$) and asymmetric ($\beta = 0.4$) nuclear matter, as a function of nucleon momentum p.

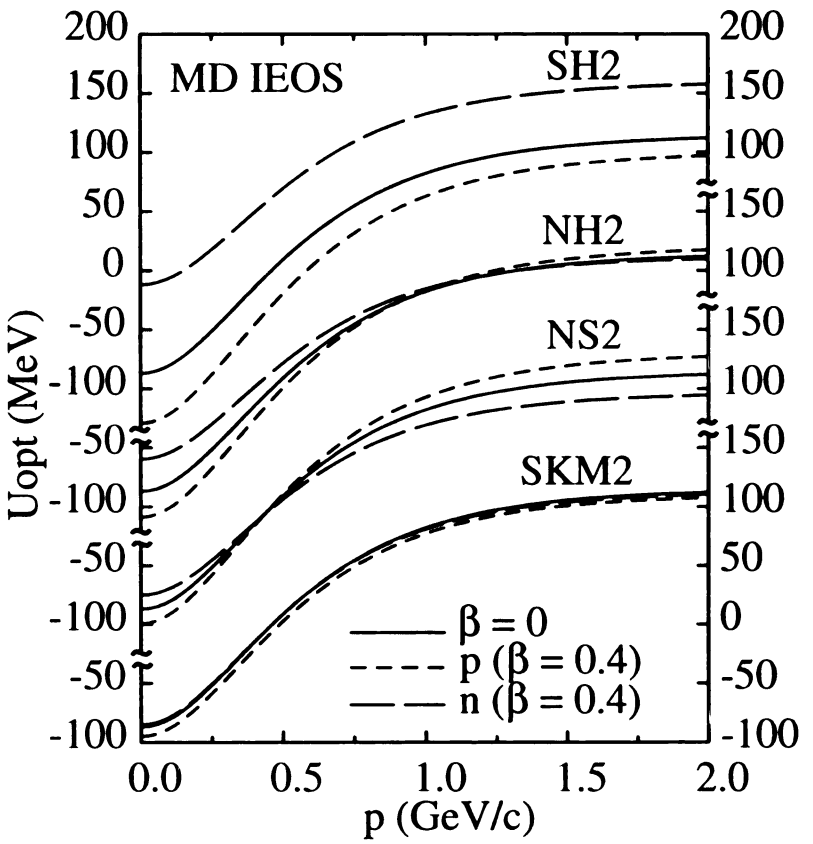

Figure 3.5: Optical potential for protons and neutrons at twice normal density, in symmetric ($\beta = 0$) and asymmetric ($\beta = 0.4$) nuclear matter, as a function of nucleon momentum p.

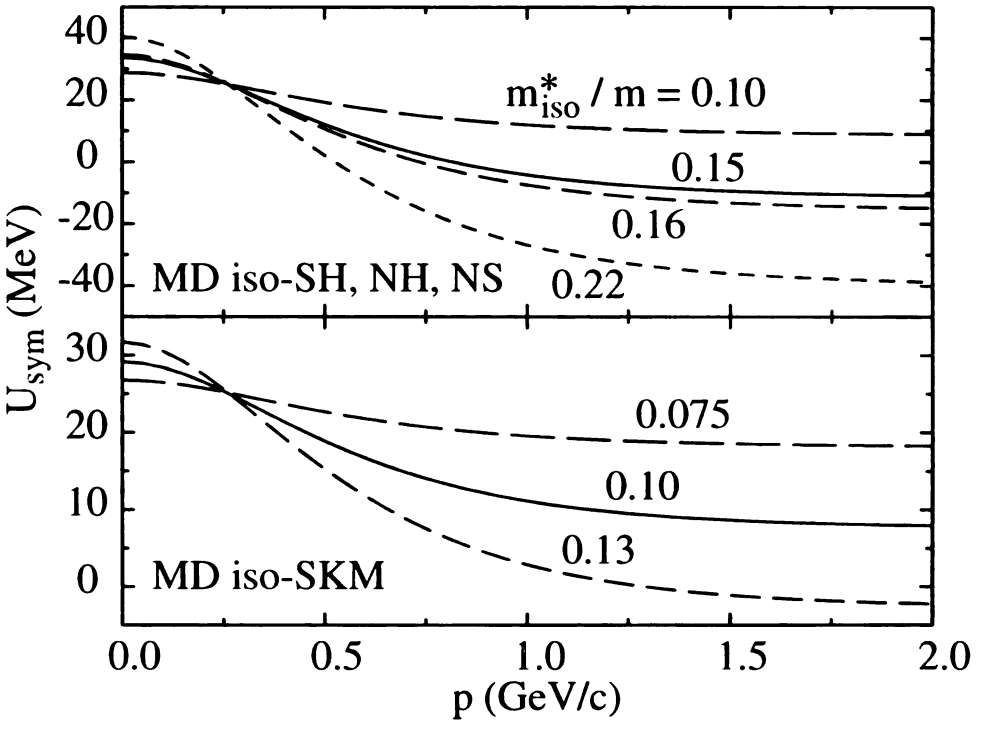

Figure 3.6: Symmetry potential as a function of momentum p for different MD IEOS. The three of the MD IEOS, iso-SH, NH and NS, give rise to the same symmetry potentials, for the same effective mass parameter m^*_{iso}. The different momentum dependencies for each the two types of parameterizations are labeled by respective m^*_{iso}/m values.

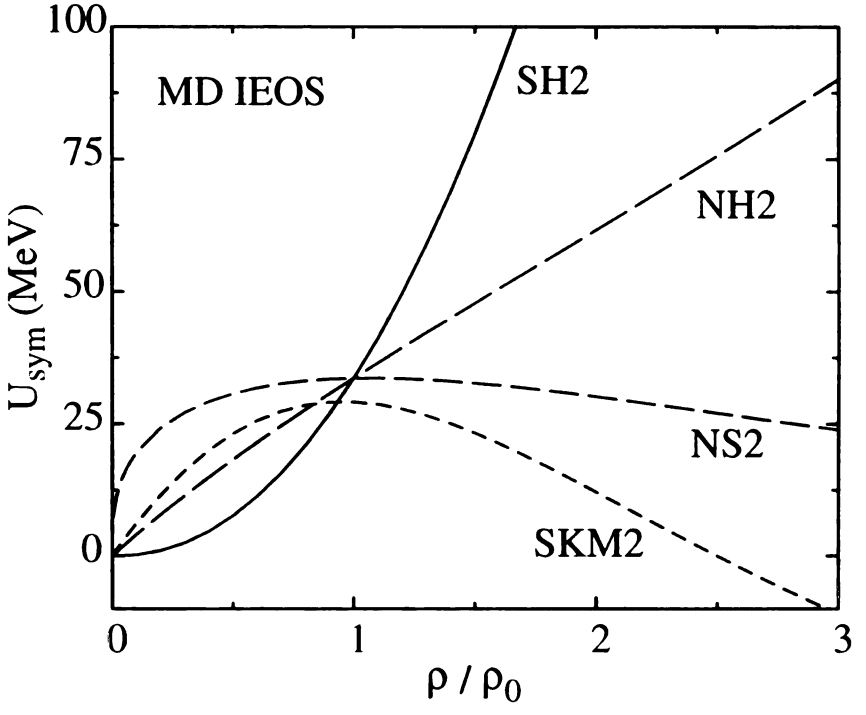

Figure 3.7: Symmetry potential at zero-momentum as a function of nuclear matter density ρ for different MD IEOS.

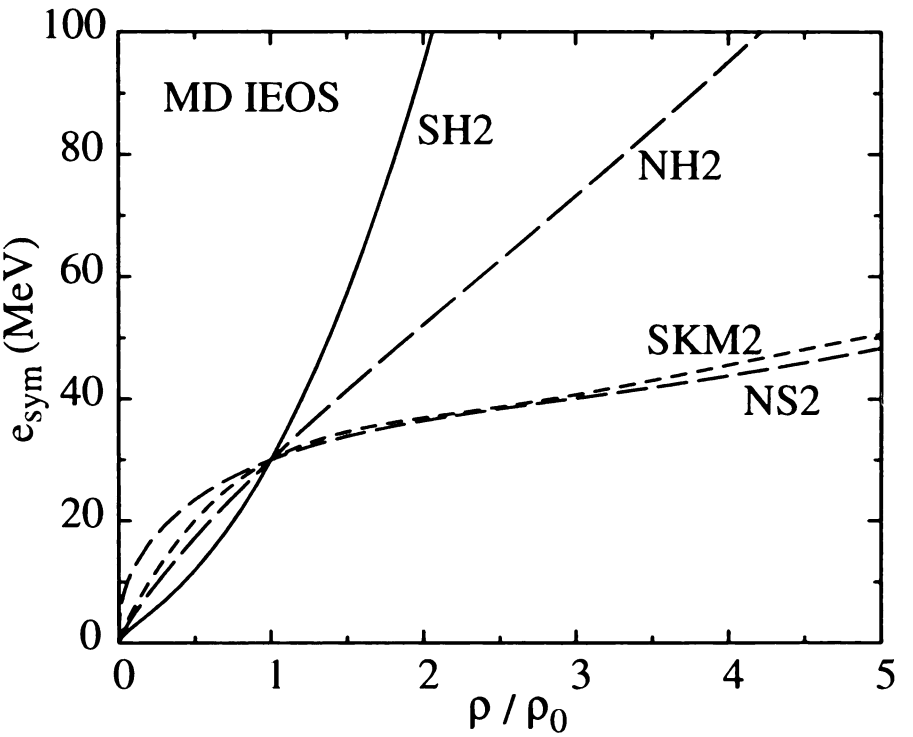

Figure 3.8: Net symmetry energy as a function of density for different MD IEOS. The iso-NS and iso-SKM cases almost overlap for the momentum dependent cases here.

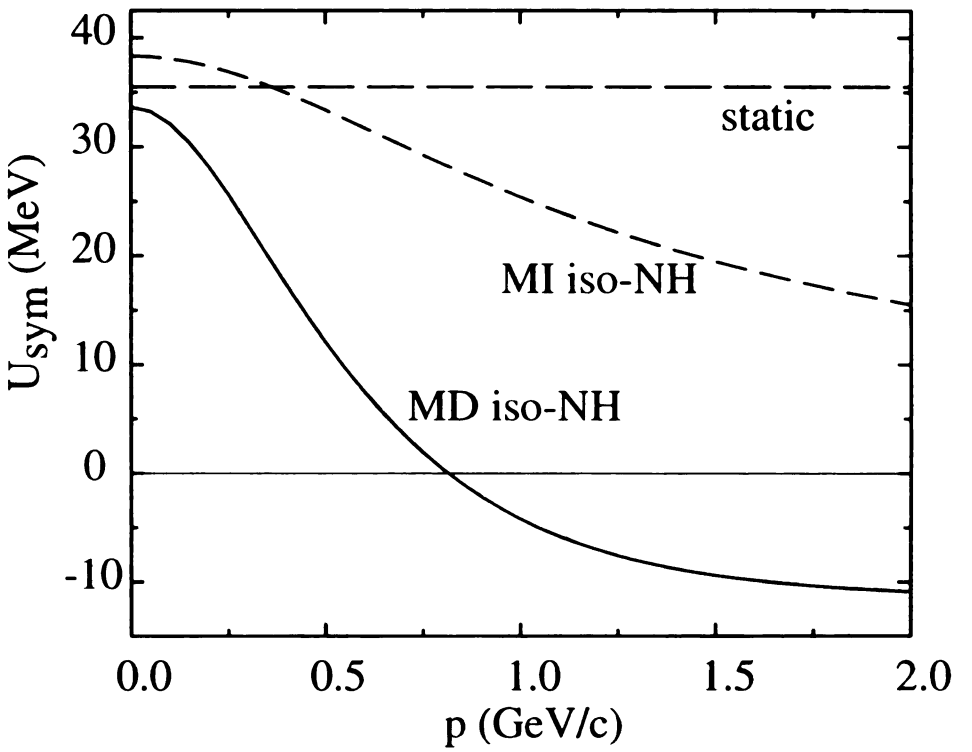

Figure 3.9: Symmetry potential as a function of momentum p for the iso-NH type of IEOS. The different lines correspond to the NH2 parameter set for the MD IEOS (see table 3.4), the iso-NH set for the MI IEOS (table 3.3) and the static form of the same MI IEOS in Eq. (3.55). The momentum-dependence for the symmetry potential in MI IEOS stems from the use of scalar quantities in parameterizing the effects of interactions.

Table 3.4: Parameters for the MD IEOS, where the parameters are adjusted so that they have the same symmetry energy at normal density $e_{sym} = 30$ MeV.

MD IEOS	A_i MeV	B_i MeV	C_i	τ	a	b	m^*_{iso}/m
SH1	16.3417			2.0	0.2		0.10
SH2	21.2522			2.0	0.45		0.15
SH3	22.2405			2.0	0.5		0.16
SH4	28.2159			2.0	0.8		0.22
NH1	16.3417			1.0	0.2		0.10
NH2	21.2522			1.0	0.45		0.15
NH3	22.2405			1.0	0.5		0.16
NH4	28.2159			1.0	0.8		0.22
NS1	16.3417			1/3	0.2		0.10
NS2	21.2522			1/3	0.45		0.15
NS3	22.2405			1/3	0.5		0.16
NS4	28.2159			1/3	0.8		0.22
SKM1	28.4267	-11.3707	0.2		0.2	0.4	0.075
SKM2	33.28	-13.312	0.2		0.5	0.4	0.10
SKM3	38.3067	-15.3227	0.2		0.8	0.4	0.13

change for the isospin momentum dependence parameter at some intermediate density. For the case of iso-SKM type of IEOS, this can be accomplished with:

$$v^*_X = p/\sqrt{p^2 + m_X^2/\left(1 + c\frac{m_N}{m_X}\frac{A_X\,\xi[1.0 - 2t_{3x}a\beta(1-b\xi)/(1+b\xi)]}{(1+\lambda p^2/m_X^2)^2}\right)^2}. \quad (3.64)$$

The additional parameter b controls the sign change of the isospin momentum dependence. However, it should be cautioned that such a sign change is neither based on any physical argument nor supported by any microscopic theory.

The Isospin Momentum Dependence

The sensitivity of momentum dependence to isospin asymmetry is characterized by the parameter a (or a and b in the case of iso-SKM), while the sensitivity of density dependence to asymmetry is characterized by the potential parameters A_i and τ (or A_i, B_i, and C_i in the case of iso-SKM). The impact of the isospin

momentum dependence parameter a is demonstrated in Figs. 3.10 and 3.11. Note that the difference in effective masses has both contributions from the difference in proton and neutron Fermi momenta and from the sensitivity of the optical potential to isospin momentum dependence. To characterize the sensitivity of the momentum dependence to isospin, in a model independent way, one can introduce the following parameter to characterize the isospin dependence of the effective mass:

$$m^*_{iso} = \frac{1}{2} \left. \frac{\partial(m^*_n - m^*_p)}{\partial \beta} \right|_{\beta=0} . \tag{3.65}$$

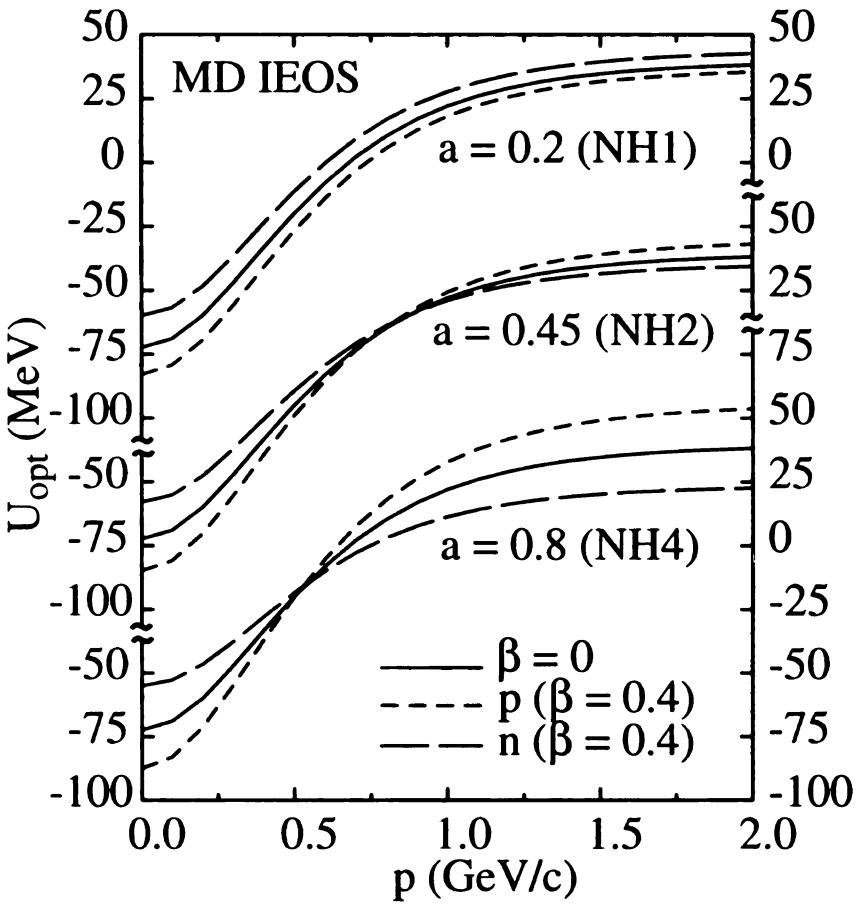

Figure 3.10: The isospin momentum dependence parameter a controls the relative difference of proton and neutron velocities, as a function of changing momentum of the particles. A high value of the parameter a will significantly raise the velocity for protons relative to neutrons in neutron-rich matter by strengthening the momentum dependence of the optical potential of protons and weakening the dependence for neutrons.

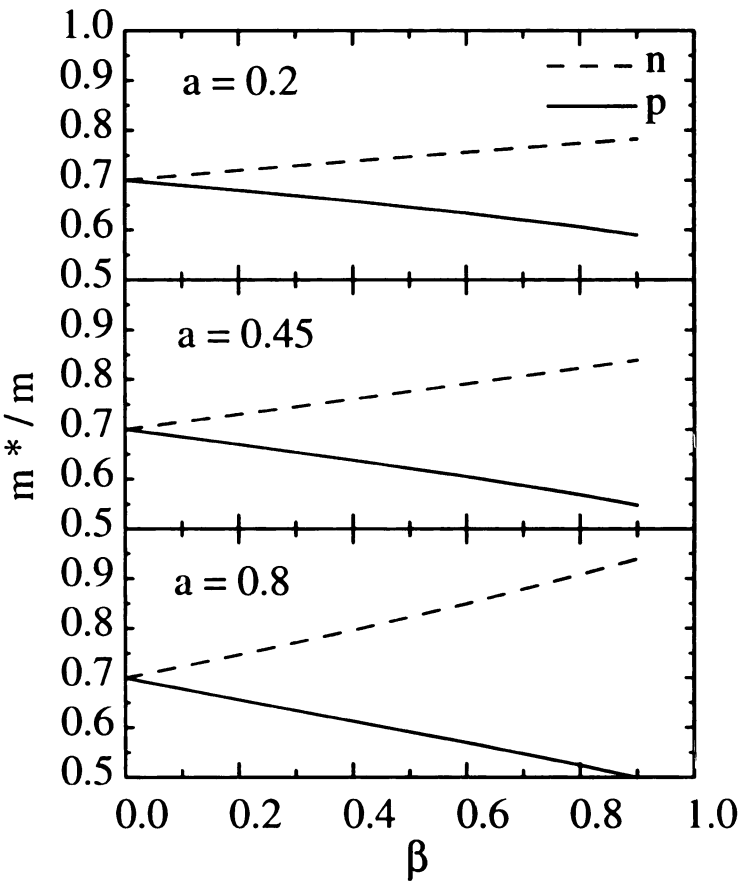

Figure 3.11: The isospin momentum dependence parameter a affects the effective mass at non-zero asymmetries. Shown is the effective mass vs asymmetry β for the iso-NH type of MD IEOS. The split between the proton and neutron effective mass increases with the parameter a.

3.5.4 Direct Urca Process in Neutron Stars

The isospin dependence of the nuclear equation of state has direct astrophysical implications. I will discuss here the effect of IEOS on the direct Urca cooling process in this section. The direct Urca process is an efficient cooling process in hot neutron stars, and at high proton fraction, the direct Urca process will dominate over the modified Urca process and lead to a fast cooling of neutron stars. The direct Urca process in neutron stars is believed to be an important cooling process in hot neutron stars [105]. Recent data from Chandra observatory demonstrates a fast cooling of neutron stars [127], in support of the direct Urca process.

Within the direct Urca process, neutrinos are produced in a two step cycle: neutrons decay into protons and emit antineutrinos, subsequently the protons convert back into neutrons via electron capture and emit neutrinos. Thus, the cycle is:

$$\begin{aligned} n &\rightarrow p + e^- + \overline{\nu}_e \,, \\ e^- + p &\rightarrow n + \nu_e . \end{aligned} \tag{3.66}$$

For the sequence to take place, momentum conservation requires:

$$p_f^p + p_f^e \geq p_f^n \geq \mid p_f^p - p_f^e \mid \,. \tag{3.67}$$

Because of the ultra-relativistic nature of the electron, the energy constraints are less stringent than the momentum constraints and could be ignored for most densities and forms of IEOS. The charge neutral condition requires equal proton and electron density $\rho_p = \rho_e$ and consequently equal Fermi momentum,

$$p_f^p = p_f^e . \tag{3.68}$$

One also knows that Fermi momentum scales as $p_f \sim \rho^{1/3}$, so that the above condition gives the critical proton fraction:

$$y_{cr} = \frac{\rho_p}{\rho_p + \rho_n} = \frac{1}{9}\,. \tag{3.69}$$

I will show how the different IEOS will affect the onset of the direct Urca process. Here I will only consider a cold neutron star, and examine the equilibrium proton concentration in a neutron star. If the equilibrium proton concentration y_{eq} is larger than the critical proton fraction y_{cr} for momentum conservation, then the direct Urca process becomes a favorable cooling process for the corresponding hot neutron star. A more thorough investigation would require calculation of a reaction rate for the modified and direct Urca processes at non-zero temperatures in order to determine the dominant process.

The electron gas is treated here as an ultra-relativistic ideal gas, where single particle energies are $\epsilon = \sqrt{p^2 + m_e^2} \sim p$, and the energy density corresponds to the sum of single particle energy up to the Fermi momentum. The variation of the total energy with respect to the proton fraction gives the equilibrium condition:

$$\mu_e = \mu_n - \mu_p\,, \tag{3.70}$$

where the chemical potentials are the respective single particle energies at the Fermi surface. From this condition, I find the equilibrium proton fraction y needs to satisfy the relation:

$$4e_{sym}(1 - 2y) = p_F y^{1/3}\,. \tag{3.71}$$

where p_F is the Fermi momentum for the corresponding symmetric nuclear matter. The equilibrium proton fraction in a neutron star depends sensitively on the ratio of the nuclear-matter Fermi-momentum to the net symmetry energy for the given

density. If the symmetry energy turns negative, the equilibrium proton fraction vanishes, *i.e.*, pure neutron matter becomes energetically favorable; if the symmetry energy stays positive, then equilibrium proton fraction will be always non-zero. On the other hand, if the symmetry energy is positive and large, the symmetric nuclear matter may become favorable. Such a conclusion is independent of the density dependence of the terms in the EOS or momentum dependence of the optical potential.

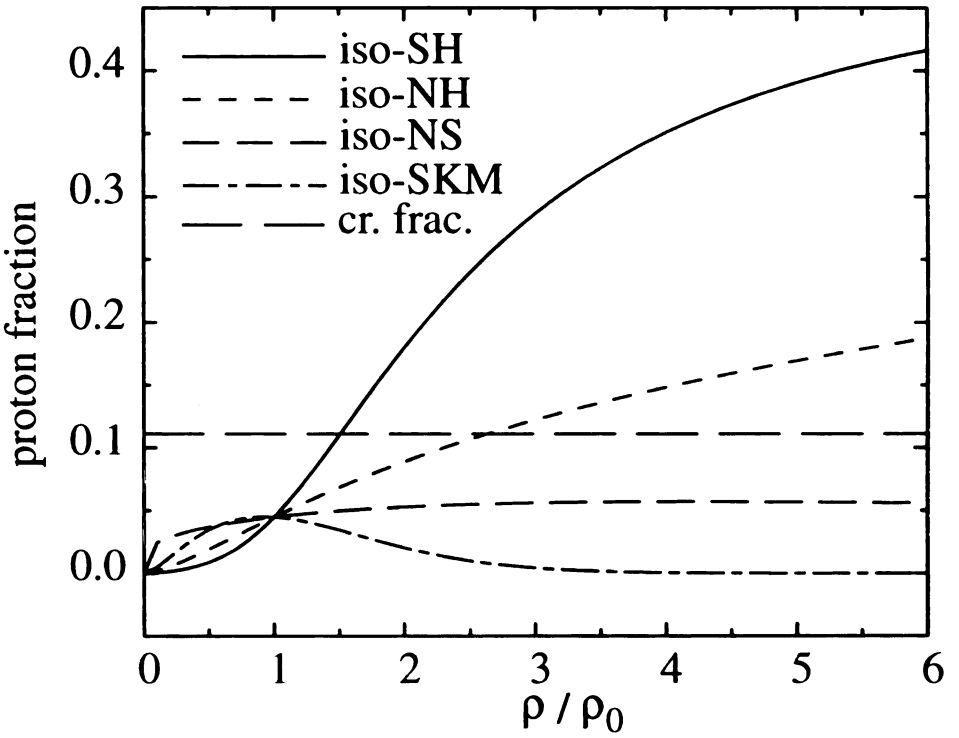

Figure 3.12: Equilibrium proton fraction for the different MI IEOS: iso-SH, iso-NH, iso-NS, and iso-SKM, together with the critical proton fraction.

The proton equilibrium fraction in a neutron star and the critical proton fraction for direct Urca process are plotted in Fig. 3.12 for four of the IEOS with no momentum dependence in optical potentials. The iso-SH and iso-NH interactions will give rise to high proton concentrations at high densities, and thus will enable the direct Urca process and fast cooling in hot neutron star; while the equilibrium

proton fractions for the other two types of EOS (iso-NS and iso-SKM) are always below the critical proton fraction for the direct Urca process, and not allow for a fast cooling in a neutron star. Since the momentum-independent iso-SKM case will lead to a negative symmetry energy at high densities, the equilibrium proton fraction vanishes at high densities, leading to pure neutron matter in the center of neutron stars. The critical proton fraction of $y_{cr} = 1/9$ is also plotted for reference.

3.6 Aspects of Transport Simulations of Heavy-ion Collisions

This section deals with details of transport theory implementations in heavy-ion collisions. The self-consistent initialization of the nuclear ground state is important for the description of the excitations during the reaction, and is given in section 3.6.1. The quasi-particle ensemble method is used for integrating the transport equations, and it is discussed in section 3.6.2. The lattice hamiltonian method is used for achieving a high accuracy in the numerical integration, and it is described in section 3.6.3. Both the in-medium cross section and free space NN cross section are used in transport simulations, and a few of the common used parameterizations of the in-medium cross section are discussed in section 3.6.4.

3.6.1 Initialization of a Reaction System

At the start of the reaction simulation the nuclei need to be initialized in their ground states. The minimization of the energy functional for the ground state nuclei, leads to the Thomas-Fermi (TF) equations for nuclear densities.

Specifically, to determine the ground state properties of a nucleus, I try to minimize the total energy of a system under the condition of fixed total neutron and proton numbers in the nuclear frame. The condition of fixed total N and Z are imposed through the introduction of Lagrange multipliers. The condition of the minimal energy subject to the constraints, under the variation of the distribution function for protons and neutrons then yields:

$$0 = \tilde{\epsilon}_p\left(p_p^F\right) - a_s \nabla^2 \left(\frac{\rho}{\rho_0}\right) + U_{iso}^p + \Phi - \mu_p, \tag{3.72}$$

$$0 = \tilde{\epsilon}_n\left(p_n^F\right) - a_s\nabla^2\left(\frac{\rho}{\rho_0}\right) + U_{iso}^n - \mu_n\,, \tag{3.73}$$

These are just the Thomas-Fermi equations in the local frame. In the above equations, μ_p and μ_n are the Lagrange multipliers for the proton and neutron numbers, respectively. The consistency for the nuclear density requires that $\nabla\rho = 0$ at the edge of the density distribution.

The role of the derivative correction in (3.72), (3.73), and (3.29) is to reduce the effect of the negative MF when the density distribution in the vicinity is primarily concave and to enhance the effect of the field when the density is convex. Such a result would be obtained for a finite-range effective two-body interaction convoluted with density expanded in position to second order. Not surprisingly, the derivative correction to single particle energy is small but it becomes important when the energies balance, such as in Eqs. 3.72 and 3.73, permitting an adequate description of the density in the ground state.

In finding the density profile, it is convenient to transform the TF equations into:

$$\frac{1}{r^2}\frac{d}{dr}\,r^2\,\frac{d}{dr}\,\rho = \frac{\rho_0}{2a_1}\left[\tilde{\epsilon}_p^F + \Phi + \tilde{\epsilon}_n^F + U_{iso}^p + U_{iso}^n - \mu_p - \mu_n\right]\,, \tag{3.74}$$

$$\mu_p - \mu_n = \tilde{\epsilon}_p^F + \Phi - \tilde{\epsilon}_n^F + U_{iso}^p - U_{iso}^n\,. \tag{3.75}$$

The net density profile $\rho(r)$ may be obtained by starting Eq. (3.75) with some density at $r = 0$. At any r, separate ρ_p and ρ_n may be found from (3.75) and Φ can be obtained from Gauss' Law. The acceptable starting ρ at $r = 0$ is the one for which $\rho = 0$ is reached in the solution simultaneously with $d\rho/dr = 0$ at the edge of the density distribution. The Coulomb potential Φ is computed in the solution by integrating the electric field from Gauss' Law. The chemical potentials are adjusted until the required proton and neutron numbers are obtained. At the end of the

calculation, the obtained potential Φ and μ_p may be renormalized, so that $\Phi \rightarrow 0$ as $r \rightarrow \infty$.

Figure 3.13 shows the calculated proton and neutron density profiles for a moderate and for a large nucleus and for MFs corresponding to $K = 210$ MeV, with and without momentum-dependence.

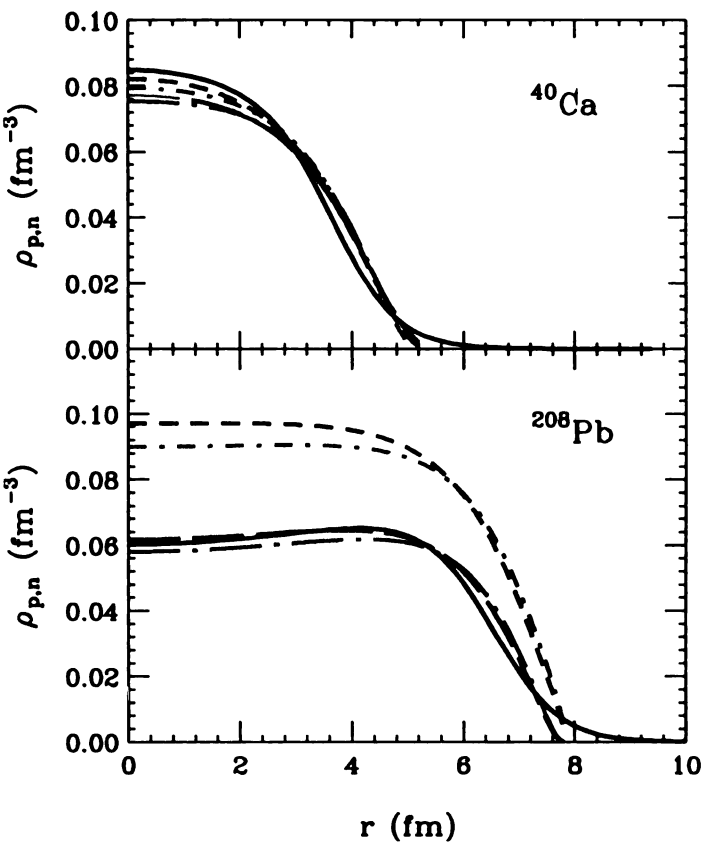

Figure 3.13: Nucleon density profiles from solving the TF equations for MFs corresponding to $K = 210$ MeV, together with the empirical charge density profiles for ^{40}Ca and ^{208}Pb. The solid lines represent the empirical profiles from Ref. [11]. The long- and short-dashed lines represent the proton and neutron profiles, respectively, for the momentum-independent field. The long- and short-dash-dotted lines represent the proton and neutron profiles, respectively, for the momentum-dependent field parameter set S3 in Table 3.2 that yields $m^* = 0.70\,m$. (From [12]).

3.6.2 Integration of Transport Equations

In integrating the Boltzmann equations, I employ the ensemble test particle method. Within that method, each quasi-particle is represented by a large number of test particles, (usually $\mathcal{N} > 170$). Each test particle represents a possible phase space location for the quasi-particle. An average over all these possible phase space configurations within some phase space volume gives the quasi-particle distribution $f(\mathbf{p}, \mathbf{r})$,

$$\frac{g}{(2\pi)^3} f(\mathbf{p}, \mathbf{r}, t) = \frac{1}{\mathcal{N}} \sum_k \delta(\mathbf{p} - \mathbf{p}_k(t))\, \delta(\mathbf{r} - \mathbf{r}_k(t))\,, \tag{3.76}$$

where it is understood that both sides are to be averaged over the phase space volumes. Without the collision in the Boltzmann equations, the quasiparticle distribution follow Vlasov equations. For the distribution in Eq. (3.76), a Vlasov equations yields:

$$\begin{aligned}
&- \sum_k \dot{\mathbf{p}}_k \delta'(\mathbf{p} - \mathbf{p}_k(t))\, \delta(\mathbf{r} - \mathbf{r}_k(t)) \\
&- \sum_k \dot{\mathbf{r}}_k \delta(\mathbf{p} - \mathbf{p}_k(t))\, \delta'(\mathbf{r} - \mathbf{r}_k(t)) \\
&+ \frac{\partial \epsilon}{\partial \mathbf{p}} \sum_k \delta(\mathbf{p} - \mathbf{p}_k(t))\, \delta'(\mathbf{r} - \mathbf{r}_k(t)) \\
&- \frac{\partial \epsilon}{\partial \mathbf{r}} \sum_k \delta'(\mathbf{p} - \mathbf{p}_k(t))\, \delta(\mathbf{r} - \mathbf{r}_k(t)) \;= 0
\end{aligned} \tag{3.77}$$

For this to hold, coefficients in front of the respective delta-functions must vanish, which demonstrates that the test particles must follow Hamilton's equations:

$$\begin{aligned}
\frac{d\,\mathbf{r}_k}{dt} &= \frac{d\,\epsilon}{d\,\mathbf{p}_k}\,, \\
\frac{d\,\mathbf{p}_k}{dt} &= -\frac{d\,\epsilon}{d\,\mathbf{r}_k}\,.
\end{aligned} \tag{3.78}$$

The quasi-particle energy ϵ, specified in terms of the MF, completely determines the quasi-particle trajectory in the absence of inter-particle collisions.

The initial test particle distribution $f(\mathbf{p}, \mathbf{r})$ is Monte-Carlo generated according to the density profiles for the initial reaction system. The particle collisions are Monte Carlo sampled according to the collision integral on the r.h.s. of the Boltzmann equations. The total particle density ρ, the total particle momentum $\mathbf{P}$ and the energy density are calculated by averaging over the corresponding quantities for the collection of test particles.

The realization of the test particle method is usually done on a spatial mesh so as to reduce the computational cost. The spatial size of the mesh then also determines the accuracy of the simulation. A coarser mesh size leads to faster calculations but may miss details of the highly nonequilibrium dynamics of the heavy-ion reaction. A too fine mesh, on the other hand, may lead to excessive fluctuations in the distribution function and other variables. The mesh size also determines the time step Δt in a simulation. Typically one requires that a test particle moves in each time step a distance short compared to the size of the mesh: $\overline{v}\Delta t < \Delta l$.

A compromise must be reached between the need for more detailed reaction description and the speed of a simulation. The accuracy of the test particle method depends on the number of test particles used, and it will improve as $\sqrt{N}$. But a large number of test particles can also slow down the simulations and is also limited by computer memory.

3.6.3 The Lattice Hamiltonian Method

The lattice Hamiltonian method is employed within transport theory to reach better numerical accuracy. This method was first proposed by Lenk and Pandharipande for momentum-independent fields [92], and it was later extended in

[93] and [128]. Here, I will summarize the method briefly.

Within the computational region, I introduce a mesh with nodes at $\mathbf{r}_\alpha$ separated by Δl_i, $i = 1, 2, 3$, in three cartesian directions. Associated with each of the nodes is a form factor $0 \leq S_\alpha \leq 1$, which is continuous and piecewise differentiable within the computational region and concentrated around the node $\mathbf{r}_\alpha$. I require the form factors to satisfy two conditions: first, every test-particle within the region is fully accounted for; second, every node gets its share of the volume. Mathematically, the first requirement is equivalent to:

$$\sum_\alpha S_\alpha(\mathbf{r} - \mathbf{r}_\alpha) = 1\,, \tag{3.79}$$

for all $\mathbf{r}$ within the region. And the second is just

$$\int d\mathbf{r}\, S_\alpha(\mathbf{r}) = \Delta V\,, \tag{3.80}$$

where $\Delta V = \Delta l_1\, \Delta l_2\, \Delta l_3$. The average Wigner function for a node, in terms of S_α, is

$$\overline{f}(\mathbf{p}, \mathbf{r}_\alpha) = \frac{1}{\mathcal{N}\Delta V} \sum_k \delta(\mathbf{p} - \mathbf{p}_k)\, S_\alpha(\mathbf{r}_k - \mathbf{r}_\alpha)\,. \tag{3.81}$$

This form is also used for the particle density $\overline{\rho}(\mathbf{r}_\alpha)$, the charge density $\overline{\rho}_{ch}(\mathbf{r}_\alpha)$ and the isospin density $\overline{\rho}_I(\mathbf{r}_\alpha)$. The single particle potential $\overline{U}(\mathbf{r}_\alpha)$, Coulomb potential $\overline{\Phi}(\mathbf{r}_\alpha)$ and isospin potential $\overline{U}_{Iso}(\mathbf{r}_\alpha)$ are calculated in terms of those averaged densities. The Coulomb potential $\overline{\Phi}$ satisfies a discretized Poisson equation [129] with $\overline{\rho}_{ch}$.

The approximate energy for the system (lattice Hamiltonian) in terms of the

spatially averaged Wigner functions is then:

$$\begin{aligned}\overline{E} &= \Delta V \sum_{\alpha} \Bigg(\tilde{\epsilon}_0\{\overline{f}(\mathbf{r}_\alpha)\} + \tilde{\epsilon}_I\{\overline{f}(\mathbf{r}_\alpha)\} + \frac{1}{2}\,\overline{\rho}_{ch}(\mathbf{r}_\alpha)\,\overline{\Phi}(\mathbf{r}_\alpha) \\ &\quad + \frac{a_s}{4\rho_0} \sum_i \frac{1}{(\Delta l_i)^2} \left[(\overline{\rho}(\mathbf{r}_\alpha + \Delta l_i\,\hat{\mathbf{u}}_i) - \overline{\rho}(\mathbf{r}_\alpha))^2 \right. \\ &\quad \left. + (\overline{\rho}(\mathbf{r}_\alpha) - \overline{\rho}(\mathbf{r}_\alpha - \Delta l_i\,\hat{\mathbf{u}}_i))^2 \right] \Bigg) . \end{aligned} \tag{3.82}$$

The single-particle energy for a test-particle is the variation of total energy with respect to the particle number, and turns out to be a weighted average of single-particle energies associated with the neighboring nodes:

$$\epsilon(\mathbf{p}, \mathbf{r}) = \sum_{\alpha} S_\alpha(\mathbf{r} - \mathbf{r}_\alpha)\,\overline{\epsilon}(\mathbf{p}, \mathbf{r}_\alpha) , \tag{3.83}$$

with

$$\overline{\epsilon}_X(\mathbf{p}, \mathbf{r}_\alpha) = \tilde{\epsilon}_X(\mathbf{p}, \{\overline{f}(\mathbf{r}_\alpha)\}) + A_X\,\overline{U}_{surf}(\mathbf{r}_\alpha) + \overline{U}^X_{Iso}(\mathbf{r}_\alpha) + Z_X\,\overline{\Phi}(\mathbf{r}_\alpha) , \tag{3.84}$$

where,

$$\overline{U}_{surf}(\mathbf{r}_\alpha) = \frac{a_s}{\rho_0} \sum_i \frac{1}{(\Delta l_i)^2} \left(2\overline{\rho}(\mathbf{r}_\alpha) - \overline{\rho}(\mathbf{r}_\alpha + \Delta l_i\,\hat{\mathbf{u}}_i) - \overline{\rho}(\mathbf{r}_\alpha - \Delta l_i\,\hat{\mathbf{u}}_i) \right) .$$

The derivatives of the the single-particle energy (3.83) yield an expression for the velocity, as an analogous average to that for the energy,

$$\mathbf{v}(\mathbf{p}, \mathbf{r}) = \sum_{\alpha} S_\alpha(\mathbf{r} - \mathbf{r}_\alpha)\,\overline{\mathbf{v}}(\mathbf{p}, \mathbf{r}_\alpha) , \tag{3.85}$$

and an expression for the force, amounting to a prescription for the gradient,

$$-\frac{\partial \epsilon(\mathbf{p},\mathbf{r})}{\partial \mathbf{r}} = -\sum_{\alpha} \frac{d\,S_\alpha(\mathbf{r}-\mathbf{r}_\alpha)}{d\mathbf{r}}\,\bar{\epsilon}(\mathbf{p},\mathbf{r}_\alpha)\,. \tag{3.86}$$

The integration precision for the lattice method will depend on the evaluation of these single-particle energy derivatives.

In the simulations, I take $S(\mathbf{r}) = \prod_i g_i(r_i/\Delta l_i)$. In the interior of the computational area, I use $g(x) = 0.5$ for $|x| < 0.5$, $g(x) = 0.75 - 0.5|x|$ for $0.5 < |x| < 1.5$, and $g(x) = 0$ for $1.5 < |x|$. At the front edge, I use $g(x) = 0.75 + 0.5x$ for $-1.5 < x < 0.5$, and $g(x) = 0$ outside of that interval.

Within the above equations, I find the physical quantities stem from averaging over a range of neighboring cells. The velocity and the force for the quasiparticles in Eq.(3.85) and (3.86) impact the long-time evolution of a reaction system. The consistency between the averaging and evaluation of derivatives here ensures good accuracy for the conservation of energy and momentum, generally improves the convergence of the numerical solution. The accuracy of energy conservation has been tested for momentum-dependent MFs by Danielewicz in the BUU simulations [12], and the method was found to work well.

3.6.4 In-Medium Cross Sections

The nucleon-nucleon cross sections inside a nuclear medium have been investigated by many authors and were found to be significantly different from the free space NN cross sections. Microscopic Bethe-Goldstone equation calculations [130, 131, 132, 133] and Dirac-Brueckner method [134, 135, 136] were used, in particular, in studying the in-medium effects, and the in-medium cross sections were found to be both density and temperature dependent. There is a possibility of a cross section enhancement near a superconducting phase transition [131], which is

often ignored in transport simulations because of the narrow parameter-range where the enhancement might occur.

At low energies, NN collisions are suppressed by the Pauli principle. This significantly increases the mean free path of the nucleons inside nuclear matter, and the effect is quite important for low energy transport simulations. In transport simulation, the Pauli blocking effect is included in the collision integral through occupation f and vacancy $1 - f$ on the r.h.s. of the Boltzmann equations, Eq.(3.14) and (3.15). The net effect is to reduce the collisions that result in particles inside the Fermi sphere, and it is less significant for high momentum particles.

Reductions of cross section inside the medium might take place due to geometrical shadowing of the collisions. Such a shadowing would result in a geometrical cut-off for the total cross section, with the maximum of the cross section taking the phenomenological form $\sigma_0 = y\rho^{-2/3}$, where $y \sim 1$. The limit on the in-medium cross section can be, in practice, implemented with [12, 7]:

$$\sigma = \sigma_0 \tanh(\sigma_{free}/\sigma_0)\,. \tag{3.87}$$

where the constant factor y is usually taken between $0.8 \sim 1.0$.

The Rostock group found the in-medium cross sections to be both density and energy dependent [137, 138]. Their results can be coarsely parameterized with:

$$\sigma = \sigma_{free} \exp\left(-0.6\,\frac{\rho}{\rho_0}\,\frac{1}{1 + (T_{cm}/150\,\mathrm{MeV})^2}\right) \tag{3.88}$$

where T_{cm} is the c.m. kinetic energy of a scattering nucleon pair.

Another employed phenomenological form the in-medium cross sections is one characterized by a linear reduction [139].

$$\sigma = (1 - \alpha\frac{\rho}{\rho_0})\sigma_{free}. \tag{3.89}$$

The linear reduction at low ρ is, *e.g.*, borne out by Eq. (3.88). But as density becomes large, the simple linear dependence might differ significantly from Eq. (3.88).

Transport simulations with free-space cross sections were found to be inadequate to explain many experimental observables. The directed flow studies and the related balance energy studies, as well as the stopping power studies have demonstrated that reduced in-medium cross sections better describe experimental results. Specifically, the Rostock and the geometry cut-off type in-medium cross sections were found to produce similar stopping power, and correspondingly to give rise to similar viscosities [7]. The linear reduction type was also extensively studied by many authors, with the linear reduction coefficients in Eq. (3.89) needing to be around $\alpha \sim 0.2$ in order to explain the stopping power and the balance energy [140, 141].

The in-medium cross sections are also likely isospin dependent, which have been reviewed by Li *et al.* [9], but few efforts have addressed this issue in terms of transport theory. Some theoretical results, in fact, point to a quite different isospin dependence of the in-medium NN cross sections from that in free space [131, 132]. I also have investigated isospin dependence of the in-medium cross sections. If one assumes the Rostock or the geometry cut-off model, then, additional reduction of the n-p cross section by 20% compared to pp only increases the balance energy by less than 10MeV. Such a change is not very significant, because the balance energy and flow are sensitive to the overall cross sections irrespective of isospin dependence. One can expect a stronger sensitivity to the isospin dependent cross section in the isospin related signals, such as signals from isospin diffusion process. The isospin diffusion coefficient, which characterizes isospin diffusion process, is directly proportional to the in-medium n-p cross section independent of the n-n or p-p cross sections in the lowest order approximation. (See chapter 4 on the isospin diffusion

coefficients and the discussion of isospin diffusion process in Chapter 5).

Chapter 4: Nuclear Isospin Diffusivity

4.1 Introduction

This chapter deals with the irreversible transport of isospin and other quantities in a nuclear system, as pertinent for reactions, for small deviations from equilibrium. In that limit, the irreversible transport acquires universal features and is characterized in terms of transport coefficients, that include the isospin-diffusion coefficients. The coefficients are derived here for the dynamics described in terms of a Boltzmann equation set such as that used in reaction simulations [10, 86]. The main diffusion coefficient or diffusivity, characterizing isospin diffusion driven by the gradient of asymmetry, is evaluated using free neutron-proton cross sections. In the past, other transport coefficients, viscosity and heat conductivity, have been investigated for nuclear matter [142, 143, 144, 145, 146]. It was subsequently found that conclusions from comparisons of reaction simulations to data on stopping can be universally formulated in terms of the nuclear viscosity [7]. It is hoped that the diffusivity can be of such utility as other coefficients, for the systems with a varying isospin content.

The past studies of irreversible linear transport for nuclear matter were primarily directed at momentum and energy. Tomonaga [142] and Galitskii *et al.* [143] obtained the low- and high-temperature limits for the shear viscosity and heat conductivity. Danielewicz [144] derived results for those coefficients valid in a wide range of nuclear densities and temperatures. Hakim and Mornas [146] studied different transport coefficients within the Walecka model following the relaxation-time approximation.

My derivation of diffusion coefficients follows the general strategy of Chapman and Enskog [76], but here for a Fermi system, with inclusion of mean-field effects appropriate for a nuclear system. In the next section, I will discuss the diffusion coefficient concept qualitatively and make simple estimates for nuclear matter. The modification of the Boltzmann equation to extend it to fermions has been first discussed by Uhlenbeck and Uehling [73, 74]. In Sec. 4.3, I will formally solve the set of Boltzmann equations for a binary system of fermions to find thermodynamic fluxes driven by specific thermodynamic forces and to find general but formal expressions for the diffusion and other transport coefficients. The transport coefficients have been (as I found) first considered for fermions by Hellund and Uhlenbeck [147]; compared to their paper, my notation here adheres more to what is now customary for nuclear reactions. Closely related to the diffusivity is the electrical conductivity that is included in my considerations. In Sec. 4.4, I obtain more specific results for the coefficients on assuming deviations from equilibrium suggested by the Boltzmann equation set, for specific thermodynamic forces present. Numerical results for the coefficients are obtained in Sec. 4.5 using free NN cross sections, where I also estimate the pace of isospin equilibration in reactions. I summarize the results in Sec. 4.6. More technical mathematical details and some reference information are provided in five appendices. In sequence, these appendices are devoted to the definitions of macroscopic quantities, the continuity equations, the continuity equations for an ideal fluid, the transformations in the driving force for diffusion and to the algebra of collision brackets.

4.2 Diffusion in a Binary System

Diffusion and other irreversible transport processes occur when a system is brought out of equilibrium. The direction of those processes is to bring the system

back to the equilibrium. For small perturbations, in terms of constraints that may be set externally, the system response is linear in the perturbation. The coefficient of proportionality between the induced flux and the perturbation is the transport coefficient.

In a multicomponent system with no net mass flow, irreversible particle flows result if particle concentrations are nonuniform. For N components, there are $N-1$ independent flows and $N-1$ independent concentrations (since the concentrations need to sum up to 1). The flows are then related to the gradients of the concentrations with an $(N-1)\times(N-1)$ matrix of diffusion coefficients. In a binary system, only a single coefficient of diffusion, or diffusivity, relates the irreversible particle flow to the nonuniformity in concentration. However, as we shall see, nonuniformities in quantities other than concentration, can induce a dissipative particle flow as well. My focus, obviously, is the binary system of neutrons and protons. However, for the sake of utility of the results elsewhere and for the ability to examine various limits, I shall consider a general two-component system of fermions. An extension of these results to bosons, outside of condensation, will be trivial. The two components will be denoted 1 and 2. Then, for the particle i, the density is $n_i = N_i/\mathcal{V}$, where N_i is the particle number in some infinitesimal volume $\mathcal{V}$. With net density $n = n_1 + n_2$, the particle concentration for 1 is $\nu = n_1/n$ and for 2 it is $1-\nu = n_2/n$. Moreover, with m_i representing the mass of particle i, the net mass density is $\rho = \rho_1 + \rho_2 = m_1\, n_1 + m_2\, n_2$, and the mass concentration for i is $c_i = m_i\, n_i/\rho$. The differential particle concentration is $\delta = (n_1 - n_2)/n$. The different concentrations are obviously related and thus we have $\nu = (1+\delta)/2$ and $c_1 = m_1\,(1+\delta)/(m_1\,(1+\delta) + m_2\,(1-\delta))$. Later in this Chapter, I shall primarily use the differential concentration δ as an independent variable.

The dissipative particle flows $\mathbf{\Gamma}_i$ are defined relative to the local mass velocity $\underline{\mathbf{v}}$,

$$\mathbf{\Gamma}_i = n_i \, (\underline{\mathbf{v}}_i - \underline{\mathbf{v}}) \, , \tag{4.1}$$

where $\underline{\mathbf{v}}_i$ is the local velocity of i'th component and

$$\underline{\mathbf{v}} = (\rho_1 \, \underline{\mathbf{v}}_1 + \rho_2 \, \underline{\mathbf{v}}_2)/\rho \, . \tag{4.2}$$

We might consider other flows such as those defined relative to the local *particle* velocity, but those flows are combinations of $\mathbf{\Gamma}_1$ and $\mathbf{\Gamma}_2$. Moreover, even $\mathbf{\Gamma}_1$ and $\mathbf{\Gamma}_2$ are redundant and we might just use $\mathbf{\Gamma}_1$ as an independent flow with the flow of 2, as easily seen, given by $\mathbf{\Gamma}_2 = -m_1 \, \mathbf{\Gamma}_1/m_2$. Another option might be to use as independent the differential flow defined as

$$\mathbf{\Gamma}_\delta = \mathbf{\Gamma}_1 - \mathbf{\Gamma}_2 \, . \tag{4.3}$$

If the system is at uniform pressure and temperature, but there is a small concentration gradient present, the fluxes develop linear in the gradient, enabling us to write, e.g.

$$\mathbf{\Gamma}_1 = -n \, D_1 \, \frac{\partial \nu}{\partial \mathbf{r}} \qquad \text{and} \qquad \mathbf{\Gamma}_2 = -n \, D_2 \, \frac{\partial (1-\nu)}{\partial \mathbf{r}} \, . \tag{4.4}$$

These are so-called Fick's laws. Notably, the stability of an equilibrium state requires $D_i > 0$. Since $m_1 \, \mathbf{\Gamma}_1 + m_2 \, \mathbf{\Gamma}_2 = 0$, One has $m_1 \, D_1 = m_2 \, D_2$. For the differential flow, one has

$$\mathbf{\Gamma}_\delta = -n \, D_1 \frac{\partial \nu}{\partial \mathbf{r}} + n \, D_2 \, \frac{\partial (1-\nu)}{\partial \mathbf{r}} = -n \, D_\delta \, \frac{\partial \delta}{\partial \mathbf{r}} \, . \tag{4.5}$$

Here, the differential coefficient is $D_\delta = (D_1 + D_2)/2$.

So far, I assumed a system at a uniform pressure and temperature, with only the concentration changing with position. If the variations in a system are more complex, other nonequilibrium forces than the concentration gradient can drive the diffusion. This will be explored later in this chapter. General guidance regarding the forces which can contribute is provided by the Curie principle. This principle exploits symmetry and states that the driving forces must have the same tensor rank and parity as the flux they generate.

For the system of neutrons and protons, the differential concentration δ becomes a concentration of the isospin and the differential flow becomes the isospin flow, $\Gamma_\delta \equiv \Gamma_I$. Moreover, the differential diffusion coefficient becomes an isospin diffusion coefficient, $D_\delta \equiv D_I$, and for equal masses one expects $D_I = D_p = D_n$.

It is popular to relate the concept of a diffusion coefficient to a diffusion equation. Indeed, if one considers a uniform system of protons and neutrons at rest, but with the nucleon concentration changing in space, then, from the continuity equation for the differential density

$$\frac{\partial (n\,\delta)}{\partial t} = -\nabla \cdot \mathbf{\Gamma}_I\,, \tag{4.6}$$

I get the familiar equation

$$\frac{\partial \delta}{\partial t} = D_I\,\nabla^2 \delta\,. \tag{4.7}$$

Here, for D_I, I have assumed a weak dependence on the concentration δ.

Before turning to a derivation of rigorous results for the diffusion and other transport coefficients, it may be instructive to produce simple mean-free-path estimates for those coefficients. Let us consider components of equal mass (the mass then becomes a simple normalization coefficient in density that may be factored out) and consider the gradient of concentration along the x axis, in the medium at rest. If one takes the three coordinate axes, then 1/6 of all particles will be

primarily moving along one of those axes in the positive or negative direction, with an average thermal velocity $\underline{V} = \sqrt{3T/m}$, for the distance of the order of one mean free path λ, without a collision. Considering the particles 1 moving through the plane at $x = 0$, they will be reflecting density at a distance λ away. Including the particles moving up and down through the plane, I find for the flux

$$\Gamma_1 \approx \frac{1}{6}\left(n_1(x-\lambda) - n_1(x+\lambda)\right)\underline{V} \approx -\frac{1}{3}\lambda\underline{V}\frac{\partial n_1}{\partial x}\,.$$

With (4.4), I then get for the diffusion coefficient

$$D \sim \frac{1}{3}\lambda\underline{V} \sim \frac{1}{n\,\sigma}\sqrt{\frac{T}{3m}}\,. \tag{4.8}$$

with $\lambda \sim 1/(n\,\sigma)$. A more thorough investigation shows that it is the cross section σ_{12} for interaction *between* the two species that enters the diffusion coefficient.

Let us now evaluate the magnitude of the isospin diffusion coefficient. At temperature $T \sim 60$ MeV and normal density $n_0 = 0.16$ fm^{-3}, with $\sigma_{np} \sim 40$ mb, one finds $D_I \sim 0.2$ fm c. As will be seen, this is in a rough agreement with thorough calculations.

Similarly to the above, one could employ the mean-free path arguments to determine the better investigated coefficients: shear-viscosity η and heat conduction κ. One finds $\eta \sim \frac{1}{3}n\,m\,\underline{V}\,\lambda$ and $\kappa \sim \frac{1}{3}n\,\underline{V}\,\lambda\,c_V$, where c_V is the specific heat per particle. For $T \sim 60$ MeV and $\sigma \sim 40$ mb, I find $\eta \sim 30$ MeV/(fm^2 c) and $\kappa \sim 0.06$ c/fm^2. Up to factors, the shear viscosity and heat conduction coefficients play the role of diffusion coefficients in the diffusion equation for velocity vorticity and in the heat conduction Fourier equation identical in form to the diffusion equation.

In the estimates above, I just considered the free motion of particles in-between collisions. If self-consistent mean fields produced by the particles depend on

concentration, then this dependence, on its own, contributes to the diffusion. In the case of nuclear matter, the interaction energy per nucleon may be well approximated in a form that is quadratic in isospin asymmetry, $e^{int}_{sym}\,\delta^2$, where $\delta = (n_p - n_n)/n$ and e^{int}_{sym} is the interaction contribution to the symmetry energy e_{sym}. At normal density, the interaction symmetry energy is $e^{int}_{sym} \approx 14$ MeV. The naive expectation for two-body interactions is that e^{int}_{sym} is linear in density. At constant net density, the quadratic dependence of the interaction energy on δ leads to the force $\mathbf{F}_{p,n} = \mp(4\,e^{int}_{sym}/n)\,(\partial n_p/\partial \mathbf{r})$, of opposite sign on protons and neutrons. The direction of the force for positive e^{int}_{sym} is to reduce nonuniformity in isospin. Under the influence of this force, a proton accelerates for a typical time between collisions $\Delta t = \lambda/\underline{V}$ and then, in a collision, resets its velocity. The described polarization effect augments then the proton flow by

$$\Delta\mathbf{\Gamma}_p = n_p\,\Delta\underline{\mathbf{v}}_p = -4\,e^{int}_{sym}\,\frac{n_p}{n}\,\frac{\lambda}{2\,m\,\underline{V}}\,\frac{\partial n_p}{\partial \mathbf{r}}\,. \tag{4.9}$$

In comparing with (4.8), after correcting for the local center of mass motion, I find that the polarization increases the diffusion coefficient by

$$D'_I \sim (1-\delta^2)e^{int}_{sym}\,\frac{1}{T}\,D^0_I\,, \tag{4.10}$$

where D^0_I represents the previous estimate in Eq. (4.8). It is apparent that the contribution of the polarization effect is negligible for temperatures $T \gg e^{int}_{sym}$. However, at temperatures comparable to e^{int}_{sym}, the contribution could be significant; notably, at those temperatures Fermi effects also need to play a role.

The isospin diffusion induced by mechanical forces has analogy in an electric current induced by the electric fields. Indeed, for large enough systems, the Coulomb interactions can contribute currents altering the concentration and, for completeness, I evaluate the conductivity σ_E for nuclear matter, relating the isospin

flux to the electric field,

$$\mathbf{\Gamma}_I = \sigma_E \mathcal{E} \,, \tag{4.11}$$

where $\mathcal{E}$ is the local electric field.

4.3 Fluxes from the Boltzmann Equation Set

4.3.1 Coupled Boltzmann Equations

The two components of the binary system will be described in terms of the quasiparticle distribution functions $f_i(\mathbf{p}, \mathbf{r}, t)$. The local macroscopic quantities $h(\mathbf{r}, t)$ are expressed as momentum integrals of f,

$$h(\mathbf{r}, t) = \frac{g}{(2\pi\hbar)^3} \int d\mathbf{p}\, \chi(\mathbf{p}) f(\mathbf{p}, \mathbf{r}, t) \,, \tag{4.12}$$

where g is the intrinsic degeneracy factor. Different standard expressions for macroscopic quantities in terms of f, such as pressure and heat flow, are listed in Appendix A.

The components are assumed to follow the nonrelativistic set of coupled fermion Boltzmann equations, without momentum-dependence in the MFs,

$$\frac{\partial f_i}{\partial t} + \frac{\mathbf{p}}{m_i} \cdot \frac{\partial f_i}{\partial \mathbf{r}} + \mathbf{F}_i \cdot \frac{\partial f_i}{\partial \mathbf{p}} = J_i \,. \tag{4.13}$$

The terms on the l.h.s. account for the changes in f_i due to the movement of quasiparticles and their acceleration under the influence of mean-field and external forces, included in $\mathbf{F}_i$, while the r.h.s. accounts for the changes in f_i due to collisions. In the following, I shall often denote the l.h.s. of a Boltzmann equation as $\mathcal{D}_i$. With $d\sigma/d\Omega$ and v^* representing the differential cross section and relative

velocity, respectively, the collision integral for particle 1 is

$$\begin{aligned} J_1 &= J_{11} + J_{12} \\ &= \frac{g}{2(2\pi\hbar)^3} \int d^3p_{1a}\, d\Omega'\, v^* \left(\frac{d\sigma_{11}}{d\Omega}\right) \left(\tilde{f}_1\, \tilde{f}_{1a}\, f_1'\, f_{1a}' - f_1\, f_{1a}\, \tilde{f}_1'\, \tilde{f}_{1a}'\right) \\ &\quad + \frac{g}{(2\pi\hbar)^3} \int d^3p_2\, d\Omega'\, v^* \left(\frac{d\sigma_{12}}{d\Omega}\right) \left(\tilde{f}_1\, \tilde{f}_2\, f_1'\, f_2' - f_1\, f_2\, \tilde{f}_1'\, \tilde{f}_2'\right) . \end{aligned} \tag{4.14}$$

Here, $\tilde{f} = 1 - f$ is the Pauli principle factor. The factor of $1/2$ in front of the first r.h.s. J_{11} term, compared to the J_{12} term, compensates for the double-counting of final states when integration is done over the full spherical angle in scattering of identical particles. The subscript a and the primes in combination with the particle subscripts 1 and 2 are used to keep track of incoming and outgoing particles for a collision. Other than in the context of particle components, such as here, the 1 and 2 subscripts will not be utilized in this chapter. The collision integral J_2 for particles 2 follows from (4.14) upon interchange of the indices 1 and 2. As it stands, the set of the Boltzmann equations (4.13), with (4.14), preserves the number of each species.

In the macroscopic quantities (4.12), the distribution function f gets multiplied by the degeneracy factor g. When considering changes of macroscopic quantities (4.12) dictated by the Boltzmann equation (4.13), the changing distribution function f continues to be multiplied by g. In these equation, the factor of f for the other particle in the collision integral J is accompanied by its own factor of g. As a consequence, in the variety of physical quantities I derived, the factor of f is always accompanied by the factor of g, while, however, $\tilde{f}$ is not. To simplify the notation, in the derivations that follow, I will suppress the factors of g, only to restore those factors towards the end of the derivations.

When the Boltzmann equation set is used to study the temporal changes of densities of the quantities conserved in collisions, i.e. number of species, energy and momentum, local conservation laws follow. Those conservation laws are discussed in

Appendix B.

4.3.2 Strategy for Solving the Boltzmann Equation Set

Irreversible transport takes place when the system is brought out of equilibrium such as under the influence of external perturbation. Aiming at the transport coefficients, I shall assume that the deviations from the equilibrium are small, of the order of some parameter ϵ that sets the scale for temporal and spatial changes in the system. Then the distribution functions may be expanded in the power series in ϵ [76, 75]

$$f = f^{(0)} + f^{(1)} + f^{(2)} + \dots . \tag{4.15}$$

where $f^{(k)}$ represent the consecutive terms of expansion and $f^{(0)}$ is the strict local equilibrium solution. The terms of expansion in f may be nominally found by expanding the collision integrals in ϵ, following (4.15), expanding, simultaneously, the derivative terms in the equations and by demanding a consistency,

$$\mathcal{D}_i^{(1)} + \mathcal{D}_i^{(2)} + \ldots = J_i^{(0)} + J_i^{(1)} + J_i^{(2)} + \dots . \tag{4.16}$$

Here, one recognizes that the derivatives, themselves, bring in a power of ϵ into the equations and, thus, the derivative series starts with a first order term in ϵ.

While I nominally included the zeroth-order term in the expansion of the collision integral J_i, the integral vanishes for the equilibrium functions

$$f_j^{(0)} = 1 \Big/ \left\{ \exp\left[\left(\frac{(\mathbf{p} - m_j \mathbf{v})^2}{2m_j} - \mu_j \right) / T \right] + 1 \right\} , \tag{4.17}$$

where μ_j, $\mathbf{v}$ and T are the local kinetic chemical potential, velocity and temperature which are functions of $\mathbf{r}$ and t, consistent with the Euler equations (B.7). Notably, the vanishing of the collision integrals is frequently exploited in deriving the form of

the equilibrium functions, leading to the requirement that $f_j/\tilde{f}_j$ is given by the exponential of a linear combination of the conserved quantities. In the context of specific transport coefficients, the boundary conditions for the Euler equations (B.7) may be chosen to generate just those irreversible fluxes, and forces driving those fluxes, that are of interest.

The equation set (4.16) can be solved by iteration, order by order in ϵ, requiring

$$\mathcal{D}_i^{(k)} = J_i^{(k)} \,. \tag{4.18}$$

Thus, $f_j^{(0)}$ may be introduced into $\mathcal{D}_i$, producing $\mathcal{D}_i^{(1)}$ and allowing to find $f_j^{(1)}$. Next, inserting $f_j^{(1)}$ into $\mathcal{D}_i$ yields $\mathcal{D}_i^{(2)}$ that allows to find $f_j^{(2)}$ and so on.

For finding the coefficients of linear transport, only one iteration above is necessary, since $f_i^{(1)}$, as linear in gradients, yield dissipative fluxes that are linear in those gradients. The local equilibrium functions on its own produce no dissipative fluxes, as the species local velocities $\mathbf{V}_j$ and heat flux $\mathbf{Q}$ vanish, while the kinetic pressure tensor $\overline{\overline{P}}$ is diagonal,

$$n_i \mathbf{V}_i^{(0)} = \int \frac{d^3p}{(2\pi\hbar)^3} \frac{\mathbf{p}}{m_i} f_i^{(0)}(\mathbf{p},\mathbf{r},t) = 0 \,, \tag{4.19a}$$

$$\mathbf{Q}^{(0)} = \sum_j \int \frac{d^3p}{(2\pi\hbar)^3} \frac{p^2}{2m_j} \frac{\mathbf{p}}{m_j} f_j^{(0)}(\mathbf{p},\mathbf{r},t) = 0 \,, \tag{4.19b}$$

$$\overline{\overline{P}}^{(0)} = \sum_j \int \frac{d^3p}{(2\pi\hbar)^3} \frac{\overline{\overline{\mathbf{p}\,\mathbf{p}}}}{m_j} f_j^{(0)}(\mathbf{p},\mathbf{r},t) = \frac{2}{3} n \underline{E} \overline{\overline{1}} \,, \tag{4.19c}$$

in the frame where the local velocity vanishes $\mathbf{v}(\mathbf{r},t) = 0$, with $\underline{E}$ representing the local kinetic energy per particle. The above fluxes reduce the local continuity equations to the ideal-fluid Euler equations.

4.3.3 Boltzmann Set in the Linear Approximation

I now consider the terms linear in derivatives around a given point, i.e. the case of $k = 1$ in (4.18), for the Boltzmann equation set. On representing the distribution functions as $f_j = f_j^{(0)} + f_j^{(1)}$, I expand the collision integrals J_i, to get terms $J_i^{(1)}$ linear in $f_j^{(1)}$. Upon representing $f_j^{(1)}$ as $f_j^{(1)} = f_j^{(0)}\,\tilde{f}_j^{(0)}\,\phi_j$, I get for the $k = 1$ $i = 1$ version of (4.18):

$$\frac{\partial f_1^{(0)}}{\partial t} + \frac{\mathbf{p}}{m_1}\cdot\frac{\partial f_1^{(0)}}{\partial \mathbf{r}} + \mathbf{F}_1\cdot\frac{\partial f_1^{(0)}}{\partial \mathbf{p}} = -I_{11}(\phi) - I_{12}(\phi)\,, \tag{4.20}$$

where

$$I_{ij}(\phi) = \frac{1}{1+\delta_{ij}}\int \frac{d^3p_{ja}}{(2\pi)^3}\,d\Omega'\,v^*\left(\frac{d\sigma_{ij}}{d\Omega}\right) f_i^{(0)}\,f_{ja}^{(0)}\,\tilde{f}_i^{(0)\prime}\,\tilde{f}_{ja}^{(0)\prime}\,\left(\phi_i + \phi_{ja} - \phi_i' - \phi_{ja}'\right)\,, \tag{4.21}$$

and where I have utilized the property of the equilibrium functions

$$f_i^{(0)}\,f_{ja}^{(0)}\,\tilde{f}_i^{(0)\prime}\,\tilde{f}_{ja}^{(0)\prime} = \tilde{f}_i^{(0)}\,\tilde{f}_{ja}^{(0)}\,f_i^{(0)\prime}\,f_{ja}^{(0)\prime}\,. \tag{4.22}$$

The result for $i = 2$, analogous to (4.20), is obtained through an interchange of the indices 1 and 2.

The l.h.s. of Eq. (4.20) contains the derivatives of equilibrium distribution functions with respect to t, $\mathbf{r}$ and $\mathbf{p}$. These derivatives can be expressed in terms of the parameters describing the functions (4.17), i.e. μ_i, T and $\mathbf{v}$. Through the use of the Euler equations (Appendix B) and equilibrium identities (Appendix C), moreover, the temporal derivatives may be eliminated to yield for the rescaled l.h.s. of (4.20)

$$\frac{T}{f_1^{(0)}\,\tilde{f}_1^{(0)}}\,\mathcal{D}^{(1)} = \left(\frac{p^2}{2m_1} - \frac{5}{3}\underline{E}\right)\frac{\mathbf{p}}{m_1 T}\cdot\frac{\partial T}{\partial \mathbf{r}} + \frac{\overset{\circ}{\overline{\mathbf{p}\,\mathbf{p}}}}{m_1} : \overline{\overline{\frac{\partial}{\partial \mathbf{r}}\mathbf{v}}} + \frac{\mathbf{p}}{\rho_1}\cdot\mathbf{d}_{12}\,. \tag{4.23}$$

Here, a symmetrized traceless tensor is defined as $\overline{\overline{\mathbf{x}\,\mathbf{y}}} = \frac{1}{2}\left(\overline{\overline{\mathbf{x}\,\mathbf{y}}} + \overline{\overline{\mathbf{y}\,\mathbf{x}}}\right) - \frac{1}{3}(\mathbf{x}\cdot\mathbf{y})\,\overline{\overline{1}}$, and

$$\begin{aligned}\mathbf{d}_{12} &= \frac{\rho_1\rho_2}{\rho}\left[\left(-\frac{\mathbf{F}_1}{m_1}+\frac{\mathbf{F}_2}{m_2}\right)+T\frac{\partial}{\partial\mathbf{r}}\left(\frac{\mu_1}{m_1 T}-\frac{\mu_2}{m_2 T}\right)+\frac{5}{3T}\left(\frac{\underline{E}_1}{m_1}-\frac{\underline{E}_2}{m_2}\right)\frac{\partial T}{\partial\mathbf{r}}\right], \\ &= \frac{\rho_1\rho_2}{\rho}\left[\left(-\frac{\mathbf{F}_1}{m_1}+\frac{\mathbf{F}_2}{m_2}\right)+\frac{\partial}{\partial\mathbf{r}}\left(\frac{\mu_1}{m_1}-\frac{\mu_2}{m_2}\right)+\left(\frac{s_1}{m_1}-\frac{s_2}{m_2}\right)\frac{\partial T}{\partial\mathbf{r}}\right], \qquad (4.24)\end{aligned}$$

where s_i is the entropy per particle for species i, $s_i = (5\underline{E}_i/3 - \mu_i)/T$. The result for species 2 in the Boltzmann equation is obtained by interchanging the indices 1 and 2 in Eqs. (4.23) and (4.24). Note that $\mathbf{d}_{21} = -\mathbf{d}_{12}$.

The representation (4.23) for the l.h.s. of the linearized Boltzmann equation (4.20) exhibits the thermodynamic forces driving the dissipative transport in a medium. Thus, one has the tensor of velocity gradients $\overline{\overline{\frac{\partial}{\partial\mathbf{r}}\mathbf{v}}}$ contracted in (4.23) with the tensor from particle momentum. The distortion of the momentum distribution associated with the velocity gradients gives rise to the tensorial dissipative momentum flux in a medium. As to the vectorial driving forces, they all couple to the momentum in (4.23) and they all can contribute to the vector fluxes in the medium, i.e. the particle and heat fluxes, as permitted by the Curie law. The criterion that I, however, employed in separating the driving vectors forces in (4.23) was that of symmetry under the particle interchange. When considering the diffusion in a binary system, with the two components flowing in opposite directions in a local frame, one expects the driving force to be of opposite sign for the two species. On the other hand, in the case of heat conduction, one expects the driving force to distort the distributions of the two species in the same direction.

Regarding the antisymmetric driving force in (4.24), one may note that for conservative forces we have

$$\mathbf{F}_i = -\frac{\partial}{\partial\mathbf{r}}U_i\,. \qquad (4.25)$$

One can combine then the first with the second term on the r.h.s. of (4.24) by

introducing the net chemical potentials $\mu_i^t = \mu_i + U_i$ and obtaining

$$\mathbf{d}_{12} = \frac{\rho_1 \rho_2}{\rho} \left[\frac{\partial}{\partial \mathbf{r}} \left(\frac{\mu_1^t}{m_1} - \frac{\mu_2^t}{m_2} \right) + \left(\frac{s_1}{m_1} - \frac{s_2}{m_2} \right) \frac{\partial T}{\partial \mathbf{r}} \right] . \tag{4.26}$$

For a constant temperature T, the driving force behind diffusion is the gradient of the difference between the chemical potentials per unit mass, $\mu_{12}^t = \mu_1^t/m_1 - \mu_2^t/m_2$, as expected from phenomenological considerations [148]. However, the temperature gradient can contribute to the diffusion as well, which is known as the thermal diffusion or Soret effect. Note that the vector driving forces in (4.23) vanish when the temperature and the difference of net chemical potentials per mass are uniform throughout a system.

Given the typical constraints on a system, it can be more convenient to obtain the driving forces in terms of the net pressure P^t, temperature T and concentration δ, rather than μ_{12}^t and T. Thus, on expressing the potential difference as $\mu_{12}^t = \mu_{12}^t(P^t, T, \delta)$, I get

$$d\mu_{12}^t = \left(\frac{\partial \mu_{12}^t}{\partial P^t} \right)_{T,\delta} dP^t + \left(\frac{\partial \mu_{12}^t}{\partial T} \right)_{P^t,\delta} dT + \left(\frac{\partial \mu_{12}^t}{\partial \delta} \right)_{P^t,T} d\delta , \tag{4.27}$$

and

$$\mathbf{d}_{12} = \frac{\rho_1 \rho_2}{\rho} \left(\Pi_{12}^P \nabla P^t + \Pi_{12}^T \nabla T + \Pi_{12}^\delta \nabla \delta \right) , \tag{4.28}$$

that I will utilize further on. The coefficient functions are

$$\Pi_{12}^P = \left(\frac{\partial \mu_{12}^t}{\partial P^t} \right)_{T,\delta} , \tag{4.29a}$$

$$\Pi_{12}^T = \left(\frac{\partial \mu_{12}^t}{\partial T} \right)_{P^t,\delta} + \left(\frac{s_1}{m_1} - \frac{s_2}{m_2} \right) , \tag{4.29b}$$

$$\Pi_{12}^\delta = \left(\frac{\partial \mu_{12}^t}{\partial \delta} \right)_{P^t,T} , \tag{4.29c}$$

and specific expressions for those functions in the nuclear-matter case are given in

Appendix D. Notably, however, the concentration δ may not be a convenient variable in the phase transition region where the transformation between the chemical potential difference and δ is generally not invertible.

With the l.h.s. of the linearized Boltzmann set (4.20) linear in the driving forces exhibited on the r.h.s. of (4.23), and with the collision integrals linear in the deviation form-factors ϕ, the form factors need to be linear in the driving forces,

$$\begin{aligned} \phi_1 &= -\mathbf{A}_1 \cdot \nabla T - \overline{\overline{B}}_1 : \overset{c}{\overline{\overline{\nabla \mathbf{v}}}} - \mathbf{C}_1 \cdot \mathbf{d}_{12}\,, \\ \phi_2 &= -\mathbf{A}_2 \cdot \nabla T - \overline{\overline{B}}_2 : \overset{c}{\overline{\overline{\nabla \mathbf{v}}}} - \mathbf{C}_2 \cdot \mathbf{d}_{12}\,, \end{aligned} \tag{4.30}$$

where $\mathbf{A}$, $\overline{\overline{B}}$ and $\mathbf{C}$ do not depend on the forces. On inserting (4.30) into (4.20), one gets the following equations, when keeping alternatively a selected exclusive driving force finite:

$$\frac{\mathbf{p}}{\rho_1 T} f_1^{(0)} \tilde{f}_1^{(0)} = I_{11}(\mathbf{C}) + I_{12}(\mathbf{C})\,, \tag{4.31a}$$

$$-\frac{\mathbf{p}}{\rho_2 T} f_2^{(0)} \tilde{f}_2^{(0)} = I_{22}(\mathbf{C}) + I_{21}(\mathbf{C})\,, \tag{4.31b}$$

when keeping $\mathbf{d}_{12}$,

$$\frac{\overline{\overline{\mathbf{p}\,\mathbf{p}}}}{m_1 T} f_1^{(0)} \tilde{f}_1^{(0)} = I_{11}(\overline{\overline{B}}) + I_{12}(\overline{\overline{B}})\,, \tag{4.32}$$

and another one, with indices 1 and 2 interchanged, when keeping $\overset{c}{\overline{\overline{\nabla \mathbf{v}}}}$, and, finally,

$$\left(\frac{p^2}{2m} - \frac{5}{3}\underline{E}_1\right) \frac{\mathbf{p}}{m_1 T^2} f_1^{(0)} \tilde{f}_1^{(0)} = I_{11}(\mathbf{A}) + I_{12}(\mathbf{A})\,, \tag{4.33}$$

and another one, with 1 and 2 interchanged, when keeping ∇T (while $\mathbf{d}_{12} = 0$).

The linearized collision integrals I_{ij} cannot change the tensorial character of objects upon which they operate. Moreover, the only vector that can be locally utilized in the object construction is the momentum $\mathbf{p}$. This implies, then, the

following representation within the set (4.30):

$$\mathbf{C}_i = c_i(p^2)\,\frac{\mathbf{p}}{\rho_i}\,, \tag{4.34a}$$

$$\mathbf{A}_i = a_i(p^2)\left(\frac{p^2}{2m_i} - \frac{5}{3}\underline{E}_i\right)\frac{\mathbf{p}}{m_i T^2}\,, \tag{4.34b}$$

$$\overline{\overline{B}} = b_i(p^2)\,\overline{\overline{\mathbf{p}\,\mathbf{p}}}^{\circ}\,. \tag{4.34c}$$

Here, the tensorial factors are enforced by construction. The factorization of the scalar factors is either suggested by the respective linearized Boltzmann equation or will be convenience later on. The unknown functions a, b and c can be principally found by inserting (4.34) into Eqs. (4.31)-(4.33). The resulting equations are, however, generally quite complicated and analytic solutions are only known in some special cases. In practical calculations, I shall content myself with a power expansion for the unknown functions. It has been shown that any termination of the expansion will produce lower bounds for the transport coefficients and that the lowest terms yield a predominant contribution to the coefficients [76].

4.3.4 Formal Results for Transport Coefficients

Before solving Eqs. (4.31)-(4.33), I shall obtain formal results for the transport coefficients, assuming that solutions to (4.31)-(4.33) exist. I shall start with the diffusion. The velocity for species 1 is

$$\begin{aligned}
\underline{\mathbf{V}}_1 &= \frac{1}{n_1}\int\frac{d^3p}{(2\pi\hbar)^3}\,\frac{\mathbf{p}}{m_1}\,\delta f_1 = \frac{1}{n_1}\int\frac{d^3p}{(2\pi\hbar)^3}\,\frac{\mathbf{p}}{m_1}\,\phi_1\,f_1^{(0)}\,\tilde{f}_1^{(0)} \\
&= T\int\frac{d^3p}{(2\pi\hbar)^3}\,\phi_1\,[I_{11}(\mathbf{C}) + I_{12}(\mathbf{C})] \\
&= -\nabla T\,\frac{T}{3}\int\frac{d^3p}{(2\pi\hbar)^3}\,\mathbf{A}_1\cdot[I_{11}(\mathbf{C}) + I_{12}(\mathbf{C})] \\
&\quad -\mathbf{d}_{12}\,\frac{T}{3}\int\frac{d^3p}{(2\pi\hbar)^3}\,\mathbf{C}_1\cdot[I_{11}(\mathbf{C}) + I_{12}(\mathbf{C})]\,,
\end{aligned} \tag{4.35}$$

where I have utilized (4.30) and (4.34). The contribution of a tensorial driving force to the vector flow drops out under the integration over momentum, as required by the Curie principle. With a result for $\underline{\mathbf{V}}_2$ analogous to (4.35), I get for the difference of average velocities (utilized for the sake of particular symmetry between the components)

$$\begin{aligned}
\underline{\mathbf{V}}_1 - \underline{\mathbf{V}}_2 &= -\nabla T \frac{T}{3} \left\{ \int \frac{d^3p}{(2\pi\hbar)^3} \mathbf{A}_1 \cdot [I_{11}(\mathbf{C}) + I_{12}(\mathbf{C})] \right. \\
&\quad \left. + \int \frac{d^3p}{(2\pi\hbar)^3} \mathbf{A}_2 \cdot [I_{22}(\mathbf{C}) + I_{21}(\mathbf{C})] \right\} \\
&\quad -\mathbf{d}_{12} \frac{T}{3} \left\{ \int \frac{d^3p}{(2\pi\hbar)^3} \mathbf{C}_1 \cdot [I_{11}(\mathbf{C}) + I_{12}(\mathbf{C})] \right. \\
&\quad \left. + \int \frac{d^3p}{(2\pi\hbar)^3} \mathbf{C}_2 \cdot [I_{22}(\mathbf{C}) + I_{21}(\mathbf{C})] \right\} \\
&= -\frac{T}{3} \left(\{\mathbf{A}, \mathbf{C}\} \nabla T + \{\mathbf{C}, \mathbf{C}\} \mathbf{d}_{12} \right) , \qquad (4.36)
\end{aligned}$$

where the brace product $\{\cdot, \cdot\}$ is an abbreviation for the integral combinations of vectors $\mathbf{A}$ and $\mathbf{C}$, multiplying the driving forces. The brace product has been first introduced for a classical gas [76]. The fermion generalization of the product and its properties are discussed in the Appendix E; see also [147].

The diffusion coefficient is best defined with regard to the most common conditions under which the diffusion might occur, i.e. at uniform pressure and temperature, but varying concentration. I have then, cf. (4.3),

$$\underline{\mathbf{V}}_1 - \underline{\mathbf{V}}_2 = \frac{\rho}{(m_1 + m_2)\, n_1\, n_2} \mathbf{\Gamma}_\delta = -\frac{\rho\, n\, m_{12}}{\rho_1\, \rho_2} D_\delta \nabla \delta , \qquad (4.37)$$

where m_{12} is the reduced mass, $1/m_{12} = 1/m_1 + 1/m_2$. Respectively, when P^t and

T vary, with $\mathbf{d}_{12}$ given by (4.28), I write the r.h.s. of (4.36) as

$$\underline{\mathbf{V}}_1 - \underline{\mathbf{V}}_2 = -\frac{\rho\, n\, m_{12}}{\rho_1\, \rho_2}\, D_\delta \left(\nabla\delta + \frac{\Pi^P}{\Pi^\delta}\, \nabla P^t + k_T\, \nabla T \right) , \tag{4.38}$$

where, simplifying the notation, I dropped the subscripts 12 on coefficients Π. The diffusion coefficient in the above is given by

$$D_\delta = \frac{T}{3m_{12}}\, \frac{\Pi^\delta}{n} \left(\frac{\rho_1\, \rho_2}{\rho} \right)^2 \{\mathbf{C}, \mathbf{C}\} , \tag{4.39}$$

and

$$k_T = \frac{\Pi^T}{\Pi^\delta} + \frac{1}{\Pi^\delta}\, \frac{\rho}{\rho_1\, \rho_2}\, \frac{\{\mathbf{A}, \mathbf{C}\}}{\{\mathbf{C}, \mathbf{C}\}} . \tag{4.40}$$

One can note that the expressions above contain Π^δ in the denominators. Normally, the positive nature of the derivative (4.29c) is ensured by the demand of the system stability. However, across the region of a phase transition the concentration generally changes while the chemical potentials generally do not, so that $\Pi^\delta = 0$. While the coefficient D_δ above is the one I am after as the standard one in describing diffusion, in the phase transition region it can be beneficial to resort to the description of diffusion as responding to the gradient of the potential difference in (4.28). Notably, as explained in the Appendix E, the brace product $\{C, C\}$ in (4.39) is positive definite. This ensures the positive nature of D_δ away from the phase transition and, in general, ensures that, at a constant temperature, the irreversible asymmetry flux flows in the direction from a higher potential difference μ_{12}^t to lower.

As to the Soret effect, i.e. diffusion driven by the temperature gradient, described in (4.38)-(4.40), it has its counterpart in the heat flow driven by a concentration gradient, termed Dufour effect. Transport coefficients for counterpart effects are related through Onsager relations [149] that are also borne out by my

results. Diffusion driven by pressure is rarely of interest, because of the usually short times for reaching mechanical equilibrium in nuclear systems, compared to the equilibrium with respect to temperature or concentration. However, an irreversible particle flux may be further driven by external forces, such as due to an electric field $\mathcal{E}$. With the flux induced by the field given by $\mathbf{\Gamma}_\delta = \sigma_E \mathcal{E}$, where σ_E is conductivity, with the first equality in (4.37), and with (4.36) and (4.24), I find for the conductivity

$$\sigma_E = \frac{T}{3m_{12}} \left(\frac{\rho_1 \rho_2}{\rho}\right)^2 \left(\frac{q_2}{m_2} - \frac{q_1}{m_1}\right) \{\mathbf{C}, \mathbf{C}\} = \left(\frac{q_2}{m_2} - \frac{q_1}{m_1}\right) \frac{n}{\Pi^\delta} D_\delta \,, \tag{4.41}$$

where q_i is charge of species i. One could see that conductivity is closely tied to diffusivity.

While my primary aim is to obtain coefficients characterizing the dissipative particle transport, due to the generality of the results I can also obtain the coefficients for the transport of energy and momentum. Thus, starting with the expression (A.1e) in a local frame and proceeding as in the case of (4.35) and (4.36), I get, with (4.33),

$$\begin{aligned} \mathbf{Q}_1 + \mathbf{Q}_2 &= -\frac{T}{3} \left(\{\mathbf{A}, \mathbf{A}\} \nabla T + \{\mathbf{C}, \mathbf{A}\} \mathbf{d}_{12}\right) + \frac{5}{3} \left(\underline{E}_1 n_1 \mathbf{V}_1 - \underline{E}_2 n_2 \mathbf{V}_2\right) \\ &= -\frac{T}{3} \left(\{\mathbf{A}, \mathbf{A}\} \nabla T + \{\mathbf{C}, \mathbf{A}\} \mathbf{d}_{12}\right) \\ &\quad + \frac{5}{3} \left(\frac{\underline{E}_1}{m_1} - \frac{\underline{E}_2}{m_2}\right) \frac{\rho_1 \rho_2}{\rho} \left(\mathbf{V}_1 - \mathbf{V}_2\right) \,, \end{aligned} \tag{4.42}$$

where in the second step I make use of the condition on local velocities $\rho_1 \mathbf{V}_1 + \rho_2 \mathbf{V}_2 = 0$. The standard procedure [148] in coping with the heat flux is to break it into a contribution that can be associated with the net movement of particles and into a remnant, driven by the temperature gradient, representing the heat conduction. With this, the driving force $\mathbf{d}_{12}$ needs to be eliminated from the

heat flux in favor of the species velocities. Using (4.36), I find

$$\begin{aligned}\mathbf{Q}_1+\mathbf{Q}_2 &= -\nabla T\frac{T}{3}\left(\{\mathbf{A},\mathbf{A}\}-\frac{\{\mathbf{C},\mathbf{A}\}^2}{\{\mathbf{C},\mathbf{C}\}}\right)\\ &\quad+(\mathbf{V}_1-\mathbf{V}_2)\left[\frac{5}{3}\left(\frac{\underline{E}_1}{m_1}-\frac{\underline{E}_2}{m_2}\right)\frac{\rho_1\rho_2}{\rho}+\frac{\{\mathbf{C},\mathbf{A}\}}{\{\mathbf{C},\mathbf{C}\}}\right].\end{aligned}\tag{4.43}$$

The coefficient

$$\kappa=\frac{T}{3}\left(\{\mathbf{A},\mathbf{A}\}-\frac{\{\mathbf{C},\mathbf{A}\}^2}{\{\mathbf{C},\mathbf{C}\}}\right),\tag{4.44}$$

relating the heat flow to the temperature gradient, is the heat conduction coefficient. From (4.44) and considerations in Appendix E, it follows that κ given by Eq. (4.44) is positive definite.

The final important coefficient that I will obtain, for completeness, is the viscosity. The modification of the momentum flux tensor (A.1d), on account of the distortion of momentum distributions described by (4.30), is

$$\begin{aligned}\overline{\overline{P}}^{(1)} &= \int\frac{d^3p}{(2\pi\hbar)^3}\frac{\overline{\overline{\mathbf{p}\,\mathbf{p}}}}{m_1}\delta f_1+\int\frac{d^3p}{(2\pi\hbar)^3}\frac{\overline{\overline{\mathbf{p}\,\mathbf{p}}}}{m_2}\delta f_2\\ &= -\int\frac{d^3p}{(2\pi\hbar)^3}\frac{\overline{\overline{\mathbf{p}\,\mathbf{p}}}}{m_1}\left(\overline{\overline{B}}_1:\overline{\overline{\nabla\mathbf{v}}}\right)f_1^{(0)}\tilde{f}_1^{(0)}-\int\frac{d^3p}{(2\pi\hbar)^3}\frac{\overline{\overline{\mathbf{p}\,\mathbf{p}}}}{m_2}\left(\overline{\overline{B}}_1:\overline{\overline{\nabla\mathbf{v}}}\right)f_2^{(0)}\tilde{f}_2^{(0)}\\ &= -\frac{1}{5}\overline{\overline{\nabla\mathbf{v}}}\left(\int\frac{d^3p}{(2\pi\hbar)^3}\overline{\overline{B}}_1:\frac{\overline{\overline{\mathbf{p}\,\mathbf{p}}}}{m_1}f_1^{(0)}\tilde{f}_1^{(0)}+\int\frac{d^3p}{(2\pi\hbar)^3}\overline{\overline{B}}_2:\frac{\overline{\overline{\mathbf{p}\,\mathbf{p}}}}{m_2}f_2^{(0)}\tilde{f}_2^{(0)}\right)\\ &= -\frac{T}{5}\overline{\overline{\nabla\mathbf{v}}}\{\overline{\overline{B}},\overline{\overline{B}}\}.\end{aligned}\tag{4.45}$$

The coefficient of proportionality between the shear correction to the pressure tensor and the tensor of velocity derivatives is, up to a factor of 2, the shear viscosity coefficient

$$\eta=\frac{T}{10}\{\overline{\overline{B}},\overline{\overline{B}}\}.\tag{4.46}$$

As with other results for coefficients, from Appendix E it follows that the result for η above is positive definite, as physically required [148].

On account of symmetry considerations within the linear theory, the changes in temperature or concentration do not affect the pressure tensor. However, the situation changes if one goes beyond the linear approximation. For a general discussion of different higher-order effects see Ref. [76]. As a next step, I need to find the form factors in (4.30); that requires finding the functions a, b and c in (4.34) by solving Eqs. (4.31)-(4.33).

4.4 Transport Coefficients in Terms of Cross Sections

4.4.1 Constraints on Deviations from Equilibrium

Since the zeroth-order, in derivative expansion, local-equilibrium distributions are constructed to produce the local particle densities, net velocity and net energy, corrections to the distributions cannot alter those macroscopic quantities. Thus, I have locally the constraints

$$\delta n_i = \int \frac{d^3p}{(2\pi\hbar)^3}\,\delta f_i = 0\,, \tag{4.47a}$$

$$\delta\left(\rho \underline{\mathbf{V}}\right) = \int \frac{d^3p}{(2\pi\hbar)^3}\,\mathbf{p}\,\delta f_1 + \int \frac{d^3p}{(2\pi\hbar)^3}\,\mathbf{p}\,\delta f_2 = 0\,, \tag{4.47b}$$

$$\delta\left(n \underline{E}\right) = \int \frac{d^3p}{(2\pi\hbar)^3}\,\frac{p^2}{2m_1}\,\delta f_1 + \int \frac{d^3p}{(2\pi\hbar)^3}\,\frac{p^2}{2m_2}\,\delta f_2 = 0\,. \tag{4.47c}$$

With driving forces being independent of each other and with form factors in (4.30) being independent of the forces, each of the form factors sets must separately meet the constraints. By inspection, however, one can see that the density and energy constraints are met automatically with the expressions (4.34) of form factors. Moreover, the tensorial distortion (4.34c) satisfies all the constraints. At a general level, the ability to meet the constraints while solving Eqs. (4.31)-(4.33) relies on

the fact that the linearized collision integrals I_{ij} (in Eqs. (4.20) and (4.21)) nullify quantities conserved in collisions, so a combination of the conserved quantities may be employed in constructing the form factors ϕ_i, ensuring that the constraints are met. When the transport coefficients get expressed in terms of the brace products, though, ensuring that the constraints are met becomes actually irrelevant for results on the transport coefficients, *because* the linearized integrals and the corresponding brace products nullify the conserved quantities.

Given cross sections and equilibrium particle distributions, the set of equations (4.31)-(4.33) may be principally solved. However, such a solution is generally complicated and would likely not produce clear links between the outcome and input to the calculations. On the other hand, the experience has been that when expanding the form-factor functions, a, b and c in (4.34), in power series in p^2, the lowest-order results represent excellent approximations to the complete results and are quite transparent, e.g. [144]. Thus, I adopt here the latter strategy and test the accuracy of the results in a few selected cases.

4.4.2 Diffusivity

If one inserts (4.34a) with $c_i(p^2) = c_i$ into the local velocity constraint (4.47a), one gets the requirement

$$\frac{c_1}{\rho_1}\int\frac{d^3p}{(2\pi\hbar)^3}\,p^2\,f_1^{(0)}\,\tilde{f}_1^{(0)}+\frac{c_2}{\rho_2}\int\frac{d^3p}{(2\pi\hbar)^3}\,p^2\,f_2^{(0)}\,\tilde{f}_2^{(0)}=0\,. \tag{4.48}$$

After partial integrations, I find that this is equivalent to the requirement $c_1 = -c_2 \equiv c$.

When c_i is constant within each species, then $\mathbf{C}_i$ is up to a factor equal to momentum and, thus, gets nullified by the linearized collision integral *within each species* $I_{ii}(\mathbf{C}) = 0$. To obtain a value for c, I multiply the first of Eqs. (4.31) by $\mathbf{C}_1$

and the second by $\mathbf{C}_2$, add the equations side by side and integrate over momenta. With this, I get an equation where both sides are explicitly positive definite and, in particular, the l.h.s. is similar to the l.h.s. of Eq. (4.48), but with an opposite sign between the component terms. That side of the equation can be integrated out employing the explicit form of $f^{(0)}$ from Eq. (4.17). The other side of the resulting equation represents $\{\mathbf{C},\mathbf{C}\}$ where only the interspecies integrals survive. On solving the equation for c, I find

$$c = \frac{6\,\rho_1\,\rho_2}{\rho\,\chi_{12}}\,, \tag{4.49}$$

where

$$\chi_{12} = g^2 \int \frac{d^3p_1}{(2\pi h)^3}\,\frac{d^3p_2}{(2\pi h)^3}\,d\Omega\,v^*\left(\frac{d\sigma_{12}}{d\Omega}\right)(\mathbf{p}_1 - \mathbf{p}_1')^2\,f_1^{(0)}\,f_2^{(0)}\,\tilde{f}_1^{(0)\prime}\,\tilde{f}_2^{(0)\prime}\,. \tag{4.50}$$

The integral stems from a transformed brace product $\{\mathbf{C},\mathbf{C}\}$ and I resurrect here the degeneracy factors g. For the brace product itself, I find

$$\{\mathbf{C},\mathbf{C}\} = \frac{c^2}{2}\left(\frac{\rho}{\rho_1\,\rho_2}\right)^2\chi_{12} = \frac{18}{\chi_{12}}\,. \tag{4.51}$$

On inserting this into the diffusivity (4.39), I obtain

$$D_\delta = \frac{6T}{m_{12}}\,\frac{\Pi^\delta}{n\,\chi_{12}}\left(\frac{\rho_1\,\rho_2}{\rho}\right)^2\,. \tag{4.52}$$

In the above, one sees that the diffusion coefficient depends both on the equation of state, through the factor Π^δ, and on the cross section for collisions between the species, through χ_{12}. The collisions between the species are weighted with the momentum transfer squared. Only those collisions between species that are characterized by large momentum transfers suppress the diffusivity and help localize the species. The marginalization of collisions with low momentum transfers is a common feature of all transport coefficients.

At high temperatures the Fermi gas reduces to the Boltzmann gas. In the absence of mean-field effects, one finds $\Pi^\delta \sim \frac{2T}{m}$ for small asymmetries. The integral χ_{12} is then of the order $n^2\,\sigma_{12}\,p^3/m \sim n^2\,\sigma\,\sqrt{m\,T^3}$. Together, these yield $D_\delta \sim \frac{1}{n\,\sigma_{12}}\sqrt{\frac{T}{m}}$. The precise high-$T$ result for isotropic cross-sections in the interaction of species with equal mass m is [76, 75]

$$D_\delta = \frac{3}{8n\sigma_{12}}\sqrt{\frac{T}{\pi m}}\,. \tag{4.53}$$

The square-root dependence on temperature will be evident in the numerical results at high T. With an inclusion of the mean field, with the net energy quadratic in asymmetry, the derivative Π^δ gets modified into $\Pi^\delta \sim [2\,(T + 2e^{int}_{sym})]/m$. Thus, the mean field enhances the diffusion.

At low temperatures, the derivative Π^δ is simply proportional to the symmetry energy, $\Pi^\delta \sim (4e_{sym})/m$. As to the collisional denominator of the diffusion coefficient, at low temperatures the collisions take place only in the immediate vicinity of the Fermi surface. I can write the product of equilibrium functions in the collision integral as

$$f_1^{(0)}\,f_2^{(0)}\,\tilde{f}_1^{(0)\prime}\,\tilde{f}_2^{(0)\prime} = K_1\,K_2\,K_1'\,K_2'\,, \quad \text{where } K_i = \frac{1}{2\cosh\{(\frac{p^2}{2m_i} - \mu_i)/T\}}\,, \tag{4.54}$$

and, at low T, $K_i \sim 2\pi\,m\,T\,\delta(p^2 - p_{Fi}^2)$. The integration in (4.50) yields $\chi_{12} \sim \sigma_{12}\,m^2\,T^3\,n^2/p_F^3$. In consequence, I find that the diffusion coefficient diverges as $1/T^2$ at low temperatures. For the spin diffusion coefficient, one finds within the low temperature Landau Fermi-liquid theory [90]

$$D_\sigma = \frac{v_F^2}{3}\,(1 + F_0^a)\,\tau_D\,, \tag{4.55}$$

where v_F is Fermi velocity, F_0^a is a spin-antisymmetric Landau coefficient and τ_D is

a characteristic relaxation time that scales as $\tau_D \sim T^{-2}$. The isospin diffusivity for symmetric matter should differ from the spin diffusivity in the replacement of the spin-antisymmetric Landau parameter with the isospin asymmetric parameter, neither of which has a significant temperature dependence. Thus, here consistently I find a T^{-2} divergence of the diffusivity at low temperatures. Moreover, the factor $(1 + F_0^a)$ is nothing else but a rescaled symmetry energy, with F_0^a being the ratio of the interaction to the kinetic contribution to the energy [150]. Thus, here consistently I find a proportionality of the diffusivity to the symmetry energy at low temperatures.

To summarize the above results on diffusivity, I find that the diffusivity is inversely proportional to the cross section between species for high momentum transfers. Moreover, whether at low or high temperatures, the diffusivity is sensitive to the symmetry energy in the mean-fields. The mean-field sensitivity is associated with the factor

$$\Pi^\delta = \frac{\partial \mu_{12}}{\partial \delta} + \frac{\partial}{\partial \delta}\left(\frac{U_1}{m_1} - \frac{U_2}{m_2}\right) = \frac{\partial \mu_{np}}{\partial \delta} + 4\epsilon_{sym}^{int}\frac{1}{m},$$

where the last equality pertains to the system of neutrons and protons and ϵ_{sym}^{int} represents the interaction contribution to the symmetry energy at the relevant density.

While I obtained the diffusivity here assuming constant c_i in (4.34a), I will show that the next-order term in the expansion of c_i increases the diffusion coefficient D_δ only by 2% or less in the case of my interest.

4.4.3 Heat Conductivity

Evaluation of the heat conduction and shear viscosity coefficients requires similar methodology to that utilized for the diffusivity. While these coefficients have

been obtained in the past for a one component Fermi system [144], it can be still important to find them for the two component system.

If one assumes $a_i(p^2) = a_i$ in (4.34b), then, interestingly, one finds that the momentum constraint (4.47a) is automatically satisfied. To obtain the values for a_i, I multiply Eq. (4.33) on both sides by $\mathbf{A_1}$ and integrate over momenta and I multiply the equation analogous to (4.33) by $\mathbf{A_2}$ and also integrate over momenta. As a consequence, I get a set of equations for a_i of the form

$$L_j = \mathcal{A}_{j1}\, a_1 + \mathcal{A}_{j2}\, a_2\,, \quad j = 1, 2\,, \tag{4.56}$$

where $\mathcal{A}_{ji}$ are coefficients independent of a,

$$\mathcal{A}_{ii} = \frac{1}{a_i^2}\left([\mathbf{A}, \mathbf{A}]_{ii} + [\mathbf{A}_i, \mathbf{A}_i]_{12}\right)\,, \qquad \mathcal{A}_{12} = \mathcal{A}_{21} = \frac{1}{a_1\, a_2}\,[\mathbf{A}_1, \mathbf{A}_2]_{12}\,, \tag{4.57}$$

cf. Appendix E, and

$$L_j = \frac{1}{m_j\, T}\left(7\, n_j\, \underline{E_j^2} - \frac{25}{3}\, n_j\, \left(\underline{E}_j\right)^2\right)\,, \tag{4.58}$$

where $\underline{E_j^2}$ and $\left(\underline{E}_j\right)^2$ are, respectively, the average local square kinetic energy of species j and square average local kinetic energy of the species.

The solution to the set (4.56) is

$$\begin{aligned} a_1 &= \left(\mathcal{A}_{22}\, L_1 - \mathcal{A}_{12}\, L_2\right)/\Delta_{\mathcal{A}}\,, \\ a_2 &= \left(\mathcal{A}_{11}\, L_2 - \mathcal{A}_{12}\, L_1\right)/\Delta_{\mathcal{A}}\,, \end{aligned} \tag{4.59}$$

where the determinant is

$$\Delta_{\mathcal{A}} = \mathcal{A}_{11}\, \mathcal{A}_{22} - \mathcal{A}_{12}^2\,. \tag{4.60}$$

The brace product $\{\mathbf{A}, \mathbf{A}\}$ for use in calculating the heat conduction coefficient κ in

(4.44) is

$$\{\mathbf{A},\mathbf{A}\} = a_1\, L_1 + a_2\, L_2\,. \tag{4.61}$$

The product $\{\mathbf{C},\mathbf{A}\}$ in (4.44) can be calculated given the values of a and c, and $\{\mathbf{C},\mathbf{C}\}$ was already obtained before.

4.4.4 Shear Viscosity

Evaluation of the shear viscosity coefficient η follows similar steps to those involved in the evaluation of κ. Thus, I assume $b_i(p^2) = b_i$ in (4.34c). To find the coefficient values, I convolute both sides of Eq. (4.32) with $\overset{\circ}{\overline{\mathbf{p}\,\mathbf{p}}}$ and integrate over the momenta and I do the same with the other constraint equation for $\overline{\overline{B}}$. The l.h.s. integrations produce

$$\frac{1}{m_i\,T}\int \frac{d^3p}{(2\pi\,\hbar)^3}\,\overset{\circ}{\overline{\mathbf{p}\,\mathbf{p}}} : \overset{\circ}{\overline{\mathbf{p}\,\mathbf{p}}}\, f_i^{(0)}\,\tilde{f}_i^{(0)} = \frac{2}{3\,m_i\,T}\int \frac{d^3p}{(2\pi\,\hbar)^3}\,p^4\, f_i^{(0)}\,\tilde{f}_i^{(0)} = \frac{20}{3}\,\rho_i\,\underline{E}_i\,. \tag{4.62}$$

With the above, I get the set of equations for b_i:

$$\frac{20}{3}\,\rho_j\,\underline{E}_j = \mathcal{B}_{j1}\,b_1 + \mathcal{B}_{j2}\,b_2\,, \quad j = 1,2\,, \tag{4.63}$$

where the coefficients $\mathcal{B}$ are given by,

$$\mathcal{B}_{ii} = [\overset{\circ}{\overline{\mathbf{p}\,\mathbf{p}}},\overset{\circ}{\overline{\mathbf{p}\,\mathbf{p}}}]_{ii} + [(\overset{\circ}{\overline{\mathbf{p}\,\mathbf{p}}})_i,(\overset{\circ}{\overline{\mathbf{p}\,\mathbf{p}}})_i]_{12}\,, \qquad \mathcal{B}_{12} = \mathcal{B}_{21} = [(\overset{\circ}{\overline{\mathbf{p}\,\mathbf{p}}})_1,(\overset{\circ}{\overline{\mathbf{p}\,\mathbf{p}}})_2]_{12}\,. \tag{4.64}$$

Solving the set for b, One finds

$$\begin{aligned} b_1 &= \frac{20}{3\Delta_{\mathcal{B}}}\,(\rho_1\,\underline{E}_1\,\mathcal{B}_{22} - \rho_2\,\underline{E}_2\,\mathcal{B}_{12})\,, \\ b_2 &= \frac{20}{3\Delta_{\mathcal{B}}}\,(\rho_2\,\underline{E}_2\,\mathcal{B}_{11} - \rho_1\,\underline{E}_1\,\mathcal{B}_{12})\,, \end{aligned} \tag{4.65}$$

where the determinant is

$$\Delta_{\mathcal{B}} = \mathcal{B}_{11}\,\mathcal{B}_{22} - \mathcal{B}_{12}^2\,. \tag{4.66}$$

The brace product for calculating the shear viscosity coefficient $\eta = \frac{T}{10}\{\overline{\overline{B}}, \overline{\overline{B}}\}$ becomes

$$\{\overline{\overline{B}}, \overline{\overline{B}}\} = \frac{20}{3}\left(b_1\,\rho_1\,\underline{E}_1 + b_2\,\rho_2\,\underline{E}_2\right)\,. \tag{4.67}$$

4.5 Quantitative Results

4.5.1 Transport Coefficients

I next calculate the transport coefficients as a function of density and temperature, using experimentally measured nucleon-nucleon cross sections. The cross sections may be altered in matter, compared to free space, but the modifications are presumably more important at low than at the high momentum transfers important for the transport coefficients. With regard to the diffusivity, I will first ignore any mean-field contribution to the chemical potential difference between species. This yields a reference diffusivity to which the diffusivity affected by mean fields may be compared.

The diffusivity for the experimental cross sections and no interaction contributions to the symmetry energy is shown at $\delta = 0$ and different densities n in Fig. 4.1, as a function of temperature T. At low temperatures, the diffusivity diverges due to a suppression of collisions by the Pauli principle. At high temperatures, compared to the Fermi energy, the role of the Pauli principle is diminished and the diffusivity acquires a characteristic $\sqrt{T}$ dependence. At moderate temperatures and densities in the vicinity and above normal density, the diffusion coefficient turns out to be in the vicinity of my original estimate of $D_I \sim 0.2$ fm c.

It should be mentioned that, for symmetric matter, the factors for temperature and pressure gradients in the thermodynamic force $\mathbf{d}_{12}$ (4.28) vanish, $\Pi^P = 0$ and $\Pi^T = 0$, and the brace product in (4.40) vanishes, $\{\mathbf{A}, \mathbf{C}\} = 0$, yielding $k_T = 0$ in (4.38). As physically required, the temperature and pressure gradients produce no relative motion of neutrons and protons for the symmetric matter.

The diffusivity at normal density at different asymmetries is next shown in Fig. 4.2 as a function of temperature. Because of charge symmetry, the diffusivity does not depend on the sign of δ. At low temperatures the diffusivity is generally expected to behave as

$$D_I \propto \frac{\hbar^3 p_F^2}{m^3 T^2 \sigma}, \tag{4.68}$$

while at high temperatures in the manner prescribed by (4.53). With the respective behaviors serving as a guidance, I provide a parametrization of the numerical results for D_δ as a function of n, T and δ,

$$\begin{aligned} D_I &= (1 - 0.19\,\delta^2)\left[\frac{11.34}{T^{2.38}}\left(\frac{n}{n_0}\right)^{1.54}\right. \\ &\left. + \frac{1.746}{T}\left(\frac{n}{n_0}\right)^{0.56} + 0.00585\,T^{0.913}\left(\frac{n_0}{n}\right)\right]. \end{aligned} \tag{4.69}$$

Here, temperature T is in MeV and the diffusivity D_I is in fm c. The parametrization describes the numerical results to an accuracy better than 4% within the region of thermodynamic parameters of $1.0 \leq n/n_0 \leq 4.0$, $10\,\mathrm{MeV} \leq T \leq 100\,\mathrm{MeV}$ and $|\delta| \leq 0.4$. This is, generally, the parameter region of interest in intermediate-energy reactions.

The heat conductivity is shown for symmetric matter at different densities in Fig. 4.3, as a function of temperature. The results are similar to those in Ref. [144], though there the two component nature of nuclear matter was ignored and the isospin-averaged nucleon-nucleon cross-sections have been used. A closer

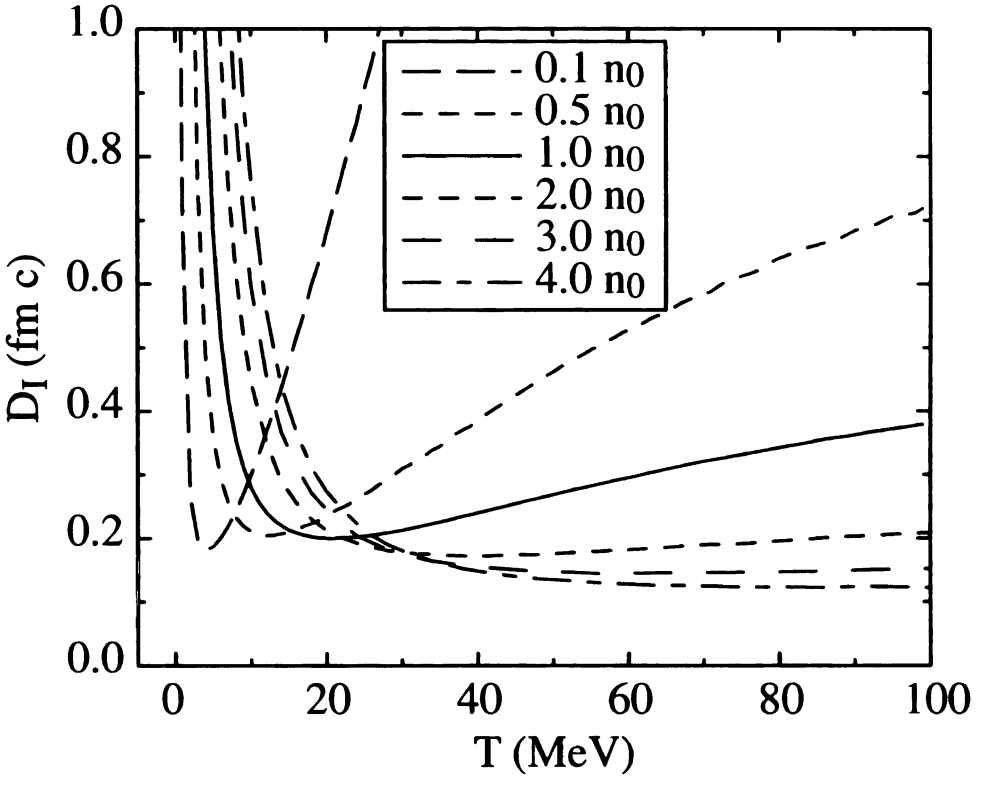

Figure 4.1: Isospin diffusion coefficient D_I in symmetric matter, for $U_i = 0$, at different indicated densities, as a function of temperature T. In the high-temperature limit, the diffusion coefficient exhibits the behavior $D_I \propto \sqrt{T}/n$. Correspondingly, at high temperatures in the figure, the largest coefficient values are obtained for the lowest densities and the lowest coefficient values are obtained for the highest densities. In the low-temperature limit, the diffusion coefficient exhibits the behavior $D_I \propto n^{3/2}/T^2$ and the order of the results in density reverses.

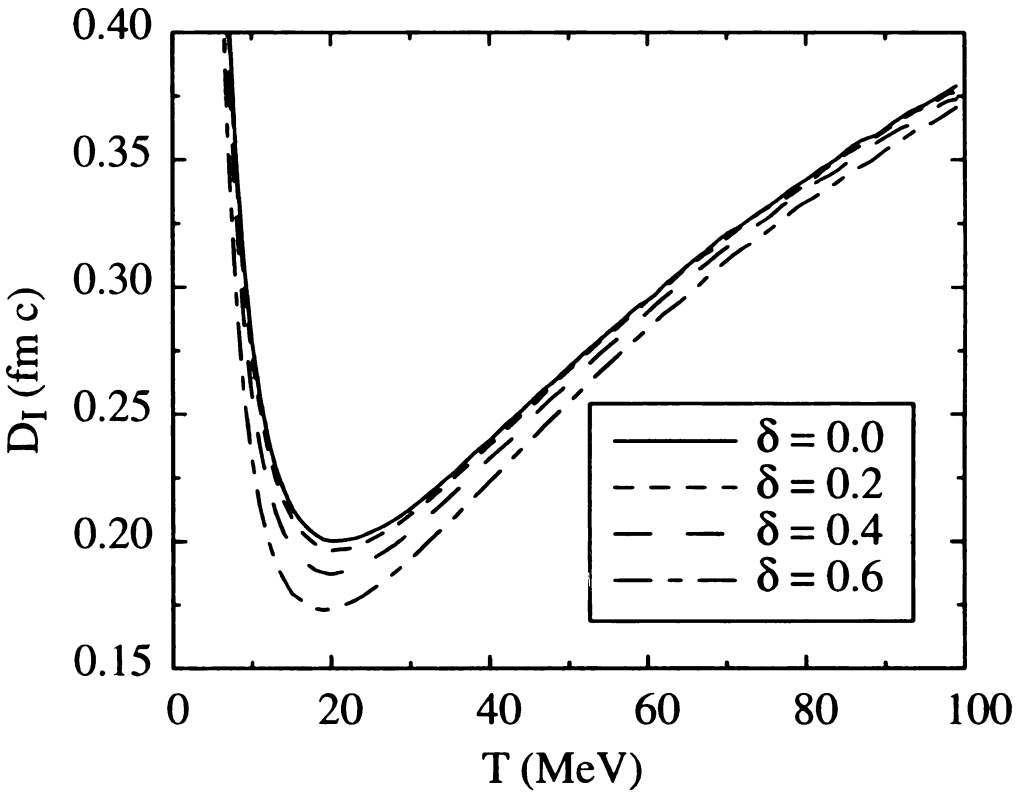

Figure 4.2: Isospin diffusion coefficient D_I at normal density $n = n_0 = 0.16\,\mathrm{fm}^{-3}$ and different indicated asymmetries δ, for $U_i = 0$, as a function of temperature T. An increase in the asymmetry generally causes a decrease in the coefficient, as discussed in the text.

examination of results in Subsections 4.4.3 and 4.4.4 indicates that the use of the isospin-averaged cross-sections is, actually, justified for symmetric matter, when calculating the heat-conduction and shear-viscosity coefficients. Otherwise, however, Fig. 4.3 has been based on a more complete set of cross sections than results in [144]. As in the case of diffusivity, the heat conductivity diverges at low temperatures and tends to a classical behavior at high temperatures, exhibiting there no density dependence and being proportional to velocity, $\kappa \propto \sqrt{T}$. As in the case of diffusivity, I next provide a parametrization of the numerical results for the heat conductivity κ as a function of n, T and δ,

$$\begin{aligned} \kappa &= (1+0.10\,\delta^2)\left[\frac{0.235}{T^{0.755}}\left(\frac{n}{n_0}\right)^{0.951}\right. \\ &\left. -0.0582\left(\frac{n}{n_0}\right)^{0.0816} + 0.0238T^{0.5627}\left(\frac{n}{n_0}\right)^{0.0171}\right]. \end{aligned} \tag{4.70}$$

Here, T is again in MeV and κ is in c/fm^2. The parameterization agrees with the numerical results to an accuracy better than 4% within the range of thermodynamic parameters indicated in the case of D_I.

The shear viscosity coefficient η is shown for symmetric matter at different densities, as a function of temperature, in Fig.4.4. Again, the results are similar to those in Ref. [144]. At high temperatures, the dependence on density weakens and the viscosity becomes proportional to velocity. The numerical results for η are well described, to an accuracy better than 4% within the before-mentioned range, by

$$\eta = (1+0.10\,\delta^2)\left[\frac{856}{T^{1.10}}\left(\frac{n}{n_0}\right)^{1.81} - \frac{240.9}{T^{0.95}}\left(\frac{n}{n_0}\right)^{2.12} + 2.154\,T^{0.76}\right]. \tag{4.71}$$

Here, η is in MeV/fm$^2\,c$ and T is in MeV.

One notes in (4.69)-(4.71), that the diffusion coefficient weakly drops with increasing magnitude of asymmetry $|\delta|$, while the viscosity and heat conduction

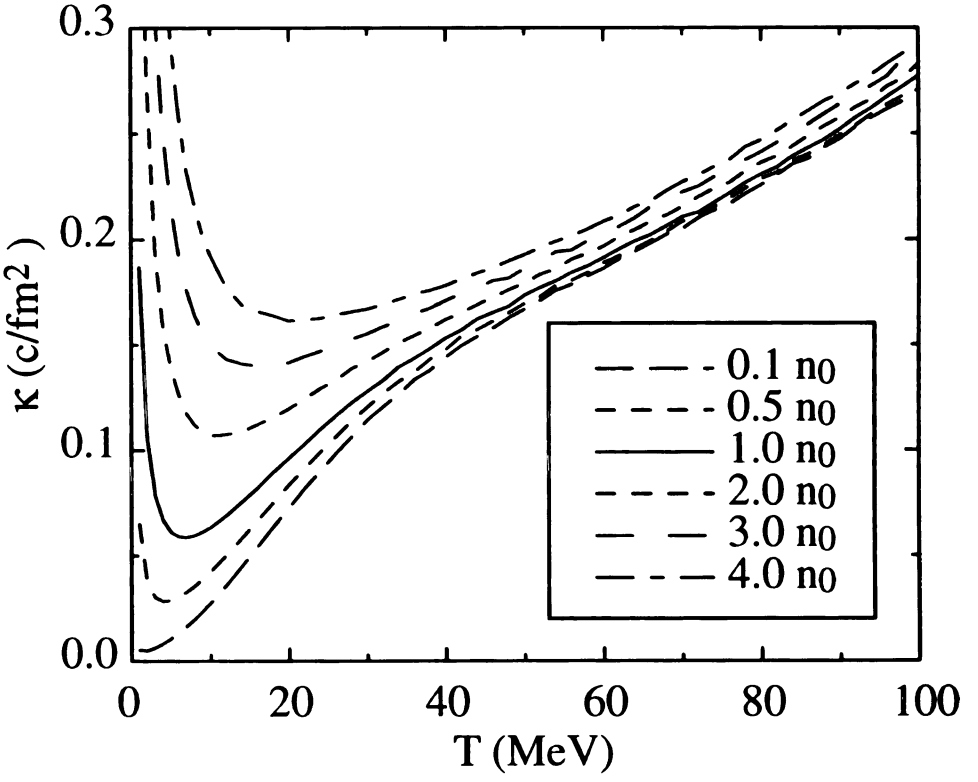

Figure 4.3: Thermal conductivity κ in symmetric nuclear matter, at different indicated densities in units of n_0, as a function of temperature T. The conductivity increases as density increases.

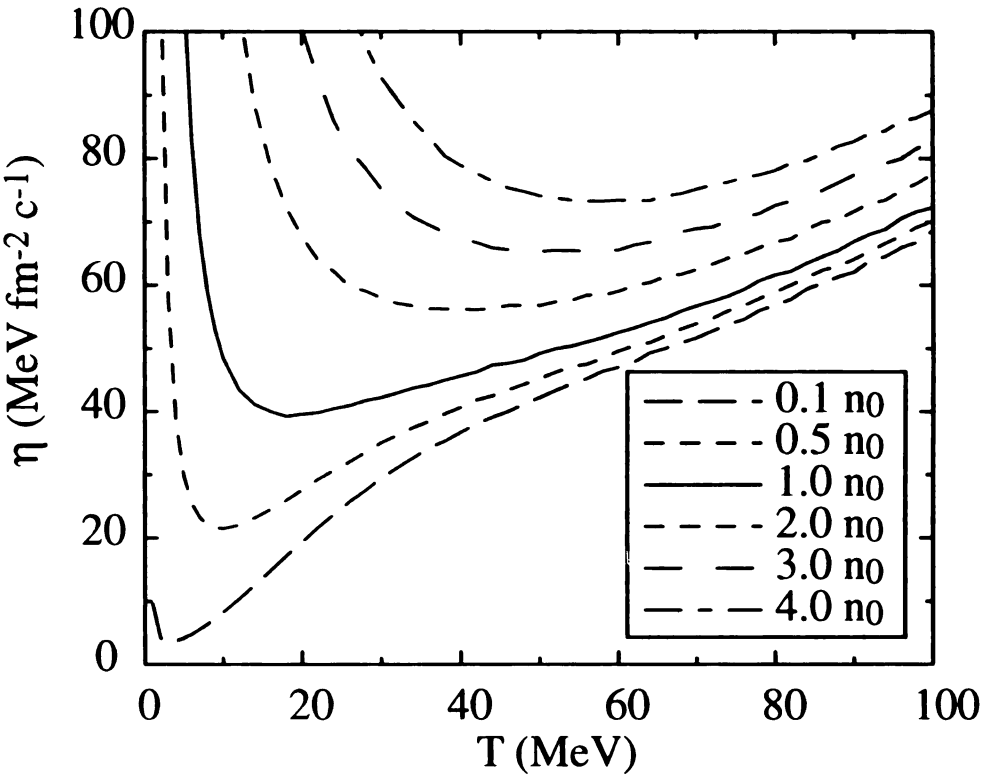

Figure 4.4: Shear viscosity η in symmetric nuclear matter, at different indicated densities in units of n_0, as a function of temperature T. The viscosity increases as density increases.

coefficients weakly increase. Given the weak dependencies, the behaviors exhibited in parametrizations represent, in practice, averages over the considered independent-parameter regions. Overall, the drop and rise in the respective coefficients with $|\delta|$ is characteristic for a situation where the local flux of a component grows faster than the concentration of that component. That type of growth, with the magnitude of asymmetry, typifies a mixture of degenerate fermion gases. The general trends can be deduced following the mean-free-path arguments from Sec. 4.2. When the average velocity rises with asymmetry, so do the heat conduction and shear viscosity coefficients. Additional rise for those coefficients, in the case at hand, can result from the Pauli principle effects and from the difference between cross sections for like and unlike particles. Regarding the diffusion coefficient, though, one needs to consider an irreversible part of relative particle flux, under the condition of the concentration varying with position. If, starting with a given configuration of concentration gradients, one introduces uniform changes of concentration on top, not just the overall relative flux undergoes change but also the reversible flux of concentration gets altered. The rise in the relative flux associated with the velocity of a dominant component rising with concentration is normally more than compensated by the rise in reversible flux, leading to a reduction in the irreversible flux and producing a reduction in diffusivity with particle asymmetry. A mean-field example where the reversible flux eats into the net flux reducing the diffusivity with increasing asymmetry is the estimate in Eq. (4.10), obtained there without invoking Fermi statistics.

As is found in Secs. 4.3.3 and 4.4.2, the dependence of mean fields on species enters the diffusivity through the factor Π^{δ} resulting from the variable change in thermodynamic driving force, from the difference of chemical potentials per mass to asymmetry. The simplest case where one can consider the impact of the mean fields is that of symmetric nuclear matter, at $\delta = 0$. In this case, the factor may be

represented as

$$\Pi^{\delta} = \frac{1}{m}\left(\frac{n}{\xi} + 4\, e_{sym}^{int}\right), \tag{4.72}$$

where $\xi_i = \partial n_i/\partial \mu_i \equiv \xi$ (cf. Appendix C). At high temperatures, one has approximately $\xi_i \approx n_i/T$, so that $n/\xi \approx 2T$. The naive expectation is that e_{sym}^{int} has a linear dependence on the net density, $e_{sym}^{int} = a_I \left(\frac{n}{n_0}\right)^{\nu}$, where $a_I = 14$ MeV and $\nu = 1$. The mean-field amplification factor $R = \Pi^{\delta}(e_{sym}^{int})/\Pi^{\delta}(e_{sym}^{int} = 0)$ for the diffusion coefficient, assuming the linear and also quadratic density-dependence of e_{sym}^{int} ($\nu = 1$ and 2) is shown in Fig. 4.5. The quadratic dependence gives higher amplification factors at $n > n_0$, than the linear dependence, while the opposite is true at $n < n_0$. At low temperatures and moderate to high densities the amplification is very strong suggesting that the diffusion could be used to probe the symmetry energy, aside from the in-medium neutron-proton cross sections.

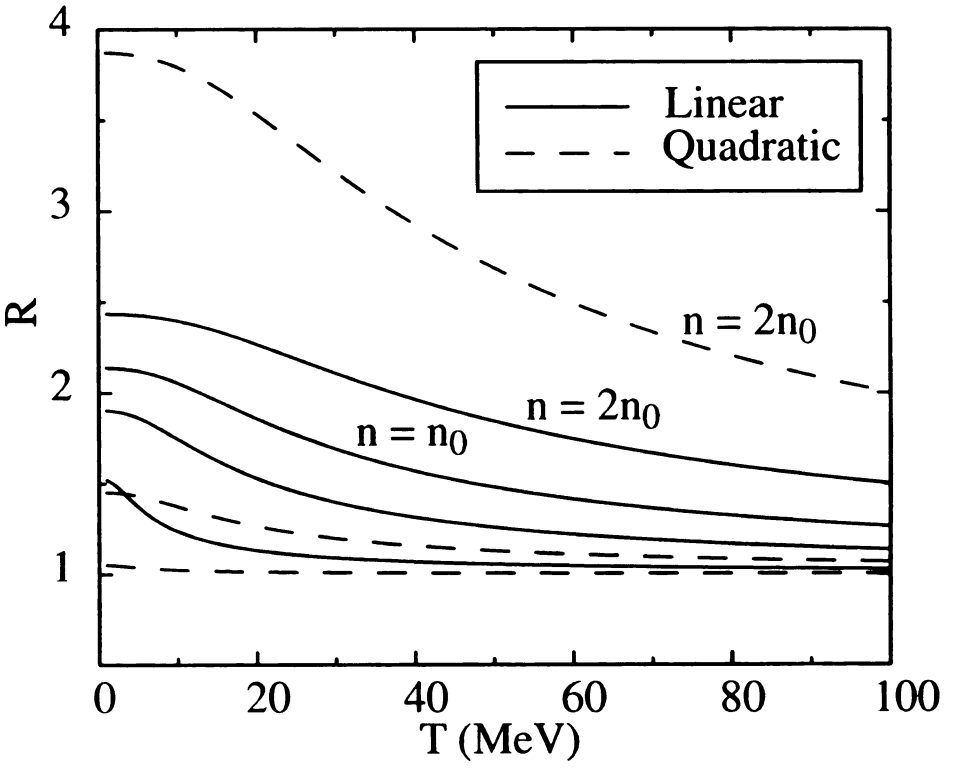

Figure 4.5: Mean-field enhancement factor of the diffusion coefficient in symmetric nuclear matter, $R \equiv D_I(U_i)/D_I(U_i = 0)$, at fixed density n, as a function of temperature T. The solid and dashed lines represent the factors for the assumed linear and quadratic dependence of the interaction symmetry energy on density. The lines from top to bottom are for densities $n = 2\,n_0$, n_0, $0.5\,n_0$ and $0.1\,n_0$, respectively. At normal density the results for the two dependencies coincide.

4.5.2 Testing the Form-Factor Expansion

The calculations of transport coefficients above have been performed assuming that the functions a_i, b_i and c_i in Eqs. (4.34) can be approximated by constants. In the more general case, the functions can be expanded in the series in p^2, e.g.

$$c_i(p^2) = c_i^{(1)} + c_i^{(2)} p^2 + c_i^{(3)} p^4 + \dots . \tag{4.73}$$

The coefficients of the expansion can be found by considering moments of the form-factor equations (4.31)-(4.33). With the more general form of the form-factor functions, the transport coefficients generally increase, but their rise is generally very limited.

To illustrate the magnitude of higher-order effects, I provide in Table 4.1 results for the diffusivity obtained in the standard first-order and in the higher-order calculations at sample densities and temperatures. In the indicated cases, the second-order calculations never increase the diffusion coefficient by more than 3% above the first-order calculations. The efficiency of my Monte-Carlo procedure employed to evaluate the integrals for coefficients worsens as the order of the calculations increases and, correspondingly, I provide only a single third-order result for illustration.

4.5.3 Isospin Equilibration

To gain a further insight whether the diffusion coefficient results are sensible, I will consider the issue of isospin equilibration in a reacting system [151] such as ^{96}Ru + ^{96}Zr at $E_{lab}/A = 100\,\mathrm{MeV}$. At this energy, the Boltzmann-limit estimate for temperature, $T \sim \frac{1}{6} E_{lab}/A \sim 16\,\mathrm{MeV}$, and the degenerate Fermi limit estimate, $T \sim \sqrt{E_{lab}/(2a)} \sim 20\,\mathrm{MeV}$ for $a \approx A/(8\,\mathrm{MeV})$, produce similar results. The typical densities in this reaction are around normal. Based on Figs. 4.1 and 4.5, one can

Table 4.1: Diffusion coefficient D_I obtained within different orders of calculation, using experimental np cross sections, at sample densities n and temperatures T in symmetric nuclear matter, for species-independent mean fields. The numerical errors of the results on D_I are indicated in parenthesis for the least-significant digits. The last two columns, separated by the '$\pm$' sign, give, respectively, the relative change in the result for the highest calculated order compared to the first order and the error for that change.

n	T	D_I			Relative Change		
		1st order	2nd order	3rd order			
fm^{-3}	MeV		fm c		%		
0.016	10	0.29949(15)	0.3055(12)		2.0	$\pm$	0.4
0.016	60	2.3891(18)	2.390(14)		0.0	$\pm$	0.6
0.16	10	0.27964(21)	0.2800(29)	0.2809(25)	0.5	$\pm$	0.9
0.16	60	0.29591(24)	0.2965(19)		0.2	$\pm$	0.7
0.32	10	0.4446(15)	0.4465(26)		0.4	$\pm$	0.7
0.32	60	0.18187(15)	0.1827(13)		0.5	$\pm$	0.7

estimate the streaming contribution to the diffusivity at 0.21 fm c and the mean-field contribution at 0.20 fm c, for a net $D_I \approx 0.41$ fm c.

Considering the direction perpendicular to the plane of contact between the nuclei, with nuclei extending a distance $L \sim (A/n_0)^{1/3} \sim 8$ fm both ways from the interface, one may use the one-dimensional diffusion equation to estimate the isospin equilibration

$$\frac{\partial \delta}{\partial t} = D_I \frac{\partial^2 \delta}{\partial x^2}\,, \tag{4.74}$$

where x is the direction perpendicular to the interface, cf. Eq. (4.7). With isospin flux vanishing at the boundaries of the region $[-L, L]$, the solution to (4.74) is

$$\delta(x,t) = \delta_\infty + \sum_{n=1}^{\infty} a_n \sin k_n x \exp\left(-D_I k_n^2 t\right) + \sum_{n=1}^{\infty} b_n \cos q_n x \exp\left(-D_I q_n^2 t\right) \tag{4.75}$$

where $k_n L = \left(n - \frac{1}{2}\right)\pi$ and $q_n L = n\pi$. The coefficients a_n and b_n are determined by the initial conditions and, in the case in question, $b_n = 0$.

The different terms in the expansion (4.75) correspond to the different levels of

detail in the distribution of concentration, as characterized by the different wavevectors. The greater the detail the faster the information is erased, with the erasure rates proportional to wavevectors squared and with the overall distribution tending towards δ_∞ as $t \to \infty$. The late-stage approach to equilibrium is governed by the rate for the term with the lowest wavevector, i.e. a_1. Defining the isospin equilibration time t_H as one for which the original isospin asymmetry between the nuclei is reduced by half, I get from (4.75)

$$t_H \approx \frac{\ln 2}{D_I k_1^2} = \frac{4 \ln 2 \, L^2}{\pi^2 D_I} \sim 44 \, \mathrm{fm}/c, \tag{4.76}$$

for the case above. When I carry out the full respective Boltzmann-equation simulations of the 100 MeV/nucleon ^{96}Ru + ^{96}Zr reactions, at the impact parameter of $b = 5 \, \mathrm{fm} \gtrsim L/2$, I find that, indeed, the nuclei need to be in contact for about $40 \, \mathrm{fm}/c$ for the isospin asymmetry to drop to the half of original value.

4.6 Summary

Diffusion and other irreversible transport phenomena have been discussed for a binary Fermi system close to equilibrium. For weak nonuniformities, the irreversible fluxes are linear in the uniformities, with the characteristic transport proportionality-coefficients dependent only on the equilibrium system. It is hoped that, in analogy to how the nuclear equation of state and symmetry energy are employed, the coefficient of diffusion can be employed to characterize reacting nuclear systems with respect to isospin transport.

Following a qualitative discussion of irreversible transport in this chapter, the set of coupled Boltzmann-Uhlenbeck-Uehling equations was considered for a binary system, assuming slow macroscopic temporal and spatial changes. The slow changes allow one to solve the equation set by iteration, with the lowest-order solution being

the local equilibrium distributions. In the next order, corrections to those distributions were obtained, linear in the thermodynamic driving forces associated with the system nonuniformities. These corrections produce irreversible fluxes linear in the forces. The transport coefficients have been formally expressed in terms of brace products of the responses of distribution functions to the driving forces. The considered coefficients include diffusivity, conductivity, heat conduction and shear viscosity.

Furthermore, the set of the linearized Boltzmann equations was explicitly solved under the assumption of simplified distribution-function responses to the thermodynamic driving forces. The solutions to the equations led to explicit expressions for the transport coefficients, with the diffusivity given in terms of the collision integral for collisions between the two species weighted by the momentum transfer squared. Besides associated sensitivity to the cross section for collisions between the species, the diffusivity is also sensitive to the dependence of mean fields on the species. The collisions *between the species* are those that inhibit the relative motion of the species; the difference between mean fields affects the relative acceleration and, in combination with the collisions, the stationary diffusive flux that is established.

I calculated the isospin diffusivity for nuclear matter, using experimental nucleon-nucleon cross sections for species-independent mean-fields. At low temperatures and high densities, the diffusivity diverges due a suppression of collisions by the Pauli principle. At high temperatures, the diffusivity is roughly proportional to the average velocity and is inversely proportional to the density. The diffusivity weakly decreases with an increase in the absolute magnitude of asymmetry. I provided an analytic fit to the numerical results. For completeness, I also calculated the heat conduction and shear viscosity coefficients and provided fits to those. Moreover, I calculated the diffuseness mean-field enhancement factor for

symmetric matter, assuming a couple of dependencies of the symmetry energy on density. At low temperatures, the enhancement factor is simply proportional to the net symmetry energy divided by the kinetic symmetry energy. Considering the expansion of the form-factors in distribution-function responses, I demonstrated that corrections to the Boltzmann-equation transport coefficients, beyond the approximations I employed, are small. Finally, I produced an elementary estimate for isospin equilibration in a low impact-parameter collision.

Chapter 5: Transport Simulations

As has been discussed, the Boltzmann equation set may be used for simulating heavy-ion reactions, and the results from such simulation can be compared with experimental data to deduce properties of nuclear matter. This chapter is specifically devoted to the reaction simulations. In the first part of this chapter, I will analyze the spectator-participant interaction in peripheral reactions and the relation of spectator observables to the nuclear equation of state (EOS). In the second part, I will discuss isospin diffusion process in reactions of isospin asymmetric systems.

5.1 Spectator Response to the Participant Blast

As already stated in Chapter 1, the participant-spectator interaction plays an essential role in the dynamics of heavy-ion reactions. In this section, I will discuss in detail, the impact of spectator shadowing on the development of elliptic flow, and the resulting close relation of the nuclear EOS to the spectator properties following the dynamic stage of a heavy-ion reaction.

A brief introduction to elliptic flow within the participant region and the past studies on the spectator region is given in subsection 5.1.1. An analysis of the evolution of a reaction system and of the participant-spectator interaction is given in subsection 5.1.2. The sensitivity of the emerging spectator characteristics to the nuclear EOS is investigated in subsection 5.1.3. The predicted speeding up of the spectator during the violent reaction has recently got support from the experiment [152] and a discussion of the spectator velocity increase is given in subsection 5.1.4. The results of this section are summarized in subsection 5.1.5.

5.1.1 Introduction

As indicated in Chapter 1, the nuclear EOS significantly impacts the development of collective flow in the participant region. Phenomenological parameterizations of the EOS are usually constrained with the properties of nuclear-matter at normal density ρ_0 and diverge at much higher densities which can be probed in energetic heavy-ion reactions. However, an important complication for heavy-ion collisions results from the fact that the duration of the initial high-density stage of the collision is very short compared to the time scale for the whole reaction process. *E.g.*, in an 800 MeV/nucleon $b = 5$ fm collision of ^{124}Sn + ^{124}Sn, the high-density stage with a central density $\rho_c > 1.5\,\rho_0$ lasts about 13 fm/c, while the elapsed time from the initial impact to the complete separation of target and projectile is $\sim$ 40 fm/c. The spectator properties continue to develop well beyond this time [153]. Given the short duration of the high-density stage, signals which carry information about the high-density phase of the collision could be easily washed out by other signals generated at a later stage. As a consequence, reaction simulations are needed to provide guidance for the measurement of signals which not only probe the high-density stage but survive through the entire duration of the collision process.

Collective flow of participants has been studied already for quite some time [154, 155, 156]. The flow is believed to result from early stage compression and an expansion [157, 158, 51, 36, 93], and can carry information on the initial high-density phase. The relation between the nuclear EOS and the flow phenomena has been explored extensively in simulations and a recent example is the analysis of the transverse-momentum dependence of elliptic flow [12]. Elliptic flow is shaped by an interplay of geometry and the mean field and, and when gated by the transverse momentum, reveals the momentum dependence of mean field at super-normal densities.

The elliptic flow pattern of the participant matter is affected by the presence of the cold spectators [93, 12, 53], as will be reiterated. When nucleons are decelerated in the participant region, the longitudinal kinetic energy associated with the initial colliding nuclei is converted into thermal and potential compression energy. In a subsequent rapid expansion or explosion, the collective transverse energy develops [51, 36, 157, 158] and many particles from the participant region get emitted in the transverse directions. The particles emitted towards the reaction plane can encounter the cold spectator pieces and, hence, get redirected. In contrast, the particles emitted essentially perpendicular to the reaction plane are largely unimpeded by the spectators. Thus, for beam energies leading to a rapid expansion in the vicinity of the spectators, elliptic flow directed out of the reaction plane (squeeze-out) is expected. This squeeze-out is related to the pace at which the expansion develops, and is, therefore, related to the EOS.

On the other hand, since the spectators serve to deflect particle emissions toward the reaction plane, their properties may be significantly modified. This suggests an analysis of the characteristics of the spectators resulting from the collision process. In one sense, the spectators can be viewed as probes which were present at the site of the nuclear explosion leading to the rapid particle emission. Thus, a careful study of their characteristics could complement the results from elliptic flow and provide further information regarding the properties of high-density nuclear matter.

Long-time evolution of spectators has been studied recently by Gaitanos *et al.*[153]. A comprehensive summary of experimental results for spectators produced in reactions at different centralities has been presented by Pochodzalla [102]. In particular, universal features of spectator multifragmentation have been well documented [102, 14]. The transverse momentum change of the spectator during a semicentral collision, to be addressed here, was studied in the past via emulsions by

Table 5.1: Parameter values for the different mean fields utilized in the simulations. First three columns refer to Eq. (3.28) and the next two to Eq. (3.33). The last column gives the Landau effective mass in normal matter at Fermi momentum.

EOS	a (MeV)	b (MeV)	ν	c	λ	m^*/m
S	187.24	102.623	1.6340			0.98
SM	209.79	69.757	1.4623	0.64570	0.95460	0.70
H	121.258	52.102	2.4624			0.98
HM	122.785	20.427	2.7059	0.64570	0.95460	0.70

Bogdanov *et al.* [159] (see also [160]). The participant-spectator interaction and spectator physics were discussed in [161]. The systematics of the longitudinal momentum transfer to spectators in energetic reactions induced by light projectiles is discussed in Ref. [162]. The spectator acceleration in certain heavy reaction systems has been observed in experiment [152], and further experiments are proposed to study the systematics of the spectator acceleration and its relation to the nuclear EOS.

5.1.2 Spectators and Participants

Within transport simulations, I will investigate here, the spectator-participant interaction and the spectator shadowing effect on elliptic flow in a heavy-ion reaction. The Boltzmann equations underlying microscopic transport theory have been already described in Chapter 3. For later reference, I have listed the parameters for the utilized Mean Fields (MF) in Table 5.1. Details of the momentum independent and momentum dependence MFs have been already given in Chapter 3 (see also Ref. [12]) and shall not be repeated here.

Figure 5.1 presents some results from simulations of ^{197}Au + ^{197}Au collisions at a beam energy T_{lab} = 1 GeV/nucleon and an impact parameter b = 8 fm. Unless indicated otherwise, the hard momentum-dependent (HM) EOS (cf. Table 5.1) was

used. Figure 5.1(a) shows the time evolution of the density for the participant and for the spectator matter. The solid and dashed curves show, respectively, the baryon density ρ_c at the center of the collision system, *i.e.*, participant density and the baryon density in the local frame at the geometric center of the spectator matter ρ_{spec}. Here, the operational definition of spectator matter is that the magnitude of the local longitudinal velocity exceeds half of the velocity in the initial state and that the local density exceeds one tenth of the normal density. The solid line in Fig. 5.1(a) clearly illustrates the rapid density build-up (for $t \leq 5$ fm/c) followed by expansion of the participant matter. The dashed-line also points to a weak compression of the spectator matter during the expansion phase of the participants. The latter observation is consistent with the expected delay associated with the time it takes a compression wave to reach the center of the spectator matter, starting from an edge.

Figure 5.1(b) shows the time evolution of the elliptic flow parameter v_2 for all mid-rapidity particles. The parameter is defined as

$$v_2 = \langle \cos(2\phi) \rangle \,, \tag{5.1}$$

where ϕ is the azimuthal angle in the X-Y plane perpendicular to the beam axis Z; the X-Z plane defines the reaction plane. The value of v_2 conveys information about the pattern of particle emission from the central participant region. The hot participant region has an initial elliptic shape in the X-Y plane due to the overlap geometry. Since the long and short axes of the ellipse point in the Y-direction and in the X-direction, respectively, the matter starts out with stronger MF and pressure gradients in the X-direction. Given the shape of the emission source and the gradients, the matter is first expected to develop a stronger expansion in the X direction and, hence, to give rise to positive values of v_2. If the spectators are nearby

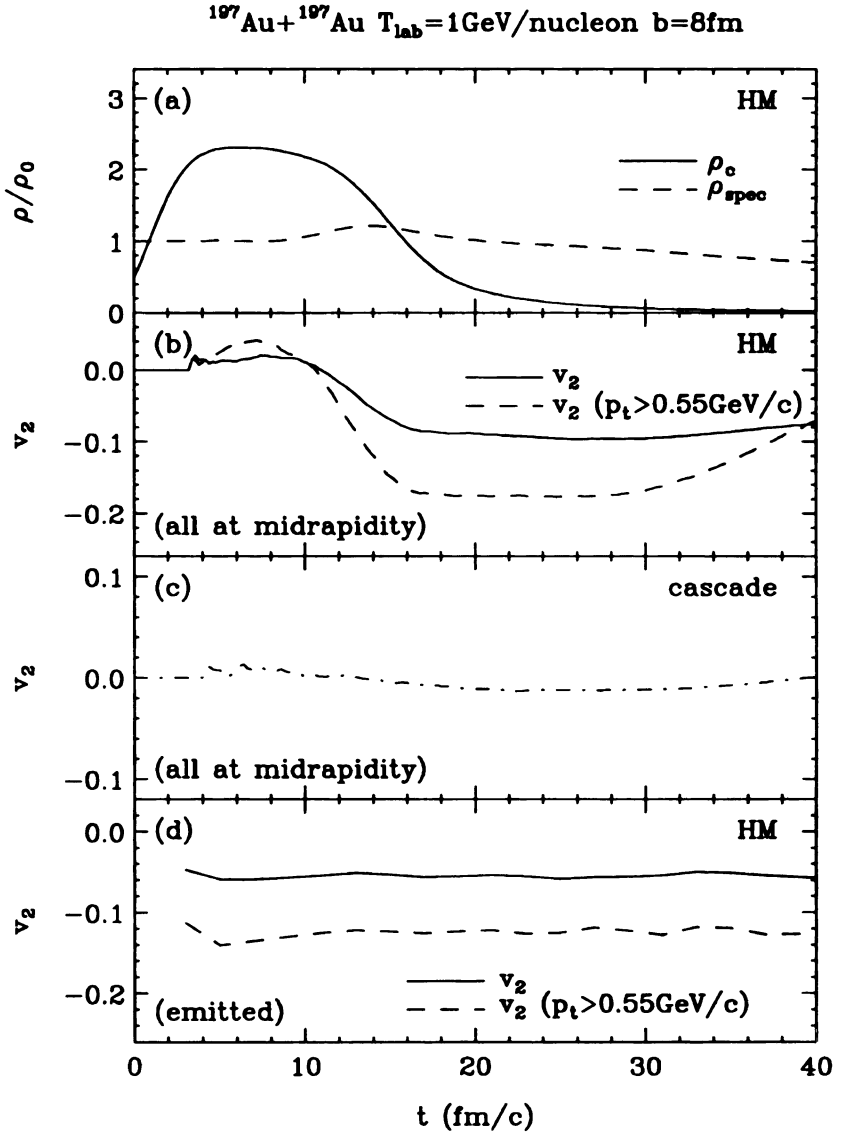

Figure 5.1: Results from a BUU simulation of the the ^{197}Au + ^{197}Au collision at 1 GeV/nucleon and b = 8 fm, as a function of time: (a) the central densities of the participant ρ_c and the spectator matter ρ_{spec}, (b-d) the midrapidity elliptic flow parameter v_2. The results are from a simulation with the HM mean field, except for those in the panel (c) which are from a simulation with no mean field. The panels (b) and (c) show the elliptic flow parameter for all particles in the system while (d) shows the elliptic flow for particles emitted in the vicinity of a given time. In the case of the HM calculations, also shown is v_2 when a high-momentum gate $p_t > 0.55$ GeV/c is applied to the particles.

during the expansion phase, they can serve to stall the expansion in the X direction and a compression wave then develops within the spectator matter (cf. Fig. 5.1(a)). The resulting dominant expansion of participant matter in the Y direction gives rise to negative values of v_2. Figure 5.1(b) indicates that this preferential out-of-plane emission pattern begins after $\sim$ 7 fm/c. The time correlation between the change in sign of v_2 and the decrease in the magnitude of the central density should be noted in the figure. The central density of participant matter ρ_c begins to drop at about 7 fm/c and the most rapid declines ends at $\sim$ 16 fm/c; during this time the elliptic flow drops from its maximum positive value to its maximum negative value.

A comparison of Figs. 5.1(b) and 5.1(c) illustrates the important role of the MF in shaping the elliptic flow magnitude. Figure 5.1(c) shows the time dependence of v_2 obtained when the calculations are performed without the inclusion of a MF (cascade mode). In contrast to the evolution with the mean field (cf. Figs. 5.1(b)) where v_2 first achieves significant positive and then negative values, Fig. 5.1(c) indicates v_2 values which stay close to zero over the entire time evolution of the system. This trend is related to the fact that in the cascade model the transverse expansion is slow compared to the time duration for which the spectators are in close proximity to the participant matter, or compared to the time required for longitudinal motion to stretch the matter to low density. The important role of the MF for the generation of elliptic flow and the sensitivity of this flow to the EOS has been stressed [93, 12, 53].

The temporal difference of v_2 for all midrapidity particles in the system, and for those particles that have left the system can be observed by comparing Figs. 5.1(b) and 5.1(d). Figure 5.1(b) shows the change in v_2 with time as discussed above. On the other hand, Fig. 5.1(d) indicates little or no change of v_2 (over time) for midrapidity particles that have left the system. That is, out-of-plane emission is favored (negative v_2) for all emission times. Figures 5.1(b) and 5.1(d) also show v_2

as a function of time for particles with transverse momentum $p_t > 0.55$ GeV/c; these panels indicate that faster particles are more sensitive to the obstructions as well as to any directionality in the collective motion.

The analyses of elliptic flow and related works have established connections between features of the participant matter resulting from the participant-spectator interaction and the nuclear EOS [51, 157, 158, 12, 93, 53]. On the other hand, it is not known whether the same interaction (during the violent stage of a reaction) leaves any lasting effects in the spectators that could be related to the EOS. Extensive studies of the statistical behavior of spectator matter have been carried out [102, 14] for time scales which are long compared to the collision time. Such studies do not address the dynamical impact of the violent reaction stage on spectators. During the violent stage of a collision, the spectators remain close to the participant matter, so they might serve as a good sensor for the explosion. Thus, I proceed to take a closer look at the changes which may occur in the spectator matter following their interaction with the participants. In addition I investigate whether or not such changes have a connection to the EOS.

Figure 5.2 shows contour plots of different quantities within the reaction plane now from ^{124}Sn + ^{124}Sn reaction simulations at the beam energy of $T_{\rm lab} = 800$ MeV/nucleon, at the impact parameter $b = 5$ fm, carried out with a soft momentum-dependent (SM) mean field. The columns from left to right represent the reaction at 5 fm/c time increments. The top and middle rows show the baryon density in the system frame ρ and the local excitation energy E^*/A, respectively. The bottom row shows the density $\rho_{\rm bnd}$ of baryons that are bound in their local frame ($\epsilon < m$). As may be expected, the excitation energies reach rather high values in the participant region but remain low within the spectator region throughout the violent stage of the reaction. Most of the particles in the participant region are found to be unbound, *i.e.*, $\rho_{\rm bnd}$ is low. On the other hand, most of the particles

within the spectator region are bound. They move with velocities that are close to each other, and this keeps $\rho_{\rm bnd}$ sizeable throughout the violent collision stage.

Figure 5.3 provides next a detailed time development of the selected quantities in the 800 MeV/nucleon ^{124}Sn + ^{124}Sn system for which the contour plots were given. Figure 5.3(a) displays the evolution of baryon density at the system center, ρ_c, and of baryon density at the center of the spectator region, $\rho_{\rm spec}$. The high-density stage for the participant matter in Fig. 5.3(a), characterized by $\rho_c > \rho_0$, lasts over a time that is short in comparison to the time needed for a clear separation of the target and projectile spectators from the participant zone, *cf.* Fig. 5.2. To observe a stabilization of the spectator properties I needed to follow the particular reaction up to $\sim$ 60 fm/c. Longer-term studies of the spectator development have been carried out within the BUU approach [153]. However, as the spectators approach equilibrium, they may be described in terms of the statistical decay method which at this stage has advantages over the BUU equation.

Figure 5.3(b) shows the average transverse momentum per nucleon of the spectator, in the reaction plane, as a function of time. In calculating the average, I include all spectator particles as specified before (dashed line in the panel) or the subset of particles that are bound in the local frames (solid line). The averages, obviously, approach the same asymptotic value over time, but the approach is faster for the bound-particle average. Note that the extra lines in Fig. 5.3(b) represent the evolution of the average momenta past the 40 fm/c of the abscissa. Calculated in either manner, the spectator average momentum $\langle P^X/A \rangle$ reaches its final magnitude during the high-density stage in the participant matter and only somewhat reduces to stable during the expansion that follows. This suggests that the spectators can, indeed, provide information on the high-density stage of the collision.

Figure 5.3(c) shows the average excitation energy per nucleon $\langle E^*/A \rangle$ of the spectator as a function a time. Within the studied time interval, the excitation

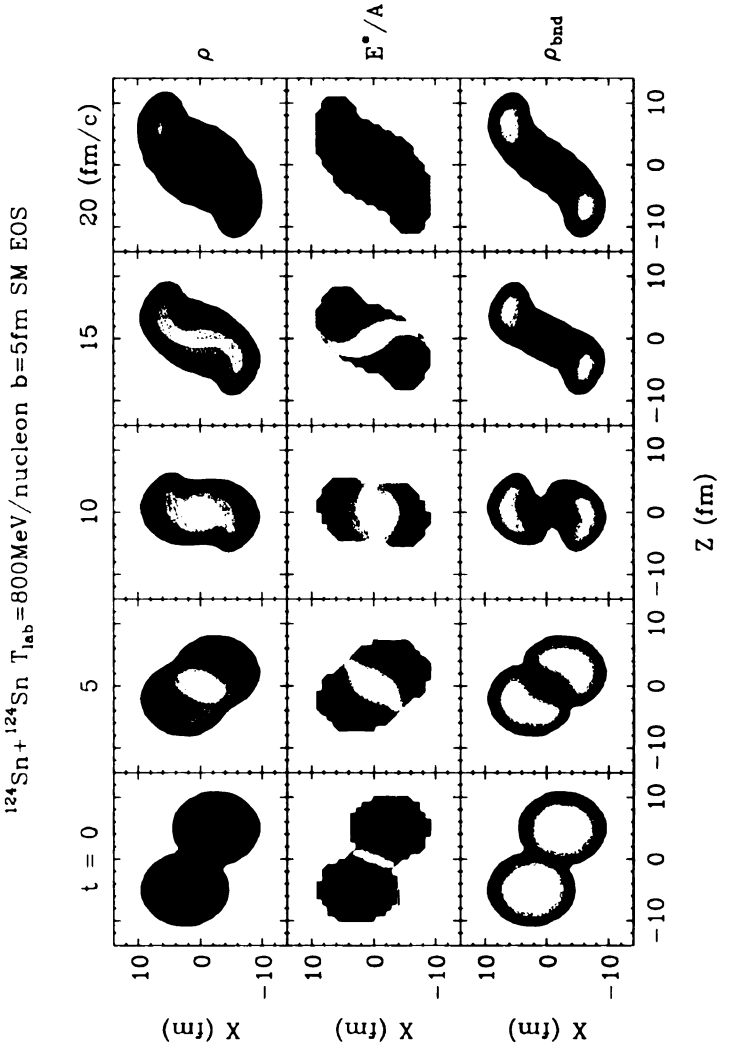

Figure 5.2: Contour plots of the system-frame baryon density ρ (top row), local excitation energy E^*/A (middle row), and of the density of bound baryons $\rho_{\rm bnd}$ (bottom row), in the ^{124}Sn + ^{124}Sn reaction at T_{lab} = 800 MeV/nucleon and b = 5 fm, at times t = 0, 5, 10, 15 and 20 fm/c (columns from left to right). The calculations have been carriered out employing the soft momentum-dependent EOS. The contour lines for the densities correspond to values, relative to the normal density, of ρ from 0.1 to 2.1 with increment of 0.4. The contour lines for $\rho_{\rm bnd}$ are from 0.1 to 1.1 with increment of 0.2. The contour lines for the excitation energy correspond to the values of E^*/A at 5, 20, 40, 80, 120, 160 MeV. For statistical reasons, contour plots for the energy have been suppressed for the baryon densities $\rho < 0.1\ \rho_0$. Note, regarding the excitation energy, that the interior of the participant region is hot while the interior of the spectator matter is cold.

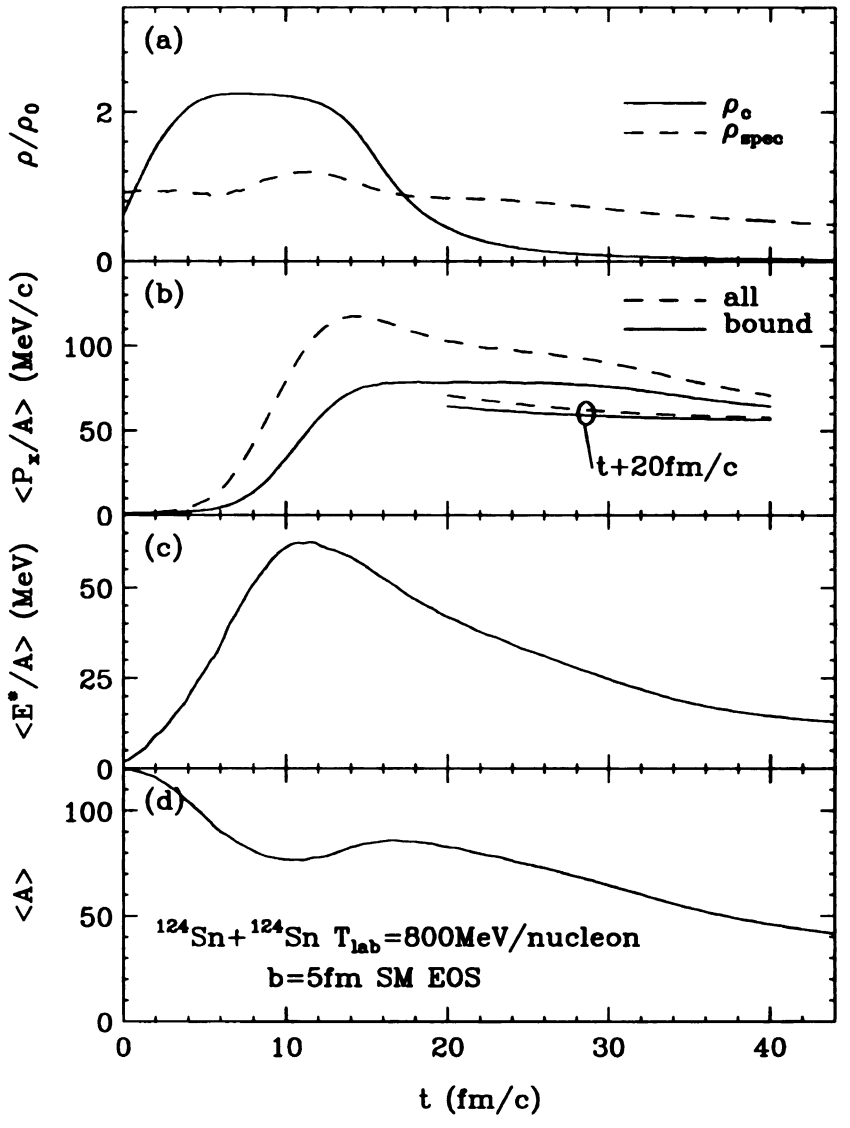

Figure 5.3: Evolution of selected quantities in the ^{124}Sn + ^{124}Sn reaction at 800 MeV/nucleon and b=5 fm, from a calculation with a soft momentum-dependent EOS. The panel (a) shows the density at the center of a spectator $\rho_{\rm spec}$ (dashed line) together with the density at the system center ρ_c (solid line). The panel (b) shows the average in-plane transverse momentum per nucleon of the spectator $\langle P^X/A\rangle$ calculated using all spectator particles (solid line) and using only bound spectator particles (dashed line). Two extra lines in the panel show evolution of the momenta past the 40 fm/c of the abscissa. The panels (c) and (d) show, respectively, the spectator excitation energy per nucleon $\langle E^*/A\rangle$ and the mass number $\langle A\rangle$ from all spectator particles.

energy rapidly rises and decreases and then changes at a slower pace. During the violent reaction stage, some particles traversing from the participant into the spectator matter contribute to the excitation of the spectator matter. As time progresses, some of those particles will travel through the matter and leave the spectators. Some other will degrade their energy within the spectator frame. (Note: I consistently continue with definition where the spectator matter is that for which the c.m. local velocity is larger than half the beam velocity and the local density exceeds the tenth of normal.)

Figure 5.3(d) shows the mass number of a spectator region as a function of time. The spectator mass number decreases rapidly as particles dive into the participant region and then the mass recovers somewhat, around the time of 20 fm/c, as some particles get through the opposite moving corona matter and join the bulk of the spectator matter moving along the beam direction. Later, a gradual deexcitation slowly reduces the spectator mass.

I have analyzed in this subsection the interplay between the participants and spectators. I have examined how elliptic flow is generated as a result of that interplay and how the interplay affects the spectator characteristics. In the next subsection I will explore the sensitivity of spectator characteristics to the EOS for nuclear matter in collision.

5.1.3 Spectator Sensitivity to the Nuclear Equation of State

In the light that the changes of the spectator properties could probe the compression and explosion of the participant matter, I follow the reaction simulations until a clear separation develops between the spectators and the participant matter and a stabilization of the spectator is attained. I explore the sensitivity of the emerging spectator properties to different assumptions on the nuclear EOS. The results could serve to initialize statistical decay calculations for a

complete description of a reaction.

In the following, I shall present a sample of my spectator investigations, within the ^{124}Sn + ^{124}Sn system in the beam energy range of 250 MeV/nucleon to 1 GeV/nucleon at impact parameters $b = 5 - 7$ fm. I shall also quote results from ^{197}Au + ^{197}Au at 1 GeV/nucleon. I utilized four different EOS explored in the past, of which the parameters are given in Table 5.1. I concentrated on the quantities that could be experimentally determined for the spectator, and thus the average transverse momentum per nucleon $\langle P^X/A \rangle$, the change in the average c.m. momentum per nucleon $\Delta|\langle \mathbf{P}/A \rangle|$, the average excitation energy per nucleon $\langle E^*/A \rangle$, and the average mass $\langle A \rangle$ following the violent stage of the reaction. The change in the average c.m. momentum is

$$\Delta|\langle \mathbf{P}/A \rangle| = \sqrt{\langle P^X/A \rangle^2 + \langle P^Z/A \rangle^2} - (P/A)_i.$$

The above mentioned quantities, towards the end of the simulations, are shown as a function of the impact parameter at $T_{\rm lab}$ = 800 MeV/nucleon in Fig. 5.4, by open symbols, and as a function of the beam energy at $b = 5$ fm in Fig. 5.5, respectively. The resulting spectator $\langle P^X/A \rangle$ exhibits a clear sensitivity to the stiffness of the EOS. I can see in both figures that a stiffer EOS results in a stronger sidewards push to the spectator. However, even more prominent is the sensitivity to the momentum dependence of the mean field. A strong momentum dependence results in a stronger push to the spectator. Recall that the interplay between the spectator and the participant matter also generates elliptic flow for the participant matter and it was possible to exploit the latter in the determination of the mean-field momentum dependence at super-normal densities [12, 53].

The final momentum of the spectator reflects the momentum exchanges with the participant zone throughout the reaction. Initially, the nucleons from the opposing nucleus move nearly exclusively along the beam axis relative to the spectators. As equilibration progresses, the momenta in the participant zone acquire

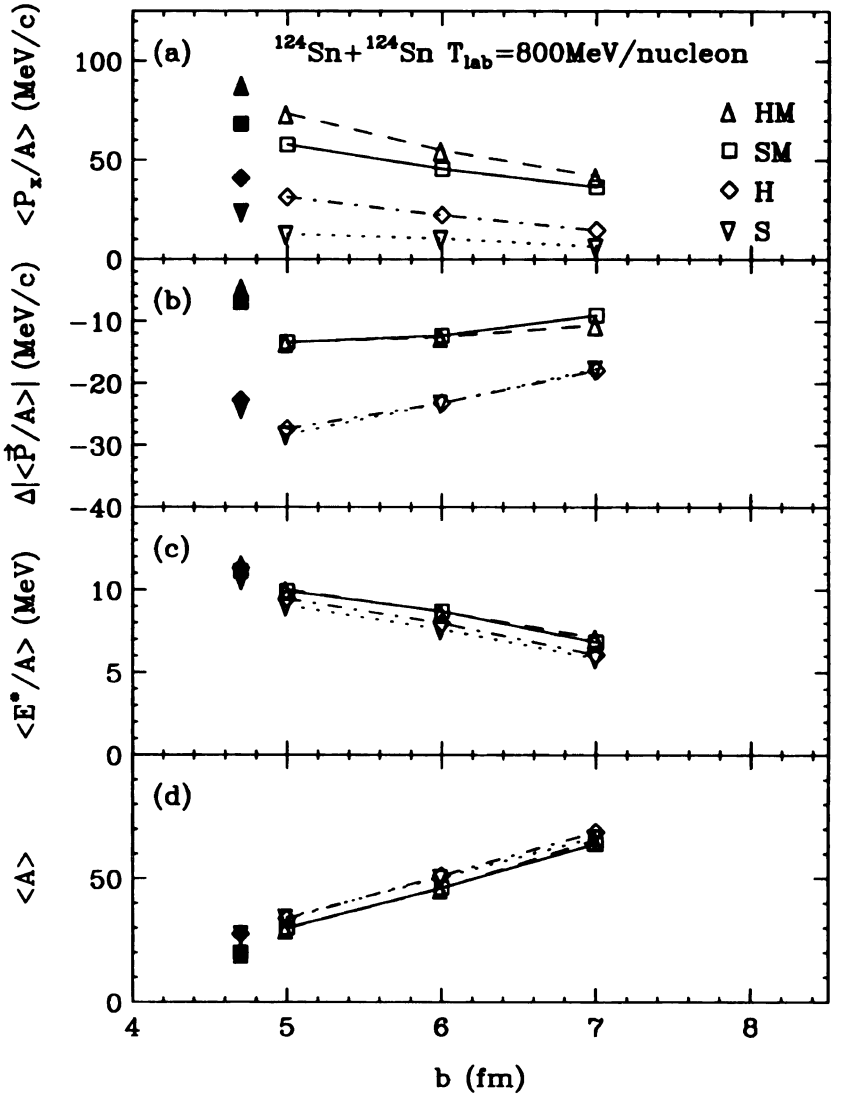

Figure 5.4: Spectator properties in the 800 MeV/nucleon ^{124}Sn + ^{124}Sn collisions, as a function of the impact parameter, for four representative EOS: hard momentum-dependent (HM), soft momentum-dependent (SM), hard momentum-independent (H) and soft momentum-independent (S). Panel (a) shows the average in-plane transverse momentum of the spectator per nucleon $\langle P^X/A \rangle$. Panel (b) shows the change in the average net c.m. momentum per nucleon $\Delta|\langle \mathbf{P}/A \rangle|$. Panel (c) shows the average excitation energy per nucleon $\langle E^*/A \rangle$, and, finally, panel (d) shows the average spectator mass $\langle A \rangle$. Open symbols represent results obtained with reduced in-medium nucleon-nucleon cross sections; filled symbols represent results obtained at $b = 5$ fm with free cross sections.

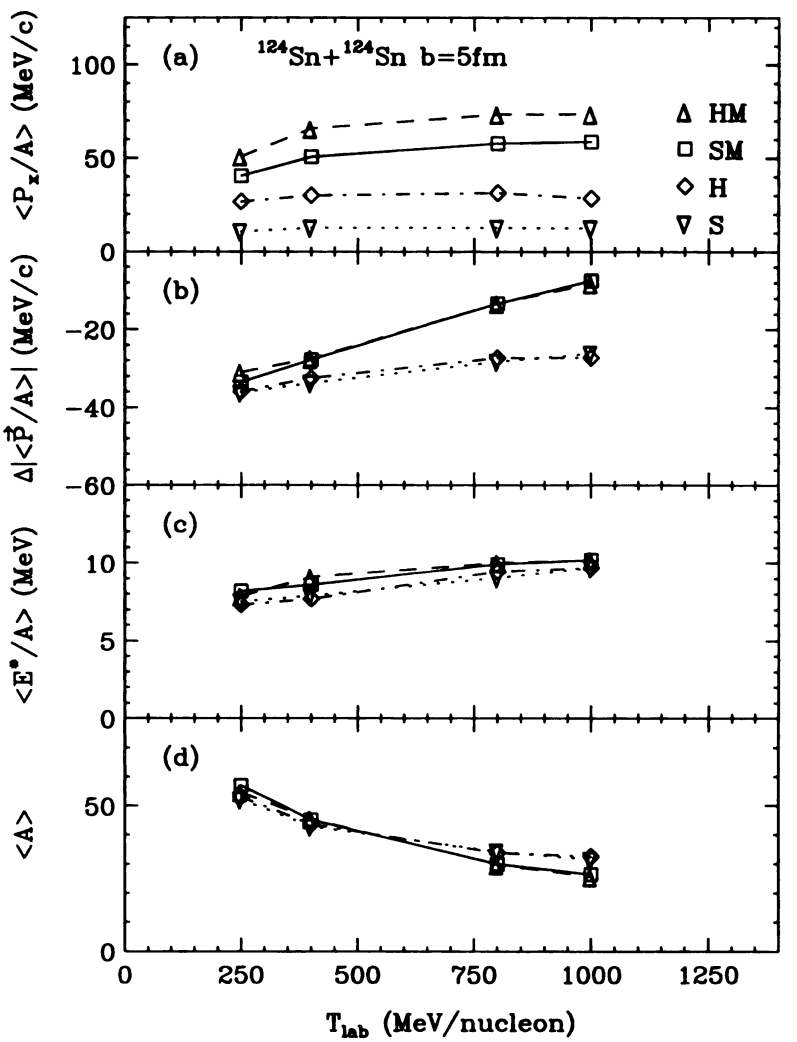

Figure 5.5: Spectator properties in the ^{124}Sn + ^{124}Sn collisions at b = 5 fm, as a function of the beam energy, for four representative EOS: hard momentum-dependent (HM), soft momentum-dependent (SM), hard momentum-independent (H) and soft momentum-independent (S). Panel (a) shows the average in-plane transverse momentum of the spectator per nucleon $\langle P^X/A\rangle$. Panel (b) shows the change in the average net c.m. momentum per nucleon $\Delta|\langle \mathbf{P}/A\rangle|$. Panel (c) shows the average excitation energy per nucleon $\langle E^*/A\rangle$. Finally, panel (d) shows the average spectator mass $\langle A\rangle$.

a level of randomness. Random exchanges of momentum between spectators and participants generally drive the spectator momentum towards the average for the system, i.e. zero. However, the participant nucleons reach the spectators moving away from the system center, coming with momentum directed on the average outward, delivering an outward push to the spectator pieces.

The order of magnitude for the transverse push may be obtained from a simple estimate. Thus, in Sn + Sn at 800 MeV/nucleon, estimating the pressure in the compressed region from the nonrelativistic ideal-gas estimate,

$$p \simeq \rho \frac{2}{3} T_{\rm lab}/4A \tag{5.2}$$

with $\rho \sim 2\,\rho_0 \sim 2/6$ fm^{-3}, I get $p \sim 40$ MeV/fm^3. The size of the high-density region in the X-Z plane for Sn + Sn at medium b is ~ 4 fm. *cf.* Fig. 5.2. The push to the spectator is then of the order of

$$P^x \approx p\,S\,\Delta t\,, \tag{5.3}$$

where S is the transverse area pushed by the participant matter and Δt is the duration of the push. With $S = \pi\,R^2/4 \sim 13$ fm^2 and $\Delta t \sim 5$ fm/c, cf. Figs. 5.2 and 5.3, I get

$$\frac{P^x}{A} = \frac{40\,\mathrm{MeV/fm^3} \times 13\,\mathrm{fm^2} \times 5\,\mathrm{fm/c}}{50} \simeq 50\,\frac{\mathrm{MeV}}{\mathrm{c}}\,, \tag{5.4}$$

This is within the general order of magnitude as found in the simulations. When the impact parameter increases, the fireball pressure decreases while the spectator mass increases. Thus, the momentum per nucleon decreases. With regard to the beam energy variation in the simulations, at low energies the pressure in the fireball region drops, resulting in smaller push to the spectators, with some compensation coming from a longer time for the spectators in the reaction zone and a longer fireball

lifetime. With the rise in the beam energy from the low energy end, the rise in the transverse fireball pressure is moderated by pion production and an increasing transparency. The spectator time in the vicinity of the explosion continuously drops resulting in a level of saturation in the spectator momentum per nucleon.

With regard to the changes in the magnitude of the c.m. momentum per nucleon $\Delta|\langle \mathbf{P}/A \rangle|$, one can see in Figs. 5.4 and 5.5 that the results for MD MFs significantly differ from the results for MI MFs for Sn + Sn, with the later MFs giving more momentum loss. The spectator mass and excitation energy, in contrast to the momentum, are rather insensitive to the MF in the present system.

While the results discussed until now have been obtained with reduced in-medium nucleon-nucleon cross sections [12], I also carried out calculations with free nucleon-nucleon cross sections. The latter calculations for the same system at $T_{\rm lab}$ = 800 MeV/nucleon b = 5 fm, are represented by filled symbol in Fig. 5.4. With free cross sections, the remnant masses are a bit lower, the excitation energies are higher, and so is the transverse push. The transverse push is more sensitive to the change in the EOS, than to the change in cross section, as evident in the figure. Contrary to what one might naively expect, less momentum per nucleon is lost in the free cross section case. I will come back to the last issue later.

In investigating the differences in results for the different EOS, I obviously looked at the details in the time development of the systems for the different EOS. Figure 5.6 shows the central participant density as a function of time. For the hard momentum-independent EOS a maximal density is reached earlier and the expansion sets faster than for the soft momentum-independent EOS. The S EOS allows for a higher compression than the H EOS. An MD EOS allows for a lower compression than a corresponding MI EOS. Moreover, the expansion develops earlier for an MD EOS than a corresponding MI EOS. Evidently, the momentum dependence plays a similar role to the stiffness of nuclear matter; it renders the

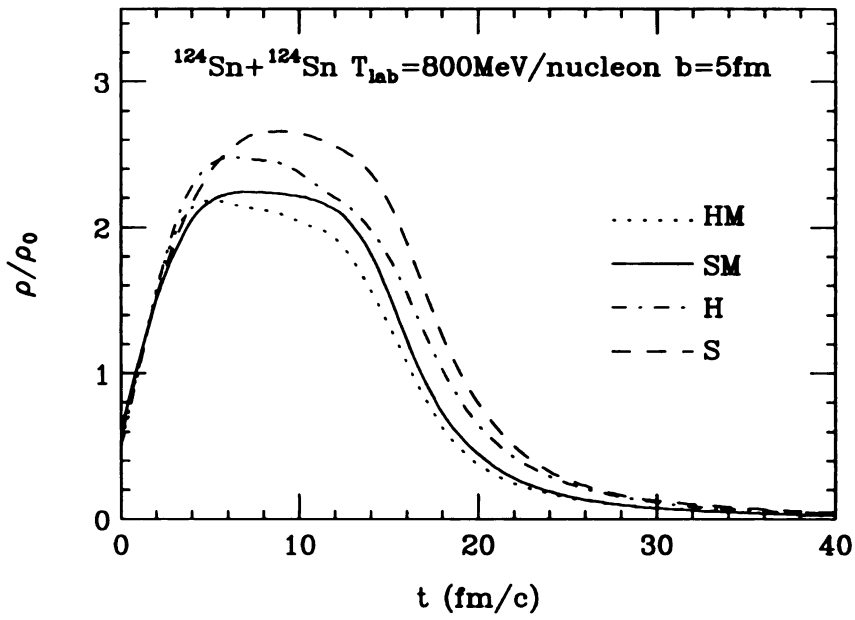

Figure 5.6: Baryon density as a function of time at the center of the ^{124}Sn + ^{124}Sn system at $T_{\rm lab}$ = 800 MeV/nucleon and b = 5 fm, for different MFs.

matter less compressible in a dynamic situation.

Figure 5.7 shows the spectator transverse momentum in the X-direction as a function of time. As I have already pointed out before, the spectator transverse momentum per nucleon rises within a relatively short time interval. The rise starts about the time when the maximal density is reached at the participant center; the rise stops due to combined effects of the spectator passing by and of the dilution of the participant zone. While there are up to 2 fm/c differences in the start and end of the rise interval in Fig. 5.7, it is apparent that the differences in the final $\langle P^X/A \rangle$ must be due to the differences in magnitude of the transverse pressure (transverse momentum flow) for the different EOS and not in the duration of the rise. In fact, the slopes of the dependence of transverse momentum on time differ considerably more than do the final transverse momenta. A faster dilution for the more incompressible EOS shuts off the momentum rise sooner than for the more

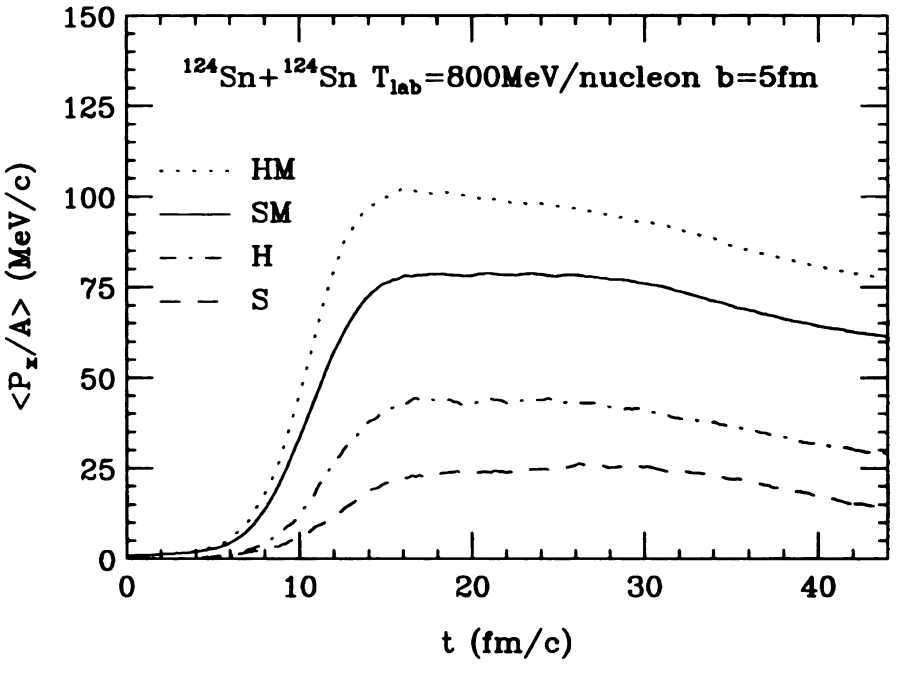

Figure 5.7: Average in-plane transverse momentum per nucleon of a spectator in b = 5 fm ^{124}Sn + ^{124}Sn collisions at T_{lab} = 800 MeV/nucleon, as a function of time, for different EOS.

compressible EOS and moderates the differences in the final spectator momenta. Figure 5.8 shows differences in the Landau effective mass, $m^* = p/v$, in cold nuclear matter at different densities for MI and MD MFs. Lower masses for the MD MF means that particles move out faster at the same momenta.

The change in the magnitude of the c.m. momentum per nucleon $\Delta|\langle \mathbf{P}/A \rangle|$ is generally dominated by the change in the longitudinal momentum per nucleon. In Figs. 5.4 and 5.5 the net momentum per nucleon is seen to decrease in the Sn + Sn reactions under all conditions. That change in the momentum might be considered a measure of the friction involved in the interaction of the spectator with the participant zone. The friction is due to mentioned random changes of momenta in collisions between participants and spectators that, besides knocking particles off spectators, over time drive the average momentum towards the system average of zero. When examining the net spectator momentum per nucleon as a function of

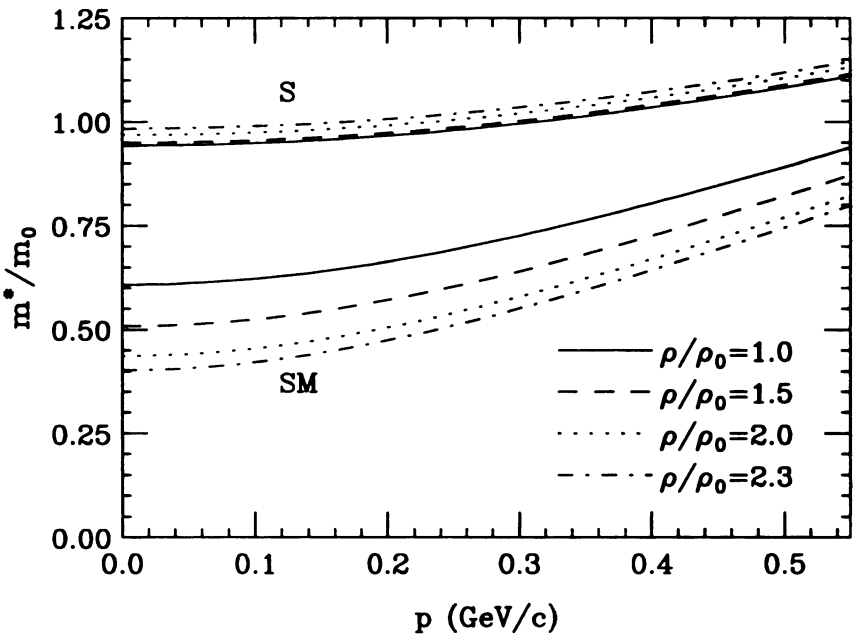

Figure 5.8: Landau effective mass $m^* = p/v$, in units of free nucleon mass, as a function of momentum at several densities in cold nuclear matter for S and SM MFs.

time in the Sn + Sn reactions, the momentum is first found to decrease but then found to recover somewhat. The late increase and part of the early momentum decrease could partly be attributed to our inability to cleanly separate the spectators from the participants, which intermittedly intermixed and then separate. The above view on the net spectator momentum, however, needs to be revised once the changes in the momentum are examined in the Au + Au system. The change in the net momentum per nucleon is shown for a 1 GeV/nucleon reaction as a function of the impact parameter in Fig. 5.9, by open symbols for the in-medium reduced cross section. For low impact parameters and MD MFs, the average spectator momentum per nucleon increases in the reaction simulations!

The mass and the excitation energy of the spectator in Figs. 5.4 and 5.5 do not exhibit a sensitivity to the EOS likely because they are determined by the geometry and the capability of matter to retain the energy, respectively. As to the momentum

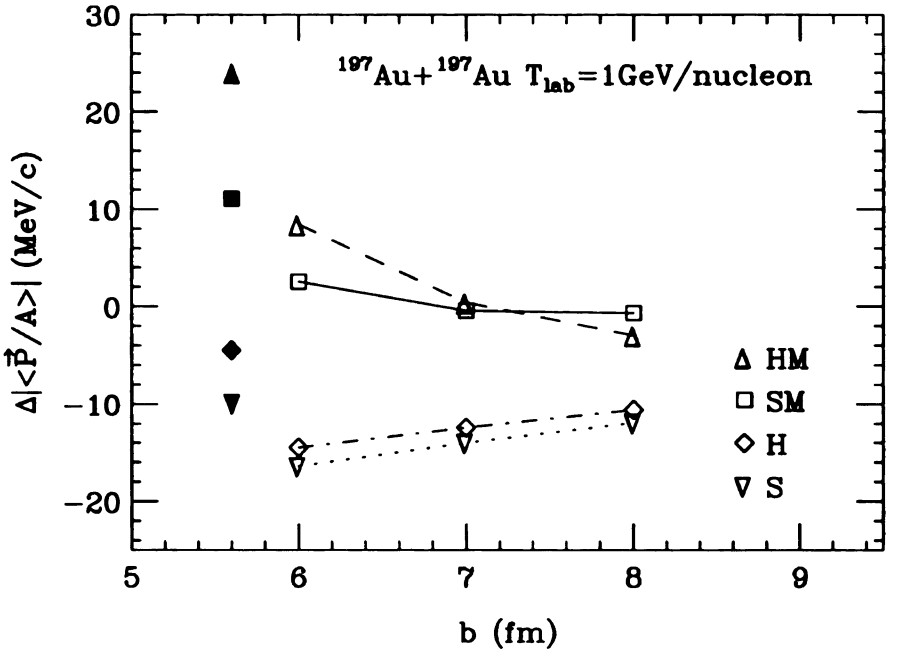

Figure 5.9: The change in the net average c.m. momentum per nucleon $\Delta|\langle \mathbf{P}/A \rangle|$ of spectators in the ^{197}Au + ^{197}Au system at T_{lab} = 1 GeV/nucleon. Open symbols represents results obtained with reduced in-medium nucleon-nucleon cross sections; filled symbols represent results obtained at b = 6 fm with free cross sections. A negative value of $\Delta|\langle \mathbf{P}/A \rangle|$ indicates a spectator deceleration, while a positive value indicates a net acceleration.

changes, though, I have demonstrated that they can provide information on the violent stage of energetic reactions and constrain the properties of high density nuclear matter.

5.1.4 Spectator Acceleration

The acceleration of the spectator during a heavy-ion reaction, is of interest on its own. After all, if we shoot a bullet through a wall, we expect the bullet to slow down, not accelerate. The systematics of the spectator velocity after a heavy-ion reaction has been studied before and the velocity decrease of the spectator piece was found to be proportional to the decrease of the spectator mass in the peripheral collisions (often known as the Morrissey systematics [162]). Such deceleration of the

spectator could be attributed to the friction between the spectator and the participant matter. However, the simulation results shown in Fig. 5.9 point to an acceleration of the spectator in a heavy-mass system at low impact parameter. The unusual prediction of the simulation has been confirmed by recent experiment [152]. Below, I will give a qualitative explanation for the spectator acceleration.

The speeding up of the spectator at low b in Au + Au may be understood in terms of the explosion of the participant zone. On one hand, the spectator acquires transverse momentum. On the other, in the longitudinal direction the explosion acts more on the rear of the spectator piece than on the front. If the explosion is strong enough, the ordered push may overcome the friction effects, producing a net longitudinal acceleration for the spectator. There is no issue of energy conservation since the work is done by the participant on the spectator zone. The difference between Sn + Sn and Au + Au is in the equilibration time scale relative to the duration of the fireball. Differences in the net final momentum per nucleon between different MFs for both systems, with significantly higher net momenta for the MD than MI MFs, may be understood in terms of the violence of the explosion that accelerates the spectator.

An important aspect of the spectator momentum per nucleon, underscoring the interpretation above, is its dependence on the nucleon-nucleon cross section. In Fig. 5.9, the results of $b = 6$ fm Au+Au simulation with the free cross sections are represented by filled symbols. With the larger free cross sections, the spectator remnants emerge even faster from the reaction than the with the lower cross sections! This is because for higher cross sections, the equilibration is faster, which allows the participant to explode more violently when the spectators are still nearby. Quantitatively, in the $b = 6$ fm HM free cross-section case, the gain in the longitudinal momentum per nucleon contributes as much as 17 out of 24 MeV/c of the gain in the net spectator momentum per nucleon in Fig. 5.9. In the $b = 6$ fm

HM reduced cross-section case, the longitudinal gain contributes about 4 out of 8 MeV/c of the net momentum gain per nucleon.

5.1.5 Summary

Within semiclassical transport simulations of energetic semicentral collisions of heavy ions, I have carried out an investigation of the interplay between the participant and spectator regions. The spectators pass by the participant region when the participant matter undergoes a violent explosion. On one hand, the spectators block the expansion of the participant matter in the in-plane direction, producing elliptic flow for the participant matter. On the other hand, the explosion pushes the spectators giving them transverse momentum pointed away from the reaction zone. The momentum transfer to the spectators and the shadow left in the pattern of the participant emission depend on the speed of the explosion. The speed, in turn, depends on the EOS of the dense matter. Due to their nature, the spectators represent a perfectly timed probe right at the reaction site. A careful analysis of in-plane transverse momentum of a spectator may yield information on the EOS comparable to that provided by elliptic flow analysis. An analysis of the longitudinal momentum transfer may yield information on the momentum dependence of the MFs in the reactions. The signatures in the spectator momenta per nucleon rise with the lowering of the impact parameter, but at the cost of the lowering of a spectator mass, reducing the chances of identifying the spectator remnants. Significantly, for most repulsive MFs and small impact parameters in a heavy system, spectators may emerge from the reaction with a higher net average momentum per nucleon than the original momentum.

5.2 Isospin Diffusion Process in HIC

In this section, I will discuss isospin diffusion process in an isospin asymmetric reaction system. Elementary discussion of isospin diffusion process in realistic heavy-ion reaction system is provided in subsection 5.2.1. The nuclear equation of state based on isospin dependent mean fields (IEOS) and the isospin diffusion coefficient for nuclear matter are discussed in subsection 5.2.2. The results from the isospin diffusion simulation in a peripheral reaction, including the time evolutions of the spectator isospin asymmetry, are discussed in subsection 5.2.3. The results from the current simulation are compared with data [100] in subsection 5.2.4. The results and the discussions on isospin diffusion are summarized in subsection 5.2.5

5.2.1 Introduction

Isospin diffusion process, which results from isospin non-equilibration, generates an isospin flow that transports isospin asymmetry from the higher concentration region to the lower concentration region. In the limit of small isospin gradient and close to equilibrium, isospin diffusion process could be described in terms of a transport coefficient (see the discussions in in Chapter 4 "Nuclear Isospin Diffusivity"). The isospin diffusion coefficient is related to the n-p cross sections σ_{np} and to the isospin dependence of the nuclear equation of state. As seen in Chapter 4, the different IEOS give rise to different isospin diffusion coefficients, and thus different isospin diffusion time scales. The direct relation between isospin diffusion process and IEOS gives us possibilities to test the different IEOS models in heavy-ion reactions.

In reactions of isospin-asymmetric reaction systems, isospin diffusion process is controlled by two competing time scales: the isospin diffusion time scale and the reaction time scale. At lower energies, the reaction time scale is much longer than

the characteristic isospin diffusion time scale, and the isospin gets close to equilibration in the reaction system. At higher energies, the reaction time scale is much shorter than the isospin diffusion time scale, thus, the projectile-like region and the target-like region will show memories of the initial system. Such a transition, from proximity to isospin equilibration at lower energies to nonequilibrium at higher energies, has been demonstrated in certain reaction systems by Johnston *et al.* [98, 163]. The isospin non-equilibrium after a heavy-ion reaction is important for the measurement of isospin diffusion process. A complete isospin equilibration would erase the asymmetry in the initial reaction system and make the isospin related observables insensitive to the diffusion process. The isospin nonequilibrium has been first used to measure nuclear stopping power by Rami *et al.* [99].

However, isospin diffusion process is complicated by other processes that affect the isospin content of the reaction system, such as, the fast particle emission process, the possible liquid-gas phase transition and the cluster formation process. Impact of the fast particle emission process will depend on the excitation and isospin content of the emitting source; the effects of the liquid-gas phase transition and the cluster formation process have already been discussed in Chapter 2, on a phenomenological basis. Here I will introduce an isospin diffusion ratio that suppresses effects of the non-diffusion processes, by taking the difference between signals from the non-symmetric and symmetric reaction systems.

5.2.2 IEOS and Isospin Diffusion

In general, isospin diffusion process will be affected by the isospin-dependence of the nucleon-nucleon interaction. Isospin dependence of elementary nucleon-nucleon interaction gives rise to different optical potential for protons and neutrons in the mean field description and to different interparticle cross sections, affecting the

motion of the protons and neutrons, and enhancing or suppressing the isospin transport process in the nuclear medium. In the limit of small isospin concentration gradient and close to equilibrium, isospin diffusion process may be characterized by an isospin diffusion coefficient which probes, in particular, the isospin dependence of the nuclear EOS (see the discussions on isospin diffusion process in Chapter 4).

While assuming the applicability of the Boltzmann equations, the isospin diffusion coefficient for nuclear matter has already been derived in Chapter 4. The different parameterizations of the isospin dependence for the nuclear EOS have been shown, in particular, to give rise to different isospin diffusion coefficients. In the low temperature limit, the isospin diffusion coefficient is proportional to the symmetry energy of nuclear matter.

In this section, I will explore four specific parameterizations of the isospin dependence of the nuclear EOS and the isospin diffusion coefficients for nuclear matter with those IEOS. For the use in later discussions, I will first produce an estimate of the relevant temperature and density in the participant matter during the violent stage for the peripheral reactions to be investigated. Afterwards, I will discuss the characteristics of the four IEOS and of the corresponding isospin diffusion coefficients for the relevant physical region.

I will specifically focus on the peripheral reactions of ^{112,124}Sn+^{112,124}Sn at the beam energy of $E_{lab}/A = 50$ MeV. The central temperature in a fully thermalized Fermi gas is estimated as $T = \sqrt{E_{lab}/(2\,A\,a)} \sim 14$ MeV, using $a \approx A/(8\text{ MeV})$. Taking into account the incomplete dissipation of kinetic energy in the participant region and possible collective motion and effects of reduced statistics, the average thermal temperature is estimated to be half of the peak value, $T_{ave} \sim 7$ MeV. The maximum density at the center of a peripheral collision at such beam energy is around normal density, but since the compression stage is usually shorter than the expansion stage for the participant region and also the spectators partially slide

over the participant matter, the average density in the participant region during the violent reaction stage is below normal density $\rho_{ave} \sim 0.7\rho_0$.

In BUU simulations, I will use four IEOS as discussed in section 3.5.2, but with slightly different value for the constants.

$$e_{sym}^{int} = \begin{cases} 14\xi^2, & \text{iso-SH;} \\ 14\xi, & \text{iso-NH;} \\ 14\xi^{1/3}, & \text{iso-NS;} \\ 38.5\xi - 21.0\xi^2, & \text{iso-SKM.} \end{cases} \tag{5.5}$$

where the reduced density is defined with $\xi = \rho/\rho_0$ and where $\rho_0 = 0.16$ fm^{-3} is the normal density of nuclear matter. The three power law types of the IEOS (iso-SH, iso-NH, and iso-NS) have the same symmetry energy at normal density; while the iso-SKM type, which was suggested by Colonna [101], has a larger symmetry energy at the normal density. The symmetry energies for the four different IEOS have very different behavior as a function of density as shown by Fig. 5.10. Following the convention introduced in section 3.5, the iso-SH and iso-NH types belong to the iso-stiff type of IEOS, while the iso-NS and iso-SKM belong to the iso-soft type. At subnormal densities of $\rho/\rho_0 \sim 0.7$, the iso-SKM has the largest value for the symmetry energy, while the iso-SH has the smallest value of the four IEOS.

The different density dependencies of the symmetry energy in Fig. 5.10 are expected to give rise to different paces for isospin diffusion process, following the considerations in Chapter 4. The left panel of Fig. 5.11 shows the isospin diffusion coefficients for nuclear matter at temperature $T = 7$ MeV, with the different lines there corresponding to five different assumptions on the IEOS: the four IEOS in Eq. (5.5) and the free Fermi-gas EOS. The different IEOS, as seen in Fig. 5.11, give rise to different isospin diffusion coefficients as a function of density. In the regions of our interest, at densities around $\rho \sim 0.7\rho_0$, the iso-stiff type of IEOS (iso-SH and

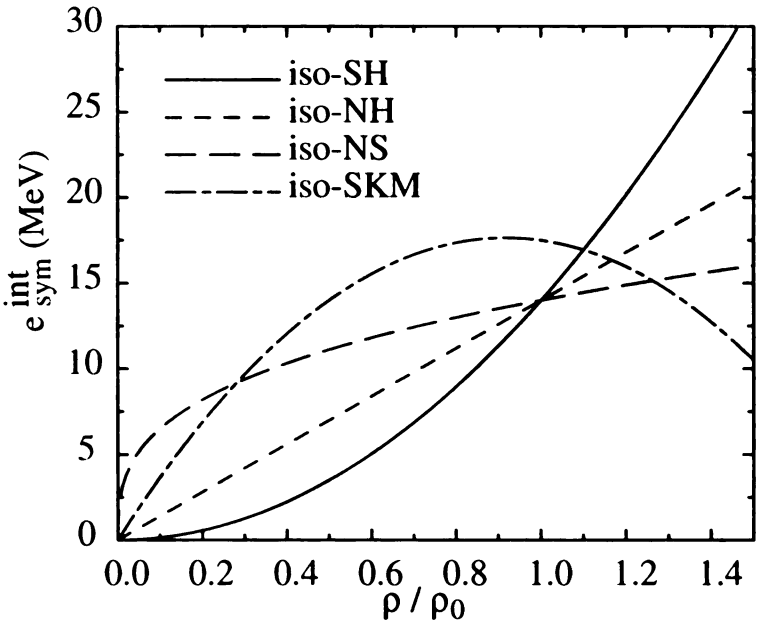

Figure 5.10: The interaction part of the symmetry energy as a function of density for four different IEOS: iso-SH, iso-NH, iso-NS and iso-SKM. The interaction symmetry energy for the first three of the IEOS yields, by construction, the same symmetry energy at the normal density, while the iso-SKM yields a different value.

iso-NH) yields less diffusion as compared to the iso-soft type IEOS (iso-NS and iso-SKM). The softest type (iso-SKM) of the four IEOS gives rise to the highest isospin diffusion coefficient at moderately subnormal densities. The ordering of the isospin diffusion coefficients for different IEOS is seen to be the same as the ordering of the symmetry energy, *cf.* Figs. 5.10 and 5.11. Such correspondence is a result of the proportionality between symmetry energy and the isospin diffusion coefficient at low temperatures (see the discussion on the low temperature limit of isospin diffusion coefficients in Chapter 4). To exhibit the effects of isospin dependence of the MFs, we may normalize the coefficients to the one without such dependence, *i.e.*, the coefficient for the free Fermi gas. The diffusion-coefficient ratio is plotted in the right panel of Fig. 5.11, which now emphasizes the relative difference in results for the different IEOS. In the next subsection, I will explore the relative strength of

the diffusion in actual simulations with different IEOS.

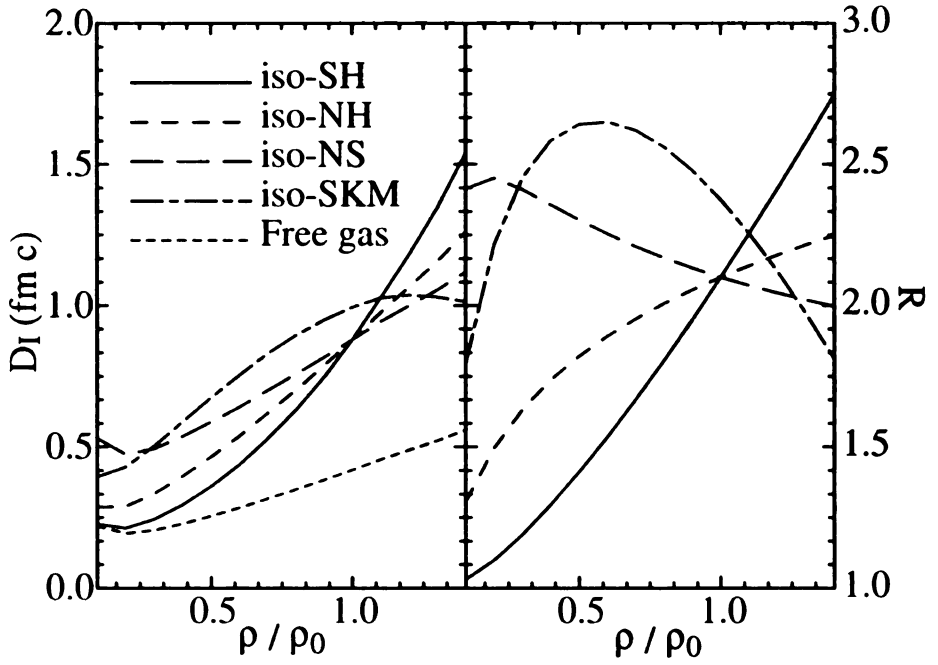

Figure 5.11: In the left panel, the isospin diffusion coefficients for nuclear matter for MFs with four different dependence on isospin and also without such dependence, plotted as a function of density; in the right panel, the isospin diffusion coefficients are normalized to that obtained with no isospin dependence in the MF. The temperature of nuclear matter is set at $T = 7$ MeV.

5.2.3 Isospin Diffusion in Reaction Simulations

The BUU simulations have been carried out for four different reaction systems: ^{124}Sn+^{124}Sn, ^{124}Sn+^{112}Sn, ^{112}Sn +^{124} Sn and ^{112}Sn+^{112}Sn, at the beam energy of $E_{lab}/A = 50$ MeV, and a peripheral impact parameter of $b = 6.5$ fm. I will analyze the isospin asymmetry of projectile-like spectators that, because of peripherity, largely keeps their original identity. The two projectile-target symmetric reaction systems, ^{124}Sn+^{124}Sn and ^{112}Sn+^{112}Sn, are the most and least neutron-rich systems. These serve as the references for the projectile-target asymmetric reaction systems, ^{124}Sn+^{112}Sn and ^{112}Sn+^{124}Sn, where isospin diffusion between the projectile and target regions takes place. The projectile-like (^{124}Sn like) spectator in the

^{124}Sn+^{112}Sn system will have about the same excitation as that in the ^{124}Sn+^{124}Sn reaction system. Since the fast particle emission process is most related to the excitation and the isospin asymmetry of the source, to the lowest order one can assume that the changes of projectile isospin asymmetry due to fast particle emission in the two systems are the same. Similar ideas apply to the other two systems with ^{112}Sn projectile.

The simulation utilized the MI IEOS as discussed in section 3.5.2, and the specific parameters for the IEOS in this simulation are already given in section 5.2.2. The isospin independent mean field is expected to have little impact on isospin diffusion process, and a soft EOS has been utilized for all the simulations. Geometrically reduced in-medium cross sections, that were shown to yield reasonable description of the stopping in the heavy-ion reactions, has been used in my simulations. In the simulations, the projectile-like spectator region was selected according to the phase space selection criteria, with employed velocity gate of higher than half of the beam velocity in the center of mass frame and a low density cut-off of $0.05\rho_0$. Such selection was shown to give reasonable description of the spectator matter during and after the violent reaction stage [161].

The isospin asymmetry of the projectile-like spectator region is plotted as a function of time in Fig. 5.12, for the peripheral reactions of ^{124,112}Sn+^{124,112}Sn. The collision systems were followed till asymptotic large time of t = 150 fm/c, where the two spectator remanent pieces from the reaction were well separated and their properties are quite stabilized.

The isospin asymmetry of the projectile-like spectator exhibits clear systematics. The projectile-like spectator isospin asymmetry in the most neutron rich system ^{124}Sn+^{124}Sn is decreasing with time and is consistently higher than in any other reaction systems throughout the reaction. In the least neutron rich system ^{112}Sn+^{112}Sn, the asymmetry changes slower than in any other system and is

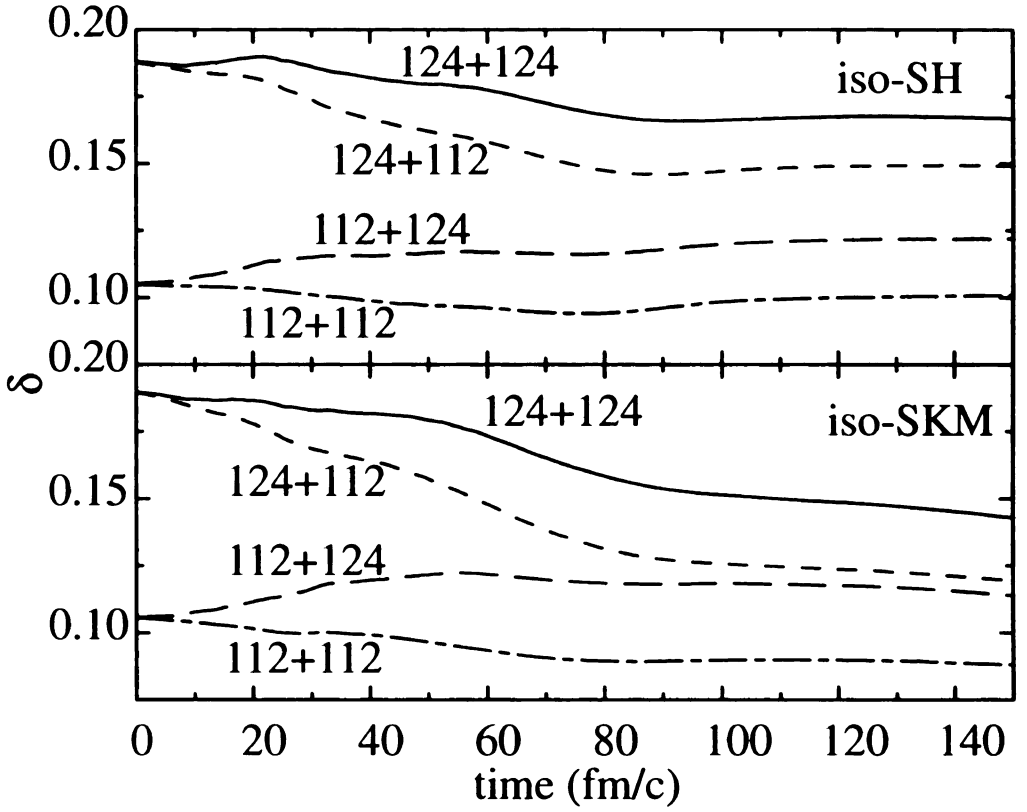

Figure 5.12: Isospin asymmetry of the projectile-like spectator region is plotted as a function of time, for four different reactions systems of ^{124}Sn+^{124}Sn, ^{124}Sn+^{112}Sn, ^{112}Sn+^{124}Sn and ^{112}Sn+^{112}Sn at beam energy E_{lab} = 50 MeV/nucleon and impact parameter b = 6.5 fm. The top panel is from a simulation with a stiff symmetry energy density dependence (iso-SH) and the lower panel is from a simulation with a soft symmetry energy density dependence (iso-SKM).

consistently lower than any other reaction system. The change of isospin asymmetry in the projectile-target symmetric reaction systems is characteristic of the fast particle emission process, where the projectile-like spectator is excited by the impact of the target and begins to emit protons and neutron. The projectile-like spectator in the mixed system ^{124}Sn +^{112}Sn changes differently from that in the symmetric system ^{124}Sn+^{124}Sn, reflecting the effect of the different target. The main difference is attributed to the extra isospin diffusion process that transports the isospin asymmetry between the projectile-like and target-like regions in the

system ^{124}Sn+^{112}Sn. The diffusion process also differentiates the other two systems ^{112}Sn+^{124}Sn and ^{112}Sn+^{112}Sn.

The two mixed systems, ^{124}Sn+^{112}Sn and ^{112}Sn+^{124}Sn, differ just in the interchange of the projectile and target. The projectile remnant in one system corresponds to the target remnant in another system. The isospin asymmetry for the projectile remnant in the ^{124}Sn+^{112}Sn decreases over time, while the opposite happens to in the counterpart system. Such behavior for the mixed system specifically expected for the process of isospin diffusion, which acts to transport the isospin asymmetry between the two spectator regions. Isospin diffusion process, if allowed to proceed forever, would eventually make the projectile-like and target-like regions to reach the same in isospin asymmetry. As the time evolution in Fig. 5.12 suggests, the scenario of a complete isospin equilibration between the two spectators was not achieved in any of the mixed systems.

By comparing the top and lower panels of Fig. 5.12, I find that isospin diffusion process is affected by isospin dependence of the nuclear equation of state. The top panel shows the simulation result assuming a stiff isospin density dependence (iso-SH) for the mean field interaction, and the lower panel shows that assuming a soft isospin density dependence (iso-SKM). The two projectile-target symmetric systems, ^{124}Sn +^{124}Sn and ^{112}Sn+^{112}Sn, exhibit differences in time evolution of asymmetry and in the asymptotic value for the asymmetry in the top and lower panel. A more significant difference, connected to isospin diffusion process in the reactions, is the separation between the mixed systems in the two panels. While in the case of iso-SH EOS, the line for the projectile-like spectator (^{124}Sn-like) in the ^{124}Sn+^{112}Sn system, is always well separated from that for the ^{112}Sn-like spectator in system ^{112}Sn+^{124}Sn. In the case of iso-SKM EOS, the separation between the lines for the two mixed system is small, signifying an increased isospin diffusion process. The different isospin diffusion process in the two simulations is anticipated

from my earlier argument on the relations between the IEOS and isospin diffusion process (Section 5.2.2).

Drawing conclusions on isospin diffusion by comparing directly the asymptotic isospin asymmetry values in the simulations is difficult because the fast particle emission process is also affected by the IEOS. To emphasize the change of isospin in the projectile-target asymmetric systems as compared to the symmetric systems, however, one may define an isospin diffusion ratio similar as that employed by Rami *et al.* [99]:

$$R_i = \frac{(2\delta_i - \delta_{^{124}\mathrm{Sn}+^{124}\mathrm{Sn}} - \delta_{^{112}\mathrm{Sn}+^{112}\mathrm{Sn}})}{(\delta_{^{124}\mathrm{Sn}+^{124}\mathrm{Sn}} - \delta_{^{112}\mathrm{Sn}+^{112}\mathrm{Sn}})}, \tag{5.6}$$

where the $\delta_{^{124}\mathrm{Sn}+^{124}\mathrm{Sn}}$ and $\delta_{^{112}\mathrm{Sn}+^{112}\mathrm{Sn}}$ are the isospin asymmetry of the projectile-like spectator region for the symmetric reaction systems(^{124}Sn+^{124}Sn and ^{112}Sn+^{112}Sn), and they set the relative scale of the isospin changes in the reactions. By definition, the ratio is $R_i = 1$ for the most neutron rich system ^{124}Sn+^{124}Sn, and $R_i = -1$ for the least neutron rich system ^{112}Sn+^{112}Sn throughout the reaction. If the spectator isospin were at any time completely equilibrated between the collision partners during the reaction, the ratios of the two asymmetric system would be $R_i = 0$.

In Fig. 5.13, the isospin diffusion ratio R_i is plotted as a function of time for the two mixed systems. The center lines and the shaded regions are the average values and the statistical uncertainties estimated from multiple runs of simulations [164]. As before, the top and lower panel are for the cases of iso-SH and iso-SKM respectively; the upper and lower lines in each panel are for the projectile-like spectators in the ^{124}Sn+^{112}Sn and ^{112}Sn+^{124}Sn systems respectively.

The isospin diffusion ratios for the mixed systems start from $R_i = \pm 1$, and gradually decrease in magnitude. The asymptotic values are reached at around 100 fm/c, which is comparable to the spectator separation time scale of $60 \sim 80$ fm/c. After 100 fm/c, the ratios R_i do not change much, indicating a stability of the ratio with respect to further particle evaporation process.

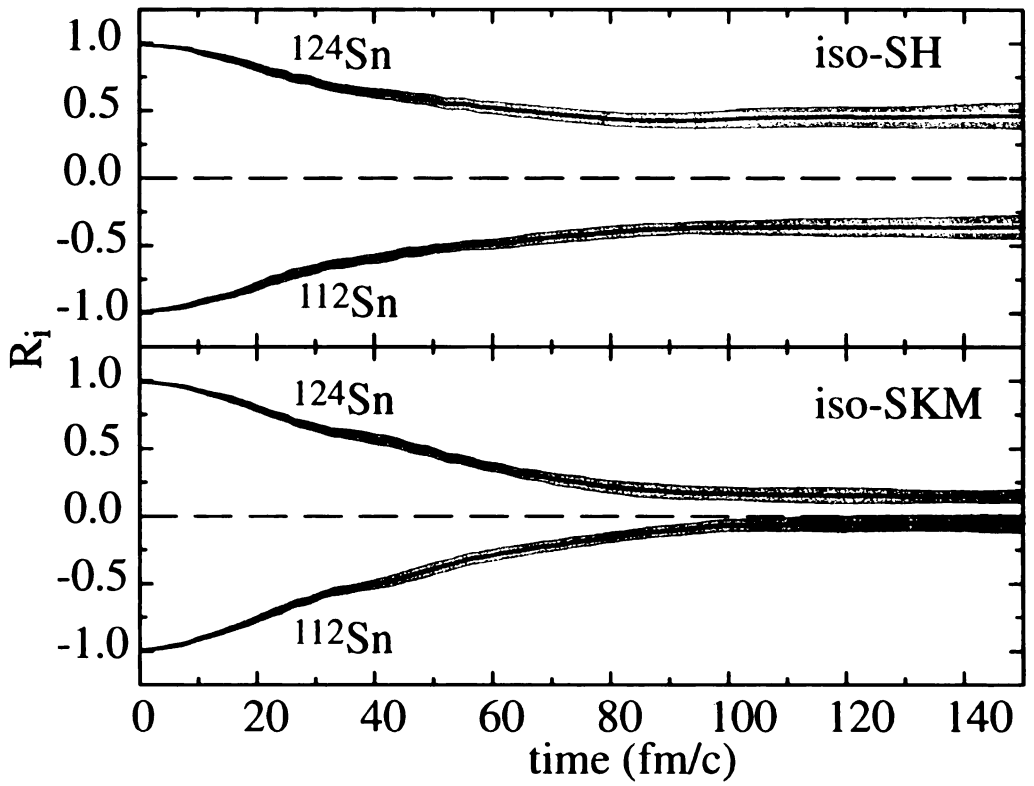

Figure 5.13: The isospin diffusion ratio as defined by Eq. (5.6) is plotted as a function of time for two IEOS. The top panel is for the most stiff symmetry energy density dependence (iso-SH), and the lower panel is for the most soft symmetry energy density dependence (iso-SKM). Note the stability of the ratio after 100 fm/c. The shaded areas around the lines indicate the statistical error from averaging over multiple simulations.

The isospin diffusion ratios in the simulations with different IEOS could be directly compared to yield information about isospin diffusion process, because effects of the fast particle emission are largely cancelled out in the ratios. In the iso-SH case, the large magnitudes for the ratios R_i, and the larger difference between the ratios at a given time for the ^{124}Sn+^{112}Sn and ^{112}Sn+^{124}Sn systems, are reflections of the less isospin diffusion between the projectile-like and the target-like spectators. On the other hand, the results for the iso-SKM case just indicate a more complete isospin diffusion within the mixed system. The degree of completeness for isospin diffusion process, is now simplified to the ratio R_i, and the effect of the

different IEOS in the simulation is more transparent in Fig. 5.13 than in Fig. 5.12. As will be shown in the next section, the isospin diffusion ratio R_i may also be compared to experimental data, and such a comparison can yield information on isospin dependence of the nuclear EOS [100].

5.2.4 Comparison to Data

In this section, I will compare the ratios R_i obtained from the experiment and the simulations, and show that the experimental result favors the iso-SH type of IEOS. I will also discuss the difficulties in comparing the simulation with the experiment as well as the many factors that could affect the isospin diffusion ratio.

The peripheral collision data from the experiment have been selected by gates in charged particle multiplicity that correspond to a reduced impacted parameter of $b/b_{max} \geq 0.8$ in the sharp cut-off approximation [165, 166], with the efficiency weighted average impact parameter equal to $< b >= 6.5$ fm. The isotope yields at rapidities $y/y_{beam} \geq 0.7$ were used for the projectile-like region isospin analysis. More details of the experiment and data selection can be found in [100].

The isospin diffusion ratios from experiment were extracted for the isoscaling parameter, which describes the change in the yield of an isotope with the change of the isospin content of a reacting system. Specifically, the experimental ratio $R_{21}(N,Z)$ of yields between two systems of similar mass and energy as a function of isotope N and Z, were found to obey a simple scaling relation [104, 167, 168, 103, 48]:

$$R_{21}(N,Z) = Y_2(N,Z)/Y_1(N/Z) = C\exp(\alpha N + \beta Z). \tag{5.7}$$

where α and β are the isoscaling parameters for the two sources, and are related to the free neutron and proton densities in the emitting source. The neutron isoscaling

parameter α is used for the experimental isospin diffusion ratio:

$$R_i = \frac{2\alpha_i - \alpha_{124+124} - \alpha_{112+112}}{\alpha_{124+124} - \alpha_{112+112}}. \tag{5.8}$$

In the Expanding-Emitting-Source model (EES) as well as in the canonical Statistical Multifragmentation Model (SMM), the isoscaling parameter α is roughly linearly related to the isospin asymmetry δ [104]. If I assume either the EES relation or the SMM relation, as derived by Tsang [104], then the isospin diffusion ratio defined by δ (Eq. 5.6) and by α (Eq. 5.8) only differs by less than 4% [100]. From the peripheral collision data of the Sn+Sn systems, the experimental isospin diffusion ratios are found to be $R_i = 0.48 \pm 0.03$ for the system ^{124}Sn+^{112}Sn, $R_i = -0.48 \pm 0.03$ for system ^{112}Sn+^{124}Sn [100].

The experimental result for isospin diffusion ratio R_i together with those from the BUU simulation results are plotted in figure 5.14. The experimental value is almost half way between the lines for no diffusion ($R_i = \pm 1$) and for complete mixing of isospin ($R_i = 0$), which indicates that the isospin diffusion time scale is comparable to the collision time scale.

For the two iso-soft type of IEOS (iso-NS and iso-SKM), the simulation suggests almost complete isospin mixing in the projectile-target asymmetric system, which is just the opposite of the experimental result. Therefore, I could safely conclude that iso-soft type of IEOS induces too much isospin diffusion to explain the experimental result. On the other hand, the iso-stiff type of IEOS (iso-SH or iso-NH) introduces much less isospin diffusion between the two spectators, and are much closer to the experimental result. The iso-SH results match the experimental results especially well, indicating a weak isospin diffusion in the reaction system.

Another interesting feature is that the experimental R_i for the ^{124}Sn+^{112}Sn and ^{112}Sn+^{124}Sn system are of opposite sign but same magnitude, or in another word,

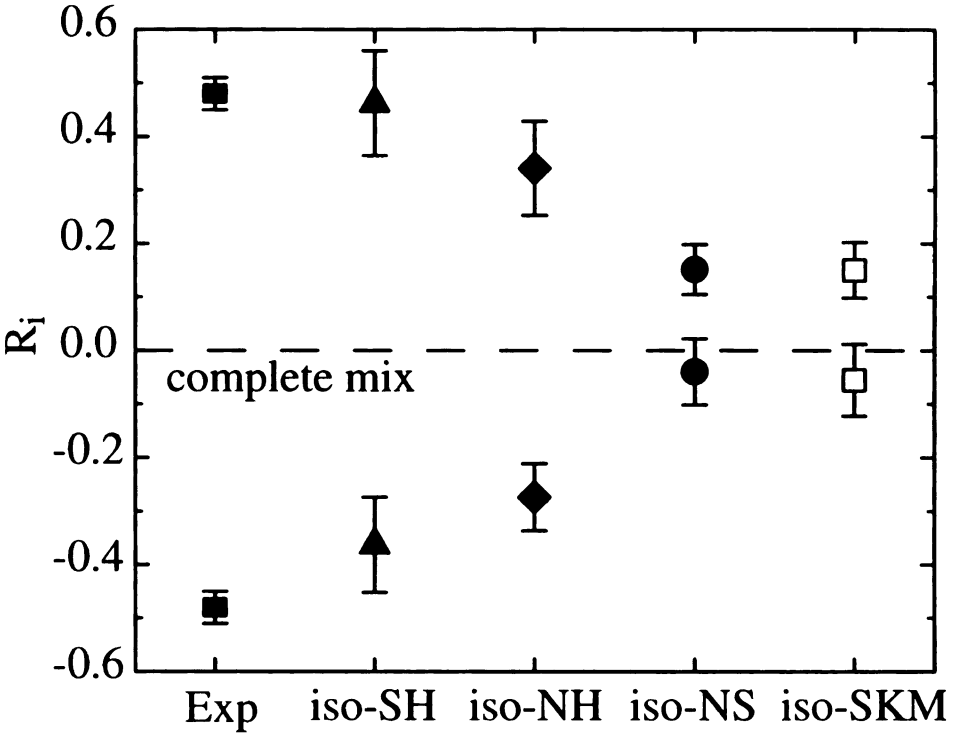

Figure 5.14: The isospin diffusion ratios from the simulations are compared to the experimental extracted isospin diffusion ratios. The symbols above the line $R_i = 0$ are for the projectile-like spectators in the ^{124}Sn+^{112}Sn system, while those below are for the system ^{112}Sn+^{124}Sn. The error bars reflect the uncertainties in the experiment or in the simulations.

they are mirror values against the line at $R_i = 0$. Such symmetry in the experiment, is not seen in the simulations. In the simulation, the pair of R_i for any given IEOS shows deviation from such a symmetry, the average of the pair is always to the positive side of the line $R_i = 0$.

The lack of symmetry in pair of ratios R_i in the simulations, may be attributed to the effect of fast particle emissions. If the system did not emit any fast particles, all isospin removed from the ^{124}Sn-like spectator would go into ^{112}Sn-like spectator, and the pair of isospin diffusion ratios from the two mixed systems should average to near zero. However, the emission of fast particles, of which isospin asymmetry need not be linear in the asymmetry of the emitting source, will affect the isospin asymmetry in the spectators directly. Furthermore, the fast particle emission from

the hot participant region will affect the isospin that flows between the two spectators, and thus affect the spectator isospin indirectly. In the mixed system, a reduced asymmetry emission in the ^{124}Sn-like spectator region, an enhanced asymmetry emission in the ^{112}Sn-like spectator region, and a reduced asymmetry emission in the participant region will all shift the average value for the pair of ratios R_i to the positive side.

On the other hand, if the experimental data for the projectile-like source happen to incorporate some of the fast particles emitted during the early reaction stage, then the resulting R_i pair will reflect more the values of the initial system. Different experimental source selection criteria are needed for a more conclusive argument. The assumption in the comparison that isotope ratios of the projectile-like region reflect the corresponding isospin content after the reaction ($t \geq 80$ fm/c), albeit supported by some correlation analysis [169, 170], may require further testing.

To understand better the effects of the fast particle emission process and isospin diffusion process, one may look in more detail at the simulation results. Table 5.2 shows the average neutron number N, proton number Z, total nucleon number A and total isospin asymmetry δ of the projectile-like spectator at the end of the simulations. The total nucleon number A for the ^{124}Sn-like spectator in the ^{124}Sn+^{112}Sn system is higher than that in the ^{124}Sn+^{124}Sn system, while the total neutron numbers in both system are quite close. The average difference of the spectators in the two system is about two protons, which are transferred from the ^{112}Sn-like spectator to the ^{124}Sn-like spectator. The same result of two proton difference also applies to the ^{112}Sn+^{124}Sn and ^{112}Sn+^{112}Sn systems. For simulations with different IEOS, I find differences in the total N, Z, and A, even for the projectile-target symmetric systems. Those differences demonstrate the complex nature of the fast particle emission process. The isospin asymmetries of the

Table 5.2: The simulation results for the four reaction systems of ^{124}Sn+^{124}Sn, ^{124}Sn+^{112}Sn, ^{112}Sn+^{124}Sn and ^{112}Sn+^{112}Sn, for the four explore IEOS of iso-SH, iso-NH, iso-NS and iso-SKM. The average N, Z, A, δ values for the spectator-like region at the end of the simulation t = 150 fm/c are listed here.

$^{124}Sn + ^{124}Sn$	N	Z	A	δ
iso-SH	56.02	40.01	96.03	0.167
iso-NH	55.61	40.45	96.06	0.158
iso-NS	55.61	40.00	95.60	0.163
iso-SKM	54.18	40.63	94.81	0.143

$^{124}Sn + ^{112}Sn$	N	Z	A	δ
iso-SH	56.30	41.70	98.00	0.149
iso-NH	55.79	42.31	98.10	0.137
iso-NS	56.00	42.57	98.57	0.136
iso-SKM	54.20	42.63	96.83	0.120

$^{112}Sn + ^{124}Sn$	N	Z	A	δ
iso-SH	48.61	38.05	86.67	0.122
iso-NH	48.26	38.06	86.32	0.118
iso-NS	49.35	37.98	87.33	0.130
iso-SKM	47.49	37.77	85.26	0.114

$^{112}Sn + ^{112}Sn$	N	Z	A	δ
iso-SH	48.62	39.71	88.33	0.101
iso-NH	48.72	40.22	88.94	0.096
iso-NS	48.86	40.02	88.89	0.099
iso-SKM	47.99	40.23	88.22	0.088

symmetric systems, which set the scale of the ratio R_i, do not follow a simple relation with the IEOS. Extrapolating from the two symmetric systems, I expect that the mixed system is also affected by the fast particle emission process.

If a free cross section is used in the above simulations, isospin diffusion process in the mixed systems will, in general, be reduced, but the effect is limited. The two type of cross sections are primarily different at low momentum transfer, *i.e.*, at low energies and/or forward scatterings. As we have learned in Chapter 4, the isospin diffusion coefficient is inverse proportional to a weighted cross section σ_{np}, with a

weighting factor of the momentum transfer squared (See Eq. 4.50 in Section 4.4.2). This weighting factor suppresses the differences between the two cross sections. As far as isospin diffusion process is concerned, the simulations with free cross section and with in-medium cross section should not yield significantly different results. However, the use of free cross sections might change the dynamical evolution of the system and the fast particle emissions. In the context of balance energy studies, one already knows that BUU simulations with free cross section give the wrong balance energy for the current system.

The almost complete isospin mixing in the simulation with the iso-soft type EOS is unique in the current energy, and was used to differentiate the different IEOS. In general, as the beam energy goes up, the reaction time scale will inevitably be reduced, and the degree of the isospin diffusion will become more incomplete even with the iso-SKM used here. At much higher energy, isospin diffusion process will be insignificant to be detected in the experiment, and the isospin diffusion ratio will be less useful.

5.2.5 Summary

A systematic study of isospin diffusion process in isospin asymmetric heavy-ion reactions has been carried out within the BUU simulations. The projectile spectator regions in the peripheral reactions of $^{124,112}Sn + ^{124,112}Sn$ at $E_{lab}/A = 50$ MeV have been studied, and the isospin asymmetry in such regions was found to be influenced by fast particle emission and by isospin diffusion process. The isospin diffusion ratio R_i defined in Eq. 5.6 reduces the fast-particle emission-effects, and improves sensitivity to isospin diffusion process in the projectile-target asymmetric reactions. The ratio R_i exhibits long-time stability following a collision. The values at which R_i stabilizes are different in simulations that rely on EOS with different isospin dependencies. In nuclear matter with weak isospin gradients, isospin diffusion

process is expected to be related to the IEOS, and such an approximate relation is indeed found in the simulations. The isospin diffusion ratios R_i from the simulations have been compared with ratios constructed from data. The two iso-soft IEOS (iso-NS and iso-SKM) were found to induce too much isospin diffusion to explain the data; the simulation results with iso-stiff IEOS (iso-SH and iso-NH), especially the iso-SH type, agree better. However, the pair of experimental isospin diffusion ratios for the mixed systems $^{124}Sn + ^{112}Sn$ and $^{112}Sn + ^{124}Sn$ show a mirror symmetry which is not quite found in all simulations. The effects of fast particle emission competing with isospin diffusion, causing difficulty in comparing simulations and experiment, and the cross section and energy scale issue have been discussed. Specific analysis of the simulations reveals that about two protons are transferred between the spectators in the mixed system. The results in this section demonstrate the new possibilities for the exploration of isospin physics in heavy-ion reactions.

Chapter 6: Conclusions

In this thesis, I have discussed various aspects of transport in heavy-ion reactions. Much of the discussion has been devoted to microscopic transport theory, which underlies the transport reaction simulations. The simulations are essential for understanding the mechanisms of central heavy-ion reactions. The phenomenological analysis helps one to understand the physical process as well as the cause-effect relationship in the simulations. Analytical solutions of the transport equations can not be developed for realistic reaction system, but can be for some very simplified cases. However, when such analytical solutions are available, they provide important insights into the physical process beyond the pure numerical understanding from transport simulations. The validity of the theories, and of the assumptions in the theories, is tested when the analytical and/or simulational results are confronted with the experimental data.

Chapter 1 introduces the general background and some of the active areas of research for nuclear transport theory and transport phenomena. Heavy-ion reaction represent an important tool for studying the properties of the hot dense nuclear matter. The possible nuclear liquid-gas phase transition and the nuclear equation of states have been extensively studied in heavy-ion reactions. The isospin related transport theory and phenomena have recently raised quite some interest.

Chapter 2 is devoted to a discussion of neutron enrichment in the midrapidity source in the heavy-ion reactions. A phenomenological phase transition model is introduced for nuclear matter, and the neutron enrichment is explained in terms of the phase equilibrium condition between the liquid and the gas phase. The cluster formation process in the neck region, when viewed as droplets in the gas phase, counteracts the trend of neutron enrichment in the midrapidity source. When the nonequilibrium nature of the heavy-ion reaction is taken into account, the phase

equilibrium conditions give the direction of isospin flow in the reaction system. A reversal in the direction of isospin flow is proposed to occur during the reactions.

Chapter 3 introduces microscopic transport theory. The reacting nuclear system may be viewed in terms of the transport and interaction of quasiparticles. The Boltzmann equation set, which is the center of transport theory, contains two essential ingredients: the mean field dynamics and the inter-particle collisions. The mean field is introduced through the energy-density functional; both the momentum independent and momentum dependent parameterizations of the functional are discussed. Isospin physics has raised much interest in recent years spurred by the development of the experimental facilities. After a brief introduction of the isospin related phenomena, I discussed isospin dependence of the mean field in detail. Both the density dependence and the momentum dependence of the neutron and proton optical potentials have been discussed. A general T-matrix argument is used to justify the high momentum behavior of the isospin dependent optical potentials. The isospin dependent mean fields have been used to access the Urca cooling process in neutron stars. Some practical issues for reaction simulations have also been discussed, including the initialization of a reaction system, test particle method for integrating transport equations, the lattice Hamiltonian method for improved accuracy and modification of cross sections inside a nuclear media.

Chapter 4 was devoted to the derivation of the isospin diffusion coefficient for nuclear matter. A systematic expansion of the Boltzmann equation gives self-consistent equations for the variations of the distribution function, from which the flux and transport coefficients could be derived. The isospin diffusion coefficient, shear viscosity and heat conductivity have been all calculated using the free space N-N cross-sections. The isospin diffusion time scale have been also estimated for a heavy-ion reaction system, and the result was compatible with that from a simulation.

Chapter 5 was devoted to transport simulations for heavy-ion reactions. In the first part of that chapter, the interplay of the participant and spectator zones in high energy reactions was examined. The interplay, on one hand, produces the elliptic flow pattern in the participant region, and on the other hand impact the properties of the spectator remnants. In transport simulations, the properties of the spectator remnants after a collision turn out to be directly linked to the features of the nuclear equation of state (EOS) in the participant zone. An acceleration of the spectator piece is found in a heavy system at low impact parameters in the simulations. The acceleration may be explained in terms of the blast of the exploding participant matter impacting the spectator. Finally, isospin diffusion process is studied in heavy-ion reaction simulations. The process is expected to be sensitive to isospin dependence of the mean fields, and such sensitivity is indeed found in transport simulations. The results from the simulation have been compared to data from the same reaction system. The experimental results are better explained with a symmetry energy characterized by a stiff dependence on the nuclear density.

APPENDICES

Appendix A: Macroscopic Quantities

I shall consider different types of macroscopic quantities, either net or for separate components, either in the general frame of observation or in a local frame. For a single component i in the observation frame, the density n_i, mean velocity $\underline{\mathbf{v}}_i$, mean kinetic energy $\underline{e}_i$, momentum flux tensor $\overline{\overline{p}}_i$ and kinetic energy flux $\mathbf{q}_i$, are given in terms of the distribution f_i, respectively, as

$$n_i(\mathbf{r},t) = \frac{g}{(2\pi\hbar)^3}\int d^3p\, f_i(\mathbf{p},\mathbf{r},t)\,, \tag{A.1a}$$

$$n_i\,\underline{\mathbf{v}}_i = \frac{g}{(2\pi\hbar)^3}\int d^3p\,\frac{\mathbf{p}}{m_i}\, f_i(\mathbf{p},\mathbf{r},t)\,, \tag{A.1b}$$

$$n_i\,\underline{e}_i = \frac{g}{(2\pi\hbar)^3}\int d^3p\,\frac{p^2}{2m_i}\, f_i(\mathbf{p},\mathbf{r},t)\,, \tag{A.1c}$$

$$\overline{\overline{p}}_i = \frac{g}{(2\pi\hbar)^3}\int d^3p\,\frac{\overline{\overline{\mathbf{p}\,\mathbf{p}}}}{m_i}\, f_i(\mathbf{p},\mathbf{r},t)\,, \tag{A.1d}$$

$$\mathbf{q}_i = \frac{g}{(2\pi\hbar)^3}\int d^3p\,\frac{p^2}{2m_i}\,\frac{\mathbf{p}}{m_i}\, f_i(\mathbf{p},\mathbf{r},t)\,. \tag{A.1e}$$

The net quantities result from combining the component contributions. Thus, the net density is $n = n_1 + n_2$, the net mass density is $\rho = \rho_1 + \rho_2 = m_1 n_1 + m_2 n_2$ while the net velocity $\underline{\mathbf{v}}$ is obtained from $\rho\,\underline{\mathbf{v}} = \rho_1\,\underline{\mathbf{v}}_1 + \rho_2\,\underline{\mathbf{v}}_2$. The kinetic energy $\underline{e}$ averaged over all particles is given by $n\,\underline{e} = n_1\,\underline{e}_1 + n_2\,\underline{e}_2$, the net momentum flux is $\overline{\overline{p}} = \overline{\overline{p}}_1 + \overline{\overline{p}}_2$ and the net kinetic energy flux is $\mathbf{q} = \mathbf{q}_1 + \mathbf{q}_2$.

Local quantities are those calculated with momenta transformed to the local mass frame, i.e. following the substitution $\mathbf{p} \rightarrow \mathbf{p} - m_i\,\underline{\mathbf{v}}$. To distinguish local quantities from those in the observation frame, when the frame matters, the local quantities will be capitalized. The local momentum flux tensor $\overline{\overline{P}}$ is the kinetic pressure tensor and the local kinetic energy flux $\mathbf{Q}$ is the heat flux.

Appendix B: Continuity Equations

The collisions in the Boltzmann equation set (4.13) conserve the quasiparticle momentum and energy and the species identity. This leads to local conservation laws for the corresponding macroscopic quantities.

Let $\chi_j(\mathbf{p})$ represent one of the quasiparticle quantities conserved in collisions, $\chi_j(\mathbf{p}) = \delta_{ij}$, $\mathbf{p}$ or $p^2/2m_j$. For those quantities, the integration with collision integrals produces

$$\sum_j \int d^3p\, \chi_j\, J_j = 0\,. \tag{B.1}$$

As a consequence, from the Boltzmann equation set, I obtain

$$\sum_j \int \frac{d^3p}{(2\pi\hbar)^3}\, \chi_j \left(\frac{\partial f_j}{\partial t} + \frac{\mathbf{p}}{m_j} \cdot \frac{\partial f_j}{\partial \mathbf{r}} + \mathbf{F}_j \cdot \frac{\partial f_j}{\partial \mathbf{p}} \right) = 0\,. \tag{B.2}$$

After a partial integration, I get from the above

$$\frac{\partial}{\partial t}\left(n\underline{\chi}\right) + \frac{\partial}{\partial \mathbf{r}} \cdot \left(n \underline{\frac{\mathbf{p}}{m}\, \chi} \right) - n\, \underline{\mathbf{F} \cdot \frac{\partial \chi}{\partial \mathbf{p}}} = 0\,, \tag{B.3}$$

where the averages are defined with

$$n\,\underline{\chi} = \sum_j \int \frac{d^3p}{(2\pi\hbar)^3}\, \chi_j\, f_j(\mathbf{p}, \mathbf{r}, t)\,. \tag{B.4}$$

Substituting for χ_j the conserved quantities ($\chi_j(\mathbf{p}) = \delta_{ij}$, $\mathbf{p}$ or $p^2/2m_j$), I get the respective continuity equations:

$$\frac{\partial n_i}{\partial t} + \frac{\partial}{\partial \mathbf{r}} \cdot (n_i\, \underline{\mathbf{v}}_i) = 0 \tag{B.5a}$$

$$\frac{\partial}{\partial t}(\rho\, \underline{\mathbf{v}}) + \frac{\partial}{\partial \mathbf{r}} \cdot \overline{\overline{p}} - n_1\, \mathbf{F}_1 - n_2\, \mathbf{F}_2 = 0\,, \tag{B.5b}$$

$$\frac{\partial}{\partial t}(n\, \underline{\epsilon}) + \frac{\partial}{\partial \mathbf{r}} \cdot \mathbf{q} - n_1\, \underline{\mathbf{v}}_1 \cdot \mathbf{F}_1 - n_2\, \underline{\mathbf{v}}_2 \cdot \mathbf{F}_2 = 0\,. \tag{B.5c}$$

Here, I made yet no use of the local frame.

The local frame is useful when wants to make use of the assumption of local equilibrium that imposes restrictions on local quantities. On representing the average velocities as $\underline{\mathbf{v}}_i = \underline{\mathbf{V}}_i + \underline{\mathbf{v}}$ in the equations above, I obtain the following set,

$$\frac{\partial n_i}{\partial t} + \frac{\partial}{\partial \mathbf{r}} \cdot (n_i \underline{\mathbf{v}}) + \frac{\partial}{\partial \mathbf{r}} \cdot (n_i \underline{\mathbf{V}}_i) = 0\,, \tag{B.6a}$$

$$\frac{\partial \rho}{\partial t} + \frac{\partial}{\partial \mathbf{r}} \cdot (\rho \underline{\mathbf{v}}) = 0\,, \tag{B.6b}$$

$$\frac{\partial}{\partial t}(\rho \mathbf{v}) + \frac{\partial}{\partial \mathbf{r}} \cdot (\rho \mathbf{v}\,\mathbf{v}) + \frac{\partial}{\partial \mathbf{r}} \cdot \overline{\overline{P}} - n_1 \mathbf{F}_1 - n_2 \mathbf{F}_2 = 0\,, \tag{B.6c}$$

$$\frac{\partial}{\partial t}(n \underline{E}) + \frac{\partial}{\partial \mathbf{r}} \cdot (n \underline{E} \mathbf{v}) + \overline{\overline{P}} : \overline{\overline{\frac{\partial}{\partial \mathbf{r}} \mathbf{v}}} + \frac{\partial}{\partial \mathbf{r}} \cdot \mathbf{Q} - n_1 \underline{\mathbf{V}}_1 \mathbf{F}_1 - n_2 \underline{\mathbf{V}}_2 \mathbf{F}_2 = 0 \tag{B.6d}$$

The equation for mass density in the set above follows from combining the equations for particle densities.

The above equations significantly simplify when the assumption of a strict local equilibrium is imposed. Under that assumption, the local species velocities and the heat flow vanish, $\mathbf{V}_i = 0$ and $\mathbf{Q} = 0$, and the kinetic pressure tensor becomes diagonal, $\overline{\overline{P}} = \frac{2}{3} n \underline{E} \overline{\overline{1}}$. The equations reduce then to the Euler set

$$\frac{\partial n_i}{\partial t} + \frac{\partial}{\partial \mathbf{r}} \cdot (n_i \underline{\mathbf{v}}) = 0\,, \tag{B.7a}$$

$$\frac{\partial}{\partial t}(\rho \mathbf{v}) + \frac{\partial}{\partial \mathbf{r}} \cdot \left(\rho \overline{\overline{\mathbf{v}\,\mathbf{v}}}\right) + \frac{2}{3} \frac{\partial (n \underline{E})}{\partial \mathbf{r}} - n_1 \mathbf{F}_1 - n_2 \mathbf{F}_2 = 0\,, \tag{B.7b}$$

$$\frac{\partial}{\partial t}(n \underline{E}) + \mathbf{v} \cdot \frac{\partial}{\partial \mathbf{r}}(n \underline{E}) + \frac{5}{3} n \underline{E} \frac{\partial}{\partial \mathbf{r}} \cdot \mathbf{v} = 0\,. \tag{B.7c}$$

Appendix C: Space-Time Derivatives for an Ideal Fluid

In an ideal fluid, all local quantities can be expressed in terms of the local temperature T and the local kinetic chemical potential μ_i. If I consider changes of the densities n_i or of the local kinetic energies $\underline{E}_i$ with respect to a parameter x representing some spatial coordinate or time, or their combination, I find

$$\begin{aligned} \frac{\partial n_i}{\partial x} &= \xi_i T \frac{\partial \alpha_i}{\partial x} + \frac{3}{2} n_i \frac{\partial \beta}{\partial x}, \\ \frac{\partial (n_i \underline{E}_i)}{\partial x} &= \frac{3}{2} n_i T \frac{\partial \alpha_i}{\partial x} + \frac{5}{2} n_i \underline{E}_i \frac{\partial \beta}{\partial x}, \end{aligned} \tag{C.1}$$

where $\alpha_i = \mu_i / T$, $\beta = \log T$ and $\xi_i = (\partial n_i / \partial \mu_i)_T$. With the trace derivative defined as

$$\frac{d}{dt} = \frac{\partial}{\partial t} + \mathbf{v} \cdot \frac{\partial}{\partial \mathbf{r}},$$

a particular version of the above relations is

$$\begin{aligned} \frac{dn_i}{dt} &= \xi_i T \frac{d\alpha_i}{dt} + \frac{3}{2} n_i \frac{d\beta}{dt}, \\ \frac{d(n_i \underline{E}_i)}{dt} &= \frac{3}{2} n_i T \frac{d\alpha_i}{dt} + \frac{5}{2} n_i \underline{E}_i \frac{d\beta}{dt}. \end{aligned} \tag{C.2}$$

A combination of the above trace-derivative relations with the Euler equations from Appendix B yields the following simple results,

$$\frac{d\alpha_i}{dt} = 0, \tag{C.3a}$$

$$\frac{d\beta}{dt} = -\frac{2}{3} \frac{\partial}{\partial \mathbf{r}} \cdot \mathbf{v}, \tag{C.3b}$$

the consistency of which with (C.2) and (B.7) is easy to verify. The results (C.3)

express basic features of the isentropic ideal-fluid evolution of a mixture. The entropy per particle in species i depends only on α_i, while the ratio of the densities of species n_1/n_2 depends both on α_1 and α_2. The conservation of α_i for both species is equivalent to the conservation of entropy per particle and of relative concentration. Finally, the density for species i is proportional to $T^{3/2}$ multiplying a function of α_i, which is equivalent to the second of the results above, given the continuity equation for species and the conservation of α_i.

Appendix D: Variable Transformation

The driving forces for diffusion are naturally expressed in terms of the gradients of temperature and of chemical potential difference per unit mass μ'_{12}. However, given the typical constraints on systems, it can be convenient to express the chemical potential in terms of other quantities, that are easier to assess or control, such as the differential concentration δ, temperature T and net pressure P'. A transformation of the variables for the driving forces has been employed, at a formal level, in Sec. 4.3.3. Here, I show, though, how the transformation can be done in practice for the interaction energy per particle specified in terms of the particle density n and concentration δ, $E^v = E^v(n, \delta)$. With the nuclear application in mind, I limit myself to the case of $m_1 = m_2 = m$.

The transformation can exploit straightforward relations between different differentials. One of those to exploit is the Gibbs-Duhem relation

$$dP' = n_1\, d\mu'_1 + n_2\, d\mu'_2 + n\, s\, dT = n\, d\mu' + \frac{m\, n\, \delta}{2}\, d\mu'_{12} + n\, s\, dT\,. \tag{D.1}$$

Here, s is the entropy per particle and $\mu' = (\mu'_1 + \mu'_2)/2$ is the median chemical potential. Two other relations stem from the differentiations of equilibrium particle distributions, already utilized in Appendix C,

$$dn_i = \xi_i\, d\mu_i + \frac{\frac{3}{2} n_i - \xi_i\, \mu_i}{T}\, dT \equiv \xi_i\, d\mu_i + \left(\frac{\partial n_i}{\partial T}\right)_{\mu_i} dT\,. \tag{D.2}$$

With $\mu'_i = \partial(n\, E^v)/\partial n_i$, on adding and subtracting the two ($i = 1, 2$) relations side

by side, I find

$$dn = (\xi_1 + \xi_2)\left[d\mu^t - \left(\frac{\partial \mu^v}{\partial n}\right)_\delta dn - \left(\frac{\partial \mu^v}{\partial \delta}\right)_n d\delta\right] + \frac{m}{2}(\xi_1 - \xi_2)$$
$$\times \left[d\mu^t_{12} - \left(\frac{\partial \mu^v_{12}}{\partial n}\right)_\delta dn - \left(\frac{\partial \mu^v_{12}}{\partial \delta}\right)_n d\delta\right] + \left[\left(\frac{\partial n_1}{\partial T}\right)_{\mu_1} + \left(\frac{\partial n_2}{\partial T}\right)_{\mu_2}\right] dT \quad \text{(D.3)}$$

and

$$\delta\, dn + n\, d\delta = (\xi_1 - \xi_2)\left[d\mu^t - \left(\frac{\partial \mu^v}{\partial n}\right)_\delta dn - \left(\frac{\partial \mu^v}{\partial \delta}\right)_n d\delta\right] + \frac{m}{2}(\xi_1 + \xi_2)$$
$$\times \left[d\mu^t_{12} - \left(\frac{\partial \mu^v_{12}}{\partial n}\right)_\delta dn - \left(\frac{\partial \mu^v_{12}}{\partial \delta}\right)_n d\delta\right] + \left[\left(\frac{\partial n_1}{\partial T}\right)_{\mu_1} - \left(\frac{\partial n_2}{\partial T}\right)_{\mu_2}\right] dT \quad \text{(D.4)}$$

Those two equations have the structure

$$G_{kn}\, dn = G_{k\mu}\, d\mu^t + G_{kd}\, d\mu^t_{12} + G_{k\delta}\, d\delta + G_{kT}\, dT\,, \quad \text{(D.5)}$$

where $k = 1, 2$ and where the coefficients G can be worked out from (D.3) and (D.4). On multiplying the sides of the first ($k = 1$) equation by G_{2n} and the sides of the second ($k = 2$) equation by G_{1n} and on subtracting the equations side by side, I can eliminate the dn differential obtaining

$$0 = (G_{2n}\, G_{1\mu} - G_{1n}\, G_{2\mu})\, d\mu^t + (G_{2n}\, G_{1d} - G_{1n}\, G_{2d})\, d\mu^t_{12}$$
$$+ (G_{2n}\, G_{1\delta} - G_{1n}\, G_{2\delta})\, d\delta + (G_{2n}\, G_{1T} - G_{1n}\, G_{2T})\, dT$$
$$\equiv R_\mu\, d\mu^t + R_d\, d\mu^t_{12} + R_\delta\, d\delta + R_T\, dT\,. \quad \text{(D.6)}$$

On eliminating next the $d\mu_t$ differential using the Gibbs-Duhem relation, I find

$$\Pi_{12}^{P} = \left(\frac{\partial \mu_{12}^{t}}{\partial P^{t}}\right)_{T,\delta} = \frac{R_{\mu}}{n\left(R_{\mu}\frac{m\delta}{2} - R_{d}\right)}, \tag{D.7a}$$

$$\Pi_{12}^{T} = \left(\frac{\partial \mu_{12}^{t}}{\partial T}\right)_{P^{t},\delta} = \frac{R_{\mu}s - R_{T}}{R_{d} - R_{\mu}\frac{m\delta}{2}}, \tag{D.7b}$$

$$\Pi_{12}^{\delta} = \left(\frac{\partial \mu_{12}^{t}}{\partial \delta}\right)_{P^{t},T} = \frac{R_{\delta}}{R_{\mu}\frac{m\delta}{2} - R_{d}}. \tag{D.7c}$$

Appendix E: Brace Algebra

The brace products are employed in finding the transport coefficients within linear approximation to the Boltzmann equation. The brace product of two scalar quantities A and B associated with the colliding particles is defined as

$$\begin{aligned}\{A,B\} &= \int \frac{d^3p}{(2\pi)^3} A_1 I_{11}(B) + \int \frac{d^3p}{(2\pi)^3} A_1 I_{12}(B) \\ &\quad + \int \frac{d^3p}{(2\pi)^3} A_2 I_{21}(B) + \int \frac{d^3p}{(2\pi)^3} A_2 I_{22}(B) \\ &= [A,B]_{11} + [A,B]_{12} + [A,B]_{22}\ , \end{aligned} \tag{E.1}$$

where, in the last step, I have broken the brace product into square-bracket products representing contributions from collisions within species 1, from collisions between species 1 and 2 and from collisions within species 2, respectively.

I will first show that the square-bracket product is symmetric. Thus, I have explicitly

$$\begin{aligned}[A,B]_{ii} &= \frac{1}{2}\int \frac{d^3p_a}{(2\pi)^3}\frac{d^3p_b}{(2\pi)^3}\, d\Omega\, v^*\left(\frac{d\sigma_{ii}}{d\Omega}\right) f_{ia}^{(0)} f_{ib}^{(0)} \tilde{f}_{ia}^{(0)\prime} \tilde{f}_{ib}^{(0)\prime} \\ &\quad \times A_{ia}\left(B_{ia} + B_{ib} - B'_{ia} - B'_{ib}\right) \\ &= \frac{1}{8}\int \frac{d^3p_a}{(2\pi)^3}\frac{d^3p_b}{(2\pi)^3}\, d\Omega\, v^*\left(\frac{d\sigma_{ii}}{d\Omega}\right) f_{ia}^{(0)} f_{ib}^{(0)} \tilde{f}_{ia}^{(0)\prime} \tilde{f}_{ib}^{(0)\prime} \\ &\quad \times \left(A_{ia} + A_{ib} - A'_{ia} - A'_{ib}\right)\left(B_{ia} + B_{ib} - B'_{ia} - B'_{ib}\right), \end{aligned} \tag{E.2}$$

where, to get the last result, I have first utilized an interchange of the particles in the initial state of a collision and then an interchange of the initial and final states within a collision. It is apparent that the r.h.s. of (E.2) is symmetric under the interchange of A and B. Moreover, one can see that a square bracket for $B = A$, $[A,A]_{ii}$, is nonnegative and that it vanishes only when A is conserved in collisions.

I next consider the contribution from collisions between different species,

$$
\begin{aligned}
[A,B]_{12} &= \int \frac{d^3p_1}{(2\pi)^3}\frac{d^3p_2}{(2\pi)^3}\,d\Omega\,v^*\left(\frac{d\sigma_{12}}{d\Omega}\right) f_1^{(0)} f_2^{(0)} \tilde{f}_1^{(0)\prime} \tilde{f}_2^{(0)\prime} \\
&\quad \times (A_1 + A_2)(B_1 + B_2 - B_1' - B_2') \\
&= \frac{1}{2}\int \frac{d^3p_1}{(2\pi)^3}\frac{d^3p_2}{(2\pi)^3}\,d\Omega\,v^*\left(\frac{d\sigma_{12}}{d\Omega}\right) f_1^{(0)} f_2^{(0)} \tilde{f}_1^{(0)\prime} \tilde{f}_2^{(0)\prime} \\
&\quad \times (A_1 + A_2 - A_1' - A_2')(B_1 + B_2 - B_1' - B_2')\,. \qquad \text{(E.3)}
\end{aligned}
$$

Here, I again utilized an interchange between the initial and final states and I again observe a symmetry between A and B on the r.h.s. Thus, indeed, all square brackets are symmetric. Moreover, for $B = A$, One sees that $[A,A]_{12} \geq 0$ and that the zero is only reached if A is conserved.

Combining the results, I find that the brace product (E.1) is symmetric. Moreover, I find that the brace product of quantity A with itself is nonnegative, $\{A,A\} \geq 0$, and vanishes only when A is conserved. As the brace product has features of a pseudo-scalar product, a version of the Cauchy-Schwarz-Buniakowsky (CSB) inequality [171] holds,

$$\{A,A\}\{B,B\} \geq (\{A,B\})^2\,. \qquad \text{(E.4)}$$

All the results from this Appendix remain valid, in an obvious manner, when the brace product (E.1) is generalized to the pairs of tensors of the same rank associated with the particles, when requiring that the tensor indices are convoluted between the two tensors in the brace, as e.g. in (4.36). The positive definite nature of the brace product is important in ensuring that expressions for transport coefficients, obtained in the Chapter 4, yield positive values for the coefficients that in this case represent a stable system.

Bibliography

[1] H. Muller and B. D. Serot, *Phase Transitions in Warm, Asymmetric Nuclear Matter*, Phys. Rev. **C52**, 2072 (1995).

[2] S. Ejiri et al., *The QCD Phase Transition at High Temperature and Low Density*, hep-lat/0209012 (2002).

[3] F. Csikor et al., *Lattice QCD at Non-Vanishing Density: Phase Diagram, Equation of State*, hep-lat/0301027 (2003).

[4] P. Braun-Munzinger and J. Stachel, *Probing the Phase Boundary between Hadronic Matter and the Quark-Gluon-Plasma in Relativistic Heavy Ion Collisions*, Nucl. Phys. **A606**, 320 (1996).

[5] P. Danielewicz, *Effects of Compression and Collective Expansion on Particle Emission from Central Heavy Ion Reactions*, nucl-th/9408018 (1994).

[6] J. Pochodzalla et al., *Probing the Nuclear Liquid - Gas Phase Transition*, Phys. Rev. Lett. **75**, 1040 (1995).

[7] P. Danielewicz, *Hadronic Transport Models*, Acta Phys. Polon. **B33**, 45 (2002).

[8] R. B. Wiringa, V. Fiks, and A. Fabrocini, *Equation of State for Dense Nucleon Matter*, Phys. Rev. **C38**, 1010 (1988).

[9] B.-A. Li, C. M. Ko, and W. Bauer, *Isospin Physics in Heavy-Ion Collisions at Intermediate Energies*, Int. J. Mod. Phys. **E7**, 147 (1998).

[10] G. F. Bertsch and S. Das Gupta, *A Guide to Microscopic Models for Intermediate-Energy Heavy Ion Collisions*, Phys. Rept. **160**, 189 (1988).

[11] C. W. De Jager, H. De Vries, and C. De Vries, *Nuclear Charge and Magnetization Density Distribution Parameters from Elastic Electron Scattering*, Atom. Data Nucl. Data Tabl. **14**, 479 (1974).

[12] P. Danielewicz, *Determination of the Mean-Field Momentum-Dependence Using Elliptic Flow*, Nucl. Phys. **A673**, 375 (2000).

[13] A. D. Panagiotou et al., *Experimental Evidence for a Liquid - Gas Phase Transition in Nuclear Systems*, Phys. Rev. Lett. **52**, 496 (1984).

[14] A. Schuttauf et al., *Universality of Spectator Fragmentation at Relativistic Bombarding Energies*, Nucl. Phys. **A607**, 457 (1996).

[15] J. B. Elliott et al., *Constructing the Phase Diagram of Finite Neutral Nuclear Matter*, Phys. Rev. **C67**, 024609 (2003).

[16] P. Danielewicz, R. Lacey, and W. G. Lynch, *Determination Of The Equation Of State Of Dense Matter*, Science **298**, 1592 (2002).

[17] P. J. Siemens, *Liquid-Gas Phase Transition in Nuclear Matter*, Nature **305**, 410 (1983).

[18] J. Pochodzalla and ALADIN Collaboration, *The Nuclear Liquid-Gas Phase Transition: Present Status and Future Perspectives*, nucl-ex/9607004 .

[19] D. Q. Lamb, J. M. Lattimer, C. J. Pethick, and D. G. Ravenhall, *Hot Dense Matter and Stellar Collapse*, Phys. Rev. Lett. **41**, 1623 (1978).

[20] H. Jaqaman, A. Z. Mekjian, and L. Zamick, *Nuclear Condensation*, Phys. Rev. **C27**, 2782 (1983).

[21] H. Jaqaman, A. Z. Mekjian, and L. Zamick, *Liquid-Gas Phase Transitions in Finite Nuclear Matter*, Phys. Rev. **C29**, 2067 (1984).

[22] P. Danielewicz, *Shock Waves in a Hydrodynamic Model of Central Heavy Ion Collisions*, Nucl. Phys. **A314**, 465 (1979).

[23] M. W. Curtin, H. Toki, and S. D. K., *Liquid-Gas Phase Instabilities in Nuclear Systems*, Phys. Lett. **123B**, 289 (1983).

[24] J. B. Elliott et al., *Nuclear Multifragmentation, Percolation and the Fisher Droplet Model: Common Features of Reducibility and Thermal Scaling*, Phys. Rev. Lett. **85**, 1194 (2000).

[25] M. D'Agostino et al., *Negative Heat Capacity in the Critical Region of Nuclear Fragmentation: an Experimental Evidence of the Liquid-Gas Phase Transition*, nucl-ex/9906004 .

[26] A. Chbihi, O. Schapiro, S. Salou, and D. Gross, *Experimental and Theoretical Search for a Phase Transition in Nuclear Fragmentation*, Eur. Phys. J. **A5**, 251 (1999).

[27] A. L. Goodman, J. I. Kapusta, and A. Z. Mekjian, *Liquid-Gas Phase Instabilities and Droplet Formation in Nuclear Reactions*, Phys.Rev. **C30**, 851 (1983).

[28] M. Baldo and L. S. Ferreira, *Nuclear Liquid-Gas Phase Transition*, Phys. Rev. **C59**, 682 (1999).

[29] S. Das Gupta and A. Mekjian, *A Study of the Phase Transition in the Usual Statistical Model for Nuclear Multifragmentation*, nucl-th/9711018 .

[30] J. F. Dempsey et al., *Isospin Dependence of Intermediate Mass Fragment Production in Heavy-Ion Collisions at E/A=55 MeV*, Phys.Rev. **C54**, 1710 (1996).

[31] P. Pawlowski et al., *Intermediate Velocity Source of Intermediate-Mass Fragments in the $^{40}Ca + ^{40}Ca$ Reaction at Elab=35 MeV/nucleon*, Phys.Rev. **C57**, 1771 (1998).

[32] J. Toke et al., *Intermediate-Mass Fragment Decay of the Neck Zone Formed in Peripheral $^{209}Bi + ^{136}Xe$ Collisions at Elab/A = 28 MeV*, Phys. Rev. Lett. **75**, 2920 (1995).

[33] L. G. Sobotka, J. F. Dempsey, R. J. Charity, and P. Danielewicz, *Clustered and Neutron-Rich Low Density "Neck" Region Produced in Heavy-Ion Collisions*, Phys.Rev. **C55**, 2109 (1997).

[34] M. Prakash, T. L. Ainsworth, and J. M. Lattimer, *Equation of State and the Maximum Mass of Neutron Stars*, Phys. Rev. Lett. **61**, 2518 (1988).

[35] W. Zuo, I. Bombaci, and U. Lombardo, *Asymmetric Nuclear Matter from Extended Brueckner-Hartree- Fock Approach*, Phys. Rev. **C60**, 024605 (1999).

[36] P. Danielewicz, *Effects of Compression and Collective Expansion On Particle Emission from Central Heavy-Ion Reactions*, Phys. Rev. **C 51**, 716 (1995).

[37] L. P. Csernai and J. I. Kapusta, *Entropy and Cluster Production in Nuclear Collisions*, Phys. Rept. **131**, 223 (1986).

[38] B.-A. Li and S. J. Yennello, *Isospin Nonequilibrium in Heavy Ion Collisions at Intermediate-Energies*, Phys. Rev. **C52**, 1746 (1995).

[39] F. D. Becchetti Jr. and G. W. Greenlees, *Nucleon-Nucleus Optical-Model Parameters, $A > 40$, $E < 50$ MeV*, Phys. Rev. **182**, 1190 (1969).

[40] S. S. M. Wong, *Introductory Nuclear Physics*, John Wiley, New York, 2nd ed edition, 1998.

[41] P. Danielewicz, *Surface Symmetry Energy*, nucl-th/0301050 (2003).

[42] P. Danielewicz and G. F. Bertsch, *Production of Deuterons and Pions in a Transport Model of Energetic Heavy Ion Reactions*, Nucl. Phys. **A533**, 712 (1991).

[43] J. Lukasik et al., *Dynamical Effects and Intermediate Mass Fragment Production in Peripheral and Semicentral Collisions Of Xe+Sn at 50 MeV/nucleon*, Phys.Rev. **C 55**, 1906 (1997).

[44] L. G. Sobotka et al., *Neutron-Proton Asymmetry of the Midvelocity Material in an Intermediate-Energy Heavy Ion Collision*, Phys. Rev. **C62**, 031603 (2000).

[45] E. Plagnol et al., *Onset of Midvelocity Emissions in Symmetric Heavy Ion Reactions*, Phys. Rev. **C61**, 014606 (2000).

[46] For an estimate of the average size of clusters in the midrapidity source, we can take data from ref. [43], and make a simple calculation.

[47] Y. Larochelle et al., *Probing Midrapidity Source Characteristics with Charged Particles and Neutrons in the $^{35}Cl+^{nat}Ta$ Reaction at 43 MeV/nucleon*, Phys.Rev. **C 59**, R565 (1999).

[48] H. S. Xu et al., *Isospin Fractionation in Nuclear Multifragmentation*, Physical Review Letters **85**, 716 (1999).

[49] M. Marie et al., *A Hot Expanding Source in 50 A MeV Xe + Sn Central Reactions*, Phys. Lett. **B 391**, 15 (1997).

[50] P. Danielewicz, *Bulk Nuclear Properties From Reactions*, nucl-th/0203002 (2002).

[51] P. Danielewicz and Q. Pan, *Blast of Light Fragments from Central Heavy-Ion Collisions*, Phys. Rev. **C 46**, 2002 (1992).

[52] Q.-b. Pan and P. Danielewicz, *From Sideward Flow to Nuclear Compressibility*, Phys. Rev. Lett. **70**, 2062 (1993).

[53] A. Larionov, W. Cassing, C. Greiner, and U. Mosel, *Squeeze-Out of Nuclear Matter in Peripheral Heavy-Ion Collisions and Momentum-Dependent Effective Interactions*, Phys.Rev. **C62**, 064611 (2000).

[54] L. P. Kadanoff and G. Baym, *Quantum Statistical Mechanics*, Benjamin, New York, 1962.

[55] P. Lipavsky, K. Morawetz, and V. Spicka, *Kinetic Equation for Strongly Interacting Dense Fermi System*, Ann. Phys. Fr. **26**, 1 (2001).

[56] P. Danielewicz, *Quantum Theory of Nonequilibrium Process, I*, Ann. Phys. **152**, 239 (1984).

[57] P. Danielewicz, *Quantum Theory of Nonequilibrium Process, II. Application to Nuclear Collisions*, Ann. Phys. **152**, 305 (1984).

[58] H. S. Kohler, N. H. Kwong, and H. A. Yousif, *A Fortran Code for Solving the Kadanoff-Baym Equations for a Homogeneous Fermion System*, Comp. Phys. Comm. **123**, 123 (1999).

[59] H. S. Kohler, *Memory and Correlation Effects in Nuclear Collisions*, Phys. Rev. **C51**, 3232 (1995).

[60] H. S. Kohler, *Quantum Effects for Collision Term in Transport Equation*, Nucl. Phys. **A583**, 339 (1995).

[61] H. S. Kohler, *Memory and Correlation Effects in the Quantum Theory of Thermalization*, Phys. Rev. **E**, 3145 (1996).

[62] H. S. Kohler and K. Morawetz, *Correlations in Many-Body Systems with Two-Time Green'S Functions*, Phys. Rev. **C64**, 024613 (2001).

[63] B. Blattel et al., *Transverse Momentum Analysis in the Relativistic BUU Approach*, Nucl. Phys. **A495**, 381c (1989).

[64] W. Cassing, A. Lang, S. Teis, and K. Weber, *Covariant Transport Approach for Heavy Ion Reactions*, Nucl. Phys. **A545**, 123c (1992).

[65] K. Weber et al., *A Relativistic Effective Interaction for Heavy Ion Collisions*, Nucl. Phys. **A539**, 713 (1992).

[66] T. Maruyama et al., *Relativistic BUU Approach with Momentum Dependent Mean Fields*, Phys. Lett. **B297**, 228 (1992).

[67] K. Weber et al., *Relativistic Potentials for a Counterstreaming Nuclear Matter Scenario with a Covariant Momentum Dependent Interaction*, Nucl. Phys. **A552**, 571 (1993).

[68] T. Maruyama et al., *Study of a High-Energy Heavy Ion Collisions in a Relativistic BUU Approach with Momentum Dependent Mean Fields*, Nucl. Phys. **A573**, 653 (1994).

[69] G. F. Bertsch and P. Danielewicz, *Off-Shell Effects in Heavy Particle Production*, Phys. Lett. **B367**, 55 (1996).

[70] M. Effenberger and U. Mosel, *Off-Shell Effects on Particle Production*, Phys. Rev. **C60**, 051901 (1999).

[71] A. B. Larionov and U. Mosel, *Off-Shell Pions in The BUU Transport Theory*, Phys. Rev. **C66**, 034902 (2002).

[72] Y. B. Ivanov, J. Knoll, and D. N. Voskresensky, *Self-Consistent Approach to Off-Shell Transport*, (2003).

[73] E. A. Uehling and G. E. Uhlenbeck, *Transport Phenomena in Einstein-Bose and Fermi-Dirac Gases. I.* Phys. Rev. **43**, 552 (1933).

[74] E. A. Uehling, *Transport Phenomena in Einstein-Bose and Fermi-Dirac Gases. II*, Phys. Rev. **46**, 917 (1934).

[75] R. L. Liboff, *Kinetic Theory. Classical, Quantum, and Relativistic Descriptions*, Prentice Hall, Englewood Cliffs, New Jersey, 1990.

[76] S. Chapman and T. G. Cowling, *The Mathematical Theory of Non-Uniform Gases*, Cambridge, New York, 1964.

[77] Y. L. Klimontovich, *Statistical Physics*, Harwood Academic, Chur, Switzerland, 1986.

[78] L. D. Landau and E. M. Lifshitz, *Statistical Physics*, volume 5 of *Course of Theoretical Physics*, Pergamon Press, Oxford, 1980.

[79] J.-P. Blaizot and E. Iancu, *The Quark-Gleon Plasma: Collective Dynamics and Hard Thermal Loops*, Phys. Rep. **359**, 355 (2002).

[80] J.-P. Blaizot and E. Iancu, *Kinetic Theory and Quantum Electrodynamics at High Temperature*, Nucl. Phys. **B390**, 589 (1993).

[81] J. P. Blaizot and E. Iancu, *Kinetic Equations for Long Wavelength Excitations of the Quark - Gluon Plasma*, Phys. Rev. Lett. **70**, 3376 (1993).

[82] P. F. Kelly, Q. Liu, C. Lucchesi, and C. Manuel, *Deriving the Hard Thermal Loops of QCD From Classical Transport Theory*, Phys. Rev. Lett. **72**, 3461 (1994).

[83] D. F. Litim and C. Manuel, *Semi-Classical Transport Theory for Non-Abelian Plasmas*, Phys. Rep. **364**, 451 (2002).

[84] R. S. Bhalerao and G. C. Nayak, *Production and Equilibration of Quark-Gluon Plasma at RHIC and LHC with Minijets*, Phys. Rev. **C61**, 054907 (2000).

[85] G. C. Nayak and V. Ravishankar, *Pre-equilibrium Evolution of Quark-Gluon Plasma*, Phys. Rev. **C58**, 356 (1998).

[86] J. Aichelin, *'Quantum Molecular Dynamics: a Dynamical Microscopic N Body Approach to Investigate Fragment Formation and the Nuclear Equation of State in Heavy Ion Collisions*, Phys. Rept. **202**, 233 (1991).

[87] A. Ono, H. Horiuchi, T. Maruyama, and A. Ohnishi, *Fragment Formation Studied with Antisymmetrized Version of Molecular Dynamics with Two Nucleon Collisions*, Phys. Rev. Lett. **68**, 2898 (1992).

[88] A. Ono, *Antisymmetrized Molecular Dynamics with Quantum Branching Processes for Collisions of Heavy Nuclei*, Phys. Rev. **C59**, 853 (1999).

[89] G. Baym and C. Pethick, *Landau Fermi-Liquid Theory*, John Wiley & Sons, New York, 1991.

[90] G. Baym and S. A. Chin, *Landau Theory of Relativistic Fermi Liquids*, Nucl. Phys. **A262**, 527 (1976).

[91] G. Holzwarth, *Static and Dynamical Thomas Fermi Theory for Nuclei*, Physics Letter **B 66**, 29 (1977).

[92] R. J. Lenk and V. R. Padharipande, *Nuclear Mean Field Dynamics in the Lattice Hamiltonian Vlasov Method*, Physics Review **C 39**, 2242 (1989).

[93] P. Danielewicz et al., *Disappearance of Elliptic Flow: a New Probe for the Nuclear Equation of State*, Phys. Rev. Lett. **81**, 2438 (1998).

[94] W. D. Myers and W. Swiatecki, *Nuclear Equation of State*, Physics Review **C 57**, 3020 (1998).

[95] A. Hombach, W. Cassing, S. Teis, and U. Mosel, *Analysis of Flow Effect in Relativistic Heavy-Ion Collisions within the CBUU Approach*, Eur. Phys. J. **A5**, 157 (1999).

[96] L. P. Csernai, G. Fai, C. Gale, and E. Osnes, *Nuclear Equation of State with Momentum Dependent Interactions*, Phys. Rev. **C46**, 736 (1992).

[97] M. Jaminon and C. Mahaux, *Effective Masses in Relativistic Approaches to the Nucleon Nucleus Mean Field*, Phys. Rev. **C40**, 354 (1989).

[98] H. Johnston et al., *Isospin Equilibration in the Reaction E/A = 33, 45 MeV* ^{40}Ar, ^{40}Ca + ^{58}Fe, ^{58}Ni, Phys. Lett. **B 371**, 186 (1996).

[99] F. Rami et al., *Isospin-Tracing: a Probe of Non-Equilibrium in Central Heavy-Ion Collisions*, Phys.Rev.Lett. **84**, 1120 (2000).

[100] M. B. Tsang et al., *Isospin Diffusion in Heavy-Ion Reaction*, Phys. Rev. Lett. (2003).

[101] M. Colonna, M. Di Toro, G. Fabbri, and S. Maccarone, *Effects of Charge Symmetry on Heavy Ion Reaction Mechanisms*, Phys. Rev. **C 57**, 1410 (1998).

[102] J. Pochodzalla and W. Trautmann, Chemical equilibrium and isotope temperatures, in *Isospin Physics in Heavy-Ion Collisions at Intermediate Energies*, edited by B.-A. Li and W. U. Schroeder, Nova Science Publishers, Inc., 2001.

[103] W. P. Tan et al., *Fragment Isotope Distributions and the Isospin Dependent Equation of State*, Phys. Rev. **C64**, 051901 (2001).

[104] M. B. Tsang et al., *Isoscaling in Statistical Models*, Phys. Rev. **C64**, 054615 (2001).

[105] J. M. Lattimer, M. Prakash, C. J. Pethick, and P. Haensel, *Direct URCA Process in Neutron Stars*, Phys. Rev. Lett. **66**, 2701 (1991).

[106] B. Friedman and V. R. Pandharipande, *Hot and Cold, Nuclear and Neutron Matter*, Nucl. Phys. **A361**, 502 (1981).

[107] P. E. Haustein, *An Overview Of The 1986-1987 Atomic Mass Predictions*, Atomic Data and Nuclear Data Tables **39**, 185 (1988).

[108] B. A. Brown, *Neutron Radii in Nuclei and the Neutron Equation of State*, Phys. Rev. Lett. **85**, 5296 (2000).

[109] A. Lejeune, U. Lombardo, and W. Zuo, *Nuclear Matter EOS with a Three-body Force*, Phys. Lett. **B477**, 45 (2000).

[110] W. Zuo, A. Lejeune, U. Lombardo, and J. F. Mathiot, *Interplay of Three-Body Interactions in the EOS Of Nuclear Matter*, Nucl. Phys. **A706**, 418 (2002).

[111] W. Zuo, A. Lejeune, U. Lombardo, and J. F. Mathiot, *Microscopic Three-Body Force for Asymmetric Nuclear Matter*, Eur. Phys. J. **A14**, 469 (2002).

[112] Z.-y. Ma and L. Liu, *Effective DBHF Method for Asymmetric Nuclear Matter And Finite Nuclei*, nucl-th/0207021 (2002).

[113] D. Alonso and F. Sammarruca, *A Microscopic Calculation of Asymmetric Nuclear Matter Properties*, nucl-th/0301032 (2003).

[114] S. Fritsch and N. Kaiser, *Single-Particle Potential in a Chiral Approach to Nuclear Matter Including Short Range NN-Terms*, Eur. Phys. J. **A17**, 11 (2003).

[115] N. Kaiser, S. Fritsch, and W. Weise, *Chiral Dynamics and Nuclear Matter*, Nucl. Phys. **A697**, 255 (2002).

[116] N. Kaiser, S. Fritsch, and W. Weise, *Nuclear Mean Field from Chiral Pion Nucleon Dynamics*, Nucl. Phys. **A700**, 343 (2002).

[117] B. Liu et al., *Asymmetric Nuclear Matter: the Role of The Isovector Scalar Channel*, Phys. Rev. **C65**, 045201 (2002).

[118] V. Greco et al., *Asymmetric Nuclear Matter in a Hartree-Fock Approach to Nonlinear QHD*, Phys. Rev. **C64**, 045203 (2001).

[119] S. Typel, T. van Chossy, and H. H. Wolter, *Relativistic Mean Field Model with Generalized Derivative Nucleon Meson Couplings*, Phys. Rev. **C67**, 034002 (2003).

[120] S. Typel and H. H. Wolter, *Relativistic Mean Field Calculations with Density Dependent Meson Nucleon Coupling*, Nucl. Phys. **A656**, 331 (1999).

[121] C. B. Das, S. D. Gupta, C. Gale, and B.-A. Li, *Momentum Dependence of Symmetry Potential in Asymmetric Nuclear Matter for Transport Model Calculations*, Phys. Rev. **C67**, 034611 (2003).

[122] W. Grein, *Analysis of The NN and N anti-N Forward Scattering Amplitudes Including Information from pi pi and pi N Scattering*, Nucl. Phys. **B131**, 255 (1977).

[123] I. Bombaci and U. Lombardo, *Asymmetric Nuclear Matter Equation of State*, Phys. Rev. **C 44**, 1892 (1991).

[124] S. Ulrych and H. Muther, *Relativistic Structure of the Nucleon Self-Energy in Asymmetric Nuclei*, nucl-th/9706030 (1997).

[125] S. Hama et al., *Global Dirac Optical Potentials for Elastic Proton Scattering from Heavy Nuclei*, Phys. Rev. **C41**, 2737 (1990).

[126] S. Typel, O. Riedl, and H. H. Wolter, *Elastic ProtonNucleus Scattering and the Optical Potential in a Relativistic Mean Field Model*, Nucl. Phys. **A 709**, 299 (2002).

[127] S. Tsuruta et al., *Confronting Neutron Star Cooling Theories with New Observations*, astro-ph/0204508 (2002).

[128] D. Persram and C. Gale, *Splintering Central Nuclear Collisions with a Momentum-Dependent Lattice Hamiltonian Theory*, nucl-th/9901019, MCGILL-98-44 (1999).

[129] H. Feldmeier and P. Danielewicz, *Fast Numerical Solution of the Poisson Equation on a Three Dimensional Grid*, MSUCL-833 (1992).

[130] J. Cugnon, P. Deneye, and A. Lejeune, *Neutron Matter Properties in an Extended Bruckner Approach*, Z. Phys. **A328**, 409 (1987).

[131] T. Alm, G. Ropke, and M. Schmidt, *Critical Enhancement of the In-Medium Nucleon-Nucleon Cross-Section at Low Temperatures*, Phys. Rev. **C50**, 31 (1994).

[132] T. Alm, G. Ropke, F. Daffin, and M. Schmidt, *The In-Medium Nucleon-Nucleon Cross Section and BUU Simulations of Heavy-Ion Reactions*, Nucl. Phys. **A587**, 815 (1995).

[133] G. F. Bertsch, B. A. Li, G. E. Brown, and V. Koch, *Pion Collectivity in Relativistic Heavy Ion Collisions*, Nucl. Phys. **A490**, 745 (1988).

[134] G. Q. Li and R. Machleidt, *Microscopic Calculation of In-Medium Nucleon-Nucleon Cross Sections*, Phys. Rev. **C 48**, 1702 (1993).

[135] G. Q. Li and R. Machleidt, *Microscopic Calculation of In-Medium Proton-Proton Cross Sections*, Phys. Rev. **C 49**, 566 (1994).

[136] H. S. Kohler, *Mean Field and Effective Cross Sections in Hot Nuclei*, Nucl. Phys. **A 529**, 209 (1991).

[137] H.-J. Schulze, A. Schnell, G. Ropke, and U. Lombardo, *Nucleon-Nucleon Cross Sections in Nuclear Matter*, Phys. Rev. **C 55**, 3006 (1997).

[138] A. Schnell, G. Ropke, U. Lombardo, and H.-J. Schulze, *Elastic Nucleon-Nucleon Cross Section in Nuclear Matter at Finite Temperature*, Phys. Rev. **C 57**, 806 (1998).

[139] D. Klakow, G. Welke, and W. Bauer, *Nuclear Flow Excitation Function*, nucl-th/9304008 (1993).

[140] G. D. Westfall et al., *Mass Dependence of the Disappearance of Flow in Nuclear Collisions*, Phys. Rev. Lett. **71**, 1986 (1993).

[141] M. J. Huang et al., *Mass Dependence of Directed Collective Flow*, Phys. Rev. Lett. **77**, 3739 (1996).

[142] S. Tomonaga, *Innere Rebung und Warmeleitfahigkeit der Kernmaterie*, Z. Phys. **110**, 573 (1938).

[143] V. M. Galitsky, Y. B. Ivanov, and V. A. Khangulian, *Kinetic Coefficients of Nuclear Matter. (In Russian)*, Yad. Fiz. **30**, 778 (1979).

[144] P. Danielewicz, *Transport Properties of Excited Nuclear Matter and the Shock Wave Profile*, Phys. Lett. **B146**, 168 (1984).

[145] R. Hakim, L. Mornas, P. Peter, and H. D. Sivak, *Relaxation Time Approximation for Relativistic Dense Matter*, Phys. Rev. **D 46**, 4603 (1992).

[146] R. Hakim and L. Mornas, *Collective Effects on Transport Coefficients of Relativistic Nuclear Matter*, Phys. Rev. **C 47**, 2846 (1993).

[147] E. J. Hellund and E. A. Uehling, *Transport Phenomena in Mixtures of Gases*, Phys. Rev. **56**, 818 (1939).

[148] L. D. Landau and E. M. Lifshitz, *Fluid Mechanics*, volume 6 of *Course of Theoretical Physics*, Addison-Wesley, Reading, 1959.

[149] S. R. De Groot and P. Mazur, *Non-Equilibrium Thermodynamics*, North-Holland, Amsterdam, 1962.

[150] V. Greco, M. Colonna, and F. Di Toro, M.and Matera, *Collective Modes of Asymmetric Nuclear Matter in Quantum Hadrodynamics*, Phys. Rev. **C67**, 015203 (2003).

[151] S. J. Yennello et al., *The Use of Radioactive Nuclear Beams to Study the Equlibration of the N/Z Degree of Freedom in Intermediate-Energy Heavy-Ion Reactions*, Phys. Lett. **B 321**, 15 (1994).

[152] M. V. Ricciardi et al., *Experimental Indications for the Response of the Spectators to the Participant Blast*, Phys. Rev. Lett. **90**, 212302 (2003).

[153] T. Gaitanos, H. H. Wolter, and C. Fuchs, *Spectator and Participant Decay in Heavy Ion Collisions*, Phys. Lett. **B478**, 79 (2000).

[154] K. G. R. Doss et al., *Nuclear Collective Flow as a Function of Projectile Energy and Mass*, Phys. Rev. Lett. **57**, 302 (1986).

[155] H. A. Gustafsson et al., *Energy and Multiplicity Dependence of Fragment Flow in High-Energy Nuclear Collisions*, Mod. Phys. Lett. **A3**, 1323 (1988).

[156] H. H. Gutbrod et al., *Squeezeout of Nuclear Matter as a Function of Projectile Energy and Mass*, Phys. Rev. **C42**, 640 (1990).

[157] W. Reisdorf and H. G. Ritter, *Collective Flow in Heavy-Ion Collisions*, Ann. Rev. Nucl. Part. Sci. **47**, 663 (1997).

[158] R. Pak et al., *Radial Flow in ^{40}Ar +^{45} Sc Reactions at E=35-115 MeV/nucleon*, Phys. Rev. **C 54**, 1681 (1996).

[159] V. G. Bogdanov, V. A. Plyushchev, and Z. I. Solov'eva, *Study of the Momentum Characteristics of the Fragments of Relativistic Nuclei ^{22}Ne in the Transverse Plane*, Sov. J. Nucl. Phys. **53**, 557 (1991).

[160] G. M. Chernov et al., *Fragmentation of Relativistic Fe-56 Nuclei in Emulsion*, Nucl. Phys. **A412**, 534 (1984).

[161] L. Shi, P. Danielewicz, and R. Lacey, *Spectator Response to the Participant Blast*, Phys. Rev. **C64**, 034601 (2001).

[162] D. J. Morrissey, *Systematics of Momentum Distributions from Reactions with Relativistic Ions*, Phys. Rev. **C39**, 460 (1989).

[163] H. Johnston et al., *Isotopically Resolved Intermediate-Mass Fragment and Light Charged Particle Production from the Reactions ^{40}Ar and ^{40}Ca with ^{58}Fe and ^{58}Ni at E_{beam} = 33 and 45 MeV/nucleon*, Phys. Rev. **C 56**, 1972 (1997).

[164] A large ensemble of $\mathcal{N} = 800$ test particles was used in the simulation to reduce the statistical errors, and a total of 20 independent runs were averaged to get best average values and the statistical error estimate.

[165] L. Phair et al., *Impact Parameter Filters for ^{36}Ar +^{197} Au Collisions at $E/A = 50, 80, 110 MeV$*, Nucl. Phys. **A548**, 489 (1992).

[166] L. Phair et al., *Impact Parameter Filters for Ar-36 + Au-197 collisions at E/A = 50, 80, and 110 MeV*, MSUCL-831 .

[167] M. B. Tsang et al., *Conditions for Isoscaling in Nuclear Reactions*, Phys. Rev. **C64**, 041603 (2001).

[168] M. B. Tsang et al., *Isotopic Scaling in Nuclear Reactions*, Phys. Rev. Lett. **86**, 5023 (2001).

[169] D. R. Bowman et al., *Space-Time Characteristics of Fragment Emission in the E/A = 30 MeV ^{129}Xe+^{nat}Cu Reaction*, Phys. Rev. **C52**, 818 (1995).

[170] M. A. Lisa et al., *Observation of Lifetime Effects in Two-Proton Correlations for Well-Characterized Sources*, Phys. Rev. Lett. **71**, 2863 (1993).

[171] I. S. Gradshteyn and I. M. Ryzhik, *Table of Integrals, Series, and Products*, Academic Press, New York, 1979.